UNIVERSITA' DEGLI STUDI DI VERONA

GRADUATE SCHOOL OF

Natural Sciences and Engineering

DOCTORAL PROGRAM IN

Nanoscience and Advanced Technologies

Cycle XXXIV/ 2018

Sb_2Se_3 thin film solar cells via low temperature thermal evaporation technique.

Coordinator	: Prof. Adolfo Speghini
Tutor	: Prof. Alessandro Romeo
Co- Tutor	: Dr Elisa Artegiani
Doctoral Student	: Vikash Kumar

Acknowledgment

In pursuit of this academic endeavour, I feel that I have been especially fortunate as inspiration, guidance, direction, co-operation, love and care all came in my way in abundance and it seems almost an impossible task for me to acknowledge the same in adequate terms.

On this auspicious moment I give profound thanks to all concerned who have extended their selfless guidance to assist in completing my research work. First my most sincere gratitude and deep devotion goes to my supervisor Prof. Alessandro Romeo, who gave me encouragement, courage, continuous support and care to accomplish this work. I thank him for giving his valuable insight at every stage of work because of which I got good results.

I am also thankful to Dr Elisa Artegiani and Dr Prabeesh Punathil who also helped me in the lab by counselling to overcome bottleneck issues during the work. I am also thankful to the other members of the department for extending their co-operation specially to Dr Laura Marcazzan who was always there to help in matters related to administration. I am also thankful to University of Verona for giving me the opportunity and financial support to complete my research work and obtain a Ph.D.

Dedicated to
My
Mother and Father.

Abstract

There has been a lot of anomalies in the climate in recent years. The situation is getting worse with every passing day, this alarming situation is the talk of the town amongst the world's scientific community. There has been a consistent search for cleaner and sustainable source of energy which can replace the conventional fossil fuel. To this date renewable energy such as solar, wind, ocean, hydrothermal are in application. Among these, solar photovoltaic (PV) is the most effective and widely used one due to its abundant availability and zero contribution to pollution. In order to harness this energy conventional wafer based solar cells were used which have high cost of production and a longer by back time. Second generation thin film based solar cells are the talk of the time as they can be produced with less consumption of material and energy and hence are economical. Three materials are currently in the market; they are amorphous silicon (a-Si), cadmium telluride (CdTe) and copper indium gallium selenide (CIGS). Amongst them, CIGS has shown the highest efficiency of above 20% in laboratory scale, while CdTe has the highest market share. A drawback with CIGS and CdTe technologies is the use of scarce and expensive elements indium and tellurium.

It is therefore clear that these are issues which are of concern for long-term availability of CdTe and CIGS. It is in this context; investigations have been initiated all over the world for an alternative, abundant and non-toxic absorber material. Antimony chalcogenide (Sb_2Se_3, Sb_2S, $Sb_2(S,Se)_3$) are promising absorber materials for thin film photovoltaic cells due to their high absorption coefficient ($>10^4 cm^{-1}$) and optimum direct band gap (~1.2eV). Sb_2Se_3 has excellent optoelectronic properties with low processing temperature these are key factors responsible for the growing interest within the PV community. The best performing cells have reached above 10% till date.

This thesis entitled "Sb_2Se_3 thin film solar via low thermal evaporation technique" is a detailed study of the fabrication of Sb_2Se_3 absorber films by low temperature thermal evaporation technique. Films have been as deposited, vacuum annealed as well selenized and studied in detail in this thesis. The studies included in the thesis are divided into eight chapters.

List of Papers Published in International Journals.

1. Analysis of Se Co-evaporation and Post-selenization for Sb_2Se_3 based solar cells. Vikash Kumar, Elisa Artegiani, Prabeesh Punathil, Matteo Bertoncello, Matteo Meneghini, Fabio Piccinelli, and Alessandro Romeo. ACS Applied energy materials 4(11) (2021) 12479-12486.

2. Raman Spectroscopy and in situ XRD Probing of the Thermal Decomposition of Sb_2Se_3 Thin Films. Kumar Arun, Kumar Vikash, Romeo Alessandro, Wiemer Claudia, Mariotto Gino. Journal of Physical Chemistry *C* 125(2021) 19858–19865.

3. Effects of post-deposition annealing and copper inclusion in superstrate Sb_2Se_3 based solar cells by thermal evaporation. Vikash Kumar, Elisa Artegiani, Arun Kumar, Gino Mariotto, Fabio Piccinelli, Alessandro Romeo. Solar energy 193 (2019) 452-457.

List of Conference Papers.

1. Low temperature co-selenised antimony selenide (Sb_2Se_3) based solar cells by vacuum evaporation. V. kumar, E. Artegiani, P. Punathil and A. Romeo, 38 th European Photovoltaic Solar Energy Conference and Exhibition (EU-PVSEC 2021).

2. Analysis of Selenization processes for Antimony selenide solar cells by vacuum evaporation. V.kumar, E. Artegiani, P.Prabeesh, A.Romeo, 37th European Photovoltaic Solar Energy Conference and Exhibition(EU-PVSEC 2020).

3. Antimony Selenide based solar cells by Vacuum evaporation. V.kumar, E.Artegiani, A.Romeo, 36th European Photovoltaic Solar Energy Conference and Exhibition (EU-PVSEC 2019).

CONTENTS

Chapter 1
Introduction and Motivation

1. Introduction.

1.1 The global need for sustainable energy sources.

In classical thermodynamics energy is defined as the capacity to do work. Energy can be associated directly or indirectly with the evolution, growth and survival of all living beings. Energy plays vital role in the human welfare and economic development of a country. Indisputably, humanity depends on energy, without it the proper functioning of our society would be impossible. The current global electricity consumption accounts to nearly 23,398 TWh which [1].There is increase in energy consumption day by day, due to quick advancement and growing world population. Historically, fossil fuels (coal, petroleum and natural gas) have dominated our energy production. Today roughly 80% of our energy is supplied by fossil fuels; nuclear energy provides 5%, and the remaining share, which constitutes nearly 14%, is from renewable sources (biomass, wind, hydro, solar) [2] shown in fig. 1.1.

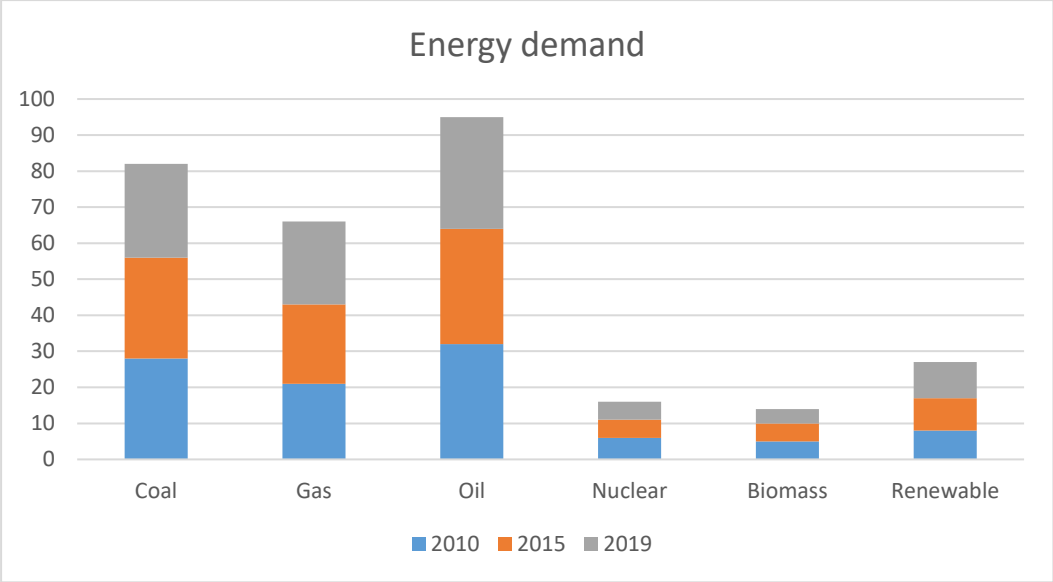

Figure 1.1 Energy demand graph of last ten years [2].

Development of technologies which are not fossil fuels based is the current requirement in order to minimize pollution or environmental problems during the

energy generation stage. The global electricity demand is outweighed and thus harnessing it by means of photovoltaics is an extremely challenging and attractive prospect. Solar is a powerful renewable source: the energy that reaches the earth in one hour is enough to meet the global needs of one year. It can be used directly or indirectly for energy supply. Fig 1.2 presents the solar radiation spectrum at both the top of Earth's atmosphere and at sea level.

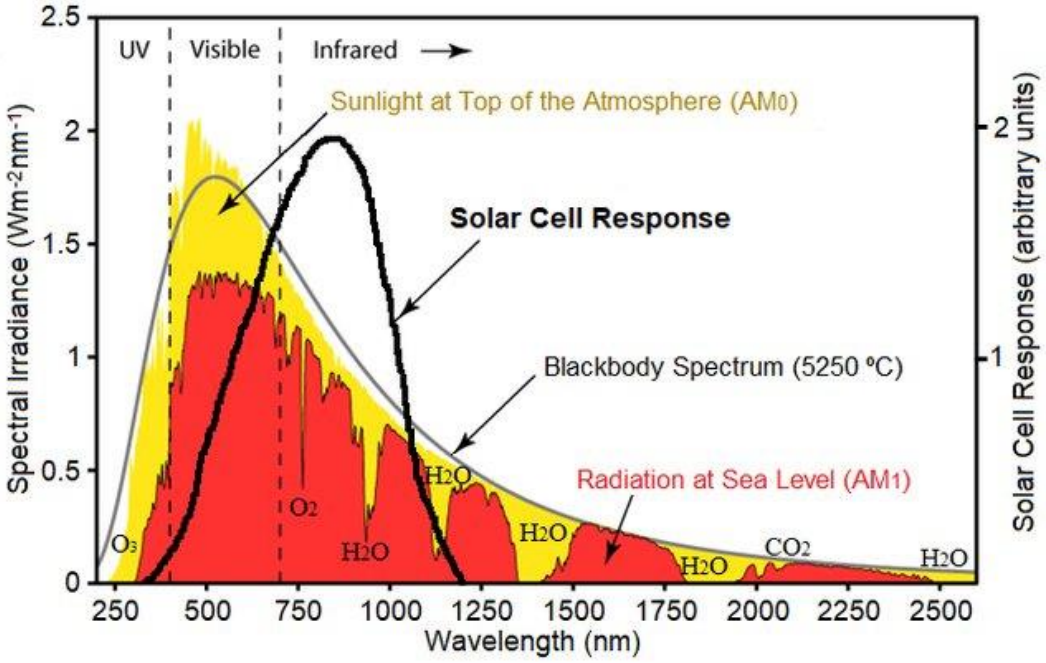

Figure 1.2. Solar radiation spectrum for direct light at both the top of Earth's atmosphere (yellow area) and at sea level (red area) [3].

Solar spectrum can be divided into three regions (I) UV which is on the left and extends up to 400 nm, (II) Visible which is in the range of 400-700 nm and (III) Infrared which is beyond 700 nm. The yellow portion depicts the sunlight without any atmospheric absorption. The red band is the primary sunlight energy that is available at the sea level. There is some deterioration from yellow to red in the figure: 1367 W/m^2 reaches the Earth's top, but after consecutive losses it reduces to 1000 W/m^2 near the sea level.

Solar energy is essentially useful and exploited in two contexts: solar thermal and photovoltaics. Solar thermal reflectors concentrate the light on absorbers that convert it into heat, which is transmitted to an internal fluid that can be used to generate

electricity or for other purposes [4]. Providing clean and sustainable energy is, the main driving force. As such, solar PV must strive to outperform fossil fuel technologies sufficiently enough to provide ample financial incentive to replace the already established modes of energy generation.

1.2 P-N Junction.

A p-n junction consists of two semiconductor regions with opposite doping. First,we consider two separate pieces of semiconductor - one being n-type and the other being p-type. The n-type material has large numbers of free electrons or negatively charged that can move through the material. Similarly, for the p-type material, there are large numbers of free holes or positively charged that can move through the material. The doped n-type and p-type semiconductor materials are electrically neutral.

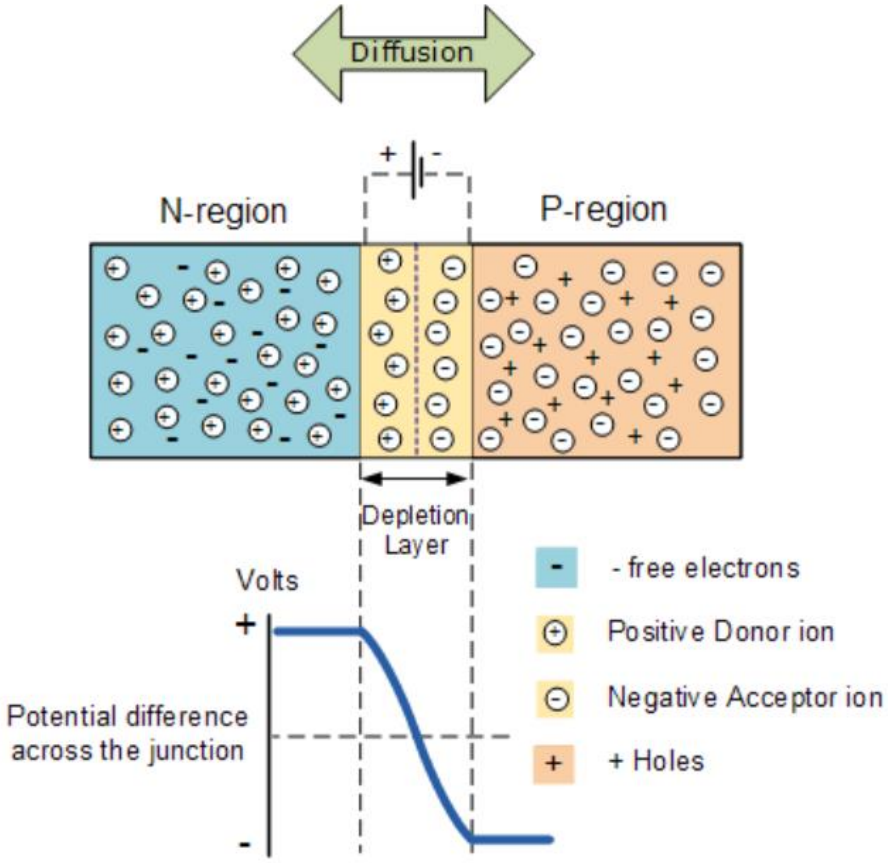

Figure 1.3. Working of a p-n junction [5].

Now when the n-type and the p-type materials are mergerd together they behave differently with the formation of p-n junction. Upon joining them together a large density gradient exists between both sides of the p-n junction. The free electrons from the donor impurity atoms begin to migrate across the newly formed junction to fill up the holes in the p-type region producing negative ions. However, because the electrons moves from the n-region to the p-region , they leave behind positively charged donor ions (N_D) on the negative side and now the holes from the acceptor impurity migrate across the junction in the opposite direction into the region where there are large numbers of free electrons [5–7].

The charge density of the p-type along the junction is filled with negatively charged acceptor ions (N_A), so consecutively the charge density along the n-type becomes positive. This charge transfer of electrons and holes across the p-n junction is known as diffusion. The width of the p and n layers depends on doping with acceptor density N_A, and donor density N_D, respectively.

The process continues until the number of electrons which have crossed the junction have enough charge to repel any more charge carriers from crossing the junction. State of equilibrium occurs producing a barrier zone near the junction as the donor atoms repel the holes and the acceptor atoms repel the electrons. The area around the **p-n junction** is known as the depletion region.

If a positive voltage and negative voltage is applied to the p and n side, the current will flow depending upon the magnitude of the applied voltage this is forward biased configuration. If a negative voltage is applied to the p-type side and a positive voltage to the n-type side, then this configuration is a reverse biased one.

1.2.1 Solar cell operation.

Photovoltaics is the direct conversion of photons into electricity, using semiconductor materials that exhibit photovoltaic effect. The photovoltaic effect was first introduced by A. E Becquerel in 1839. After a long research in this field, researchers could convert photons into electrons (light into electricity). Mainly, solar cell is a *p-n*

junction under illumination. The operation of a photovoltaic cell or solar cell requires three basic attributes:

- ***Excitation of charge carrier***

When solar cell is illuminated under sunlight, electrons in the ground state (valence band) absorb light energy and jump to higher energy levels (conduction band). This generates electron-hole pairs .

- ***Separation of charge carrier***

By juxtaposing *p*- and *n*-type semiconductors, a *p*-*n* junction is formed: electrons flow from the region with highest concentration (*n*) to the one with lowest (*p*) (diffusion), creating a potential across the junction. Drift and diffusion are the two major mechanism in a p-n junction [8]. Minority carriers, electrons in *p* side and holes in *n* side move to *n* and *p* side through the junction, respectively.

- ***Collection of charge carrier***

Separated electrons and holes flow through front and back contact, respectively, and power the external circuit [9,10].

1.2.2 Solar cell parameters.

In this section we will discuss the cell parameters such the current-voltage (IV) curve, short circuit , open circuit voltage, fill factor, efficiency etc.

1.2.2.0 I-V curve.

The I-V characteristic curve shown in fig 1.4 shows the current voltage characteristics of a photovoltaic (PV) cell, module. It gives a detailed description of its solar energy conversion ability. Knowing the electrical I-V characteristics of a solar cell, or panel is critical in determining the device's performance. The power delivered by a single solar cell is the product of its output current and voltage (IxV). If the multiplication is done, point for point, for all voltages from short-circuit to open-circuit conditions, the power curve above is obtained for a given radiation level.

The equation for the IV curve in the first quadrant is:

$$I = I_L - I_o [\exp (qV/nKT) - 1] \quad \text{(i)}$$

The -1 term in the above equation can be neglected. The exponential term is mostly >> 1 except for voltages below 100 mV. at low voltages, the I_L dominates the I_o .So the equation can be re written as.

$$I = I_L - I_o [\exp (qV/nKT)] \quad \text{(ii)}$$

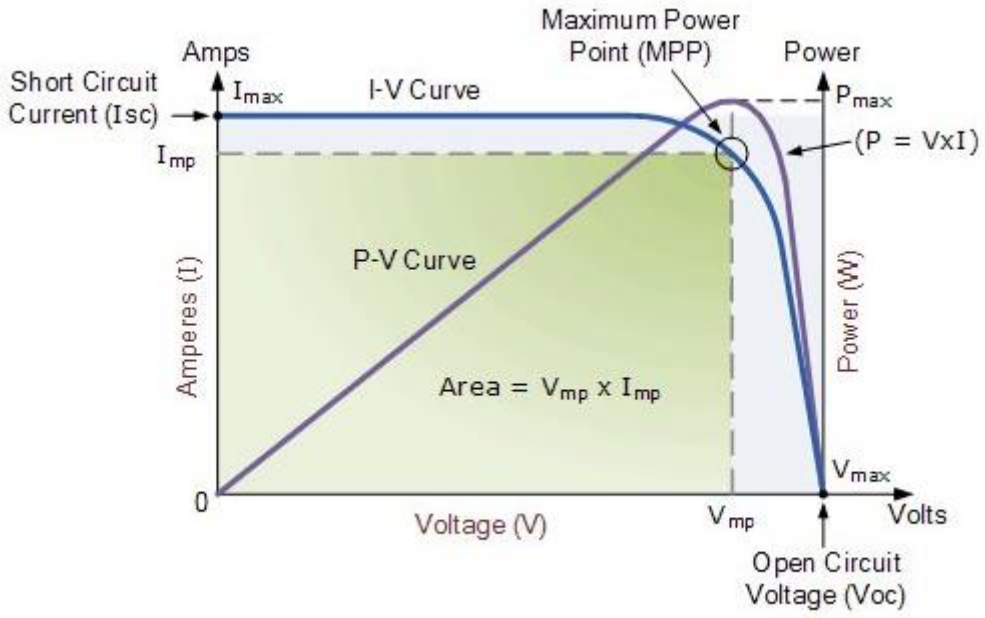

Figure 1.4 Current voltage (IV) cure of a solar cell [11].

The power curve shown above the maximum power (P_{MP}) where the solar cell gives the maximum power output P_{MAX} occurs at a voltage of V_{MP} and a current of I_{MP} [9,12].

1.2.2.1 Short ciruit current.

The short-circuit current is the current through the solar cell when the voltage across the solar cell is zero. For an ideal solar cell, the short-circuit current and the light-generated current are identical and the short-circuit current is the largest current which can be drawn from the solar cell.

The short-circuit current depends on several factors [13]:

1. Area of the solar cell
2. Number of photons
3. Optical properties
4. Collection probability

1.2.2.2 Open circuit voltage.

The open circuit voltage is the maximum voltage that the array provides when the terminals are not connected to any load. This value is higher than V_{mp}. The equation for V_{oc} can be calculated by setting the net current equal to zero and is given below in equation (iii)

$$Voc = \frac{nkT}{q} \ln (I_L/I_o + 1) \qquad \text{(iii)}$$

The above equation indicates that V_{oc} is linearly dependent on temperature and saturation current of the solar cell [14–16].

1.2.2.3 Fill factor.

The fill factor (FF) is the relationship between the maximum power that is actually provided under normal operating conditions and the product of the open-circuit voltage and short-circuit current ($P = V_{oc} \times I_{sc}$) [17,18].

The FF is calculated by equation (iv),

$$FF = \frac{V_{mp} \times I_{mp}}{V_{oc} \times I_{oc}} \quad \text{(iv)}$$

FF is the measure of the area of the largest rectangle which will fit in the IV curve as shown in the figure 1.5 below.

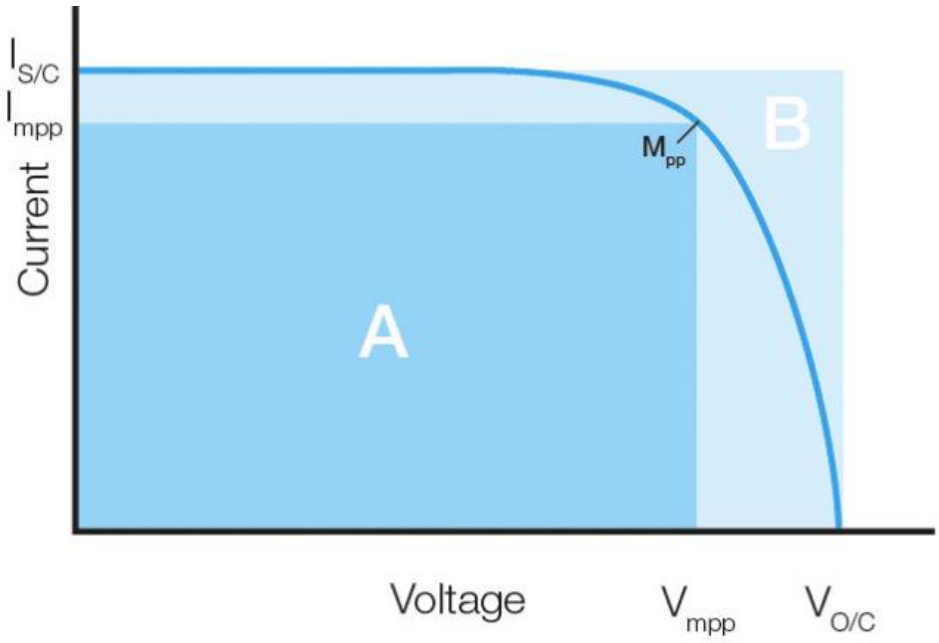

Figure 1.5 Graph showing the FF [19].

1.2.2.4 Efficiency.

The efficiency is the most important parameter which describes performance of a solar cell. Efficiency can be defined as the ratio of energy output to energy input from the sun. The efficiency of solar cell depends on the spectrum, intensity of incident light and the operating temperature of the solar cell. Terrestrial solar cells are measured under standard AM1.5 and temperature of 25°C. The efficiency of a solar cell is determined by the ratio of incident power which is converted to electricity and is represented below in eq (v, vi):

$$P_{max} = V_{oc} \text{ x } I_{sc} \text{ x } FF \quad \text{(v)}$$

$$\eta = (V_{oc} \times I_{sc} \times FF) / P_{in} \quad \text{(vi)}$$

Where:

V_{oc}: open circuit voltage.

I_{sc}: short-circuit current.

FF: fill factor.

η : efficiency.

1.3 Solar PV technology.

PV cells are made of light-sensitive semiconductor materials that use photons to dislodge electrons to drive an electric current.There are many ways in which the solar cells have been classified some of which we will be discussing briefly here. Primarily classifications are based on generation of solar cell.

(a) First generation solar cells: These are also called conventional or traditional solar cells where wafers of cells are made of crystalline silicon. This is till date the predominant technology and includes materials such as monocrystalline and polycrystalline silicon.

(b) Second generation solar cells: These are thin film based solar cells and they CdTe, CIGS, CZTS, CZTSSe, Sb_2Se_3, Sb_2S etc. and they can be commercially significant in building integrated photovoltaics.

(c) Third generation solar cells: These cells include emerging photovoltaics. Most of them have not yet been commercially applied as they are still in the research or development phase. Many use organic materials, often organometallic compounds as well as inorganic substances [20].

The other classification of the solar cell which we are going to discuss is shown in fig 1.6. and is based on silicon, thin film and organic. Competitive devices are already on the market with good performance, however there is still room for novel high efficiency and, low-cost materials. The absorber layer is the heart of a *p-n* junction solar cell, where the main part of electron-hole pairs production takes place. The cells, in fact, also take their name from this layer: example,

silicon (Si), cadmium telluride (CdTe), copper indium gallium diselenide (CIGS), etc. Most of the technologies are based on non-organic materials. The dominant technology is based on crystalline silicon, where the typical cell thickness is around 200-300 microns, because of the low absorption coefficient of the absorber. On the other hand, CdTe, CIGS, a-Si, GaAs, etc, can be used in thin film form (2-10 microns) due to their higher absorption coefficient. As compared to competing technologies, crystalline silicon is the most mature because of its abundant availability and oldest presence in the semiconductor industry. Furthermore, it possesses an optimal band gap of nearly 1.1 eV, which however is indirect, implying the low absorption coefficient. Modules with efficiencies up to 26 % are now available on the market, and in recent years the price has rapidly decreased. Nevertheless, a further price reduction, related to production cost, is difficult to achieve due to the high purity of the material required for solar cell application. Thin film technologies are potentially cheaper: unlike crystalline silicon devices, the modules can be fabricated in a single manufacturing line. In fact, these absorber materials are suitable for simpler and faster deposition techniques [21].

Moreover, they are direct band gap semiconductors, therefore with a higher absorption coefficient that allows to absorb all the light in a few microns of thickness. This leads to the use of a much smaller amount of material, ensuring further economic savings. Another huge advantage of thin film technology is its compatibility with the use of cheap substrates such as ordinary soda lime glass, but also and above all flexible substrates such as ultra-thin glasses, metal foils and polymers [22,23]. This allows to manufacture light and flexible modules that have greater potential for integration into buildings. On the other hand, the most mature thin film technologies are limited by the scarcity of rare earths elements such as In and Te.

Shockley-Queisser (S-Q) model predicts that an absorber layer with a band gap (E_g) ≈1.14 eV possesses a maximum power-conversion efficiency (PCE) around 33 %. CdTe and CIGS have achieved a conversion efficiency of 22.1 % and 23.4 % respectively, slightly lower than crystalline silicon [21,24]. Organic and

perovskite solar cells are another attractive area in PV technology; their efficiency has recently exceeded 18 % and 25 % respectively [25,26]. However, stability is the main concern for these devices.

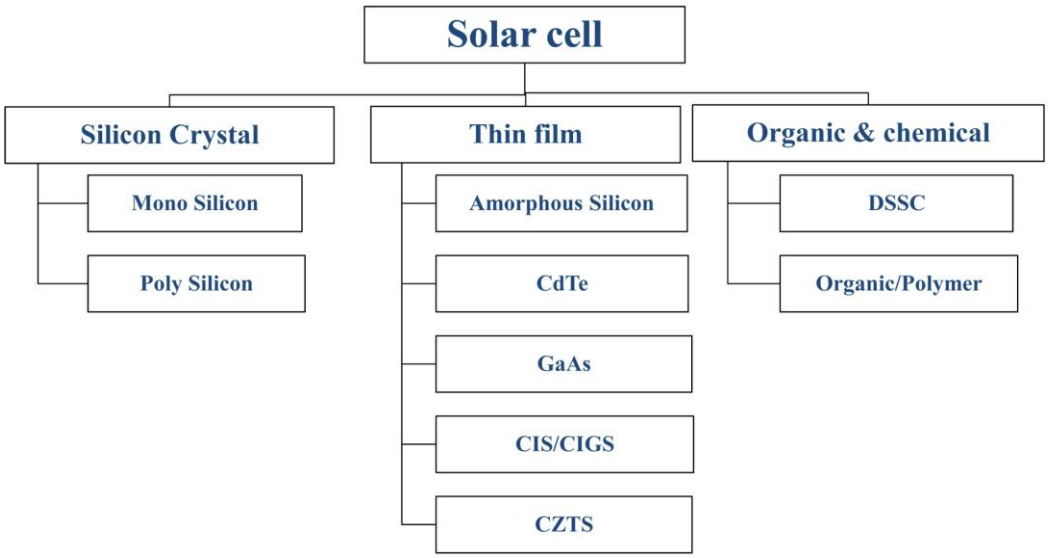

Figure 1.6 Classification of solar cell.

The third class of thin-film solar cells that is largely discussed is the one that includes chalcogenides. Chalcogenides are all chemical compounds consisting of at least one chalcogen anion of group 16. The five elements that belong to group 16 are: oxygen (O), sulfur (S), selenium (Se), tellurium (Te), and the radioactive polonium (Po). Cu_2SnS_3 [27], $CuSbS_2$ [28], $Cu_2ZnSnSe_4$ [29], $CuSbSe_2$ [30], $Sb_2(S,Se)_3$ [31], Sb_2Se_3 [32], CdTe [33] and CIGS [34] are some of the earth-abundant metal chalcogenides with attractive PV properties. These materials can act as good alternative absorbers by being cost-effective, environmentally friendly and having good stability and high theoretical efficiency.

The kesterite $Cu_2ZnSn(S,Se)_4$ (CZTS/Se), a I_2-II-IV-VI_4 quaternary compound, is a promising absorber material for low-cost thin film solar cells. This material has a band gap of 1.4 - 1.5 eV and an absorption coefficient $>10^4$ cm^{-1} in the visible region. CZTS based solar cell is expected to have a theoretical efficiency of more than 30 % and has been being extensively investigated in recent years. CZTS can be obtained from the chalcopyrite CIGS, by substituting the trivalent In/Ga with a bivalent Zn and tetravalent Sn. Each component of CZTS is abundant in earth's crust (Cu: 50ppm, Zn:

75ppm, Sn: 2.2ppm, S: 260ppm) and these elements possess extremely low toxicity. On the other side, in the case of CIS/CIGS, the abundance of indium and selenium in the earth's crust is very low. The highest conversion efficiency reported for CZTSSe solar cells is 11.0 % by IBM [35].

1.4 Conclusion.

Solar power is energy from the sun that is converted into thermal or electrical energy. The energy moves from sun and reaches the earth surface where human collects it through solar collectors and convert it into desirable form of energy. To convert sunlight into electricity solar panels, photoelectric technologies and thermoelectric technologies are used. Next-generation solar cells could be more useful present day most solar cells use silicon as the absorber material to absorb light, however the drawbacks in the material have led scientists to investigate alternate materials to enhance the light absorption capabilities. New generation of solar cells made from chalcogenide and perovskite have shown the potential to convert solar energy effectively and have the potentials to replace silicon.

1.5 Reference.

[1] Székely GJ, Rizzo ML. Energy statistics: A class of statistics based on distances. Journal of statistical planning and inference. 143(2013):1249-72.

[2] Global Energy Review 2019, Glob. Energy Rev. 2019. (2020). https://doi.org/10.1787/90c8c125-en.

[3] C.A.F. Ramos, A.N. Alcaso, A.J.M. Cardoso, Photovoltaic-thermal (PVT) technology: Review and case study, IOP Conf. Ser. Earth Environ. Sci. 354 (2019). https://doi.org/10.1088/1755-1315/354/1/012048.

[4] R.K. Musunuri, D. Sánchez, R. Rodriguez, Solar Thermal Energy Engineering, Renew. Energy. (2007).

[5] K.K. Ng, pn Junction Diode, Complet. Guid. to Semicond. Devices. (2015). https://doi.org/10.1109/9780470547205.ch1.

[6] M.B. Structures, No 主観的健康感を中心とした在宅高齢者における健康関連指標に関する共分散構造分析Title, (n.d.).

[7] R. Nicholson, Understanding the context, Springer Optim. Its Appl. 102 (2015) 37–56. https://doi.org/10.1007/978-3-319-15030-7_3.

[8] M. Zeman, Chapter 3. Semiconductor materials for solar cells, Syllabus Course Sol. Cells. (n.d.) 3.1-3.27. https://ocw.tudelft.nl/wp-content/uploads/Solar-Cells-R3-CH3_Solar_cell_materials.pdf.

[9] R. Bright, Selecting cable strain reliefs, Electron. Prod. (Garden City, New York). 50 (2008).

[10] Y. Growth, Solar Cell : Working Principle & Construction (Diagrams Included) What is a Solar Cell ? Construction of Solar Cell Working Principle of Solar Cell x V-I Characteristics of a Photovoltaic Cell Materials Used in Solar Cell, (2020).

[11] Kadhum JA. Design and construction of a tracking device for solar electrical systems. Journal of Scientific and Engineering Research. 2018;5(7):225-36..

[12] I. Curve, I-V Curves : A Guide to Measurement Measuring and Analysing an I-V Curve Examples of I-V Curves Resistor, (2019) 1–4.

[13] Lecture, FUNDAMENTAL PROPERTIES On today ' s menu fundamental solar cell properties dark current Efficiency internal and external QE, 8 (2015) 25–32.

[14] A. Augusto, S.Y. Herasimenka, R.R. King, S.G. Bowden, C. Honsberg, Analysis of the recombination mechanisms of a silicon solar cell with low bandgap-voltage offset, J. Appl. Phys. 121 (2017). https://doi.org/10.1063/1.4984071.

[15] R.A. Sinton, A. Cuevas, Contactless determination of current-voltage characteristics and minority-carrier lifetimes in semiconductors from quasi-steady-state photoconductance data, Appl. Phys. Lett. 69 (1996) 2510–2512. https://doi.org/10.1063/1.117723.

[16] M.Y. Levy, C. Honsberg, Rapid and precise calculations of energy and particle flux for detailed-balance photovoltaic applications, Solid. State. Electron. 50 (2006) 1400–1405. https://doi.org/10.1016/j.sse.2006.06.017.

[17] A. Jain, A. Kapoor, Exact analytical solutions of the parameters of real solar cells using Lambert W-function, Sol. Energy Mater. Sol. Cells. 81 (2004) 269–277. https://doi.org/10.1016/j.solmat.2003.11.018.

[18] M.A. Green, Solar cell fill factors: General graph and empirical expressions, Solid State Electron. 24 (1981) 788–789. https://doi.org/10.1016/0038-

1101(81)90062-9.

[19] Seaward, What is the PV Fill Factor, 44 (2021) 3511. https://www.seaward.com/gb/support/solar/faqs/31170-what-is-the-pv-fill-factor/#:~:text=Fill factor (FF) is the,by the light blue box.

[20] M. Arun, Types of Solar Cells and its Applications, IJSDR1902043 Int. J. Sci. Dev. Res. 4 (2019) 260–267. www.ijsdr.org.

[21] A. Romeo, E. Artegiani, CdTe-Based Thin Film Solar Cells: Past, Present and Future, Energies. 14 (2021). https://doi.org/10.3390/en14061684.

[22] A. Salavei, D. Menossi, F. Piccinelli, A. Kumar, G. Mariotto, M. Barbato, M. Meneghini, G. Meneghesso, S. Di Mare, E. Artegiani, A. Romeo, Comparison of high efficiency flexible CdTe solar cells on different substrates at low temperature deposition, Sol. Energy. (2016). https://doi.org/10.1016/j.solener.2016.09.004.

[23] J. Ramanujam, D.M. Bishop, T.K. Todorov, O. Gunawan, J. Rath, R. Nekovei, E. Artegiani, A. Romeo, Flexible CIGS, CdTe and a-Si:H based thin film solar cells: A review, Prog. Mater. Sci. (2019). https://doi.org/10.1016/j.pmatsci.2019.100619.

[24] M. Nakamura, K. Yamaguchi, Y. Kimoto, Y. Yasaki, T. Kato, H. Sugimoto, Cd-Free Cu(In,Ga)(Se,S)2 thin-film solar cell with record efficiency of 23.35%, IEEE J. Photovoltaics. 9 (2019) 1863–1867. https://doi.org/10.1109/JPHOTOV.2019.2937218.

[25] J. Wang, J. Zhang, Y. Zhou, H. Liu, Q. Xue, X. Li, C.C. Chueh, H.L. Yip, Z. Zhu, A.K.Y. Jen, Highly efficient all-inorganic perovskite solar cells with suppressed non-radiative recombination by a Lewis base, Nat. Commun. 11 (2020) 1–9. https://doi.org/10.1038/s41467-019-13909-5.

[26] Q. Liu, Y. Jiang, K. Jin, J. Qin, J. Xu, W. Li, J. Xiong, J. Liu, Z. Xiao, K. Sun, S. Yang, X. Zhang, L. Ding, 18% Efficiency organic solar cells, Sci. Bull. 65 (2020) 272–275. https://doi.org/10.1016/j.scib.2020.01.001.

[27] L.L. Baranowski, K. McLaughlin, P. Zawadzki, S. Lany, A. Norman, H. Hempel, R. Eichberger, T. Unold, E.S. Toberer, A. Zakutayev, Effects of Disorder on Carrier Transport in Cu2SnS3, Phys. Rev. Appl. 4 (2015) 1–9. https://doi.org/10.1103/PhysRevApplied.4.044017.

[28] H. Dittrich, A. Bieniok, U. Brendel, M. Grodzicki, D. Topa, Sulfosalts - A new class of compound semiconductors for photovoltaic applications, Thin Solid

Films. 515 (2007) 5745–5750. https://doi.org/10.1016/j.tsf.2006.12.071.

[29] S. Hartnauer, S. Körbel, M.A.L. Marques, S. Botti, P. Pistor, R. Scheer, Research Update: Stable single-phase Zn-rich Cu2ZnSnSe4 through in doping, APL Mater. 4 (2016). https://doi.org/10.1063/1.4953435.

[30] D.S. Ginley, Pursuant to the DOE Public Access Plan, this document represents the authors' peer-reviewed, accepted manuscript. The published version of the article is available from the relevant publisher. ^, (n.d.) 1–45.

[31] R. Tang, X. Wang, W. Lian, J. Huang, Q. Wei, M. Huang, Y. Yin, C. Jiang, S. Yang, G. Xing, S. Chen, C. Zhu, X. Hao, M.A. Green, T. Chen, Hydrothermal deposition of antimony selenosulfide thin films enables solar cells with 10% efficiency, Nat. Energy. 5 (2020) 587–595. https://doi.org/10.1038/s41560-020-0652-3.

[32] V. Kumar, E. Artegiani, A. Kumar, G. Mariotto, F. Piccinelli, A. Romeo, E ff ects of post-deposition annealing and copper inclusion in superstrate Sb 2 Se 3 based solar cells by thermal evaporation, Sol. Energy. 193 (2019) 452–457. https://doi.org/10.1016/j.solener.2019.09.069.

[33] Romeo A, Artegiani E. CdTe-Based Thin Film Solar Cells: Past, Present and Future. Energies. 2021 Jan;14(6):1684.

[34] Wang Y, Lv S, Li Z. Review on incorporation of alkali elements and their effects in Cu (In, Ga) Se2 solar cells. Journal of Materials Science & Technology. 2022 Jan 10;96:179-89.

[35] W. Wang, M.T. Winkler, O. Gunawan, T. Gokmen, T.K. Todorov, Y. Zhu, D.B. Mitzi, Device characteristics of CZTSSe thin-film solar cells with 12.6% efficiency, Adv. Energy Mater. 4 (2014) 1–5. https://doi.org/10.1002/aenm.201301465.

Chapter 2
Solar cell Fabrication and Characterization

In this chapter, a framework of deposition methods and brief descriptions of the equipment's used to characterize thin films and opto-electronic devices produced in this work are given. Substrate is also important factor for thin film deposition, therefore before describing the deposition methodology and characterization. A brief summary of substrates used have been discussed.

2.1 Substrate and cleaning process and selection:

For thin film deposition, mostly flourine doped tin oxide (FTO) or ZnO:Al (ZAO) coated on soda lime glass (SLG) is used as front electrode because of its good conductivity, availability and low cost. Physical adhesion and other physical properties of thin film depend on substrate surface; therefore, it must be cleaned for obtaining high quality thin films. The substrates are glass squares with a side of 3 cm, and 4 mm thick.

Particulates were removed using compressed argon gun, followed by mechanical washing to remove greasy residues from its surfaces by using commercial soap. The substrate is then rinsed with deionized water and subsequently placed in a beaker with deionized water on a hot plate at 400 °C for 30 minutes. In the last phase of its cleaning, the sample undergoes four subsequent ultrasonic baths (10 minutes per bath) with acetone and isopropyl alcohol. The substrate is finally dried with the compressed argon gun, to remove the solvent and to avoid its evaporation from the substrate.

In our work we used the commercially available substrate, we adopted superstrate configuration. Transparent conducting films are used as electrodes when we are looking for low resistance electrical contacts without blocking light. Transparent materials possess wide bandgap whose energy value is greater than those of visible light. As such, photons with energies below the bandgap value are not absorbed by these materials and visible light passes through it**.**

2.2 Thin film deposition:

Thin films are important for advanced applications in optical, telecommunication and energy storage devices. The crucial issue for all applications is the morphology and stability. The morphology of thin films strongly depends on deposition techniques [1]. Good quality films can be obtained by two common depositions: physical and chemical depositions. It can be summarized as shown in Table 1. Thin film undergoes the following series of steps [2]:

a) Conversion from the solid phase to the vapor phase.

b) Transportation of that vapor from source to substrate.

c) Condensation of vapor on the substrate.

Table 2.I. Various deposition techniques.

Physical deposition	Chemical deposition
1. Evaporation techniques a. Vacuum thermal evaporation. b. Electron beam evaporation. c. Laser beam evaporation. d. Arc evaporation. e. Molecular beam epitaxy. f. Ion plating evaporation. 2. Sputtering techniques a. Direct current sputtering (DC sputtering). b. Radio frequency sputtering (RF sputtering)	1. Sol-gel technique 2. Chemical bath deposition 3. Spray pyrolysis technique 4. Plating a. Electroplating technique. b. Electroless deposition. 5. Chemical vapor deposition (CVD) a. Low pressure (LPCVD) b. Plasma enhanced (PECVD) c. Atomic layer deposition (ALD)

2.2.1 Thermal evaporation:

Thermal evaporation is a basic PVD technique, and it works on the principle of mean free path of particles. Evaporating particles travel in the medium and collide with the particles which are present in environment. Therefore, in order to increase the path length of the particles, it is necessary to minimize the unwanted gas particles in the deposition environment. In case of thermal evaporation, material is heated up to its evaporation temperature in vacuum (~10^{-6} mbar). The material to be evaporated is kept on the boat or filament and a high current is passed to heat it (shown in figure 2.1a). Boat or the filaments are made of molybdenum or tungsten.

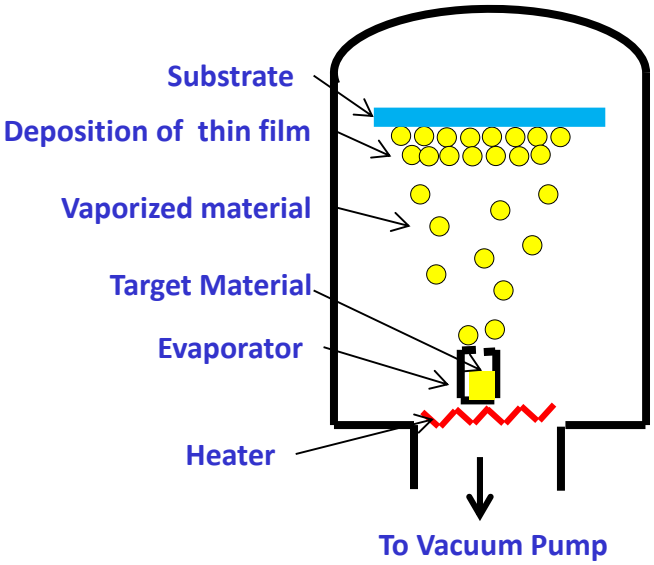

Figure 2.1 (a) Schematic diagram [3].

By controlling the vacuum, current and the distance between the source and substrate one can control the quality of film. The mass evaporation rate from a free surface follows the Hertz-Knudsen relation shown in eq.(i), where α_v the sticking coefficient, m is the evaporant molecular mass, P* the equilibrium vapor pressure of the evaporant which is a function of the temperature (T) and pressure (P).

$$\Gamma = \alpha_v \cdot (P^* - P) \cdot \sqrt{m/2\pi mkBT} \qquad \text{(i)}$$

Evaporation from a free surface is isotropic whereas evaporation through an orifice is angular. Fig. 2.2 depicts the Knudsen cell the mass deposition rate per unit of

condensation surface dM_c/dA_c and per unit of time can be calculated using equation (ii):

$$dM_c/dA_c \cdot dt = (\Gamma/\pi r^2) \times cos\ \phi \times \cos\theta.$$

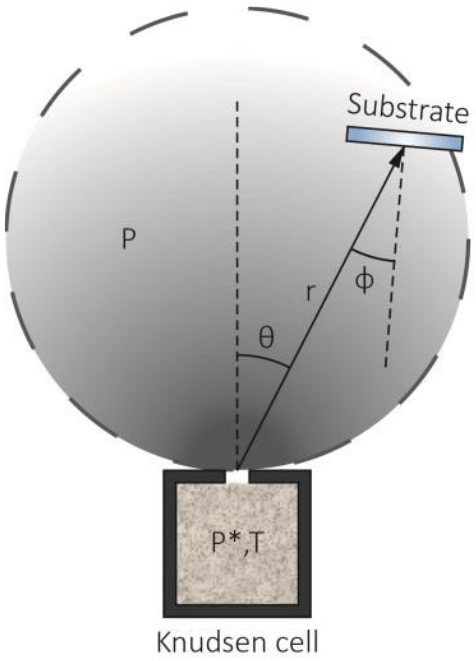

Figure 2.2 Evaporation from a Knudsen cell. The vapour condenses on a substrate located at a distance r from the source [4].

Γ is the mass evaporation rate and it depends on the source temperature, chamber pressure, evapforant vapour pressure, molecular mass and the geometrical factors. The process of thin film deposition follows the following steps (1) Adsorption: in addition to the momentum, energy must be also considered (energy exchange between the impinging atoms or molecules and the substrate surface). (2) Diffusion: molecules that are trapped in a weakly-adsorbed state spend their residue momentum diffusing from site to site, upon the surface (physisorption). (3)Nucleation and growth: adsorbed molecules could then interact one another forming nucleation centres which grow into clusters (island); clusters then coalesce into new bigger clusters [5]. For the deposition of Sb_2Se_3 films we used our home developed thermal evaporation unit.

2.2.2 Sputtering:

Sputtering is a well-known technique used in lab as well as in industries. Almost all materials can be sputtered using sputtering. Sputtering is very popular because of uniform deposition, good film quality, adhesion control and compositional control. Sputtering can be used as DC and RF configurations according to the requirement. It can be categorized according to configuration of sputter guns as well; such as co-sputtering, single gun sputtering and sequential sputtering (many sputtering guns). In the present study single gun sputtering and sequential reactive sputtering with DC power supply have been used to deposit thin film.

2.2.2.1 DC magnetron sputtering:

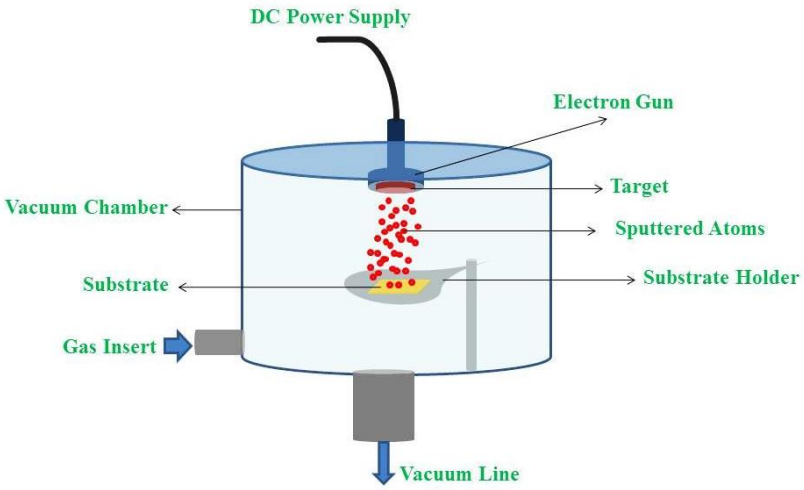

Figure 2.3 Schematic of DC sputter deposition system [3].

The basic construction of a DC sputter is shown in Figure 2.3 DC sputtering system is composed of a pair of planar electrodes the cathode and the anode. The front surface of cathode is covered with target material to be deposited. The substrates are placed on the anode. The sputtering chamber is filled with argon at 1-10 × 10^{-3} mbar. Under the application of dc voltage glow discharge is maintained between the electrodes. The Ar^{+} ion generated in the glow discharge are accelerated at the cathode and the sputter target, resulting in deposition of thin films on the substrates. To increase the ionization rate, a ring magnet is used below the target in the magnetron sputtering. The magnetic field in the magnetron is oriented parallel to the cathode surface. The

local polarity of the magnetic field is oriented such that E x B drift of the emitted secondary electrons forms a closed loop. In magnetron sputtering, substrate heating is eliminated due to lesser bombardment of secondary electrons.

2.2.3 Spin Coating:

Spin coating is solution-based technique which provides better distribution of elements at molecular scale. It has also been an age-old technology to deposit uniform thin film over a flat substrate. A small puddle of a fluid resin is put on the center of the substrate and then the substrate is spined at high speed. The centripetal acceleration causes the resin to spread across the substrate and eventually off the edge leaving behind a thin film of resin. The properties of the films and thickness depends on the viscosity, drying rate, surface tension etc. Spin coating is widely used in micro-fabrication. Spin coating has four distinct stages.

(a) Dispense stage: In this process the resin is deposited onto the substrate by either static dispense or dynamic dispense.

(b) Substrate acceleration stage: This is the second stage and is characterized by expulsion of fluid from the surface due to the rotational motion. The spin speed can range from 1500 to 9000 rpm which can last from 10 sec to a minute.

(c) Substrate spinning stage with a constant rate and viscous fluid: In this stage of the process the fluid gradually gets thinner. The fluid thinning is uniform with solutions containing volatile solvents, often it is possible to see interference colors.

(d) Stage spinning at a constant rate with solvent evaporation: In the final stage of the spinning process the fluid thickness reaches a point where the viscosity effects yield minor net fluid flow. The coating effectively “gels” as the solvents [6][7].

Drying (Solvent evaporation): After the thin film deposition by spinning an additional drying step is added. Drying removes all the remaining volatiles substance and increases the stability of the film. Mostly drying is carried out on a hot plate at varying temperature and time. For the present work we used spin coater as shown in fig 2.4 for TiO_2 deposition.

Figure 2.4 Spin coater.

2.2.4 Chemical Bath deposition:

Chemical bath deposition is the simplest methods of thin film depositions among the chemical methods. The process requires a vessel which contains the solution (an aqueous solution of chemical) and the substrate on to which the deposition takes place [8]. Chemical bath deposition technique works on the controlled precipitation of the desired compound from the solution on to the substrate. Generally, three stages are involved in chemical bath deposition.

a) Generation of the species (ions, atoms, molecules)
b) Transport of these species
c) Condensation of these on the substrate.

Thin film coated on the substrate can be by ion-by-ion or cluster-by-cluster mechanism [9]. At the earlier stage ion-by-ion growth mechanisum is more prominent which results in a compact and highly oriented film which is then followed by, fast formation of the colloids (material being depsoited) leading to the cluster-by-cluster deposition [10]. Due to good surface coverage and nm range thickness CBD is preferred. Ideally a vessel containing solution, a stirring mechanism, a heating mechanism with thermostat and a suitable substrate on which deposition takes are required.

Figure 2.5 Spin coater.

2.3 Solar Cell characterization

Superstrate Sb_2Se_3 thin films were characterized to study the optical, electrical properties, phase analysis was done by X-ray diffraction (XRD), AFM, FE-SEM, Raman spectroscopy, and transmittance studies were conducted by UV-Vis Spectrometer.

2.3.1 X-ray Diffraction Technique (XRD):

X-ray diffraction is a non-destructive analytic technique which gives first-hand information about the materials crystalline phase. The structural properties such as lattice parameters, crystallite size, lattice strain, preferred orientation, phase composition, etc can be measured. When a monochromatic X-ray beam is incident on a sample surface, a portion of the beam will be scattered in all direction by the electrons associated with an atom or ion that lies within the path of the beam. Diffraction of monochromatic x-rays takes place for particular angles which satisfy the Bragg law [11]. Bragg's condition is such that when a monochromatic intense beam of light falls on parallel lattice planes of a crystal, the incident beam is reflected from various planes of crystal. This can happen only when the extra distance travelled

be an exact multiple of the wavelength of the radiation. This means that the peak of each wave is aligned with each other. The Bragg's condition is:

$$2\, d_{hkl} \mathrm{Sin}\, \theta_B = \lambda_{hkl} \qquad \text{(i)}$$

Were,

d_{hkl} =The perpendicular distance between lattice planes and miller indices (h, k, l).
$2\theta_B$ = The deviation of the diffracted beam from the incident beam.
λ_{hkl} = Wavelength of the incident x-ray of the sample.

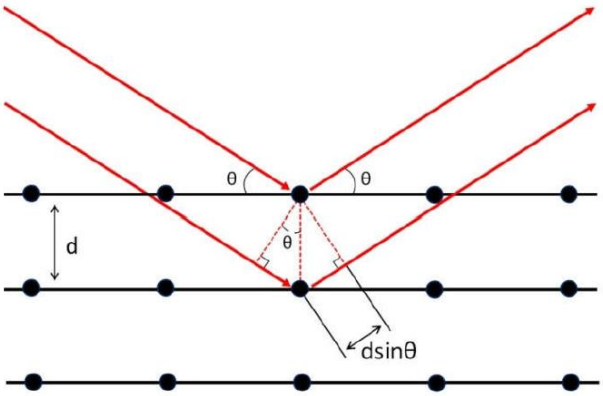

Figure 2.6 Schematic diagram of diffraction in a crystal [12].

As the wavelength is fixed for X-ray, we get the d value by varying θ, every phase has a particular d value. Thus, by matching the d value from the JCPDS database we can identify the different phase formed. For thin films generally low angle XRD is to be performed by keeping the incident beam at low angle which allows investigation of phases of interest by minimizing the substrate interference.

All the XRD patterns were collected at the Solid-State Chemistry Laboratory of the University of Verona with a Thermo ARL XTRA powder diffractometer and is shown in fig 2.6. The instrumentation works in Bragg-Brentano geometry, and it is equipped with an X-Ray source emitting at a wavelength of λ = 1.5418 Å by exciting a Cu-anode. The diffraction pattern is recorded with a Si (Li) solid state detector cooled by Peltier effect.

2.3.1.0. Estimation of Crystallite Size:

X-ray diffraction can also be used for determination of crystallite size. The analysis of the crystallite size has been carried out using the broadening of the X-ray diffraction peaks. Peak broadening can be observed due to instrumental effect, finite crystallite size and also due to the strain within the crystal lattice[13]. The crystallite size can be calculated by using Scherer's formulae and Williamson- Hall plot. The Scherrer's formula is given as:

$$D = \frac{\kappa\lambda}{ß\, Cos\, \theta} \qquad \text{(ii)}$$

Where *D* is the crystallite size, *k* is a constant and depends upon the shape of the crystallite size (=0.89, assuming the circular grain), λ is the wavelength of the X-ray, θ is Bragg's diffraction angle and. *β* = Full width at Half Maximum (FWHM) which is defined as:

$$ß = \sqrt{ßobs^2 + ßins^2} \qquad \text{(iii)}$$

Here *βobs* is the FWHM of observed pattern. *βins* is the observed recording from XRD pattern. It is a powerful tool for nanocrystalline material as here the crystallite size is equal to grain size.

2.3.2. Atomic Force Microscopy (AFM):

To study the morphology of a material microscopy is the most important instrument. Traditionally, optical microscopy based on the transmission of light supported by different glasses and lenses has been largely used for the investigation of morphological properties at micrometric size scale. A new type of microscope which can measure extremely small forces on an atomic scale has been developed. AFM works like the methods used with stylus profilometer and tunneling microscope as shown in fig 2.7. The sharp tip of the AFM is brought in proximity of the sample and scanned over it to map the contours of the surface. AFM measures the variations in

the force between the tip and the surface atoms[14–16]. AFM provides a 3D profile of the surface on a nanoscale. Van der Waals force is the dominant interaction force at a short probe-sample distance. During contact with the sample, the probe predominately experiences repulsive Van der Waals forces (contact mode). As the tip moves further away from the surface attractive Van der Waals forces are dominant (non-contact mode).

There are three primary imaging modes in AFM [17][18]:

(1) Contact mode AFM (< 0.5 nm probe-surface separation): The cantilever bends when the spring constant of the cantilever is less than surface. The tip undergoes repulsive force. By maintaining a constant cantilever deflection, the force between the probe and the sample remains constant. Contact mode study is good for rough samples and friction analysis.
(2) Intermittent contact (tapping mode, 0.5-2 nm probe-surface separation): A high resolution image like the contact mode is generated. However, in this mode the cantilever is oscillated at its resonant frequency. The probe slightly "taps" on the sample surface during scanning. A constant oscillation amplitude (20-100 nm) is maintained during the semi contact mode. Tapping is very helpful in studding biological samples.
(3) Non-contact mode (0.1-10 nm probe-surface separation): As the name suggests in the non-contact mode the probe does not contact the sample surface during scanning. The change in amplitude due to the attractive vander waal force can be monitored by a feedback loop.

The thin films morphology was studied in our laboratory with a NT-MDT Smena-A Atomic Force Microscopy as shown in fig 2.7 below in semi-contact mode with NSG01 high resolution non-contact golden coated silicon. AFM probes from NT MDT with nominal radius < 10 nm (cantilever length about 125 μm).

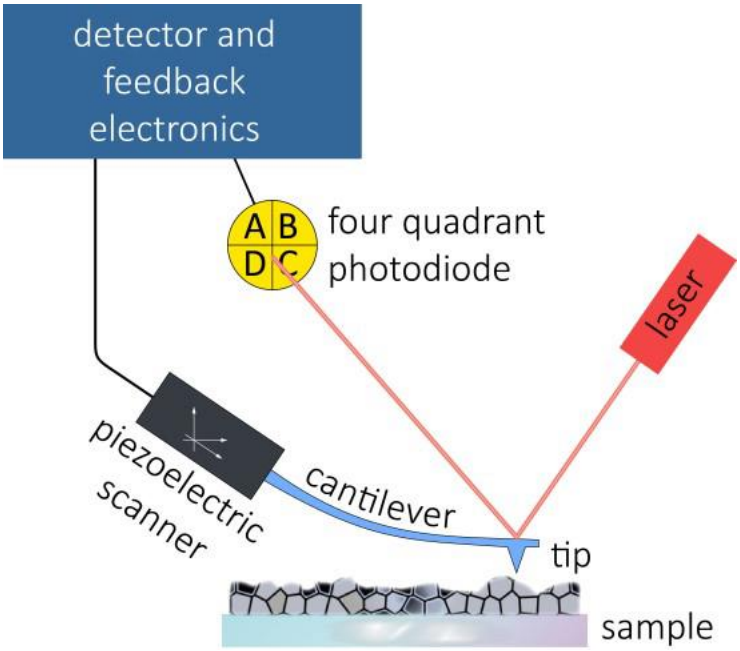

Figure 2.7 Block diagram of an Atomic Force Microscope [4].

2.3.3. Scanning Electron Microscopy (SEM):

Scanning electron microscopy (SEM) is a versatile instrument available for the study of the topography, morphology and composition of the bulk as well as nanomaterials with higher resolution. The SEM and EDX analyses were carried out at the Department of Neurosciences of the University of Verona with a Philips FEI XL30 Environmental Scanning Electron Microscope equipped with an Energy Dispersive X-ray analyser. Typical electron beam energies are in the 10 - 25 kV range.

When a sample is irradiated by electron beam, secondary electrons are emitted from the surface of the sample. SEM requires a source of electron, series of electromagnetic coil, vacuum system, detectors and a display device. In a SEM series of electromagnetic coils are used as lenses to focus the electron beam. Under high vacuum electrons are generated by a field emission source and are accelerated in a field gradient. The high energetic electron beam passes through electromagnetic lenses, focusing onto the specimen. The electron beam is scanned over the specimen surface by deflection coils. As a result, there is interaction of electrons with the atoms of the sample which then after produces signals that contains information about the

sample's surface morphology and topography. There is various type of signals produced which includes secondary electrons (ejected by low energy electron striking), backscattered electrons (ejected by high energy electron striking) and photons.

The secondary electron has energy less than 50 eV due to the less energy range; it is responsible for the topological contrast and provides information about the surface morphology. The backscattered electrons (BSE) are highly energetic beam of electrons which are elastically scattered from the sample. These BSE images provide information about the distribution of different elements in the sample. Samples which are electrically conductive do not need any preparation for samples which are non-conducting or insulating in nature require some special treatment otherwise there would be accumulation of charges at the surface and images will be blurred. In order to have a conducting surface a thin metal (Au, Pt) coating of about 10nm is done on the sample as metal films are highly stable and their secondary electron yield is also higher. Other ways to eliminate surface charging can be having a low accelerating voltage and low vacuum SEM observation [19–22].

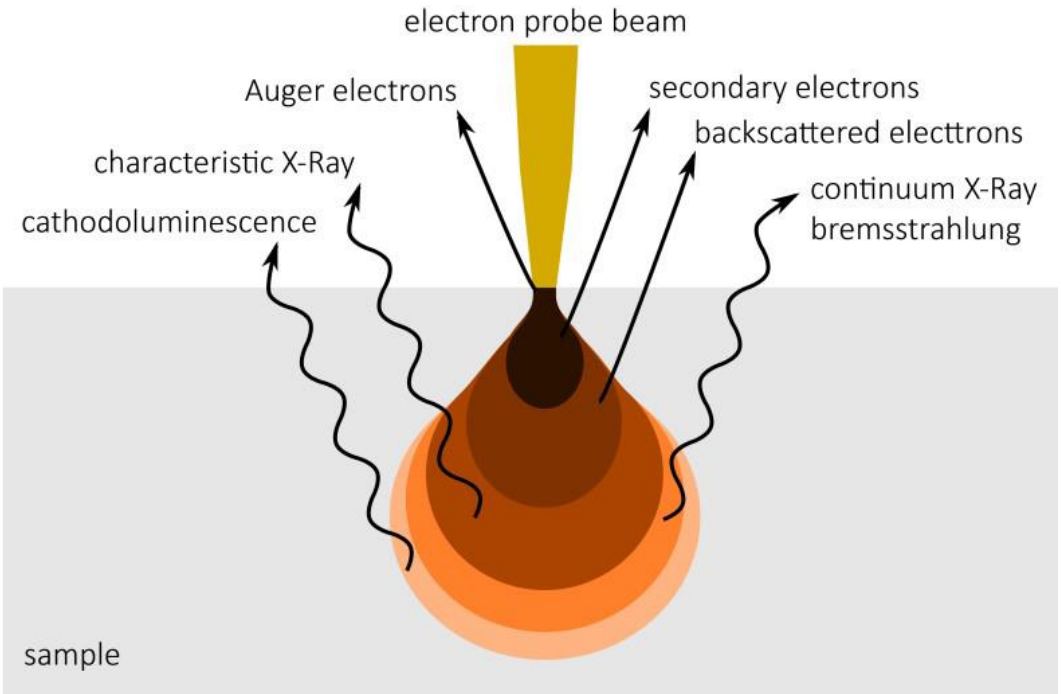

Figure 2.8 Electron-matter interaction [4].

2.3.4. Raman Spectroscopy:

When an electromagnetic radiation with energy $h\nu_0$ is irradiated on a molecule or crystal, it may be transmitted, absorbed or scattered. Most of the photons are elastically scattered i.e., the scattered photons have the same energy and wavelength, as that of the incident photons, but a very tiny portion (1 in 10^7) of the scattered radiation is shifted to a different wavelength, this inelastic scattering is known as Raman scattering. Raman spectroscopy is a non-destructive material characterization technique employed to study vibrational, rotational, and other low frequency modes in a system. It is quite sensitive to structural disorder. It relies on inelastic scattering, of monochromatic light, usually from a laser in the visible, near infrared, or near ultraviolet range. The laser light interacts with phonons or other excitations in the system, resulting in the energy of the laser photons being shifted up or down. The phonon modes in the system are identified by the shift in energy levels. Raman spectroscopy is a form of vibrational spectroscopy, quite like infrared (IR) spectroscopy, however IR bands arise from a change in the dipole moment of a molecule whereas Raman bands arise from the change in polarizability.

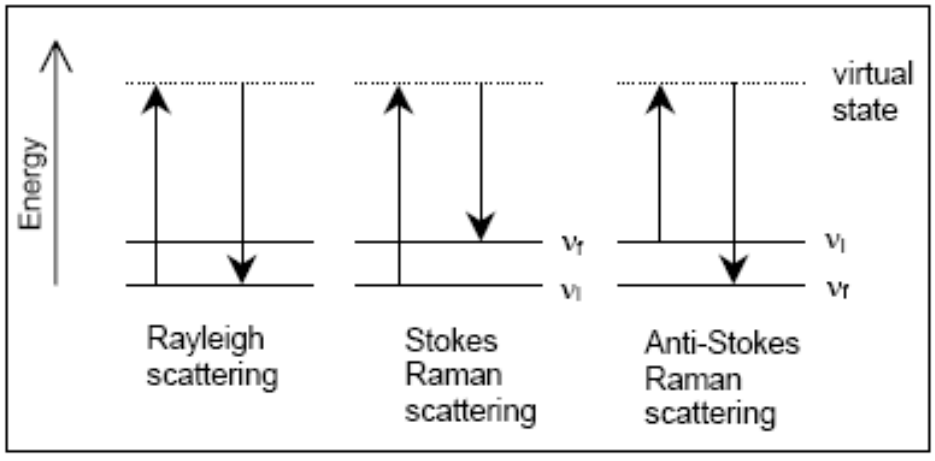

Figure 2.9 Raman Scattering[23].

At room temperature the thermal population of the vibrational excited states is very low. The initial state is the ground state, and the scattered photon will have lower

energy (longer wavelength) than the excited photon. This shift in stokes is what is observed in Raman spectroscopy. Stokes occurs when the final energy level is higher than the initial level, while anti-Stokes occurs when the final energy level is lower than the starting level. Stokes scattering is much more common than anti-Stokes scattering and so it is ignored and removed by the filters. Only Stokes Raman scattering is commonly used in spectroscopy. As mentioned above, Raman is a form of vibrational spectroscopy. A Raman spectrum is a plot of the intensity of Raman scattered radiation as a function of its frequency difference from the incident radiation (cm^{-1}). Raman spectroscopy is useful for chemical analysis for several reasons: it exhibits high specificity, it is compatible with aqueous systems, no special preparation of the sample is needed, and the timescale of the experiment is short [24–27].

The Raman spectroscopy measurements shown in the present text were recorded at the Raman Laboratory of University of Verona. A He-Ne laser emitting at 632.8 nm was used to excite the samples. An 80x objective (NA = 0.75) is used to focus the laser beam to a spot size of about 1 μm^2. The acquisition system is a Horiba-Jobin-Yvon Lab Ram HR800 Micro-Raman microprobe (focal length of 80 cm, grating of 600 lines/mm) with a cryogenically cooled CCD detector. A notch filter is used to filter the elastically scattered light.

2.3.5. UV-Visible Spectroscopy:

Spectroscopy involves the investigation of electromagnetic field with the matter. UV-Vis-IR spectroscopy is an important tool which exploits light in all the regions of the electromagnetic spectrum (ultraviolet, visible, and near infrared). The wavelength of UV ranges from 100 to 400 nm. In a standard UV-Vis spectrophotometer, a beam of light is split; one half of the beam is directed through the sample, and the other half through the reference as shown in fig 2.10. The instrument is designed so that it can make a comparison of the intensities of the two beams as it scans over the desired region of wavelengths. When light passes through or is reflected from a sample, the amount of light that is absorbed is the difference between the incident radiation (I_o) and the transmitted radiation (I) which can be expressed as either transmittance or absorbance[28–31]. Transmittance is generally expressed in percentage or fraction and is defined as:

$$T = I / I_o \quad \text{or} \quad \%T = (I / I_o) \times 100 \qquad \text{(i)}$$

Absorption is the inverse of the transmittance and is denoted by A

$$A = (1/ \log T) \qquad \text{(ii)}$$

The standard UV-Vis spectrophotometer used in our university is UV-2550 works on both reflectance and transmittance mode. By measuring absorption coefficient, we can calculate band gaps of the material. Knowledge of band gaps is extremely critical which making selection of the semiconductor material to be used for PV application.

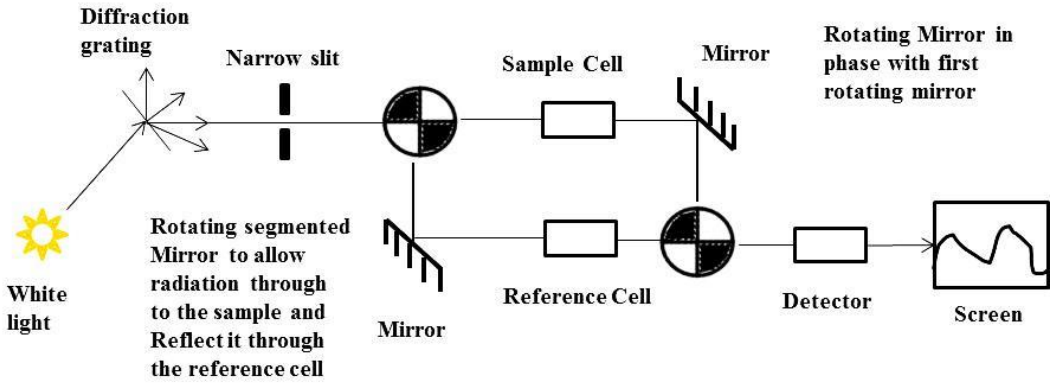

Figure 2.10 Schematic diagram of Uv-Vis spectroscopy [3].

2.4 Reference

[1] V.O. Sukmanov, O. V. Radchuk, M.Y. Savchenko-Pererva, N. V Budnik, Оптичний П'Єзометр Та Прецизійні Дослідження Властивостей Харчових Продуктів При Тисках Від 0 До 1000 Мпа, J. Chem. Technol. 28 (2020) 68–87. https://doi.org/10.15421/082009.

[2] K. Seshan, Handbook of Thin Film Deposition Techniques Principles, Methods, Equipment and Applications, Second Editon, 2002. https://doi.org/10.1201/9781482269680.

[3] O.P. Singh, Effect of Sodium on Optical, Structural, Morphological and

Electronic Properties of Cu 2 ZnSn(S/Se) 4 Thin Films for Electronic Device Applications, (n.d.).

[4] Tin Sulphide Solar Cells By Thermal Evaporation, (2014).

[5] Use ALL Your Product Data, (n.d.).

[6] M.D. Tyona, A theoritical study on spin coating technique, Adv. Mater. Res. 2 (2013) 195–208. https://doi.org/10.12989/amr.2013.2.4.195.

[7] Spin Speed, Coating. (n.d.).

[8] D. Mugle, G. Jadhav, Short review on chemical bath deposition of thin film and characterization, AIP Conf. Proc. 1728 (2016). https://doi.org/10.1063/1.4946648.

[9] P.O. Brien, J. Mcaleese, bath deposition of ZnS and CdS, J. Mater. Chem. 8 (1998) 2309–2314.

[10] L. Fan, P. Wang, Q. Guo, H. Han, M. Li, Z. Chen, H. Zhao, D. Zhang, Z. Zheng, J. Yang, RSC Advances, RSC Adv. 5 (2015) 10018–10025. https://doi.org/10.1039/C4RA13921F.

[11] P.B. Hirsch, Elements of X-Ray Diffraction, Phys. Bull. 8 (1957) 237–238. https://doi.org/10.1088/0031-9112/8/7/008.

[12] D. Of, P. In, PREPARATION AND CHARACTERIZATION OF SOLUTION PROCESSED KESTERITE Cu 2 ZnSnS 4 THIN FILMS FOR PHOTOVOLTAIC APPLICATIONS, (2018).

[13] 1998 Suryanarayana, Grant Norton, Xray Diffraction: Practical Approach, 2013.

[14] G. Binnig, C. Gerber, E. Stoll, T.R. Albrecht, C.F. Quate, Atomic resolution with atomic force microscope, Epl. 3 (1987) 1281–1286. https://doi.org/10.1209/0295-5075/3/12/006.

[15] A. Alessandrini, P. Facci, AFM: A versatile tool in biophysics, Meas. Sci. Technol. 16 (2005). https://doi.org/10.1088/0957-0233/16/6/R01.

[16] R. Splinter, Action potential transmission and volume conduction, Handb. Phys. Med. Biol. 56 (2010) 5-1-5–9. https://doi.org/10.1201/9781420075250.

[17] Nanosurf, AFM Modes Overview, (2020) 1. https://www.nanosurf.com/en/support/afm-modes-overview.

[18] M. Marrese, V. Guarino, L. Ambrosio, Atomic Force Microscopy: A Powerful Tool to Address Scaffold Design in Tissue Engineering, J. Funct. Biomater. 8 (2017) 7. https://doi.org/10.3390/jfb8010007.

[19] ThermoFisher, Scanning Electron Microscopy Working Principle Table of contents, (2019). https://assets.thermofisher.com/TFS-Assets/MSD/Reference-Materials/WP0016-scanning-electron-microscopy-working-principle.pdf.

[20] A. Kaech, An Introduction To Electron Microscopy Instrumentation, Imaging and Preparation, Cent. Microsc. Image Anal. (2013) 1–26. http://www.zmb.uzh.ch/static/bio407/assets/Script_AK_2014.pdf.

[21] Module I Scanning Electron Microscope (Sem), (n.d.).

[22] A.D. Weiss, Scanning Electron Microscopes., Semicond. Int. 6 (1983) 90–94. https://doi.org/10.1016/s0026-0576(03)90123-1.

[23] V. Kumar, Dedicated To My Beloved Parents, (2015).

[24] V.R. Spectroscopy, D.L. Scattering, Raman Spectroscopy 1. Vibrational Raman Spectroscopy 2. Dynamical Light Scattering 3. Resonance Raman Spectroscopy of Cytochrome C, (2009). http://www.eng.uc.edu/~beaucag/Classes/Characterization/RamanCALTECH.pdf.

[25] A. Of, M4 b r s, (2019) 1–19.

[26] B.R. Instrumentation, Understanding Raman Spectroscopy Principles and Theory Basic Raman Instrumentation Raman Theory Raman Scattering, (2020) 2–7.

[27] D.E. Bugay, H.G. Brittain, Raman spectroscopy, Spectrosc. Pharm. Solids. (2006) 271–312. https://doi.org/10.1380/jsssj.13.79.

[28] Π* (Pi Star) Orbital, (n.d.).

[29] O. T., Fundamentals of modern UV-visible spectroscopy, Hewlett-Packard Co. (1996) 38–61. https://doi.org/10.1017/CBO9781107415324.004.

[30] T. Spectronic, Basic UV-Vis Theory, Concepts and Applications Basic UV-Vis Theory, Concepts and Applications, Protocol. (2012) 1–28.

[31] C. A. De Caro, UV / VIS Spectrophotometry, Mettler-Toledo Int. (2015) 4–14.

Chapter 3
Antimony selenide (Sb_2Se_3)

3.1 Antimony selenide material.

Antimony chalcogenides have emerged as a promising alternative absorber material due to their high stability, high absorption coefficient (>10^4 cm^{-1}), suitable bandgap (1.1 - 1.8 eV), low toxicity and low cost. Antimony chalcogenide solar cells include Sb_2S_3, Sb_2Se_3 and $Sb_2(S_xSe_{1-x})_3$. The best performing Sb_2S_3 solar cells have achieved power conversion efficiencies (PCEs) of 7.5 % [1], while Sb_2Se_3 and $Sb_2(S_xSe_{1-x})_3$ have demonstrated PCEs of 9.2 % [2] and 10.1 % [3], respectively.

Bi_2Se_3, Bi_2Te_3, Sb_2S_3, Sb_2Te_3, Sb_2Se_3 etc. belong to the V-VI inorganic binary compounds family. The excellent optoelectronic properties and low processing temperature exhibited by antimony selenide (Sb_2Se_3) are one of key factors responsible for the growing interest within the PV community. In this chapter we will introduce the Sb_2Se_3 properties which will include crystal structure, electronic structure, electrical properties, point defects, defect chemistry and optical properties for both crystalline and amorphous Sb_2Se_3 materials. Then, we discuss the fabrication and performance of Sb_2Se_3 devices (Section 4), including absorber deposition methods, buffer layers, hole-transport layer and back contacts, and transparent electrode layers. Also, we debate the effect of shunt resistance (R_{Sh}) and series resistance (R_S) on device performance and summarize the results at the present stage, the challenges as well as the future directions of research in Sb_2Se_3 field.

3.2 Structural properties of Sb_2Se_3.

The abundance of Sb and Se elements in the Earth's crust is 0.2 and 0.05 ppm, respectively. Sb_2Se_3 has an orthorhombic crystal structure (a = 11.6330 Å, b = 11.7800 Å, c = 3.9850 Å as the lattice constants and Pnma-62 space group) and the material is derived from Stibnite. In Sb_2Se_3 antimony has a formal oxidation state (+3) and selenium (-2). The bond distance between Sb-Se ranges from 2.576 Å

to 2.777 Å, whereas the separation of the non-bonded Sb-Se begins at 2.98 Å. The Se-Sb-Se bond angle varies between 86.6° and 96.0° while that of Sb-Se-Sb is between 91.0° and 98.9°.

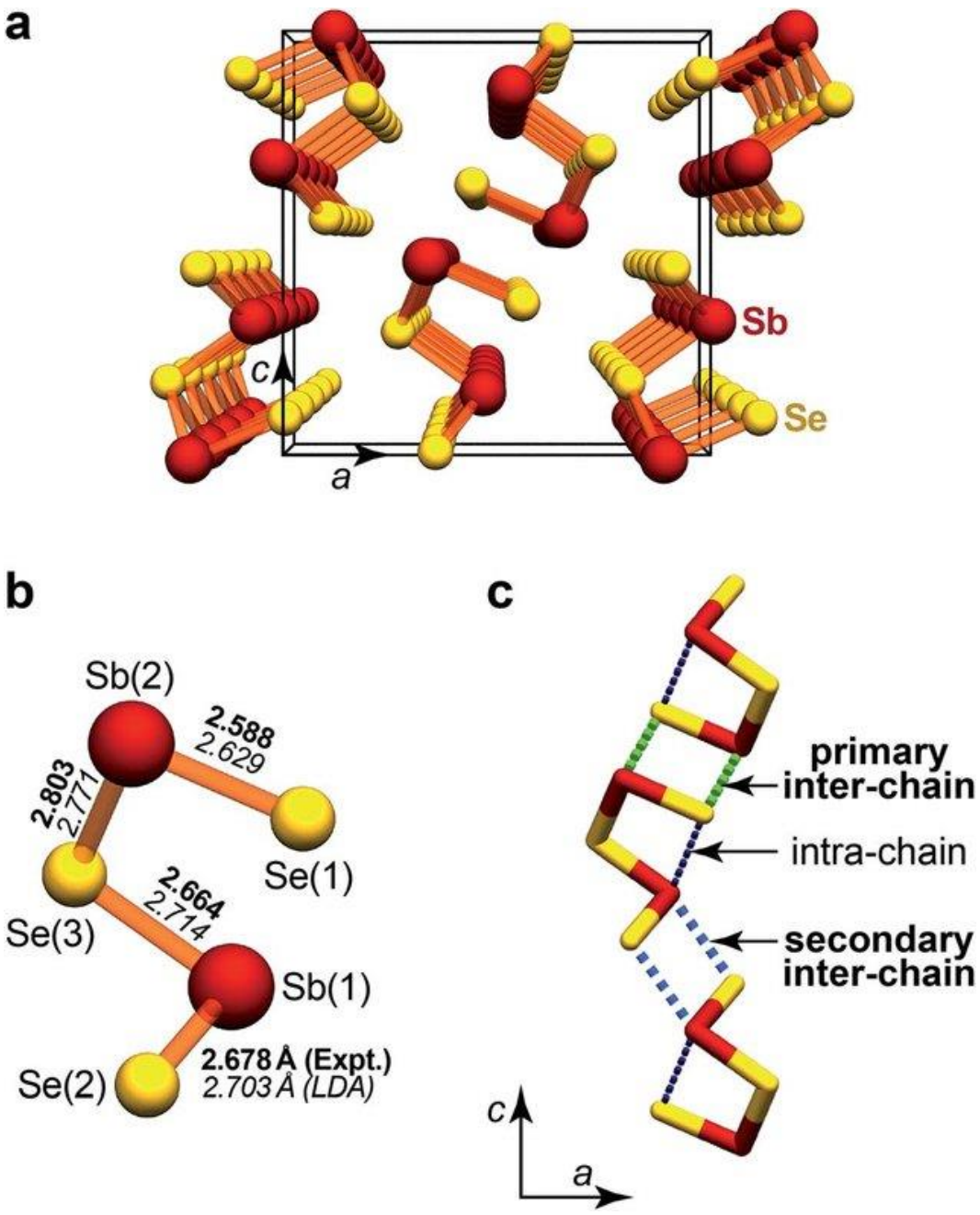

Figure 3.1 Crystal structure of Sb_2Se_3[4] (a) perspective view down the short b-axis, highlighting the infinite chains (b) Fragment from the above chain, with atomic labelling Sb–Se distances (c) Structural drawing emphasizing the weak contacts along the c-axis.

Sb_2Se_3 has a one-dimensional (1D) crystal structure consisting of $[Sb_4Se_6]_n$ units, where the ribbons are bound together by weak Se–Se interactions. The $[Sb_4Se_6]_n$ ribbons assemble through van der Waals forces along a and b axes, whereas strong covalent bond exists inside $[Sb_4Se_6]_n$ nanoribbon [5]. The bonds within the ribbons are much stronger compared to the bonds between the ribbons, which explains the anisotropic carrier transport mechanism. The presence of grain boundaries (GBs) parallel to the ribbons inherently reduces charge-carrier recombination, which is beneficial for PV performance [6]. Sb_2Se_3 is a binary compound that exists in orthorhombic phase at room temperature and ambient pressure. Its low melting point (~ 610 °C) and high vapour pressure allows deposition of high-quality thin films using vacuum evaporation method. Phase pure Sb_2Se_3 material can be obtained at low temperature, paving the way for the manufacturing of flexible solar cells on polymer substrate.

Table 3.I Chalcogenide material parameters [7][8][9][10][11][12].

Properties	CZTS	CZTSSe	CIGS	CIGSe	Sb_2Se_3	Sb_2S_3	$Sb_2(S,Se)$
Crystal structure	Tetragonal	Tetragonal	Tetragonal	Tetragonal	Orthorombic	Orthorombic	Orthorombic
Lattice constants	5.42,10.84, 5.42	a=b=5.40 c=10.846	a=b=5.6–5.8, c=11.0–11.5	a=b=5.6–5.8, c=11.0–11.5	a=11.63 b=11.78 c=3.985	a=11.62 b=11.77 c=3.962	
Space group	$I\bar{4}$/I42m	$I\bar{4}$/I42m	$I\bar{4}2d$	$I\bar{4}2d$	Pnma 62	Pnma 62	Pnma 62
Density (gm/cm^3)	4.56	4.56	5.7	5.7	5.84		
Band gap (eV)	1.4–1.5	1.4–1.5	1.0–1.7	1.0–1.7	1.0-1.17	1.7	1.45-1.7
Absorption coeff. (cm^{-1})	10^4	10^4-10^5	10^4–10^5	10^4–10^5	$>10^5$	$\sim 10^5$	
Carrier concentration	10^{15}–10^{20}	10^{15}–10^{20}	10^{17}–10^{18}	10^{17}–10^{18}	10^{15}	10^{12}	10^{15}-10^{16}

s (cm^{-1})							
Carriers' lifetime majority/minority (ns)	15/2.5	15/2.5	250	-	60		9.1
Melting point (˚C)	990	990	1070-990	1070-990			
Efficiency (%)	8.4	12.6	23.4	-	9.2	6.3	10

3.2.1 Opto-Electronic properties.

From experimental studies it is found that polycrystalline Sb_2Se_3 exhibits band gap around 1.03 eV (indirect) and 1.17 eV (direct) (Si-1.14 eV), which is suitable for an absorber layer for PV cells [13]. In UV-VIS region Sb_2Se_3 has an absorption coefficient (α) greater than 10^5 cm^{-1}, which indicates that a thin film (~400 nm) is sufficient to absorb ~90% of the incident photons. High photocurrent is expected for Sb_2Se_3 as the major portion of the light intensity of the solar spectrum is dispensed in the visible region where the absorption coefficient is quite high. Charge-carrier transport properties are very important for device performance: for Sb_2Se_3 electron mobility and hole mobility is ~15 and ~42 $cm^2V^{-1}s^{-1}$ respectively which are significantly high. Moreover, the minority carriers life time of electrons (τ_e, i.e. the life time of electrons in a p-type absorber) has been determined to be around 67 ± 7 ns using time-resolved transient absorption spectroscopy [14].

The dielectric constant in the IR region (852-1693 nm) of polycrystalline Sb_2Se_3 is in the range of 14.3 to 19.8, which is greater than that of CIGS and CdTe. This means that Sb_2Se_3 has smaller exciton binding energy and that the excitons immediately dissociate into free electrons and holes when excited by a photon [13]. While designing and optimising a PV device the carrier mobility cannot be overlooked. Sb_2Se_3 is a 1D structure with persistent covalent bond along the [hk1] plane and van der Waals bond along [hk0]. Under strong and weak irradiation the diffusion length is in the range of 1.7 to 0.29 μm along the [hk1] direction [14].

3.2.2 Defects.

The most explored absorber materials are Si, GaAs, CIGS, CdTe, CZTS, etc. they have a three-dimensional (3D) crystal structure, which means that they are bonded by both covalent and ionic bonds. Dangling bonds at the grain boundaries (GB) act as recombination centres which this is one of the major limiting factors for high efficiency. A simpler understanding of device operation should prevail for Sb_2Se_3 as it has a 1D crystal structure. The parallel-stacked $(Sb_4Se_6)_n$ ribbons substantially do not provide dangling bonds, even at GBs, which is advantageous for PV application [15]. Defect study becomes critical as they affect the device performance.

Defect mechanism in Sb_2Se_3 has been studied using admittance spectroscopy. First principle calculation and hybrid Density Functional Theory (DFT) have been used. According to first principles calculation three defect states denoted by D1, D2, D3 were found at 352-402 meV, 440-452 meV and 490-606 meV respectively [16]. Deep defect studies carried out for Vacuum transport deposition (VTD) and rapid thermal evaporation (RTE) indicate one electron (E1) and two-hole traps (H1, H2). H1 and H2 are attributed to the antimony vacancy (V_{Sb}) and selenium antisite (Se_{Sb}) defects whereas E1 is attributed to antimony antisite (Sb_{Se}) donor defects. C. Chen et al. found that in both VTD and RTE E1 and H2 have similar defect densities, which led to the formation of the defect pair (Sb_{Se}+Se_{Sb}) [17]. A large amount of selenium vacancies (V_{Se}) is created during thermal evaporation process, due to the decomposition of Sb_2Se_3 and Se loss at high temperatures. Selenium vacancies act as n-type donor defects and exterminate the generated carriers in their trapping state. Sometime an additional post deposition selenization process is performed to attenuate the loss of selenium [5].

According to M. Huang et. al the implementation of first principles calculations for 1D Sb_2Se_3 is complicated and unconventional, since the defect physics employed for three dimensional semiconductors cannot simply be adopted for 1D system. Due to the low symmetry of Sb_2Se_3, Se vacancies on different sites might have different properties, although these types of point defects are very few. The cation-anion

antisites and vice versa defects can be dominant in Sb_2Se_3 due to their high concentration, unlike in binary semiconductors (CdS, CdTe). There are two Sb vacancies (V_{Sb1}, V_{Sb2}), two Se_{Sb} antisites (Se_{Sb1}, Se_{Sb2}), three Se vacancies (V_{Se1}, V_{Se2}, V_{Se3}), and three Sb_{Se} antisites (Sb_{Se1}, Sb_{Se2}, Sb_{Se3}) reported, of which V_{Se1}, V_{Se2}, V_{Se3}, Sb_{Se1}, Sb_{Se2}, Sb_{Se3} are donor and V_{Sb1}, V_{Sb2}, Se_{Sb1}, Se_{Sb2} are acceptor defects [18].

Using hybrid density functional theory for Sb rich and Se rich extremes the reports are contrasting. The literature suggests that defects study of all sites is necessary especially in the case of Se as its behaviour changes with the local environment. A reasonable concentration of V_{Se}, Sb_{Se} and Sb interstitials with formation energy less than 1.5 eV is found for Sb rich condition. Regardless of site, all three V_{Se} act as deep donors and all the three Sb_{Se}
behave as possible trap states for electrons and holes. In Se rich condition the defects move to higher formation energies and the intrinsic defects have lower concentration, which is the reason for the soaring performance of the devices [19].

3.3 Literature review of solar cell fabrication.

Antimony selenide (Sb_2Se_3) has been chosen as absorber material in the fabrication of PV devices due to its potential optoelectronic properties. The synthesis and characterization of Sb_2Se_3 devices using different methods have been extensively explored in the literature, with fewer reports on device performance. To identify the developments in antimony selenide (Sb_2Se_3), we have summarized the number of publications and citations of original research studies from 2000 to 2021. The data plotted below in fig 3.2 have been extracted from Web of Science and Pub med.

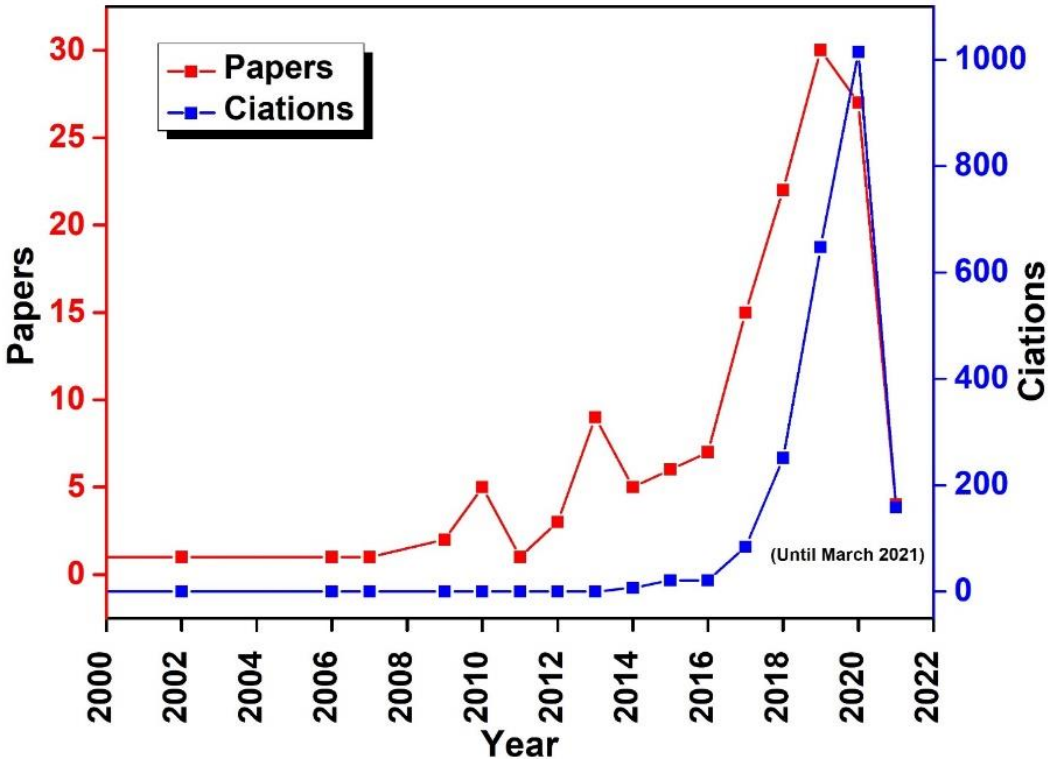

Figure 3.2 Literature review of paper published and citation.

Thin-film solar cells can be manufactured in two configurations: substrate and superstrate. In a substrate configuration a bottom-up approach is used, where the back contact is deposited first and the device ends with a transparent electrode layer, which is exposed to light. In substrate configuration the material on which the stacks are deposited does not have to be transparent; this allows the use of opaque substrates such as flexible thin metallic foils, ceramics, and polymers. The substrate configuration gives possibility of annealing the absorber layer at higher temperatures without affecting the buffer layer. Superstrate configuration is instead deposited with a top-down approach: the fabrication begins by depositing a transparent electrode layer from where the light enters and ends with the deposition of a metallic back contact. In the superstrate configuration the front contact must be highly transparent because the light passes through the substrate and TCO layer to reach the absorber. In the case of the superstrate Sb_2Se_3 configuration (which is the most common) the p-n junction is formed with a n-type semiconductor window layer, usually CdS, which transmits the photons to the Sb_2Se_3. Photons with energy greater than the band gap of

the buffer-window layer (>2.4 eV for CdS) will not contribute to the creation of excitons, due to the parasitic absorption of the buffer. The photo-generated minority-charge electrons move towards the n-type buffer due to the formation of built-in electric field at the p-n heterojunction. Finally, these electrons reach the TCO layer and are collected in the external circuit. On the other hand, the photo-generated holes move through the p-type hole-transport layer and are collected by the back contact.

3.4 Synthesis Methods for Sb_2Se_3.

A chart with various synthesis methods adopted and the respective efficiencies obtained is shown in Table 3 II. The efficiency of Sb_2Se_3 devices varies with the synthesis method, the rate of deposition and the thickness of the absorber layer. Different synthesis techniques such as thermal evaporation, CSS, sputtering, spin coating, etc. can be used to fabricate solar cells in superstrate as well as in substrate configuration. Each method shows its uniqueness, which is observed in the performance of the solar cell.

3.4.1 Vacuum evaporation.

In vacuum deposition technique the raw material is loaded into the vacuum chamber and heated up to its evaporation temperature, this causes the atoms or molecules to vaporize and reach the surface of the substrate. The substrate which is at a lower temperature enables the material to condense on the substrate, resulting in thin film of the evaporated material. Superstrate configuration CdS/Sb_2Se_3 solar cells via thermal evaporation with performance of 1.9 %, Voc = 300 mV, Jsc = 13.2 mA/cm^2 and FF = 48 % were presented in 2014. The presence of defects in the bulk and unfavourable band alignment limits the performance of the devices [20]. Thermally evaporated Sb_2Se_3 films were p-type but selenium deficient. During evaporation Sb_2Se_3 decomposes and the vapour pressure of Se is higher compared to that of Sb and Sb_2Se_3. Se vacancies act as recombination centres and in order to mitigate the recombination losses and increase doping density an additional selenization step was employed, which led to the fabrication of a champion cell with 3.7 % efficiency (Voc = 335 mV, Jsc = 24.4 and FF= 46.8%) [21]. In the same year the same group adopted

substrate structure FTO/Sb_2Se_3/CdS/ZnO/ZnO:Al/Au, and achieved a power conversion efficiency (PCE) of 2.1 % (Voc = 354 mV, Jsc = 17.84 mA/cm^2, and FF = 33.5 %). They were able to develop Sb_2Se_3 films with large grain size without pinholes, depositing it at a low substrate temperature of 290 °C [22]. In order to enhance the junction and passivate the defects near CdS/Sb_2Se_3 interface Y. Liu et. al. added oxygen and found a significant increase in Voc and Jsc. Upon optimization, they successfully obtained a CdS/Sb_2Se_3 solar cell with 4.8 % efficiency, with a Voc = 0.36 V, Jsc = 25.3 mA/cm^2, and FF = 52.5 % [23]. In CdTe based solar cells, $CdCl_2$ treatment in air is always applied to the absorber surface to promote grain growth, passivate grain boundaries and, to reduce the reticular mismatch between the absorber and the CdS window layer [24]. This step significantly improves the heterojunction quality and device performance. In this technology, various chlorine treatments have also been applied to the CdS, obtaining a better recrystallized and more stable film [25–27].

Consequently, this trial was also performed with CdS/Sb_2Se_3 solar cells. L. Wang et. al. performed $CdCl_2$ treatment on CdS, with Sb_2Se_3 films deposited by rapid thermal evaporation (RTE), and reached a certified efficiency of 5.6 % [28]. X. Hu et. al. also performed a similar $CdCl_2$ treatment on CdS coated ITO glass substrate, and the absorber was synthesized by vapour transporting deposition (VTD) method. In this case an additional post deposition annealing step was carried out, that resulted in a better crystallite size, lower defect density and larger built-in voltage with the champion cell reporting an efficiency of 5.72 % [29].

Researchers have also studied ZnO, TiO_2 and SnO_2 as buffer layer due to their stability, non-toxicity, and easy to fabricate. The large band gap of ZnO could lead to a better band alignment with Sb_2Se_3. FTO/ZnO/Sb_2Se_3/Au devices were fabricated by depositing ZnO and Sb_2Se_3 by spray pyrolysis technique and Rapid thermal deposition (RTE), respectively. Sb_2Se_3 films grew with preferred [211] orientation and the stability of ZnO was comparable to that of CdS. A good adhesion was observed between Sb_2Se_3 and ZnO, with few interfacial defects and no oxygen diffusion. Cd diffusion into Sb_2Se_3 was detected at CdS/Sb_2Se_3 interface, causing the degradation of the V_{OC}. The champion ZnO/Sb_2Se_3 solar cell reported an efficiency of 6 % [30]. The limited performance of Sb_2Se_3 solar cells could be due to the

recombination loss caused by the deep defect centres. To mitigate the influence of these recombination sites, the spatial separation of the electron-hole pairs should be improved. C. Chen et. Al. tried to do this by inverting the grain boundaries into n-type by external doping, thus creating an electric field from grain boundaries (GBs) to grain interiors. Cu ions were diffused by soaking the film in aqueous ammonia $CuCl_2$ where the ions moved along the GBs of Sb_2Se_3 (deposited by RTE process). Copper formed interstitial (Cu_i) defects that doped the GBs as n-type. This inversion created a local electric field which facilitated the spatial separation of electrons and holes, enhancing carrier collection and restraining carrier recombination; the process led to a PCE of 7.04 % [31].

3.4.2 Closed space sublimation (CSS).

Close-spaced sublimation (CSS) is a physical vapour deposition technique that can be employed for materials particularly semiconductors, with evaporation temperature below 800 °C. They can be deposited on substrates in both vacuum and atmospheric pressure within a few minutes or seconds depending on the required thickness [32]. These key features have made CSS a widely adopted technique in laboratory as well as on industrial scale, as it is suitable for large scale production. As an example, it is largely used for the industrial manufacturing of CdTe panels. Sb_2Se_3 has also been deposited and studied by CSS technique. K. Shen et. al. fabricated glass/FTO/CdS/Sb_2Se_3/Au superstrate cells, with 550 nm thick absorber layer by CSS. The device had a relatively large and non-ohmic shunt current, which reduced subsequently with the introduction of a high-resistance SnO_2 buffer between FTO and CdS. This increased the efficiency and the open circuit voltage by 38 % and 17 %, respectively, thereby achieving a PCE of 5.18 % [33].

By CSS method, high quality Sb_2Se_3 films were deposited for the first time on Si substrate, both to produce heterojunction solar cells and to explore its potential application in photodetector. The Sb_2Se_3/Si devices exhibited a power conversion efficiency of 1.05 % with a Voc of 0.251 V, Jsc of 10.42 mA/cm^2 and FF of 40.23 % [34]. Sb_2Se_3 films deposited by CSS typically presented pinholes that limits the FF and the efficiency of the cells. To eradicate this, O. S. Hutter et. al. introduced a two-

stage CSS process, depositing a compact seed layer before the main stack with larger grains. The seed layer produced compact and dense films, improving the peak performance from 4.96 % to 6.56 %, which was mainly due to the increase in current density. TiO_2 was used as electron extraction layer, avoiding toxic elements such as lead and Cd from lead sulphide quantum dots and CdS. Moreover, a PCDTBT pinhole-blocking layer was inserted to contact the Sb_2Se_3, improving the average device characteristics, with same peak efficiency [35].

D. B. Li et. al. deposited (4,4',4",4"'-(9-octylcarbazole-1,3,6,8-tetrayl)tetrakis(N,N-bis(4-methoxyphenyl)aniline) CZ-TA by spin coating as hole transport layer to construct n-i-p CdS/Sb_2Se_3/CZ-TA solar cells. The introduction of CZ-TA film reduced the back contact barrier and improved carrier collection achieving a device efficiency of 6.84 % [36]. Etching has also been employed by researchers to remove unwanted impurities and to modify the surface. H. Shiel et. al. investigated the chemical etching of Sb_2Se_3 by $(NH4)_2S$ and CS_2. Etching successfully removed Sb_2O_3, reducing the back contact barrier from 0.43 to 0.26 eV and thus improving the contact. However, the etching damaged the film, which led to the decrease in the J_{sc} and overall efficiency. By diluting the $(NH_4)S_2$ etch and optimizing the treatment, the cells improved efficiency up to 6.6% [37]. Sb_2Se_3 was found to behave as n-type because of chlorine dopant. Cl doping lead to a higher carrier concentration in the range of 10^{16}–10^{17} cm^{-3}.This n-n heterojunction reported an efficiency of 7.3% [38]. Kai et.al. demonstrated n–i–p Sb_2Se_3 solar cells through Sb_2Se_3 surface modification. Highly crystalline Sb_2Se_3 films were deposited by two step CSS process, it was found that due to high deposition temperature loss of selenium was evident in order to cater it trigonal selenium (t-Se) was deposited. Due to the addition of t-Se the champion cell rose overall by 40% in which 8.7% was contributed by the open-circuit voltage (V_{OC}), 13.8% by short-circuit current density (J_{SC}), and 13.1% in fill factor (FF) resulting in an overall 7.45% PCE [39].

3.4.3 Sputtering.

Sputtering is a widely used technique to deposit thin films on substrates. Magnetron sputtering is the most common approach to grow thin films in which positive ions

present in the plasma are used to knock down the target and deposit them onto the substrate. This technique has control over the film growth and quality [40]. Traditional Mo/Sb_2Se_3/CdS/ZnO/Al:ZnO/Al (substrate configuration) stacked structure was used, where Sb_2Se_3 films were prepared by depositing Sb precursor layer on Mo coated glass by DC magnetron sputtering followed by selenization using a vacuum tubular furnace at temperature ranging from 280 °C to 460 °C. The morphology and structure improved with increased annealing temperature. Solar cells with efficiency of 0.72% was obtained by this method [41]. Tang. et al. prepared Sb_2Se_3 amorphous thin films using radiofrequency (RF) magnetron sputtering and studied the influence of post deposition selenization temperature. Selenization at right temperature leads to a better adhesion, defect passivation and 6.06% efficiency was reported with device structure Mo/Sb_2Se_3/CdS/ITO/Ag [42]. G.X Liang et al. grew Sb_2Se_3 nanorods with a simple and effective magnetron sputtering process. The substrate temperature of 325 °C played key role in microstructure, morphology, optical and electrical properties of the Sb_2Se_3. Well crystalized films with an average grain size of 350 nm and PCE of 3.35% were reported [43].

Table 3.II Antimony selenide deposition methods, parameters, process and efficiency.

Absorber	Substrate/Buffer	Deposition Method	Treatment	Processing temperature	Solar cell structure*	η(%)	Voc (mV)	Jsc (mA cm^{-2})	FF (%)	Cell area (cm^2)	Reference
Sb_2Se_3	Si	CSS	-	T_{sub}- 250 °C T_{sou}- 450 °C	In/Si/Sb_2Se_3	1.05	251	10.42	40.23	-	[34]
Sb_2Se_3	CdS	CSS	-	T_{sub}-320 °C, T_{sou}- 520 °C	G/FTO/CdS/Sb_2Se_3/Au	3.7	329	22.8	49.8	-	[33]
Sb_2Se_3	SnO_2/CdS	CSS	-	T_{sub}-320 °C, T_{sou}- 520 °C	G/FTO/SnO_2/CdS/ Sb_2Se_3/Au	5.1	385	24.5	55	-	[33]
Sb2S3	SnO_2/CdS	CSS	-	T_{sub}-310 °C, T_{sou}-510 °C	G/FTO/SnO_2/CdS/Sb_2Se_3/Au	5.32	380	25.4	55.1	-	[39]
			t-Se			7.45	413	28.9	62.3		
Sb_2Se_3	TiO_2	CSS	-	T_{sou}- 350-450 °C	TEC/TiO_2/Sb_2Se_3/Au	6.5	419	32.2	48.5	-	[35]
Sb_2Se_3	CdS	RTE	-	T_{sub}-300 - 350 °C ,T_{sou}- 550 °C	G/FTO/CdS/Sb_2Se_3	5.6	400	25.15	55.7	0.095	[15]
Sb_2Se_3	TiO_2	CSS	Un-etched	T_{sou}- 470 °C	G/FTO/TiO_2/Sb_2Se_3/Au	5.7	420	30.7	44.2	-	[37]
			CS_2 etch		G/FTO/TiO_2/Sb_2Se_3/CS_2 etch/Au	5.5	400	29.2	47.5	-	

			$(NH_4)_2S$ etch		G/FTO/TiO_2/Sb_2Se_3/$(NH_4)_2S$/Au	4.8	420	25.1	46.4	-	
Sb_2Se_3	CdS	CSS	-	T_{sou}- 490 °C T_{sub}- 300-450 °C	G/CdS(CSS)/Sb_2Se_3/Au	2.8	380	19.5	38	-	[44]
	CdS		-		G/CdS(CBD)/Sb_2Se_3/Au	2.0	350	15.6	38	-	
	TiO_2		-		G/TiO_2/Sb_2Se_3/Au	5.2	430	24.6	50	-	
Sb_2Se_3	CdS	TE	-	T_{sub}- 25, 150, 290 °C	FTO/Sb_2Se_3/CdS/ZnO/ZnO:Al/Au	2.1	354	17.84	33.5	-	[22]
Sb_2Se_3	CdS	RTE	Untreated	-	G/FTO/CdS/Sb_2Se_3	5.6	391	25.8	56.1	-	[31]
			NH_4Cl	-	G/FTO/CdS/Sb_2Se_3	5.6	392	26	55.6	-	
			$CuCl_2$	-	G/FTO/CdS/Sb_2Se_3	6.3	413	28.1	54.4	-	
			$(NH_4)_2S$	-	G/FTO/CdS/Sb_2Se_3	7.0	-	-	59.3	-	
Sb_2Se_3	CdS	EBE	-	-	G/FTO/CdS/Sb_2Se_3/Au	2.4	280	21.3	40.1	-	[21]
			Selenisation	-		3.7	335	24.4	46.8	-	
Sb_2Se_3	CdS	TE	-	T_{sub}- 290 °C	G/FTO/CdS/Sb_2Se_3	1.9	300	13.2	48	0.09	[20]
Sb_2Se_3	CdS	TE	Oxygen	T_{sub}- 290 °C	G/ITO/CdS/Sb_2Se_3/Au	4.8	360	25.3	52.5	0.09	[23]
Sb_2Se_3	CdS	TE	Cu	T_{sub}-300 °C	G/ITO/ZnO/CdS/Sb_2Se_3/Au	3.5	339	20.7	49	0.13	[11]
Sb2Se3	CdS	TE	-	T_{sub}- 290 °C G/ITO/CdS/Sb_2Se_3/Au		2.9	301	21.2	46.2	0.09	[45]
			I*-			4.5	363	24.8	50.1		

			Selenisation								
			W*-Selenisation			5.7	383	26.3	57.1		
Sb_2Se_3	r-ZnO	RTE		T_{sou}- 570 °C, T_{sub}- 310 °C	G/FTO/ZnO/Sb_2Se_3/Au	5.9	391	26.2	57.8	-	[46]
Sb_2Se_3		VTD	w/o Anneal	-	G/ITO/CdS/Sb_2Se_3	4.8	343	25.8	52	0.09	[16]
			Anneal 200 °C	-		5.7	371	26	55.7	-	
Sb_2Se_3	CdS	RTE	Control	-	G/FTO/CdS/Sb_2Se_3/Au	4.0	370	23.9	45.5	0.095	[28]
			N_2-CdS	-		4.0	370	24.1	45.8	-	
			$CdCl_2$-N_2-CdS	-		4.4	370	24.3	47.8	-	
			Air-CdS	-		4.7	380	24.6	50.2	-	
			$CdCl_2$-Air-CdS	-		5.2	400	25.1	52.8	-	
Sb_2Se_3	ZnO	RTE	-	T_{sou}- 570 °C, T_{sub}- 300-450 °C	G/FTO/ZnO/Sb_2Se_3	3.2	336	23.6	40.5	0.09	[47]
	MgZnO			-	G/FTO/ZnO/MgZnO/Sb_2Se_3	4.4	360	26.2	48	-	
Sb_2Se_3	CdS, TiO_2	CSS	-	-	ZnO:Al/ZnO/CdS/TiO_2/Sb_2Se_3 nanorod arrays/$MoSe_2$/Mo	9.2	400	32.5	70.3	0.26	[2]

Sb_2Se_3	CdSe	PLD	-	T_{sub}- 100-400 °C	FTO/CdSe/Sb_2Se_3/Au	3.6	357	20.1	50.7	-	[48]
Sb_2Se_3	CdSe	CSS	-	T_{sou}-500-580 °C, T_{sub}-250-350 °C	G/FTO/CdSe/Sb_2Se_3/graphite architecture	4.5	354	27.5	46.1	-	[49]
Sb_2Se_3	CdS	Sputtering	Selenisation	-	Mo/Sb_2Se_3/CdS/ITO/Ag	6.0	494	25.9	47.7	-	[42]
Sb_2Se_3	CdS	Sputtering		T_{sub}- RT-450 °C	ITO/CdS/Sb_2Se_3/Au	3.3	437	15.9	48	-	[43]
Sb_2Se_3	CdS	Sputtering	-	-	G/Mo/Sb_2Se_3/CdS/ITO/Ag	5.5	448	24.9	53.2	-	[50]
Sb_2Se_3	CdS, ZnO	Sputtering	-	T_{sub}- 375 °C	G/Mo/ Sb_2Se_3/CdS/ZnO/AZO	2.1	420	12.2	41	0.09	[51]
Sb_2Se_3	TiO_2	Spin coating	-	-	G/FTO/TiO_2 /Sb_2Se_3/Au	2.2	520	10.3	42.3	0.45	[52]
Sb_2Se_3	TiO_2	Spin coating	-	-	G/FTO/TiO_2/Sb_2Se_3/Spiro-OMeTAD/Au	2.0	275	19.7	37.7	-	[53]
	CdS		-	-	G/FTO/TiO_2/CdS/Sb_2Se_3/Spiro-OMeTAD/Au	3.9	340	27.2	41.9	-	
Sb_2Se_3	TiO_2	Spin coating	-	-	G/FTO/mp-TiO_2/Sb_2Se_3/HTM/PEDOT:PSS/Au	3.21	304	22.3	47.2	0.09	[54]
Sb_2Se_3	CdS	Spin coating	-	-	G/FTO/CdS/Sb_2Se_3	3.3	312	21.6	48.2	-	[55]
			Te doping	-		5.4	360	29.0	51.5	-	

CSS: Closed space sublimation; RTE: Rapid thermal evaporation; EBE: Electron beam evaporation; VTD: Vacuum transport deposition; TE: Thermal evaporation; RT: Room temperature; T_{sub}: Temperature of substrate; T_{sou}: Temperature of source. I-: Interface, W-: Throughout *G: Glass; FTO: Fluorine doped tin oxide; ZnO: Zinc oxide; ITO: Indium doped tin oxide; TiO_2: Titanium dioxide.

3.4.4 Solution based Technique.

Chemical solution deposition (CSD) technique is recently gaining momentum for the fabrication of Sb_2Se_3 due to its cost-effectiveness, high yield, and simplicity of the process requirements. In order to attain a 2:3 ratio in Sb_2Se_3 equimolar aqueous solution of $SbCl_3$ and selenium dioxide (SeO_2) was mixed along with tartaric acid (which avoids the Sb to precipitate). Aqueous as well as non-aqueous solvents were used to deposit Sb_2Se_3 films using spray pyrolysis technique. Amorphous films were formed while depositing the material using aqueous based precursor solution, while non-aqueous medium leads to a polycrystalline film with an efficiency of 0.03% [56].

Sb_2Se_3 thin film device was fabricated from hydrazine-based solution process. 1:3.5 molar fraction of antimony and selenium were dissolved in hydrazine to prepare the solution for spin coating. Phase-pure, crack-free, micrometer grain sized Sb_2Se_3 film reported a band gap of 1.06 eV and hole mobility of 5.1 $cm^2\ V^{-1}\ s^{-1}$. Hydrazine based Sb_2Se_3 heterojunction devices using TiO_2 as a buffer layer obtained a PCE of 2.26% [52].Choi. et al. deposited Sb_2Se_3 film by spin coating technique using single source (Se-SSP) in multiple cycles followed by thermal annealing which led to decomposition and deposition on mesoporous TiO_2, PCPDTBT was used as HTM. Sb_2Se_3-based inorganic–organic heterojunction solar cells reported an efficiency of 3.2% [54]. Interfacial engineering was carried out by a group in order to increase the performance of the solar cells. Sb_2Se_3 films were prepared by spin coating of the antimony–selenium (Sb-Se) molecular solution followed by subsequent annealing. An interfacial layer of CdS was deposited in between TiO_2 and Sb_2Se_3 which act as a hole blocking layer. CdS incorporation aligned the band gap, increased charge transport across the interface and suppressed charge recombination. Incorporation of CdS layer improves the PCE from 2.0% to 3.9% [46]. In order to reduce the deep level defects which arises in Sb rich layer or Se rich layer, Te was doped by Y. Ma et al. using spin coating and they were able to reduce the recombination losses and attained 5.6% PCE with J_{sc} of 29 mA cm^{-2} and FF of 51.5% for the device structure FTO/CdS/Sb_2Se_3/Spiro-OMeTAD/Au [55].

A summary of the different methods used to synthesize Sb_2Se_3 thin films for solar cell application has been shown in table 3.II which shows the voltage, current density, fill factor, efficiency etc. of devices fabricated by the growth techniques. CSS-grown cell has the highest FF and efficiency, whereas the cell prepared by spin coating had the lowest. VTD and RTE devices have a similar performance. However, the former cell has a slightly higher current density compared to the latter which is due to the improved crystalline quality of the VTD Sb_2Se_3 film. CSS based device have a higher EQE in the longer-wavelength spectral region compared to its other competitors. The EQE of the solar cell at the IR is related to rear surface recombination, absorption of photons and the diffusion length. The champion device showed excellent EQE in the entire working wavelength range indicating long-range carrier transport. Interestingly double buffer layer CdS/ZnO and CdS/TiO_2 based device leads to an improved V_{OC}, FF as well as PCE.

3.5 Buffer layer study.

Discussing the solar cells without any discussion of the buffer layer would be inappropriate. Buffer layer is usually n-type material that is used to form a p-n heterojunction. The selection of buffer layer is based on many factors, such as bandgap, lattice matching, carrier type, band alignment etc. The material should have a band gap wide enough to transmit light into the absorber layer. Photo-generated electrons in the absorber layer move toward the transparent electrode (TE) layer through the buffer layer. A proper band alignment and lattice matching should be done to avoid energy losses. Lattice mismatch leads to interfacial defects, Fermi-level pinning, and improper band alignment which intern limits the device performance.

CdS is one of the most commonly used buffer layer in thin-film solar cells despite of the fact that it has dissimilarity in lattice matching with other absorbers [57]. For example, the lattice mismatch for the CdS/CdTe interface was found to be 10% which was improved with $CdCl_2$ treatment of CdTe followed by annealing [58].The lattice mismatch of Sb_2Se_3 is expected to be comparable to that as in CdTe (>10 %), however till date it is one of the widely used buffer layers. In CdS/Sb_2Se_3 interface lattice mismatch and dangling bond leads to defect states which ultimately hinders the

performance of the device. A small modification during the growth process can attenuate the lattice mismatch. Oxygen addition during Sb_2Se_3 deposition passivated the dangling bond and recombination losses there by influencing the cell performance [23]. Replacing CdS by an alternate CdSe buffer layer showed an improvement in photocurrent collection which was due to the suppression of interfacial diffusion which reduced the recombination sites at the interface [49]. Widely used buffer layers such as ZnO, TiO_2 and CdS were investigated by in-situ high resolution photoemission spectroscopy (HRPES) to study the interfacial properties. The HRPES results reveal that during the initial stage of Sb_2Se_3 deposition it reacted with the buffer layer as CdS $\geq$ ZnO > TiO_2 respectively. Distinct transition layers were observed in CdS/Sb_2Se_3 and ZnO/Sb_2Se_3 interfaces whereas absent in TiO_2/Sb_2Se_3. The CdS/Sb_2Se_3 hetrojunction shows spike like conduction band offsets (CBOs) whereas ZnO/Sb_2Se_3 and TiO_2/Sb_2Se_3 heterojunction shows cliff-like and almost flat conduction band offsets respectively. High stability and high performance device can be made by combining CdS and TiO_2 buffer layers, which makes a favorable spike like band alignment [59].

TiO_2, ZnO, SnO_2 have similar lattice parameters with Sb_2Se_3 and are being investigated by many groups; in which TiO_2, ZnO have been the most investigated buffer layers. TiO_2 and ZnO have been synthesized by both chemical and physical techniques. Till date TiO_2 performance has been comparatively better than other counterparts. Buffer layer engineering is also important to obtain higher PCE for the solar cells.

3.6 Sb_2Se_3 various applications.

Chalcogenide based glasses find potential application in solid state optical and electrical devices because of its optoelectronic properties. Selenium (Se) has wide acceptability in glass forming because of its reversible phase transformation ability. Se has a short lifetime and low sensitivity which can be overcome by alloying Se with Ge, As and Sb. To synthesize Sb_2Se_3 M. Malligavathy et al. quenched glass ampoule in ice cold water and then mixed it with sodium hydroxide. Sb_2Se_3 thin films with four different thicknesses (220, 500, 600 and 720 nm) were synthesized by thermal

evaporation technique and the effect of thickness on structural, morphological and optical properties were investigated. The deposited films were amorphous in nature and with the increase in thickness the band gap decreased. The I–V characteristic of Sb_2Se_3 films showed memory switching behavior, this can have potential application in semiconductor industry [60]. Layered semiconductor which are grown parallel to growth direction have potential application in TV cameras, thermoelectric and optoelectronic devices. Zhai. et al. fabricated Sb_2Se_3 nanowires by a simple hydrothermal method to study field emission and photoconductivity. Field-emission measurements showed low turn on field of 2.6 V μm^{-1} and low threshold field of 4.9 V μm^{-1}. Sb_2Se_3 nanowires shows photo detection property in the visible light and also suggest that this material can be used as field emitters and photodetector [61]. In present day scenario health monitoring system are quite important and the photodetectors are key to it. Sb_2Se_3 shows low toxicity, high carrier mobility and a 1D structure which concedes to its application on flexible substrate. Researchers in C. Chen et al. group have fabricated flexible Sb_2Se_3 photodiode to detect the heart rate, which are very sensitive, they were successful in detecting linear dynamic of 95 dB and photo responsivity of 0.42 A W^{-1}. Finally, they were employed for heart rate detection along with LED [62]. Sb_2Se_3 have wide application in electronic industry including Bio medical applications.

3.4 Conclusion and prospects

In this chapter we studied the progress and understanding of Sb_2Se_3 material properties and device performance. The focus on various synthesis process, electrical characterization, defects, etc. Sb_2Se_3 champion cells fabricated by CSS had J_{SC}, V_{OC}, and FF values equivalent to 74%, 48%, and 81% of the S-Q limit respectively[2]. In the case of Sb_2Se_3 device fabricated by a chemical method (spin-coating) obtained a PCE of 5.6%, by doping tellurium into the crystal lattice. In these devices the J_{SC} values are low because of incomplete carrier collection and light absorption. Sb_2Se_3 devices show good current collection (Jsc) despite the performance is lower due to its lower Voc. In a nutshell the issue related to carrier management has to be addressed for higher PCE devices. There are some important key points raised in this chapter addressing them would ultimately result in a higher performing device in the future.

3.8 Reference.

[1] Y.C. Choi, D.U. Lee, J.H. Noh, E.K. Kim, S. Il Seok, Highly improved Sb2S3 sensitized-inorganic-organic heterojunction solar cells and quantification of traps by deep-level transient spectroscopy, Adv. Funct. Mater. 24 (2014) 3587–3592. https://doi.org/10.1002/adfm.201304238.

[2] Z. Li, X. Liang, G. Li, H. Liu, H. Zhang, J. Guo, J. Chen, K. Shen, X. San, W. Yu, R.E.I. Schropp, Y. Mai, 9.2%-Efficient Core-Shell Structured Antimony Selenide Nanorod Array Solar Cells, Nat. Commun. 10 (2019) 1–9. https://doi.org/10.1038/s41467-018-07903-6.

[3] R. Tang, X. Wang, W. Lian, J. Huang, Q. Wei, M. Huang, Y. Yin, C. Jiang, S. Yang, G. Xing, S. Chen, C. Zhu, X. Hao, M.A. Green, T. Chen, Hydrothermal deposition of antimony selenosulfide thin films enables solar cells with 10% efficiency, Nat. Energy. 5 (2020) 587–595. https://doi.org/10.1038/s41560-020-0652-3.

[4] M. Arun, Types of Solar Cells and its Applications, IJSDR1902043 Int. J. Sci. Dev. Res. 4 (2019) 260–267. www.ijsdr.org.

[5] K. Zeng, D. Xue, J. Tang, Antimony selenide thin- fi lm solar cells, (2016).

[6] A. Mavlonov, T. Razykov, F. Raziq, J. Gan, J. Chantana, Y. Kawano, T. Nishimura, H. Wei, A. Zakutayev, T. Minemoto, X. Zu, S. Li, L. Qiao, A review of Sb2Se3 photovoltaic absorber materials and thin-film solar cells, Sol. Energy. 201 (2020) 227–246. https://doi.org/10.1016/j.solener.2020.03.009.

[7] P. Prabeesh, V.G. Sajeesh, I. Packia Selvam, M.S. Divya Bharati, G. Mohan Rao, S.N. Potty, CZTS solar cell with non-toxic buffer layer: A study on the sulphurization temperature and absorber layer thickness, Sol. Energy. 207 (2020) 419–427. https://doi.org/10.1016/j.solener.2020.06.103.

[8] W. Wang, M.T. Winkler, O. Gunawan, T. Gokmen, T.K. Todorov, Y. Zhu, D.B. Mitzi, Device characteristics of CZTSSe thin-film solar cells with 12.6% efficiency, Adv. Energy Mater. 4 (2014) 1–5. https://doi.org/10.1002/aenm.201301465.

[9] A.G. Komilov, Influence of CdS Buffer Layer Thickness on the Photovoltaic Parameters of Solar Cells, Appl. Sol. Energy (English Transl. Geliotekhnika).

54 (2018) 308–309. https://doi.org/10.3103/S0003701X18050092.

[10] M. Nakamura, K. Yamaguchi, Y. Kimoto, Y. Yasaki, T. Kato, H. Sugimoto, Cd-Free Cu(In,Ga)(Se,S)2 thin-film solar cell with record efficiency of 23.35%, IEEE J. Photovoltaics. 9 (2019) 1863–1867. https://doi.org/10.1109/JPHOTOV.2019.2937218.

[11] V. Kumar, E. Artegiani, A. Kumar, G. Mariotto, F. Piccinelli, A. Romeo, E ff ects of post-deposition annealing and copper inclusion in superstrate Sb 2 Se 3 based solar cells by thermal evaporation, Sol. Energy. 193 (2019) 452–457. https://doi.org/10.1016/j.solener.2019.09.069.

[12] B. Yang, D.J. Xue, M. Leng, J. Zhong, L. Wang, H. Song, Y. Zhou, J. Tang, Hydrazine solution processed Sb2S3, Sb2Se3 and Sb2 (S1-xSex)3 film: Molecular precursor identification, film fabrication and band gap tuning, Sci. Rep. 5 (2015) 1–11. https://doi.org/10.1038/srep10978.

[13] C. Chen, W. Li, Y. Zhou, C. Chen, M. Luo, X. Liu, K. Zeng, B. Yang, C. Zhang, J. Han, J. Tang, Optical properties of amorphous and polycrystalline Sb2Se3 thin films prepared by thermal evaporation, Appl. Phys. Lett. 107 (2015). https://doi.org/10.1063/1.4927741.

[14] C. Chen, D.C. Bobela, Y. Yang, S. Lu, K. Zeng, C. Ge, B. Yang, L. Gao, Y. Zhao, M.C. Beard, J. Tang, Characterization of basic physical properties of Sb2Se3 and its relevance for photovoltaics, Front. Optoelectron. 10 (2017) 18–30. https://doi.org/10.1007/s12200-017-0702-z.

[15] Y. Cao, E.H. Sargent, S. Chen, Y. Cheng, J. Chen, D.-J. Xue, M. Luo, X. Liu, J. Tang, L. Wang, Y. Zhou, S. Qin, Thin-film Sb2Se3 photovoltaics with oriented one-dimensional ribbons and benign grain boundaries, Nat. Photonics. 9 (2015) 409–415. https://doi.org/10.1038/nphoton.2015.78.

[16] X. Hu, J. Tao, S. Chen, J. Xue, G. Weng, Kaijiang, Z. Hu, J. Jiang, S. Chen, Z. Zhu, J. Chu, Improving the efficiency of Sb2Se3 thin-film solar cells by post annealing treatment in vacuum condition, Sol. Energy Mater. Sol. Cells. 187 (2018) 170–175. https://doi.org/10.1016/j.solmat.2018.08.006.

[17] C. Chen, R. Kondrotas, J. Tang, C. Wang, W. Chen, X. Wen, G. Niu, L. Gao, Y. Zhao, K. Li, S. Lu, J. Zhang, Vapor transport deposition of antimony selenide thin film solar cells with 7.6% efficiency, Nat. Commun. 9 (2018). https://doi.org/10.1038/s41467-018-04634-6.

[18] M. Huang, Z. Cai, S. Wang, X. Gong, S. Wei, S. Chen, More Se Vacancies in

Sb 2 Se 3 under Se-Rich Conditions: An Abnormal Behavior Induced by Defect-Correlation in Compensated Compound Semiconductors , Small. (2021). https://doi.org/10.1002/smll.202102429.

[19] M. Huang, P. Xu, D. Han, J. Tang, S. Chen, Complicated and Unconventional Defect Properties of the Quasi-One-Dimensional Photovoltaic Semiconductor Sb 2 Se 3, ACS Appl. Mater. Interfaces. 11 (2019) 15564–15572. https://doi.org/10.1021/acsami.9b01220.

[20] M. Luo, M. Leng, X. Liu, J. Chen, C. Chen, S. Qin, J. Tang, Thermal evaporation and characterization of superstrate CdS/Sb 2Se3 solar cells, Appl. Phys. Lett. 104 (2014). https://doi.org/10.1063/1.4874878.

[21] M. Leng, M. Luo, C. Chen, S. Qin, J. Chen, J. Zhong, J. Tang, Selenization of Sb2Se3 absorber layer: An efficient step to improve device performance of CdS/Sb2Se3 solar cells, Appl. Phys. Lett. 105 (2014). https://doi.org/10.1063/1.4894170.

[22] X. Liu, J. Chen, M. Luo, M. Leng, Z. Xia, Y. Zhou, S. Qin, D.J. Xue, L. Lv, H. Huang, D. Niu, J. Tang, Thermal evaporation and characterization of Sb2Se3thin film for substrate Sb2Se3/CdS solar cells, ACS Appl. Mater. Interfaces. 6 (2014) 10687–10695. https://doi.org/10.1021/am502427s.

[23] Y.Z. and J.T. Xinsheng Liu, Chao Chen, Liang Wang, Jie Zhong, Miao Luo, Jie Chen, Ding-Jiang Xue*, Dengbing Li, Wuhan, Improving the performance of Sb2Se3 thin film solar cells over 4% by controlled addition of oxygen during film deposition, Prog. Photovoltaics Res. Appl. 23 (2015) 1828–1836. https://doi.org/10.1002/pip.

[24] A. Romeo, E. Artegiani, CdTe-Based Thin Film Solar Cells: Past, Present and Future, Energies. 14 (2021). https://doi.org/10.3390/en14061684.

[25] M. Leoncini, E. Artegiani, L. Lozzi, M. Barbato, M. Meneghini, G. Meneghesso, M. Cavallini, A. Romeo, Difluorochloromethane treated thin CdS buffer layers for improved CdTe solar cells, Thin Solid Films. (2019). https://doi.org/10.1016/j.tsf.2019.01.003.

[26] Z. Bai, L. Wan, Z. Hou, D. Wang, Effect of CdCl2 annealing treatment on CdS thin films and CdTe/CdS thin film solar cells, Phys. Status Solidi Curr. Top. Solid State Phys. 8 (2011). https://doi.org/10.1002/pssc.201000445.

[27] S.H. Cho, S.S. Kim, M.H. Park, J.H. Suh, J.K. Hong, Surface treatment of the window layer in CdS/CdTe solar cells, J. Korean Phys. Soc. 65 (2014).

https://doi.org/10.3938/jkps.65.1590.

[28] L. Wang, M. Luo, S. Qin, X. Liu, J. Chen, B. Yang, M. Leng, D.J. Xue, Y. Zhou, L. Gao, H. Song, J. Tang, Ambient CdCl2 treatment on CdS buffer layer for improved performance of Sb2Se3 thin film photovoltaics, Appl. Phys. Lett. 107 (2015) 3–8. https://doi.org/10.1063/1.4932544.

[29] X. Hu, J. Tao, S. Chen, J. Xue, G. Weng, Kaijiang, Z. Hu, J. Jiang, S. Chen, Z. Zhu, J. Chu, Improving the efficiency of Sb2Se3 thin-film solar cells by post annealing treatment in vacuum condition, Sol. Energy Mater. Sol. Cells. 187 (2018) 170–175. https://doi.org/10.1016/j.solmat.2018.08.006.

[30] L. Wang, D.B. Li, K. Li, C. Chen, H.X. Deng, L. Gao, Y. Zhao, F. Jiang, L. Li, F. Huang, Y. He, H. Song, G. Niu, J. Tang, Stable 6%-efficient Sb2Se3 solar cells with a ZnO buffer layer, Nat. Energy. 2 (2017) 1–9. https://doi.org/10.1038/nenergy.2017.46.

[31] C. Chen, K. Li, S. Chen, L. Wang, S. Lu, Y. Liu, D. Li, H. Song, J. Tang, Efficiency Improvement of Sb2Se3 Solar Cells via Grain Boundary Inversion, ACS Energy Lett. 3 (2018) 2335–2341. https://doi.org/10.1021/acsenergylett.8b01456.

[32] N. Amin, K.S. Rahman, Close-Spaced Sublimation (CSS): A Low-Cost, High-Yield Deposition System for Cadmium Telluride (CdTe) Thin Film Solar Cells, in: Mod. Technol. Creat. Thin-Film Syst. Coatings, 2017. https://doi.org/10.5772/66040.

[33] K. Shen, C. Ou, T. Huang, H. Zhu, J. Li, Z. Li, Y. Mai, Mechanisms and modification of nonlinear shunt leakage in Sb2Se3 thin film solar cells, Sol. Energy Mater. Sol. Cells. 186 (2018) 58–65. https://doi.org/10.1016/j.solmat.2018.06.022.

[34] G. Li, Z. Li, J. Chen, X. Chen, S. Qiao, S. Wang, Y. Xu, Y. Mai, Self-powered, high-speed Sb2Se3/Si heterojunction photodetector with close spaced sublimation processed Sb2Se3 layer, J. Alloys Compd. 737 (2018) 67–73. https://doi.org/10.1016/j.jallcom.2017.12.039.

[35] O.S. Hutter, L.J. Phillips, K. Durose, J.D. Major, 6.6% Efficient Antimony Selenide Solar Cells Using Grain Structure Control and an Organic Contact Layer, Sol. Energy Mater. Sol. Cells. 188 (2018) 177–181. https://doi.org/10.1016/j.solmat.2018.09.004.

[36] D.B. Li, X. Yin, C.R. Grice, L. Guan, Z. Song, C. Wang, C. Chen, K. Li, A.J.

Cimaroli, R.A. Awni, D. Zhao, H. Song, W. Tang, Y. Yan, J. Tang, Stable and efficient CdS/Sb2Se3 solar cells prepared by scalable close space sublimation, Nano Energy. 49 (2018) 346–353. https://doi.org/10.1016/j.nanoen.2018.04.044.

[37] H. Shiel, O.S. Hutter, L.J. Phillips, M. Al Turkestani, V.R. Dhanak, T.D. Veal, K. Durose, J.D. Major, Chemical etching of Sb 2 Se 3 solar cells: surface chemistry and back contact behaviour , J. Phys. Energy. 1 (2019) 045001. https://doi.org/10.1088/2515-7655/ab3c98.

[38] T.D.C. Hobson, L.J. Phillips, O.S. Hutter, H. Shiel, J.E.N. Swallow, C.N. Savory, P.K. Nayak, S. Mariotti, B. Das, L. Bowen, L.A.H. Jones, T.J. Featherstone, M.J. Smiles, M.A. Farnworth, G. Zoppi, P.K. Thakur, T.L. Lee, H.J. Snaith, C. Leighton, D.O. Scanlon, V.R. Dhanak, K. Durose, T.D. Veal, J.D. Major, Isotype Heterojunction Solar Cells Using n-Type Sb2Se3 Thin Films, Chem. Mater. 32 (2020) 2621–2630. https://doi.org/10.1021/acs.chemmater.0c00223.

[39] K. Shen, Y. Zhang, X. Wang, C. Ou, F. Guo, H. Zhu, C. Liu, Y. Gao, R.E.I. Schropp, Z. Li, X. Liu, Y. Mai, Efficient and Stable Planar n–i–p Sb2Se3 Solar Cells Enabled by Oriented 1D Trigonal Selenium Structures, Adv. Sci. 7 (2020) 1–10. https://doi.org/10.1002/advs.202001013.

[40] D. Depla, S. Mahieu, J.E. Greene, <Sputter Deposition Processes_DeplaMahieuGreene.pdf>, 281 (n.d.) 1–36.

[41] C. Yuan, X. Jin, G. Jiang, W. Liu, C. Zhu, Sb2Se3 solar cells prepared with selenized dc-sputtered metallic precursors, J. Mater. Sci. Mater. Electron. 27 (2016) 8906–8910. https://doi.org/10.1007/s10854-016-4917-3.

[42] R. Tang, Z.H. Zheng, Z.H. Su, X.J. Li, Y.D. Wei, X.H. Zhang, Y.Q. Fu, J.T. Luo, P. Fan, G.X. Liang, Highly efficient and stable planar heterojunction solar cell based on sputtered and post-selenized Sb2Se3 thin film, Nano Energy. 64 (2019) 103929. https://doi.org/10.1016/j.nanoen.2019.103929.

[43] G.X. Liang, Z.H. Zheng, P. Fan, J.T. Luo, J.G. Hu, X.H. Zhang, H.L. Ma, B. Fan, Z.K. Luo, D.P. Zhang, Thermally induced structural evolution and performance of Sb2Se3 films and nanorods prepared by an easy sputtering method, Sol. Energy Mater. Sol. Cells. 174 (2018) 263–270. https://doi.org/10.1016/j.solmat.2017.09.008.

[44] N. Spalatu, R. Krautmann, A. Katerski, E. Karber, R. Josepson, J. Hiie, I. Oja,

M. Krunks, Solar Energy Materials and Solar Cells Screening and optimization of processing temperature for Sb 2 Se 3 thin film growth protocol : Interrelation between grain structure , interface intermixing and solar cell performance, Sol. Energy Mater. Sol. Cells. 225 (2021) 111045. https://doi.org/10.1016/j.solmat.2021.111045.

[45] X. Liu, X. Xiao, Y. Yang, D.J. Xue, D.B. Li, C. Chen, S. Lu, L. Gao, Y. He, M.C. Beard, G. Wang, S. Chen, J. Tang, Enhanced Sb2Se3 solar cell performance through theory-guided defect control, Prog. Photovoltaics Res. Appl. 25 (2017) 861–870. https://doi.org/10.1002/pip.2900.

[46] X. Wang, R. Tang, Y. Yin, H. Ju, S. Li, C. Zhu, T. Chen, Interfacial engineering for high efficiency solution processed Sb2Se3 solar cells, Sol. Energy Mater. Sol. Cells. 189 (2019) 5–10. https://doi.org/10.1016/j.solmat.2018.09.020.

[47] K. Li, R. Kondrotas, C. Chen, S. Lu, X. Wen, D. Li, J. Luo, Y. Zhao, J. Tang, Improved efficiency by insertion of Zn1−xMgxO through sol-gel method in ZnO/Sb2Se3 solar cell, Sol. Energy. 167 (2018) 10–17. https://doi.org/10.1016/j.solener.2018.03.081.

[48] Y. Yang, T. Guo, D. Wang, X. Xiong, B. Li, Preparation and characterization of pulsed laser deposited CdSe window layer for Sb2Se3 thin film solar cell, J. Mater. Sci. Mater. Electron. 31 (2020) 13947–13956. https://doi.org/10.1007/s10854-020-03954-y.

[49] L. Guo, C. Grice, B. Zhang, S. Xing, L. Li, X. Qian, F. Yan, Improved stability and efficiency of CdSe/Sb2Se3 thin-film solar cells, Sol. Energy. 188 (2019) 586–592. https://doi.org/10.1016/j.solener.2019.06.042.

[50] R. Tang, X. Chen, Y. Luo, Z. Chen, Y. Liu, Y. Li, Z. Su, X. Zhang, P. Fan, G. Liang, Controlled sputtering pressure on high-quality sb2 se3 thin film for substrate configurated solar cells, Nanomaterials. 10 (2020). https://doi.org/10.3390/nano10030574.

[51] G.X. Liang, X.H. Zhang, H.L. Ma, J.G. Hu, B. Fan, Z.K. Luo, Z.H. Zheng, J.T. Luo, P. Fan, Facile preparation and enhanced photoelectrical performance of Sb2Se3 nano-rods by magnetron sputtering deposition, Sol. Energy Mater. Sol. Cells. 160 (2017) 257–262. https://doi.org/10.1016/j.solmat.2016.10.042.

[52] Y. Zhou, M. Leng, Z. Xia, J. Zhong, H. Song, X. Liu, B. Yang, J. Zhang, J. Chen, K. Zhou, J. Han, Y. Cheng, J. Tang, Solution-processed antimony

selenide heterojunction solar cells, Adv. Energy Mater. 4 (2014) 4–11. https://doi.org/10.1002/aenm.201301846.

[53] X. Wang, R. Tang, Y. Yin, H. Ju, S. Li, C. Zhu, T. Chen, Interfacial engineering for high efficiency solution processed Sb2Se3 solar cells, Sol. Energy Mater. Sol. Cells. 189 (2019) 5–10. https://doi.org/10.1016/j.solmat.2018.09.020.

[54] Y.C. Choi, T.N. Mandal, W.S. Yang, Y.H. Lee, S.H. Im, J.H. Noh, S. Il Seok, Sb2Se3-sensitized inorganic-organic-heterojunction solar cells fabricated using a single-source precursor, Angew. Chemie - Int. Ed. 53 (2014) 1329–1333. https://doi.org/10.1002/anie.201308331.

[55] Y. Ma, B. Tang, W. Lian, C. Wu, X. Wang, H. Ju, C. Zhu, F. Fan, T. Chen, Efficient defect passivation of Sb2Se3 film by tellurium doping for high performance solar cells, J. Mater. Chem. A. 8 (2020) 6510–6516. https://doi.org/10.1039/d0ta00443j.

[56] K.Y. Rajpure, C.H. Bhosale, Preparation and characterization of spray deposited photoactive Sb2S3 and Sb2Se3 thin films using aqueous and non-aqueous media, Mater. Chem. Phys. 73 (2002) 6–12. https://doi.org/10.1016/S0254-0584(01)00350-9.

[57] Y. Al-douri, Q. Khasawneh, S. Kiwan, U. Hashim, S.B.A. Hamid, A.H. Reshak, A. Bouhemadou, M. Ameri, R. Khenata, Structural and optical insights to enhance solar cell performance of CdS nanostructures, Energy Convers. Manag. 82 (2014) 238–243. https://doi.org/10.1016/j.enconman.2014.03.020.

[58] M. Terheggen, H. Heinrich, G. Kostorz, D. Baetzner, A. Romeo, A.N. Tiwari, Analysis of Bulk and Interface Phenomena in CdTe / CdS Thin-Film, (2004) 259–266.

[59] S. Lu, H. Ding, J. Hu, Y. Liu, J. Zhu, R. Kondrotas, C. Chen, J. Tang, In situ investigation of interfacial properties of Sb2Se3heterojunctions, Appl. Phys. Lett. 116 (2020) 1–6. https://doi.org/10.1063/5.0008879.

[60] M. Malligavathy, R.T. Ananth Kumar, C. Das, S. Asokan, D. Pathinettam Padiyan, Growth and characteristics of amorphous Sb2Se3 thin films of various thicknesses for memory switching applications, J. Non. Cryst. Solids. 429 (2015) 93–97. https://doi.org/10.1016/j.jnoncrysol.2015.08.038.

[61] T. Zhai, M. Ye, L. Li, X. Fang, M. Liao, Y. Li, Y. Koide, Y. Bando, D. Golberg, Single-crystalline Sb2Se3 nanowires for high-performance field

emitters and photodetectors, Adv. Mater. 22 (2010) 4530–4533. https://doi.org/10.1002/adma.201002097.

[62] C. Chen, K. Li, F. Li, B. Wu, P. Jiang, H. Wu, S. Lu, G. Tu, Z. Liu, J. Tang, One-Dimensional Sb2Se3 Enabling a Highly Flexible Photodiode for Light-Source-Free Heart Rate Detection, ACS Photonics. (2020). https://doi.org/10.1021/acsphotonics.9b01609.

Chapter 4
Study of Buffer layer

This chapter describes the study of the influence of buffer layer CdS by thermal and chemical bath deposition (CBD) as well as the application of TiO_2 as an alternate buffer layer for the antimony selenide (Sb_2Se_3) absorber thin film along with the characterization techniques used for studying their structural, surface morphological, optical and electrical properties.Sb_2Se_3 solar cell was constructed by superstrate configuration and its photovoltaic properties were studied under standard photovoltaic test conditions.

4.1 Thermally evaporated CdS buffer.

Among the II–VI semiconductors, CdS polycrystalline thin film is a very important semiconducting material with a band gap of 2.4 eV which makes it a material of choice for the buffer (window) layer. Present day high efficient solar cells (CdTe [1], CIGS, CZTS, and Sb_2Se_3 [2]) widely use cadmium sulfide (CdS) thin films as a buffer layer [3][4]. Thermal evaporation and chemical bath deposition are amongst most used techniques to fabricate CdS thin films.

The optical properties of CdS plays a crucial role when it comes to the absorption within the layer. Thus we investigated thickness dependent properties of CdS buffer [5]. In this chapter we present the results on optimization of the thickness of CdS buffer layer for the fabrication of efficient Sb_2Se_3 thin film solar cells. For this study, CdS with 50 nm, 90 nm and 150 nm were deposited on the commercial NSD TEC 12D front contact: FTO/SnO_2/CdS/Sb_2Se_3. The front contact is composed of a fluorine doped tin oxide (FTO) layer followed by a high resistivity transparent un-doped tin oxide (SnO_2) layer on soda lime glass. CdS was deposited by thermal evaporation at a pressure of 10^{-4} Pa, and substrate temperature of 150 °C. After deposition they were annealed in vacuum at 450 °C to improve its crystalline structure. The samples were then transferred to another thermal evaporation chamber for Sb_2Se_3 deposition. 800 nm thick Sb_2Se_3 films were deposited at base pressure 3.6 x 10^{-4} Pa keeping the substrate temperature at 300 °C. The material source (Sb_2Se_3) is

put in a graphite crucible which is heated in temperature range of 700-800 °C. The rate of deposition is maintained at 0.20 nm/sec. Finally, 30 nm of gold is deposited via thermal evaporation without heating the substrate.

4.1.1 Measurement and characterization.

The crystalline structure of the samples was studied using XRD, carried out with a Thermo ARL XTRA powder diffractometer in Bragg -Brentano geometry, equipped with a Cu-anode X-ray source (Kα, λ=1.5418 Å) and a Peltier Si (Li) cooled solid-state detector. AFM was pursued by a NT-MDT with NSG-01 silicon tip. J-V characteristics were measured with a Keithley Source Meter 2420, using a halogen lamp calibrated with a silicon solar cell under an irradiation of 100 mW/cm^2.

4.1.2 Structural Characterization.

The Schematic view of the sample is shown in Figure 4.1 along with the top view of AFM in Figure 4.2.

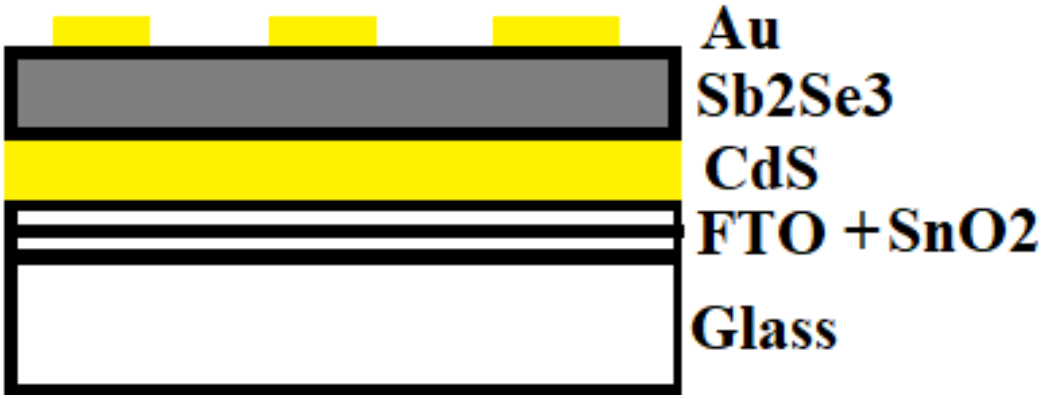

Figure 4.1. Schematic view of the superstrate configuration.

The 2D topography of vacuum deposited CdS thin films are shown in Fig. 4.2(a, b), respectively. Here, the AFM micrographs of the CdS films fabricated depicted that all nano grains were homogeneously distributed and spherical in shape over the whole film surface. The 50 nm deposited CdS film has smaller grains in comparison to the 150 nm ones. Figure 4.3 shows the AFM images of the Sb_2Se_3 deposited on the CdS. The films are compact, free of cracks and pinholes. Comparing in fig. 4.3 (a, b, c) we

notice that with the increase in the thickness of CdS the grains become larger, ranging from few nanometers to few microns.

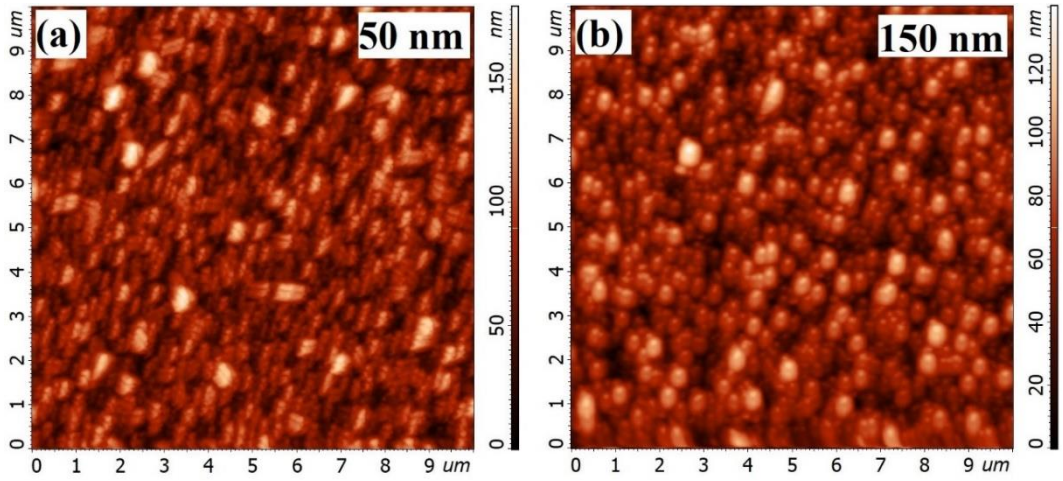

Figure 4.2. Schematic view of CdS deposited on (a, b) 50 nm and 150 nm from left to right.

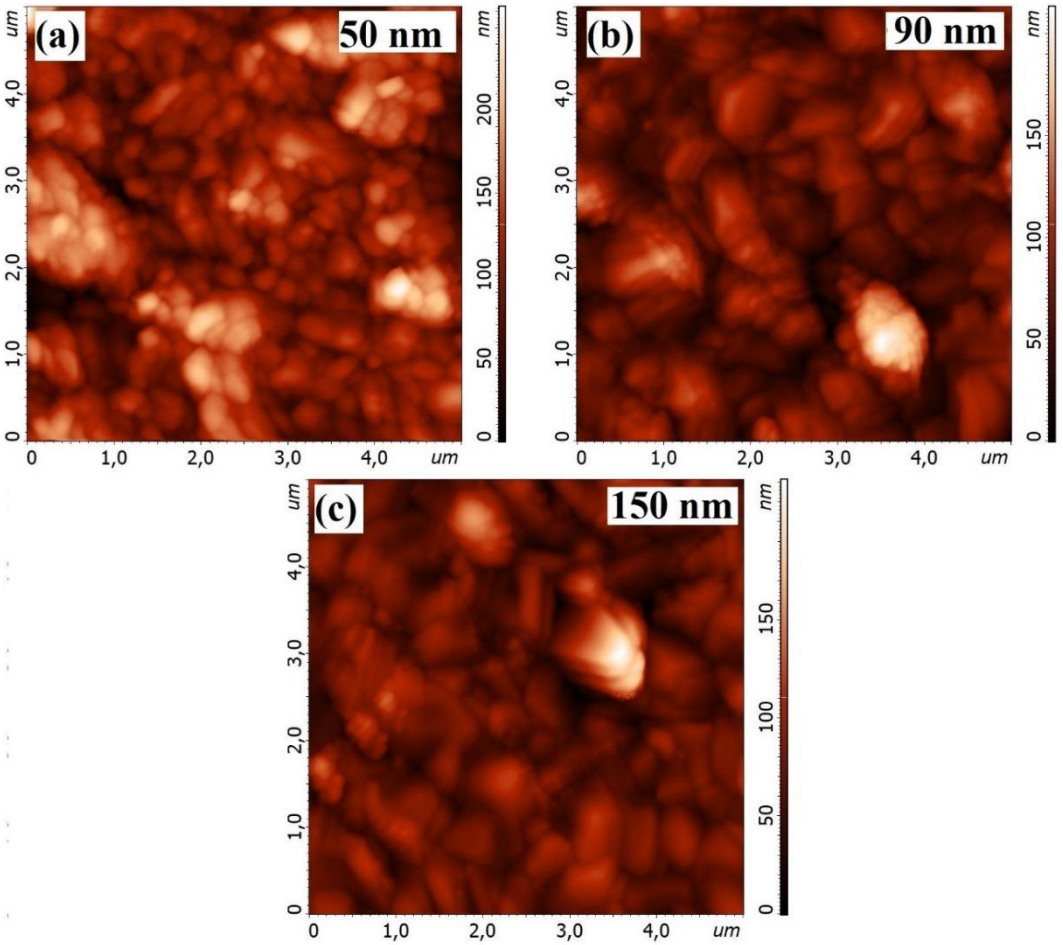

Figure 4.3. Schematic view of Sb_2Se_3 deposited on (a) 50 nm, (b) 90 nm, and (c) 150 nm Cds from left to right.

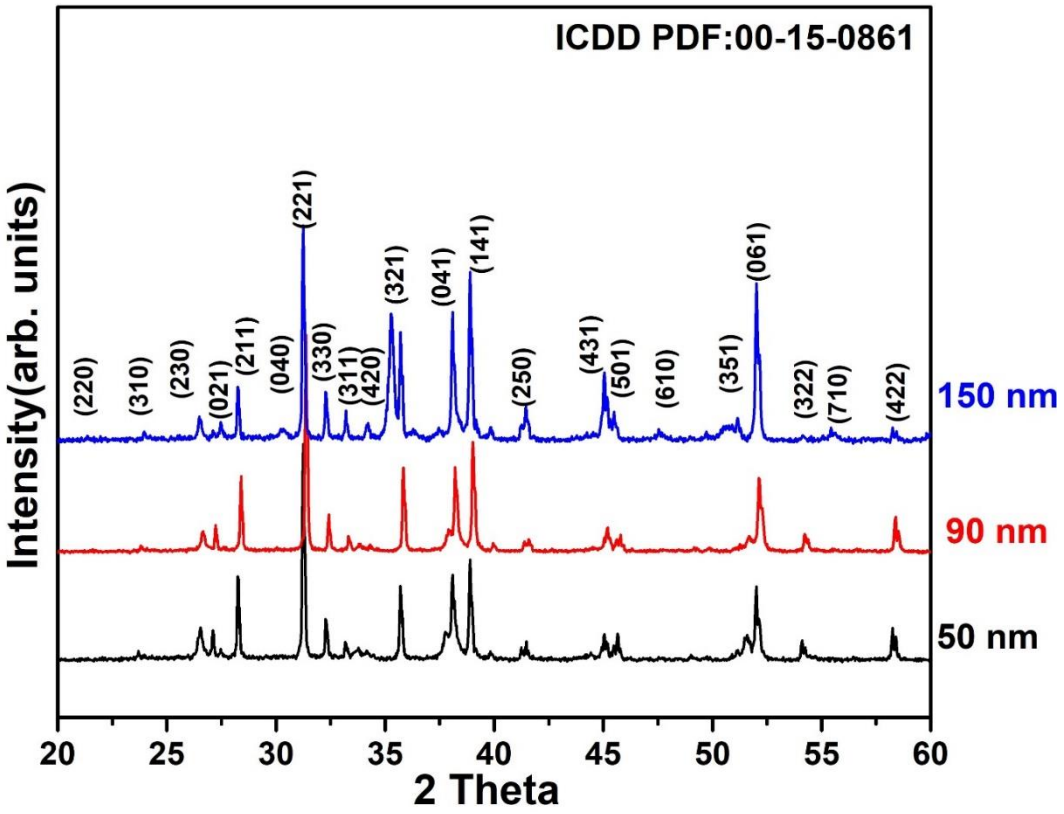

Figure 4.4. X-ray diffraction patterns of Sb_2Se_3 films.

X-ray diffraction (XRD) was applied to characterize Sb_2Se_3 thin films deposited on varying CdS thickness. As shown in figure 4.4. diffraction peaks of our samples are well indexed with the orthorhombic Sb_2Se_3 (ICDD PDF:00-15-0861). Major peaks were indexed, and no secondary phase was detected. The films exhibit both [hk1] and [hk0] preferred orientation peaks, of which the [hk1] are dominant and indicative of good electrical performance of the device. CdS as buffer layer promotes the formation of the preferred (221), (211), (321), (141), (041) which are oriented and composed of tilted $(Sb_4Se_6)_n$ ribbons stacked vertically the substrate. The (330), (250) are stacked horizontal to the substrate.

4.1.2 Electrical Characterization.

Completed devices with gold contact delivered conversion efficiencies between 0.3 and 1.7%, the values are reported in Table 4.I. Looking at the J-V curves, shown in Figure 4.5, the devices with the CdS layer thickness of 150 nm show a higher open circuit voltage and F.F. The champion cell has 1.7% PCE with 150 nm of CdS.

Table 4.I: J-V data of the Sb_2Se_3 films on CdS (50, 90 and 150 nm)

Sample I.D	CdS (nm)	Jsc (mA/cm^2)	Voc (mV)	FF (%)	η (%)
C_{50}	50	17.5	268	27.6	1.3
C_{90}	90	16.3	324	29.0	1.5
C_{150}	150	15.2	331.6	33.0	1.7

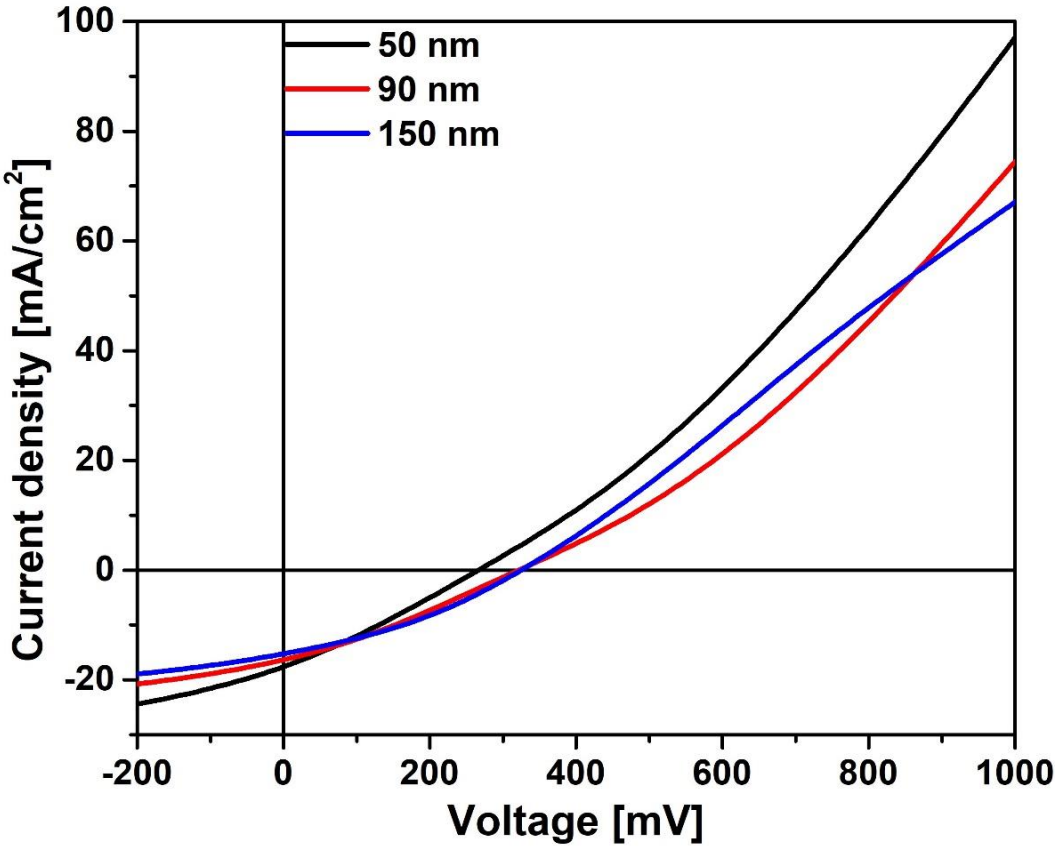

Figure 4.5. J-V characteristics of the samples.

4.2 Chemical Bath deposition of CdS.

Well-known chemical deposition methods for CdS thin films is chemical bath deposition. The chemical bath deposition (CBD) technique has been successfully used to deposit cadmium sulphide from cadmium chloride and cadmium acetate which acts as source for cadmium ion and thiourea as the sulphur source. This is used to deposit CdS on glass as well as ITO/ZnO, FTO/SnO_2 substrates[6–8].

During chemical bath deposition, ammonia acts as a complexing agent by controlling the release of metal (Cd^{2+}) and sulfur (S^{2-}) ions in the alkaline solution. The growth mechanism can be summarized by the following chemical reactions:[6,8,9]

(1) The solution of amino-cadmium complex equilibrium:

$$Cd + 4NH_3 \leftrightarrows Cd(NH_3)_4^{2+} \quad (1)$$

Formation of $Cd(NH3)_4^{2+}$ prevents the precipitation of $Cd(OH)_2$.

(2) Hydrolysis of thiourea in an alkaline medium:

$$(NH_2)_2CS + OH^- \leftrightarrows SH^- + CH_2N_2 + H_2O \quad (2)$$

SH^- ions are in equilibrium with water and give S^{2-} ions according to this equation:

$$SH^- + OH^- \leftrightarrows S^{2-} + H_2O \quad (3)$$

(3) Cadmium sulfide formation:

$$Cd(NH_3)_4^{2+} + S^{2-} \rightarrow CdS + 4NH_3 \quad (4)$$

CdS formation can be summarized as:

$$Cd(NH_3)_4^{2+} + SC(NH_2)_2 + 2OH^- NH_4OH \longrightarrow CdS + CH_2N_2 + 4NH_3 + 2H_2O \quad (5)$$

To complete the device structure nearly 150 nm of CdS buffer was deposited by CBD for this 15 ml of Cd $(CH_3COO)_2$ $2H_2O$ (0.025 M) solution, 10 ml of thiourea (0.422 M) and 25 ml of NH_4OH (20%) solution are added to 200 ml of distilled water. The substrates are coated at a temperature of 60 °C for 10 min. The optimal deposition parameters of the CdS deposition are in Table 4. II. After that the films are washed with distilled water and then dilute HCl is used to remove the unwanted CdS deposited on the opposite side of the glass. Finally, the CdS is put in a hot plate at 150 °C for 10 mins. Then the samples were transferred to thermal evaporation chamber for Sb_2Se_3 deposition. 800 nm thick Sb_2Se_3 films were deposited at base pressure 3.6 x 10^{-4} Pa keeping the substrate temperature at 300 °C. The material source (Sb_2Se_3) is in graphite crucible which is heated in temperature range of 700-800 °C. The rate of deposition is maintained at 0.20 nm/sec. Finally, 30 nm of gold is deposited via thermal evaporation without heating the substrate.

Table 4. II. Chemical bath parameters

Cadmium acetate	15 ml (0.025 M)
Ammonia	25 ml (20%)
Thiourea	10 ml (0.422 M)

4.2.1 Measurement and characterization.

4.2.1.1 Structure and morphological aspect.

Topographical analysis on the CdS and Sb_2Se_3 (grown on CdS) thin films has been done by using atomic force microscopy (AFM) Figure 4.6(a,b) where the image can be studied through the convolution of the tip of the cantilever and the samples. The non-contact AFM operation mode was used to analyze the surface of the samples. It is observed, from Fig. 4.6(a), CdS particles are uniformly distributed on the surface of the film and the surfaces are composed of nano-sized grains. CdS film were composed of a spherical shaped particulate, very well-connected grains without crack that presents an inhomogeneous compact surface. The grains were grouped together to form clusters. Figure 4.6(b) shows the top view of the as-grown Sb_2Se_3 film,

indicating dense and pin-hole free morphology with polyhedron grains. The grain size distribution is non uniform with some extremely large grains (~1µm) and some small grains (~100 nm).

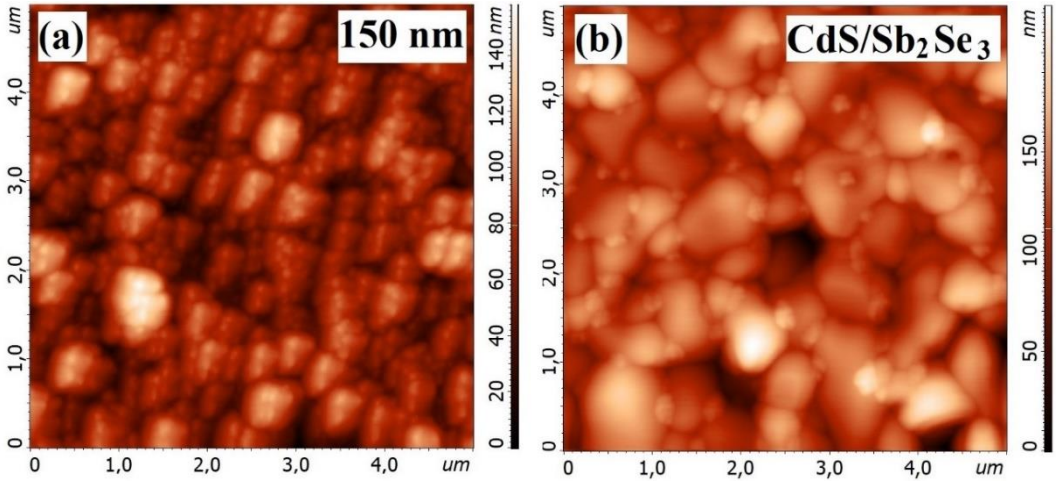

Figure 4.6. AFM image of (a) CdS grown by CBD and (b) Sb_2Se_3 grown on the CdS.

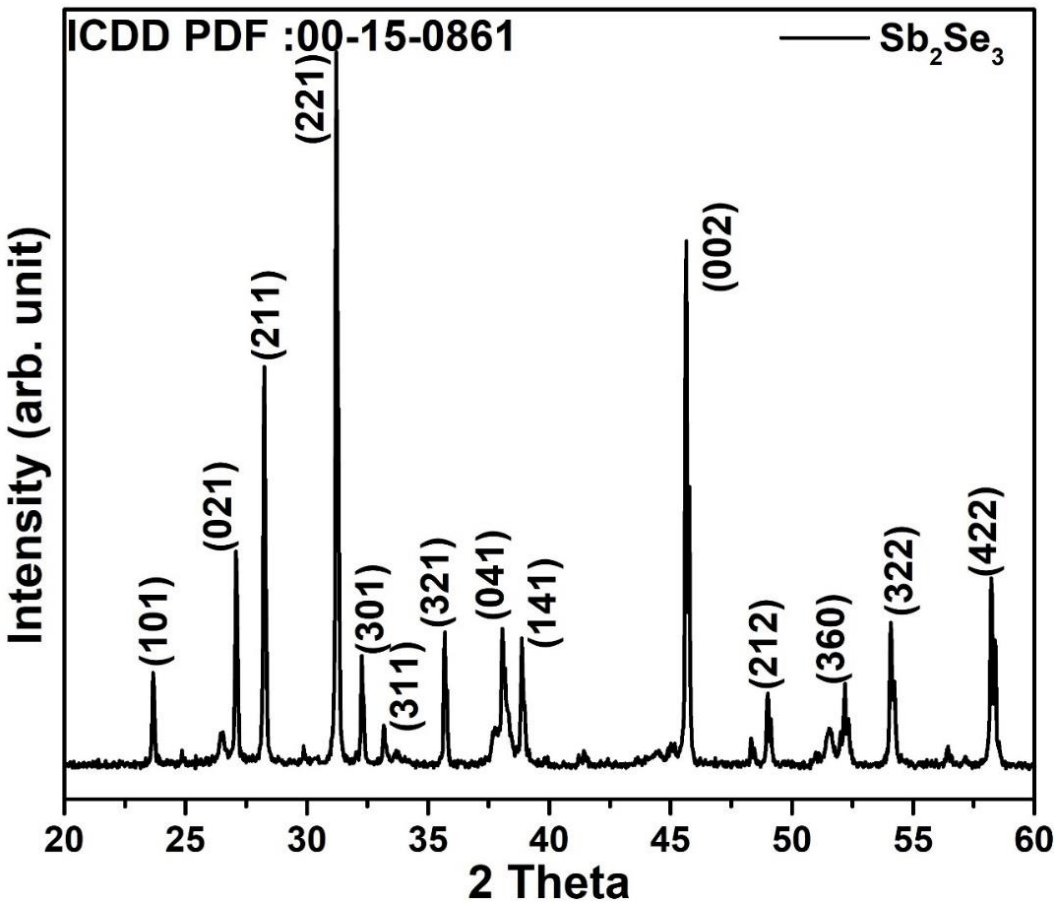

Figure 4.6. X-ray diffraction patterns of Sb_2Se_3 films on chemical bath deposited (CBD) CdS.

Fig 4.7. displays the representative XRD patterns of the Sb_2Se_3 films at 300 °C. A sharp peak at a 2θ angle of 28.20° can be observed, which is consistent with the (211) plane of Sb_2Se_3. The other diffraction peaks located at 31.16◦and 32.22◦correspond to the (221) and (301) planes, respectively. The film exhibits a higher diffraction intensity when compared with the Sb_2Se_3 deposited on thermal evaporated CdS. The XRD patterns indicate a phase- pure material (orthorhombic Sb_2Se_3 phase, ICDD PDF: card No. 15-0861).

4.2.1.2 Electrical and Optical Characterization.

Fig 4.7 shows current-density−voltage characteristics of our best Sb_2Se_3 solar cells under 100 mW/cm^2 simulated AM1.5G irradiation. The champion device exhibited a short-circuit current density (J_{sc}) of 17.0 mA/cm^2, an open circuit voltage (V_{oc}) of 254 mV, and a fill factor (FF) of 34.5%, corresponding to a PCE of 1.5%. Light enters from glass and reaches Sb_2Se_3 through CdS/Sb_2Se_3.The loss in J_{sc} may be due to the recombination at the interface or probably due to double diode behaviour at back contact.

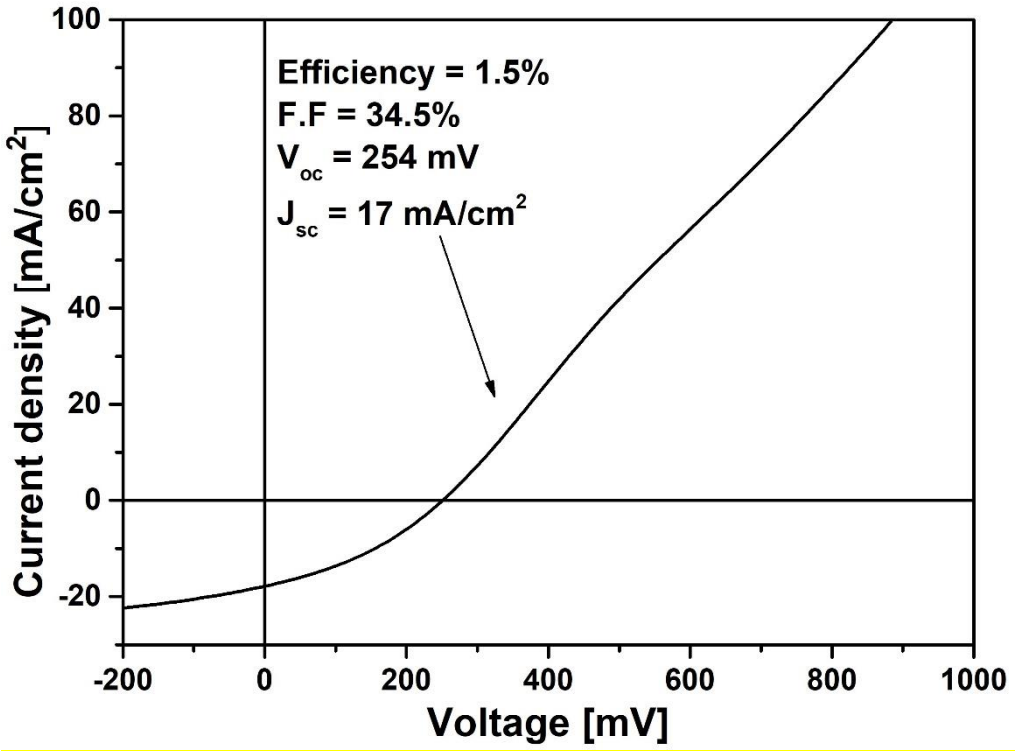

Figure 4.7. J-V characteristics

Fig 4.8 depicts the transmittance spectra of the CdS films deposited by CBD and thermal evaporation in the 200- 900 nm wavelength range. It revealed that both films exhibit very low transmittance below 450 nm, which is due to strong absorption in this wavelength regime. The transmittance increases (greater than 70 % in visible range) with increasing wavelength and shows a slight interference pattern towards higher wavelength which is good for solar application [10][11]. These reflections are observed when the films are quite thin with a smooth surface. The band gap was calculated using Taucs plot it is shown in fig 4.9, 4.10 which are found to 2.37 eV for CBD and 2.4 eV for thermal deposited samples which has also been reported in the literature [12,13].

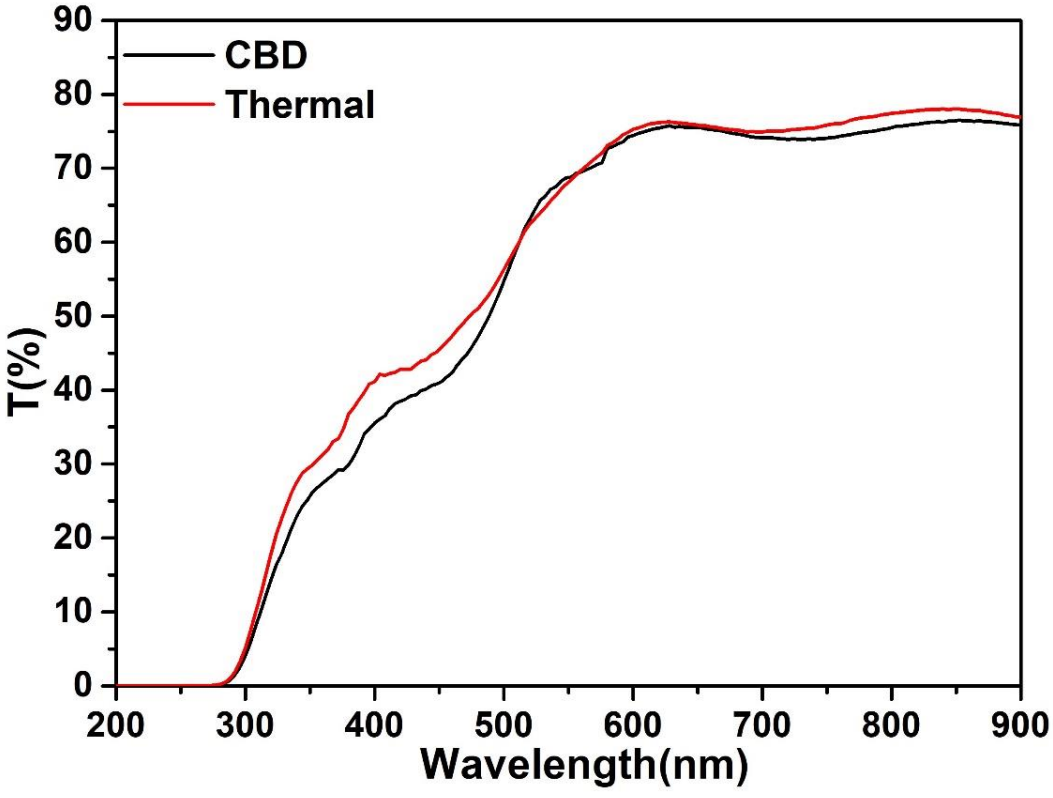

Figure 4.8. Transmission spectra of vacuum evaporated CdS and chemical bath deposited (CBD) thin films.

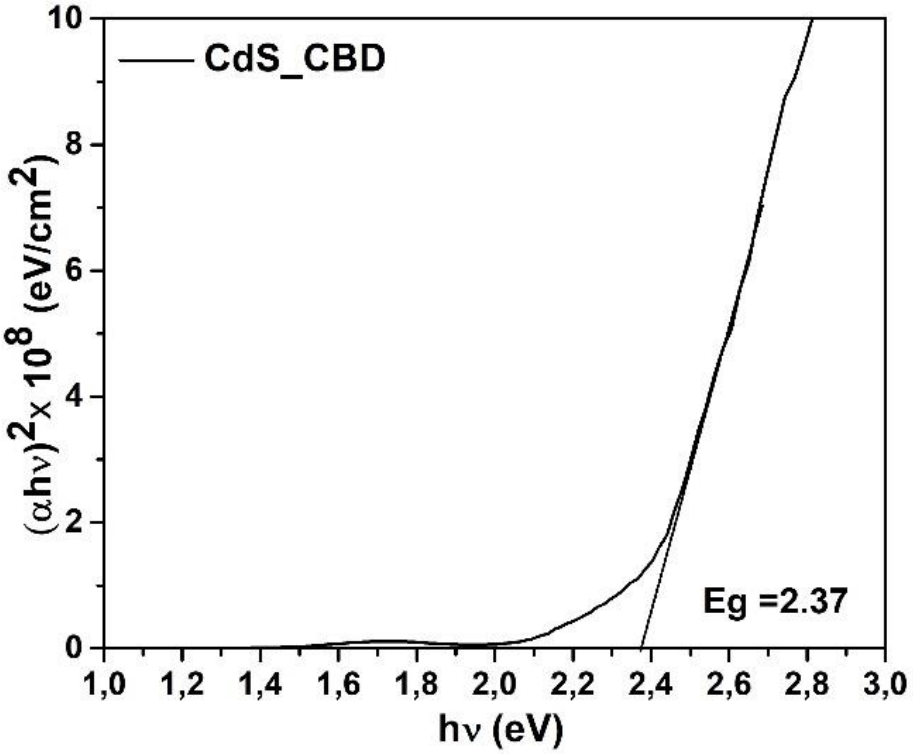

Figure 4.9 E_g calculation of CBD deposited sample.

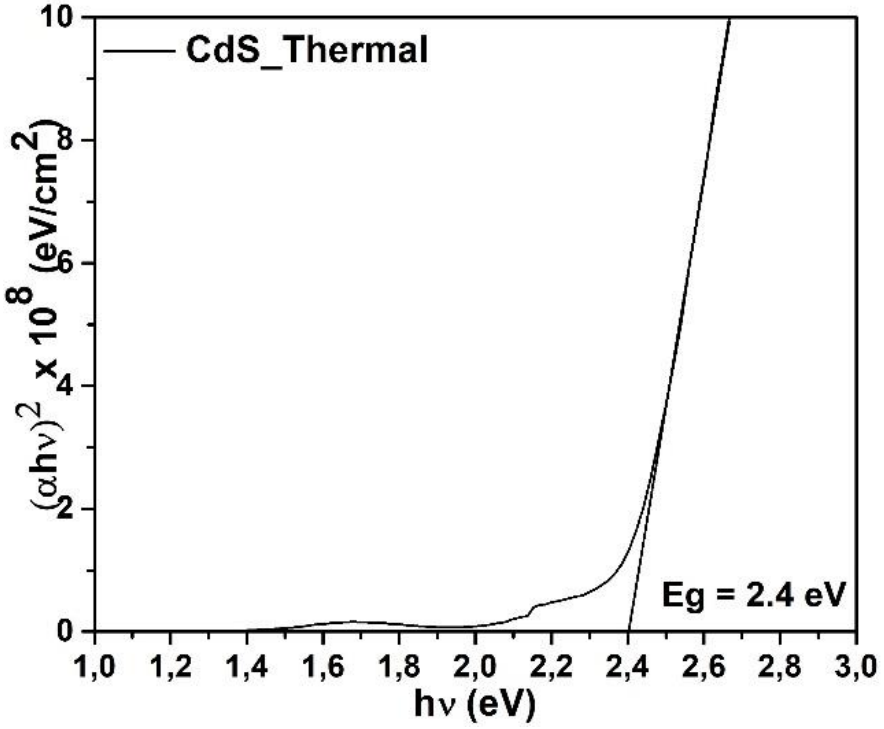

Figure 4.10. Eg calculation of thermal evaporated sample.

4.3 TiO_2 buffer layer.

Titanium dioxide (TiO_2) in solar cells is not new, it is a cheap and harmless water-insoluble inorganic material which belongs to the family of transition metal oxide. TiO_2 is chemically inert substance, and it does not promote chemical reactions in the absence of light. TiO_2 shows strong ionic character and is constituted of Ti^{4+} and O^{2-} ions. TiO_2 is used as an active material that absorbs photons and converts them into electric current. This material has a band gap around 3.2–3.8 eV, allowing it to effectively absorb in the ultraviolet light by the generation of electron–hole pair. The Absorption coefficient (α) of (TiO_2) film is about ($>10^4$ cm^{-1}) [14] which potentially limits the efficiency of photon-to-current conversion [15]. TiO_2 exists in three phases anatase, rutile, and brookite [16,17]. Deposition methods influence the optical and electrical properties of the film, so it is important to use appropriate method for the film fabrication. TiO_2 can be fabricated by methods such as electron beam evaporation, sputtering, chemical vapor deposition, sol–gel [18–21]. Of all the methods spin coating and sol–gel have large surface area coverage with minimal costing, also being a liquid-deposition process, they are deposited homogeneously on the surface.

The properties of the films can be controlled by the solution composition. The characteristics of sol–gel deposited TiO_2 thin films can be controlled by the processing conditions, including the choice of solvent, concentration of the solvent, and the post-deposition heat treatment [22]. TiO_2 films obtained by annealing at 400–550 °C, showed a predominantly anatase phase structure, which is important in solar photovoltaic application[23,24].

In this work were deposited Sb_2Se_3 on the commercial SnO_2: F (fluorine-doped tin oxide (FTO))-coated soda-lime glass TEC12D. The device structure was glass/FTO/TiO_2/Sb_2Se_3/Au. TiO_2 layer was deposited by spin-coating process. 5 layers (100µl), 7 layers (140 µl) and 10 layers (200 µl) concentration of 0.15 M titanium isopropoxide (TTIP) in ethanol solution was deposited on a 30 × 30 mm^2 substrate at 3600 rpm followed by 10 min of heating in the hot plate. Finally, the

substrates were annealed in air at 500 °C for 30 min. Sb_2Se_3 layers were deposited via thermal evaporation and has been discussed in detail in the previous chapter.

4.3.1 Measurement and characterization.

4.3.2 Material Characterization.

Fig. 4.11 (a) shows the atomic force microscopy image of the spin coated TiO_2 film annealed at 450 °C. The images show well-defined particle-like features with granular morphology which are indicative of the presence of small crystalline grains. Crystalline phase formed appears to have a high surface roughness. The image also reveals that the film is homogeneous with few pinholes but are well connected to each other. Fig. 4.11(b) shows the Sb_2Se_3 grown on the TiO_2 the film shows a columnar like structure with few pinholes.

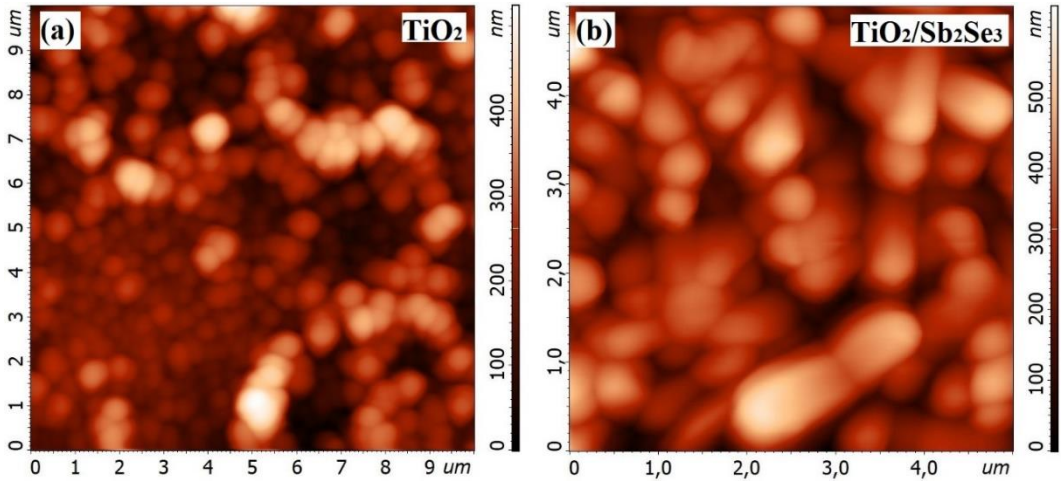

Figure 4.11. AFM images of (a) TiO_2 deposited by spin coating (b) Sb_2Se_3 film grown on TiO_2.

Fig. 4.12 displays XRD pattern of thermally evaporated Sb_2Se_3 absorber films deposited at 300 °C onto TiO_2 layers. The diffractograms of the heterostructure show the primary peaks from the (211), (221), and (301) planes. At the same time, the (020), (120), (130), (230) and (240) XRD peaks were quite pronounced in the structure with TiO_2, indicating the presence of the grains lying parallel to the substrate which can be a factor for the poor performance (low current) of the device.

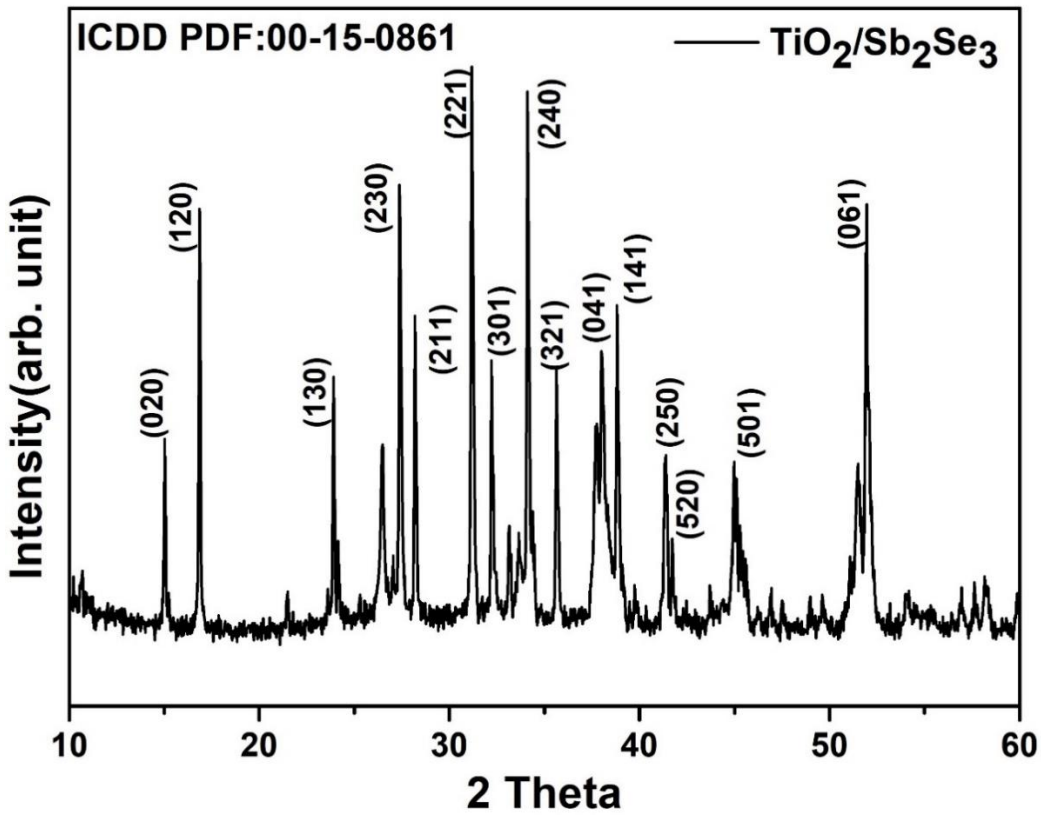

Figure 4.12. XRD pattern of Sb_2Se_3 grown on TiO_2.

4.3.3 Electrical and optical Characterization.

Fig. 4.13 illustrates that the optical transmittance of TiO_2 thin films. It is observed that maximum transmittance is in the wavelength range (420-900 nm) which is suitable for solar cell window. The film obtained 80% transmittance in the visible region after one layer of deposition. Ben et al. reported slight decrease in the transmittance of TiO_2 while annealing from 300 °C to 600 °C. [14]. The optical band gap energy of 3.97 eV was estimated for TEC/TiO_2 using the Tauc plot.

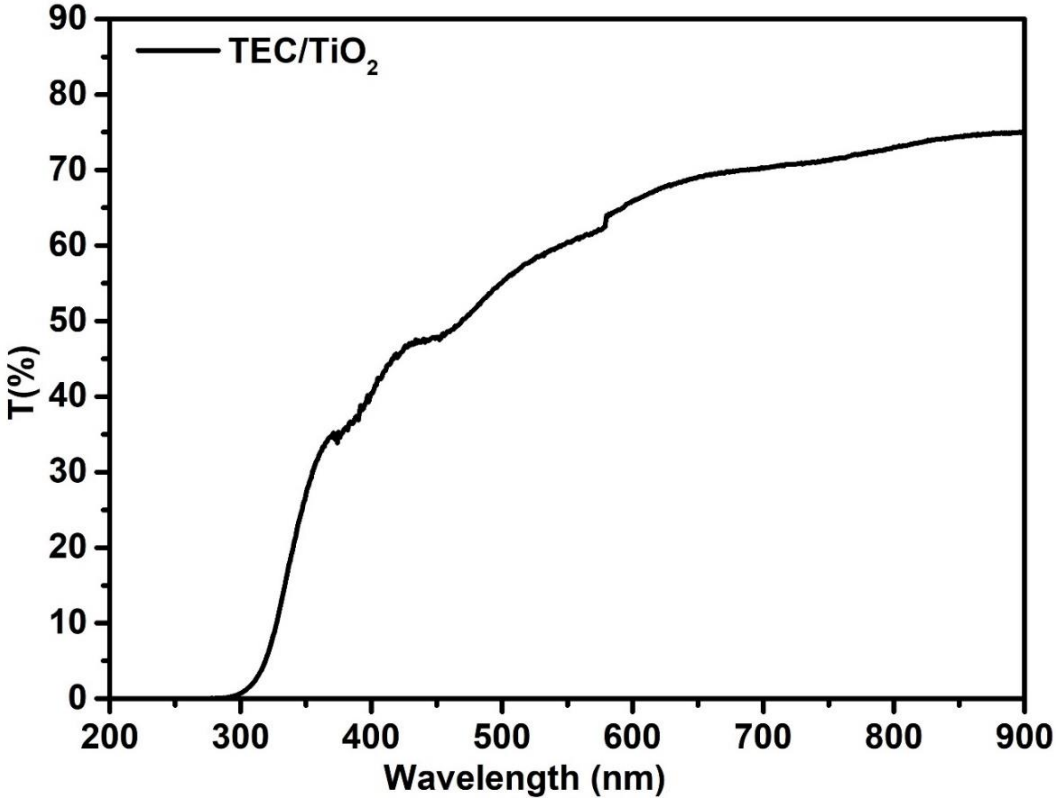

Figure. 4.13 Optical transmittances of TiO_2

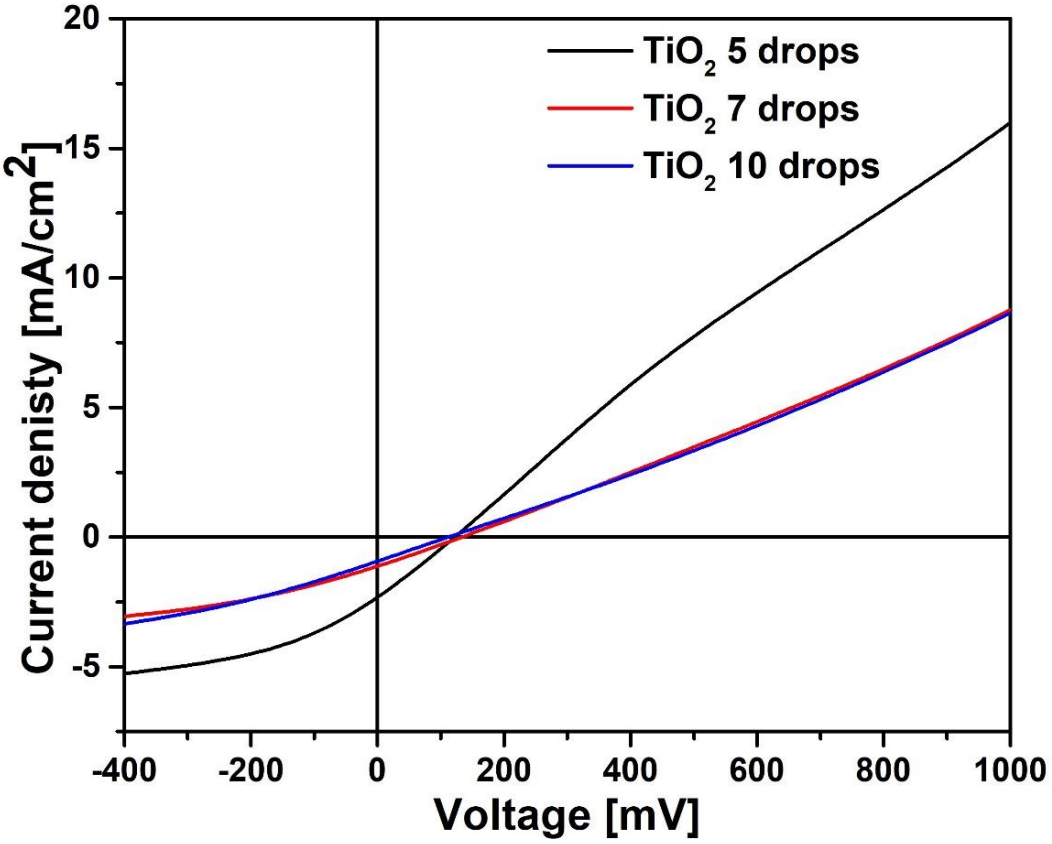

Figure 4.14. J-V plot

Table. 4.III J-V data of the TiO_2 samples.

Sample I.D	Jsc (mA/cm^2)	Voc (mV)	FF (%)	η (%)
5 drops	14.4	127.7	25.3	0.46
7 drops	8.6	134.6	25.6	0.30
10 drops	5.8	113.5	24.8	0.16

The overall performance of the device fabricated using TiO_2 is shown in table 4.III and fig 4.14. As shown in the table 5 drops of TiO_2 using spin coating attained efficiency of 0.5% with very low J_{sc},V_{oc} and FF.

4.4 Conclusion.

Overall, in this chapter we discussed Sb_2Se_3 solar cells performance with CdS and TiO_2 buffer layer. CdS buffer layer was deposited using thermal evaporation and chemical bath deposition. TiO_2 was deposited using spin coating. Firstly, we would discuss the CdS films deposited by thermal evaporation. The AFM micrographs of the CdS films fabricated depicted nano grains which are homogeneously distributed with the increase in the thickness of CdS (50, 90, 150nm) the Sb_2Se_3 grains become larger, ranging from few nanometers to few microns. The indexed Xrd have the preferred (hk1) planes and the champion cell reported an efficiency of 1.7% with 150 nm CdS thickness. Further CdS deposited using chemical bath deposition was studied. The Sb_2Se_3 films grown exhibit dense and pin-hole free structure with an efficiency of 1.5%. The CdS grown by thermal, and CBD had a band gap of 2.4 and 2.37 eV. Finally, we studied TiO_2 buffer layer with varying thickness (5, 7 and 10 drops) using spin coating. Film grown on TiO_2 shows pronounced (hk0) plane. The band gap of TEC/TiO_2 was calculated at 3.97 eV and the reported efficiency of the champion cell was less than 0.5% with 5 drops. At last, I would like to conclude that the performance of the CdS by thermal and CBD perform near about the same but for TiO_2 buffer layer a detailed study needs to be done.

4.5 References.

[1] E. Artegiani, D. Menossi, H. Shiel, V. Dhanak, J.D. Major, A. Gasparotto, K. Sun, A. Romeo, Analysis of a novel $CuCl_2$ back contact process for improved stability in CdTe solar cells, Prog. Photovoltaics Res. Appl. (2019) pip.3148. doi:10.1002/pip.3148.

[2] V. Kumar, E. Artegiani, A. Kumar, G. Mariotto, F. Piccinelli, A. Romeo, E ff ects of post-deposition annealing and copper inclusion in superstrate Sb 2 Se 3 based solar cells by thermal evaporation, Sol. Energy. 193 (2019) 452–457. doi:10.1016/j.solener.2019.09.069.

[3] B.P. Singh, R. Kumar, A. Kumar, M. Kumar, A.G. Joshi, Vacuum thermal deposition of crystalline, uniform and stoichiometric CdS thin films in ambient H2S atmosphere, Indian J. Pure Appl. Phys. 55 (2017) 463–470.

[4] A.G. Komilov, Influence of CdS Buffer Layer Thickness on the Photovoltaic Parameters of Solar Cells, Appl. Sol. Energy (English Transl. Geliotekhnika). 54 (2018) 308–309. doi:10.3103/S0003701X18050092.

[5] A. Cantas, F. Turkoglu, E. Meric, F.G. Akca, M. Ozdemir, E. Tarhan, L. Ozyuzer, G. Aygun, Importance of CdS buffer layer thickness on Cu2ZnSnS4-based solar cell efficiency, J. Phys. D. Appl. Phys. 51 (2018). doi:10.1088/1361-6463/aac8d3.

[6] J. Hiie, T. Dedova, V. Valdna, K. Muska, Comparative study of nano-structured CdS thin films prepared by CBD and spray pyrolysis: Annealing effect, Thin Solid Films. 511–512 (2006) 443–447. doi:10.1016/j.tsf.2005.11.070.

[7] B. Ghosh, B.K. Singh, P. Banerjee, S. Das, Nucleation and growth of CBD-CdS thin films on ultrathin aluminium layers and annealing induced doping, Optik (Stuttg). 127 (2016) 4413–4417. doi:10.1016/j.ijleo.2016.01.099.

[8] M. Ouafi, B. Jaber, L. Atourki, N. Zayyoun, A. Ihlal, A. Mzerd, L. Laânab, In situ low-temperature chemical bath deposition of CdS thin films without thickness limitation: Structural and optical properties, Int. J. Photoenergy. 2018 (2018). doi:10.1155/2018/4549154.

[9] M. Rami, E. Benamar, M. Fahoume, F. Chraibi, A. Ennaoui, Effect of the cadmium ion source on the structural and optical properties of chemical bath

deposited CdS thin films, Solid State Sci. 1 (1999) 179–188. doi:10.1016/S1293-2558(00)80073-4.

[10] A.Y. Jaber, S.N. Alamri, M.S. Aida, M. Benghanem, A.A. Abdelaziz, Influence of substrate temperature on thermally evaporated CdS thin films properties, J. Alloys Compd. 529 (2012) 63–68. doi:10.1016/j.jallcom.2012.03.093.

[11] A.M.A. Al-Hussam, S.A.J. Jassim, Synthesis, structure, and optical properties of CdS thin films nanoparticles prepared by chemical bath technique, J. Assoc. Arab Univ. Basic Appl. Sci. 11 (2012) 27–31. doi:10.1016/j.jaubas.2011.10.001.

[12] A.Y. Jaber, S.N. Alamri, M.S. Aida, M. Benghanem, A.A. Abdelaziz, Influence of substrate temperature on thermally evaporated CdS thin films properties, J. Alloys Compd. 529 (2012) 63–68. doi:10.1016/j.jallcom.2012.03.093.

[13] M. Dey, N.K. Das, A.K. Sen Gupta, M. Dey, M.S. Hossain, M.A. Matin, N. Amin, Deposition of CdS Thin Film by Thermal Evaporation, 2nd Int. Conf. Electr. Comput. Commun. Eng. ECCE 2019. (2019) 1–5. doi:10.1109/ECACE.2019.8679325.

[14] M. Ben Karoui, Z. Kaddachi, R. Gharbi, Optical properties of nanostructured TiO2 thin films, J. Phys. Conf. Ser. 596 (2015). doi:10.1088/1742-6596/596/1/012012.

[15] D.Y. Rahman, M. Rokhmat, E. Yuliza, E. Sustini, M. Abdullah, New design of potentially low-cost solar cells using TiO2/graphite composite as photon absorber, Int. J. Energy Environ. Eng. 7 (2016) 289–296. doi:10.1007/s40095-016-0213-5.

[16] Z. Wang, U. Helmersson, P.O. Käll, Optical properties of anatase TiO2 thin films prepared by aqueous sol-gel process at low temperature, Thin Solid Films. 405 (2002) 50–54. doi:10.1016/S0040-6090(01)01767-9.

[17] R. Zhang, L. Gao, Q. Zhang, Photodegradation of surfactants on the nanosized TiO2 prepared by hydrolysis of the alkoxide titanium, Chemosphere. 54 (2004) 405–411. doi:10.1016/S0045-6535(03)00588-5.

[18] C. Garlisi, G. Scandura, J. Szlachetko, S. Ahmadi, J. Sa, G. Palmisano, E-beam evaporated TiO2 and Cu-TiO2 on glass: Performance in the discoloration of methylene blue and 2-propanol oxidation, Appl. Catal. A Gen. 526 (2016) 191–

199. doi:10.1016/j.apcata.2016.08.022.

[19] R. Valencia-Alvarado, A. De La Piedad-Beneitez, R. López-Callejas, A. Mercado-Cabrera, R. Peña-Eguiluz, A.E. Muñoz-Castro, B.G. Rodríguez-Méndez, J.M. De La Rosa-Vázquez, TiO2 thin and thick films grown on Si/glass by sputtering of titanium targets in an RF inductively coupled plasma, J. Phys. Conf. Ser. 591 (2015). doi:10.1088/1742-6596/591/1/012042.

[20] Y. Liang, S. Sun, T. Deng, H. Ding, W. Chen, Y. Chen, The preparation of TiO2 film by the sol-gel method and evaluation of its self-cleaning property, Materials (Basel). 11 (2018) 1–12. doi:10.3390/ma11030450.

[21] A. Hosseini, K. Içli, M. Özenbaş, Erçelebi, Fabrication and characterization of spin-coated TiO2 films, Energy Procedia. 60 (2014) 191–198. doi:10.1016/j.egypro.2014.12.332.

[22] L. Hu, T. Yoko, H. Kozuka, S. Sakka, Effects of solvent on properties of sol-gel-derived TiO2 coating films, Thin Solid Films. 219 (1992) 18–23. doi:10.1016/0040-6090(92)90718-Q.

[23] T.D.C. Hobson, L.J. Phillips, O.S. Hutter, H. Shiel, J.E.N. Swallow, C.N. Savory, P.K. Nayak, S. Mariotti, B. Das, L. Bowen, L.A.H. Jones, T.J. Featherstone, M.J. Smiles, M.A. Farnworth, G. Zoppi, P.K. Thakur, T.L. Lee, H.J. Snaith, C. Leighton, D.O. Scanlon, V.R. Dhanak, K. Durose, T.D. Veal, J.D. Major, Isotype Heterojunction Solar Cells Using n-Type Sb2Se3 Thin Films, Chem. Mater. 32 (2020) 2621–2630. doi:10.1021/acs.chemmater.0c00223.

[24] N. Spalatu, R. Krautmann, A. Katerski, E. Karber, R. Josepson, J. Hiie, I. Oja, M. Krunks, Solar Energy Materials and Solar Cells Screening and optimization of processing temperature for Sb2Se3 thin film growth protocol : Interrelation between grain structure , interface intermixing and solar cell performance, Sol. Energy Mater. Sol. Cells. 225 (2021) 111045. doi:10.1016/j.solmat.2021.111045.

Chapter 5
Study of Absorber layer

This chapter describes the study of thickness dependence of the absorber layer by thermal evaporation along with the characterization techniques used for studying their structural, surface morphological, optical and electrical properties. Sb_2Se_3 solar cell was constructed by superstrate configuration and its photovoltaic properties were studied under standard photovoltaic test conditions.

5.1 Thermally evaporated Sb_2Se_3 absorber.

In this chapter we present the results on optimization of Sb_2Se_3 buffer layer for the fabrication of efficient solar cells. The TEC front contact is composed of a fluorine doped tin oxide (FTO) layer followed by a high resistivity transparent un-doped tin oxide (SnO_2) layer on soda lime glass, while a stack of 400 nm thick indium tin oxide (ITO) film was deposited on a 3×3 cm^2, 4mm thick, soda-lime glass by radio frequency (RF)-magnetron sputtering with 90% In_2O_3 and 10% SnO_2 target in Ar+2% O_2 atmosphere and with a substrate temperature of 400 °C. Subsequently, the ITO layer was covered by a 100 nm thick i-ZnO film, deposited by RF magnetron sputtering in an atmosphere of Ar+2% O_2 again with a substrate temperature of 400 °C. The stack was then annealed in vacuum at 10^{-4} Pa at 450 °C. CdS was deposited on the TEC and ITO/ZnO stack by thermal evaporation at a pressure of 10^{-4} Pa, and substrate temperature of 150 °C, with a thickness of 150 nm. After deposition, the layer was annealed in vacuum at 450 °C to improve its crystalline structure.

The samples were then transferred into another vacuum evaporation unit where Sb_2Se_3 with varying thickness (1000, 800, 450 nm) was deposited on glass/TEC/CdS and glass/ITO/ZnO/CdS stack at a base pressure of 3.6×10^{-4} Pa and with a substrate temperature of 300 °C. The material source (Sb_2Se_3 lumps) is heated in a graphite crucible at a temperature range of 700–800 °C in order to be evaporated at a deposition rate of approximately 0.20 nm/sec. To complete the cell 30 nm of gold was deposited by thermal evaporation.

5.1.1 Measurement and characterization.

5.1.2 Structural Characterization.

High quality Sb_2Se_3 films with high quality, optimal thickness and large grains are generally desired for solar cell application. In order to achieve the goal, we explored the Sb_2Se_3 film deposition condition by varying the thickness keeping the source temperature and the substrate temperatures independent. Fig 5.1. (a, b) shows the schematic view of the films grown on TEC/CdS and ITO/ZnO/CdS. Samples with different Sb_2Se_3 thickness on TEC/CdS and ITO/ZnO/CdS were prepared at a substrate temperature of 300 °C and studied. Samples from these batches were selected for material characterization and device analysis.

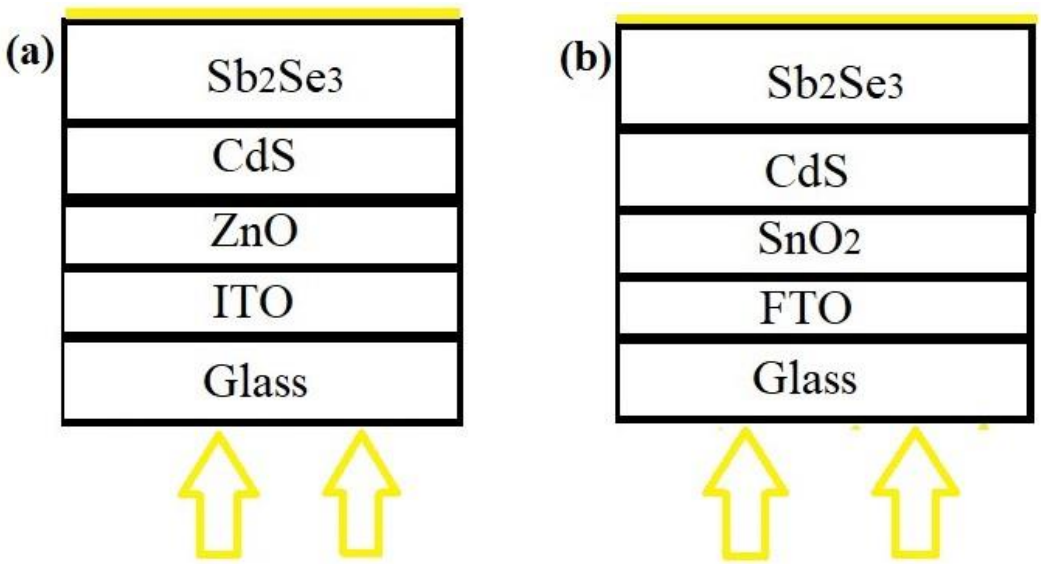

Figure 5.1 (a, b). Schematic view of Sb_2Se_3 film grown on ITO/ZnO/CdS and TEC/CdS.

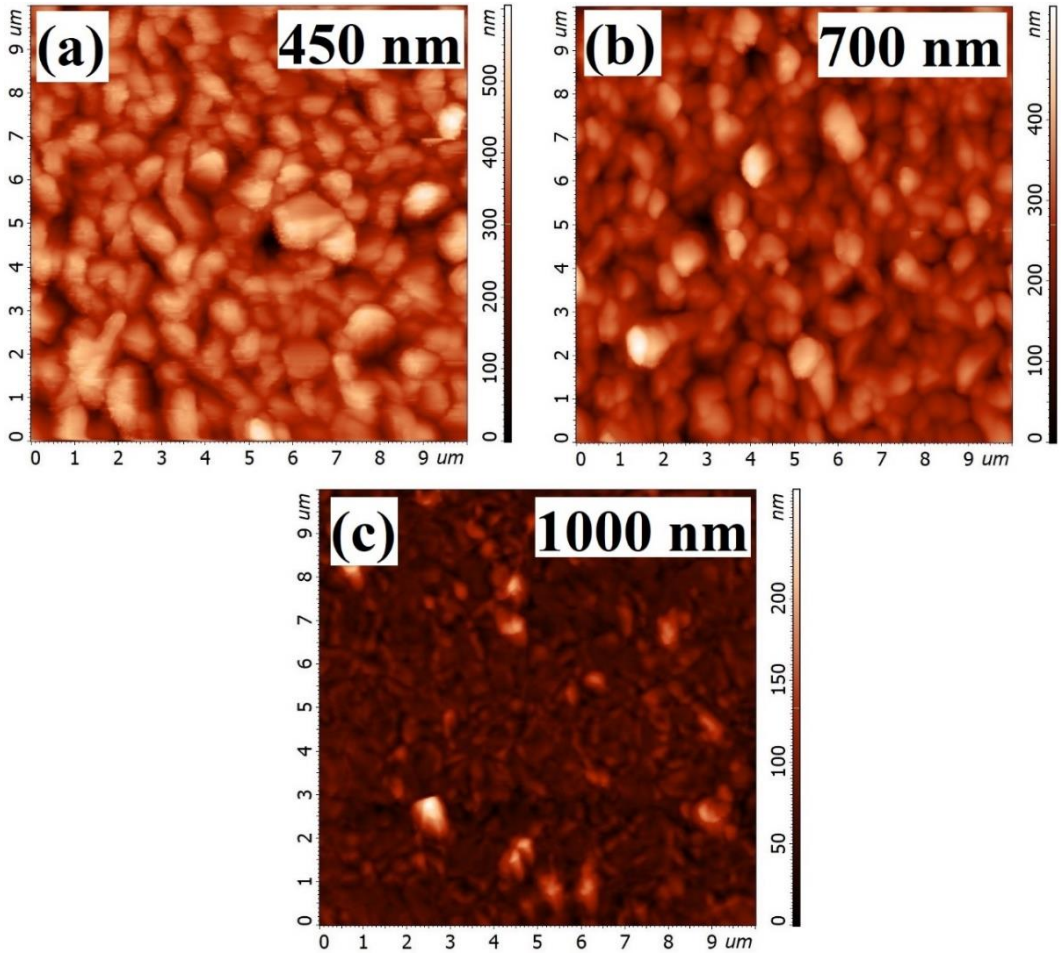

Figure 5.2 (a, b, c). AFM images of Sb_2Se_3 deposited on ITO/ZnO/CdS.

The surface morphology was examined by recording atomic force microscopy (AFM) images using non-contact mode. The films grown on ITO/ZnO/CdS superstrate structure shows homogeneous growth of Sb_2Se_3 films, the films are crack free with very few pinholes as shown in Fig 5.2. The variation in size of the ranges from few nanometers to few microns as we go down with the thickness from 1000 nm to 450 nm.

Fig 5.3. demonstrates the films growth on TEC/CdS substrate the 2D view shows that the film are spherical in nature and with few pinholes. The films deposited with 1000 nm thickness shows a different grin structure compared to that of the ones grown with 700 and 450 nm thickness. On comparing both TEC and ITO we see that on TEC the grain growth intially has bigger grains but as we go down with the thickness the grains follow the same trend, whereas in ITO case the the grains become larger as we scale down the thickness. But in both the cases we have good electrical conductivity

and we could hardly observe any notable difference making both as a choice of the deposition.

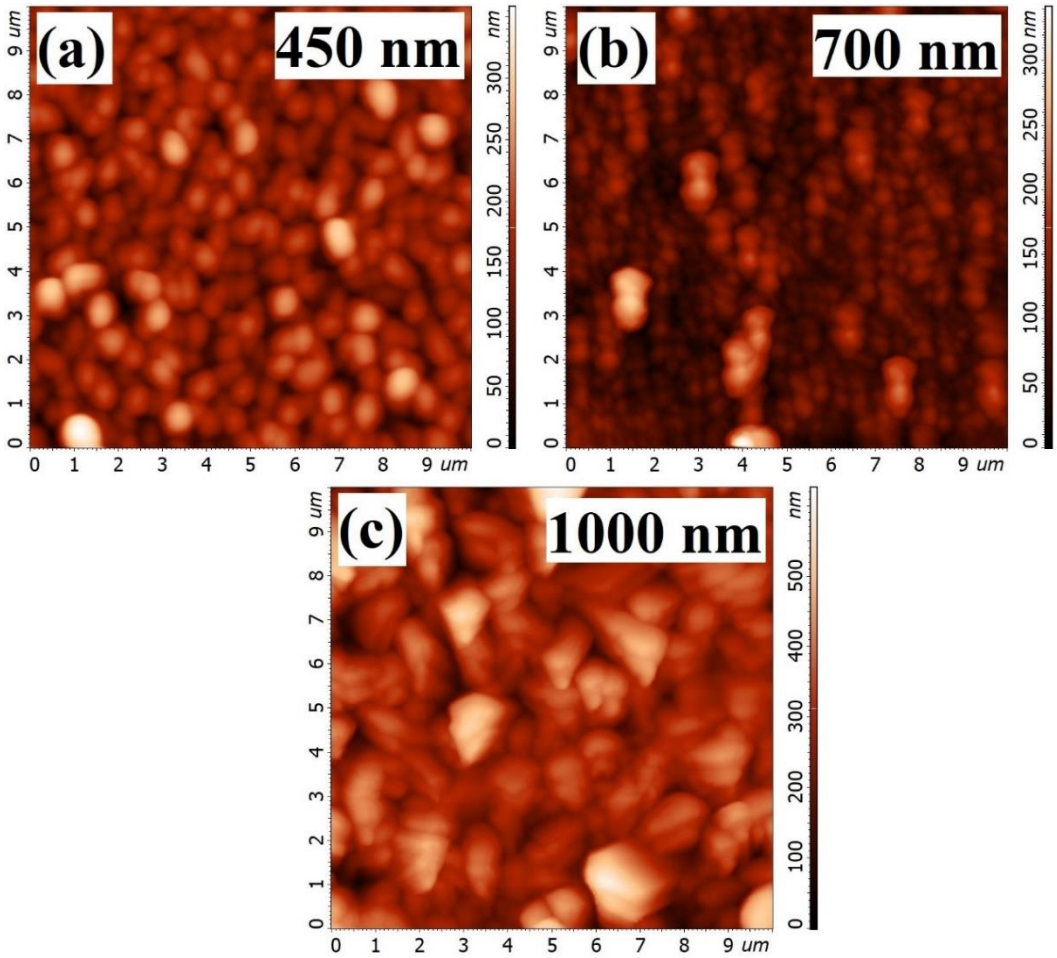

Figure 5.3(a, b, c). AFM images of Sb_2Se_3 grown on TEC/CdS.

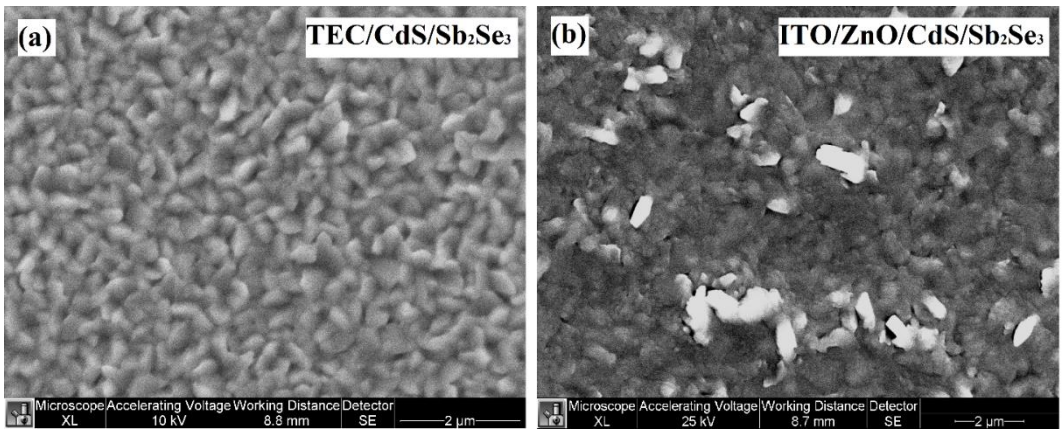

Figure 5.4(a, b) SEM images of Sb_2Se_3 on TEC/CdS and ITO/ZnO/CdS.

Morphology of Sb_2Se_3 film was studied by SEM. Top-view SEM image Fig 5.4. (a, b) revealed the film was composed of large Sb_2Se_3 grains free of pinholes and cracks. The chemical composition result of the Sb_2Se_3 thin films deposited by thermal evaporation was analysed by energy dispersive X-ray spectroscopy (EDS) are summarized in Table 5.I The stoichiometric composition of Sb/Se is greater than 0.66 which is the ideal ratio suggesting that the as deposited films are Se poor or Sb rich it has also been reported by Rong et.al.[5].

Table 5.I. EDX of Sb_2Se_3.

Element	Atomic (%)
Sb	55.53
Se	44.47
Total	100

Fig 5.5. shows the XRD pattern for the Sb_2Se_3 thin film grown via thermal evaporation at a substrate temperature of 300 °C on ITO/ZnO/CdS. All the diffraction peaks in the patterns were indexed to the orthorhombic phase of Sb_2Se_3 (JCPDS 15-0861) with space group of P*nma*. The sample with thickness of 1000 nm is indexed with diffracting peaks of (211), (221), (041), (141), (321) indicating Sb_2Se_3 film have a strong preferred orientation along the (001) direction and the $(Sb_4Se_6)_n$ ribbons. In contrast, the intensity of the (040), (420), (250) peak are indicative of (hk0) planes, which are unfavourable for solar cell as they hinder the charge transfer and hence affect the performance which has also been reported by Xiaobo et.al. [6]. As we scale down the thickness of Sb_2Se_3 from 1000 nm to 450 nm the growth and orientation of the film changes. We see that major preferred orientation (hk1) peak shift from (321) to (621) it is to note that (621) was not detected in the thicker film which is an indicative that with change in thickness there is change in the orientation. Also, the (hk0) peak intensity of (330) and (360) increases. Overall, the (hk1) peaks in 450 nm thin films have higher orientation than those of the 1000 nm films.

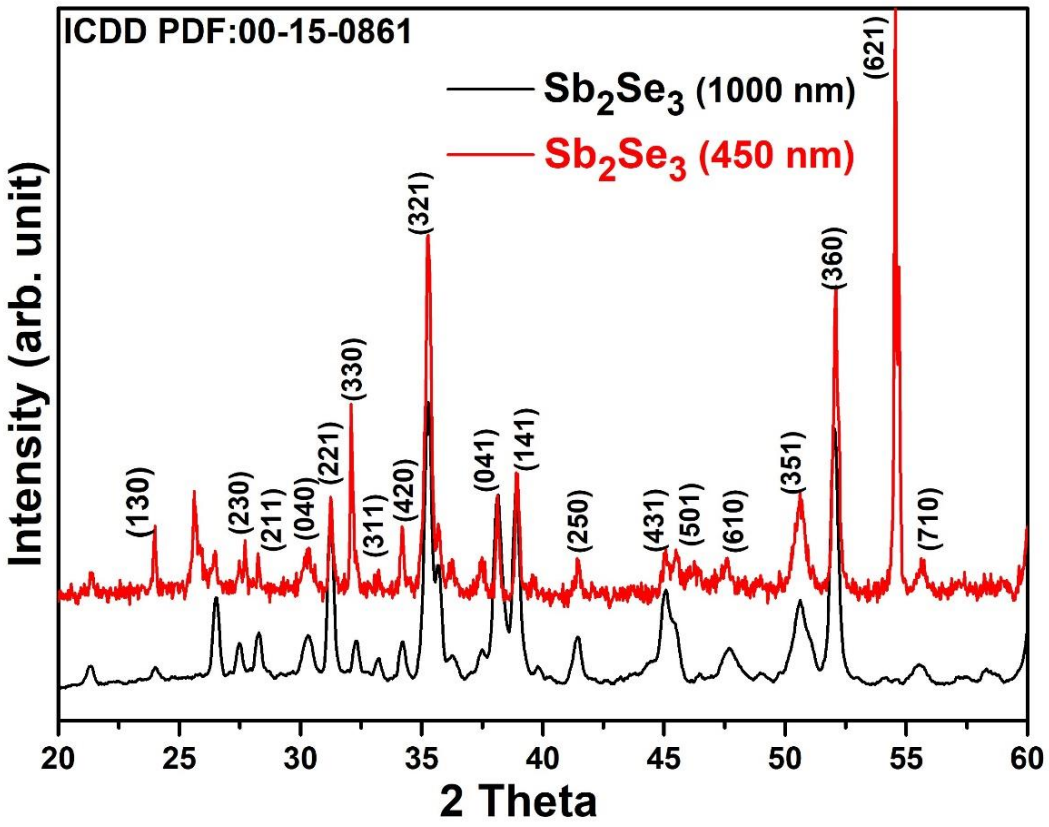

Figure 5.5. XRD pattern of Sb_2Se_3 on ITO/ZnO/CdS.

Further Sb_2Se_3 film is grown on TEC/CdS substrate as shown in Fig 5.6. The (221), (321), (041), (141) oriented grains are composed of tilted $(Sb_4Se_6)_n$ ribbons which are vertically stacked, where as the (240), (250) oriented grains arrange themselves horizontally parallel with the substrate. For the charge to transport vertical movement is easy as it does not has to hopp between the ribbon. The (hk1) grains reduces recombination losses due to benign boundaries hence they are preffered film orientation which is quite evident in our case and is also the reason for good performance of the device. When we compare both ITO/ZnO/CdS and TEC/CdS according to the Xrd data TEC/CdS is preffereable as they have very only couple of (hk0) planes which has also been stated by et. al Ying [7].

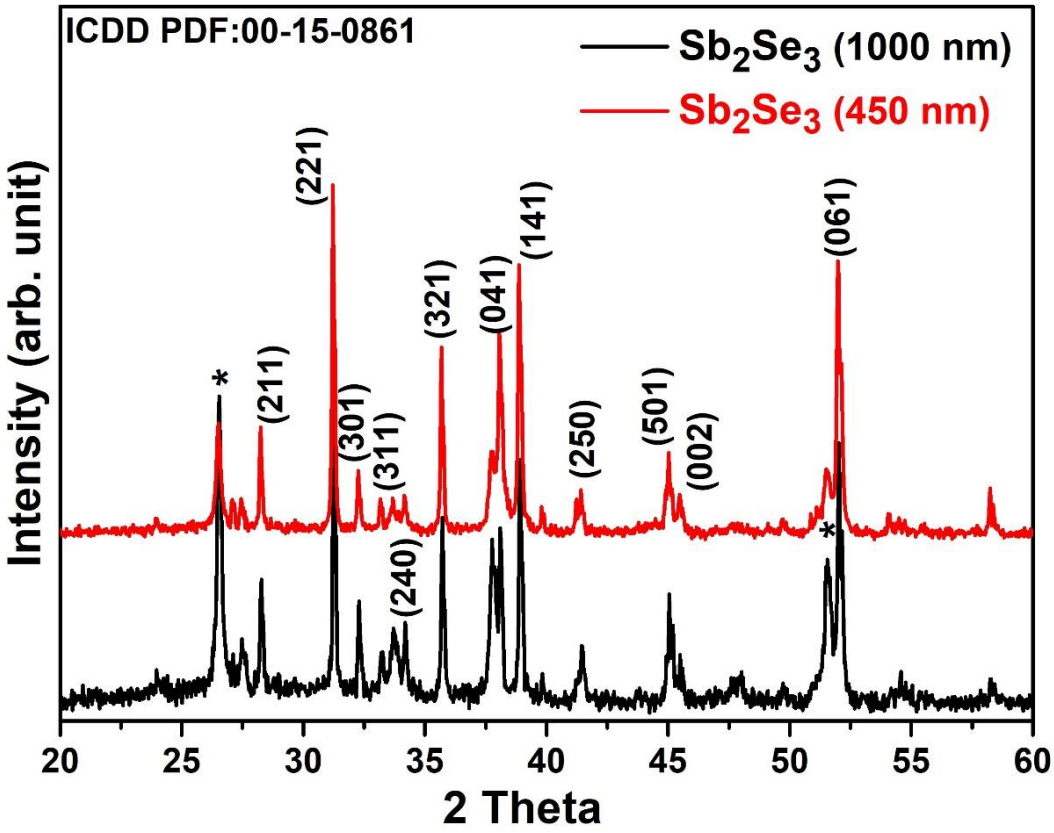

Figure 5.6. XRD of Sb_2Se_3 on TEC/CdS.

Raman spectra of Sb_2Se_3 films (ITO/ZnO/CdS and TEC/CdS) were performed at room temperature with a 532 nm laser as excitation source. The results are shown in Figure 5.7 and 5.8. The collected peaks for all the samples are in good agreement with the results reported by Ivanova et al. [8]. Raman spectrum of the samples deposited at substrate temperature of 300 °C exhibits a paramount band peaked at about 189 cm^{-1} and some other more less pronounced bands at about 154, and 211 cm^{-1}, and 151 and 210 cm^{-1} for the respective samples which is commonly attributed to vibrational modes of Sb_2Se_3 in orthorhombic phase. The paramount band at 189 cm^{-1} is clearly defined in terms of intensity and spectral profile, suggesting a good crystallinity of the films. Peak at 154 cm^{-1} is pronounced while the later shows peak broadening and shift towards the shorter wavelength 151 cm^{-1} which is of Sb_2Se_3 as also reported by Shongalova. et. al. [9]. Raman spectra revels that Sb_2Se_3 shows better crystal growth.

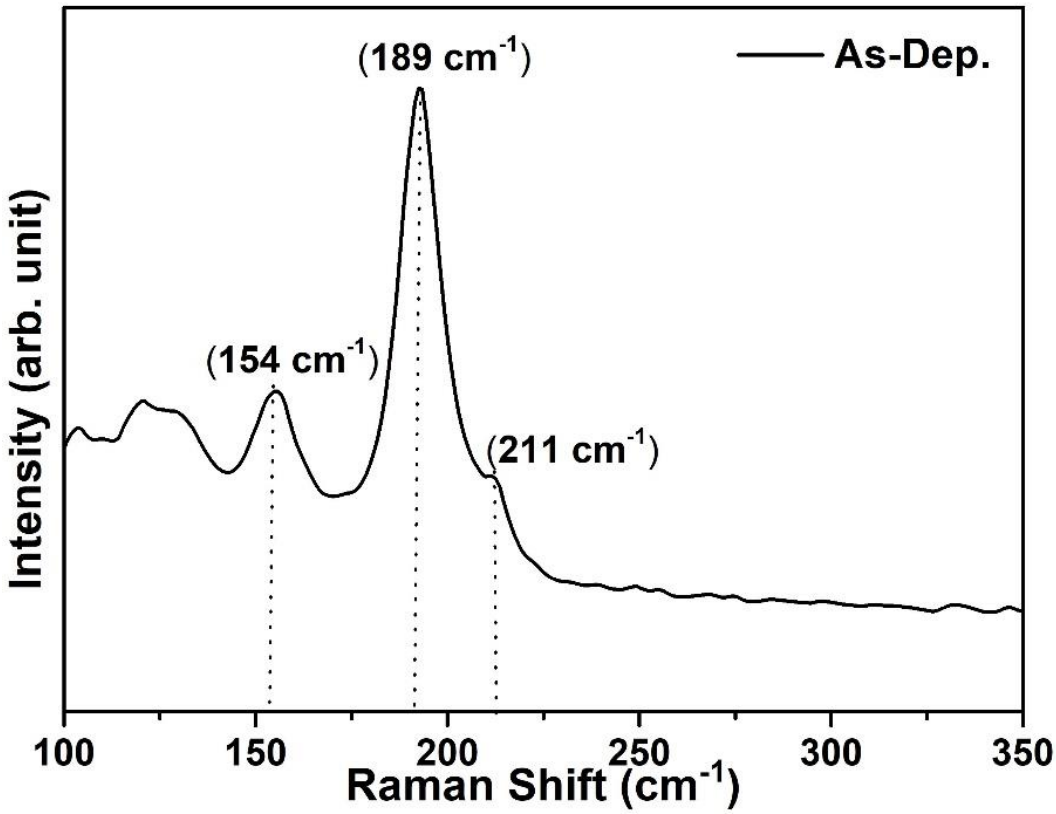

Figure 5.7. Raman Spectra of Sb_2Se_3 on ITO/ZnO/CdS.

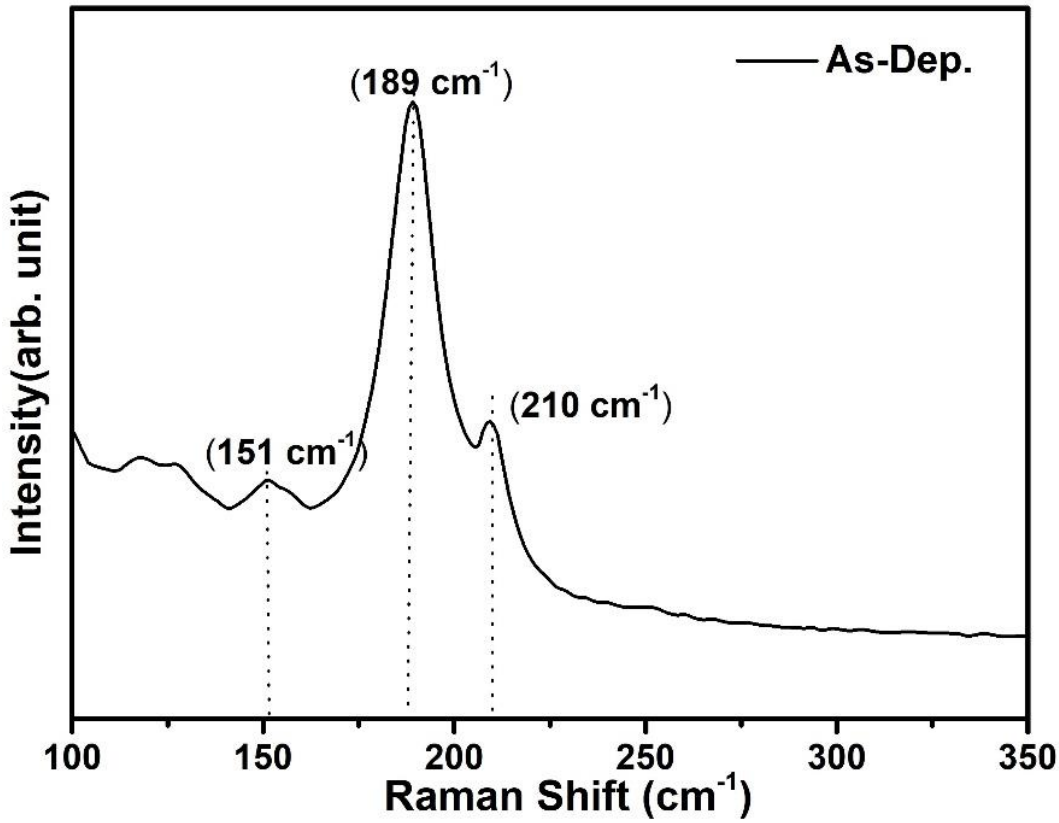

Figure 5.8. Raman Spectra of Sb_2Se_3 on TEC/CdS

5.1.3 Electrical Characterization.

Fig 5.9. shows the current density-voltage characteristics of our Sb_2Se_3 solar cells under 100 mW/cm^2 simulated AM1.5G irradiation. The champion device exhibited a short-circuit current density J_{sc} of 17.8 mA/cm^2, an open circuit voltage V_{oc} of 296.5 mV, and a fill factor FF of 40.0 %, corresponding to a solar to electricity conversation efficiency (η) of 2.1%.

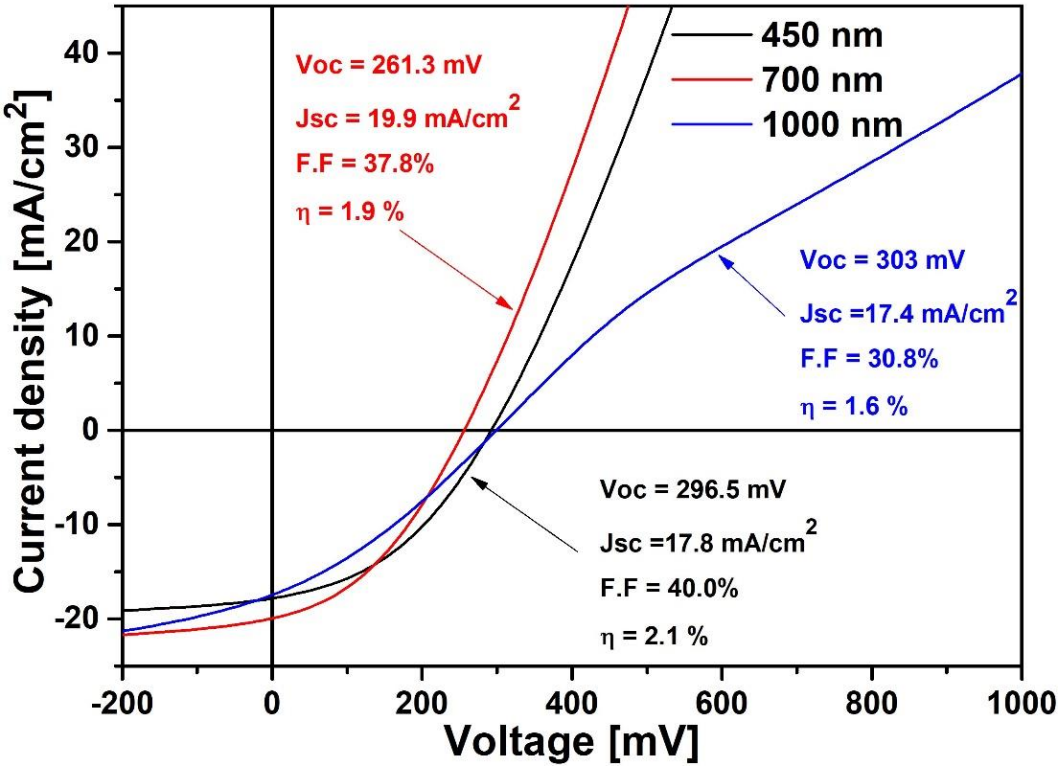

Figure 5.9. J-V of Sb_2Se_3 on ITO/ZnO/CdS

In all the devices reported herein Fig 5.10. illumination is from the front side i.e FTO side and the photogenerated charge carriers separate at p-Sb_2Se_3/n-CdS interface. Electrons move towards the CdS side and are collected by the FTO, while the holes travel through the Sb_2Se_3 absorber and are collected at the back contact by Au. The certified device exhibited a J_{sc} of 18.4 mA/cm^2, a V_{oc} of 317.6 mV and an FF of 35.1%, which corresponds to a power-conversion efficiency (PCE) of 2.0 %.

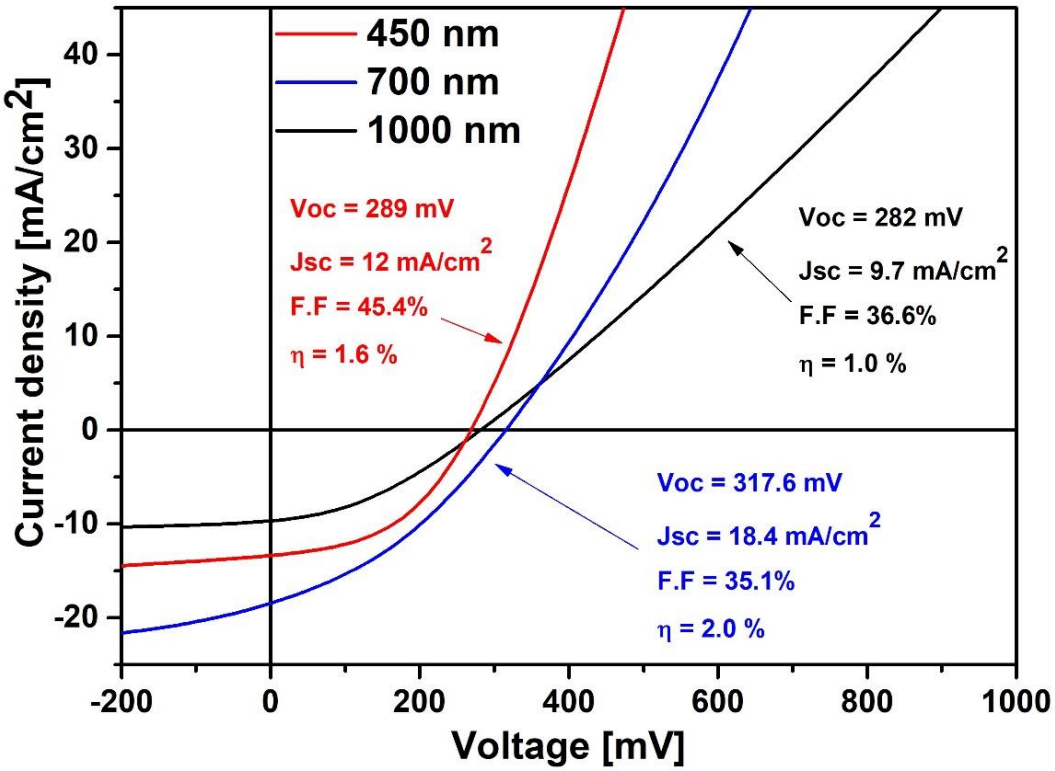

Figure 5.10. J-V of Sb_2Se_3 on FTO/SnO_2.

5.1.4 Conclusion.

To sum up we present non-toxic, stable method of solar-cell fabrication with a certified device efficiency of 2.0 % irrespective of the front contact. The optimized thickness was 450 nm. Our work reveals that 1D Sb_2Se_3 is a promising absorber when the films are oriented in the desired (hk1) for the unhindered transport of charge. This is possible due to minimal recombination along that direction. The SEM images and the AFM images also reveal that the films are homogeneous, crack free and with few pin holes. The grains range from nanometer to few microns. Raman studies also suggest the formation of good crystalline quality of Sb_2Se_3. Our study also concludes that the as deposited films are Sb rich which might be the reason for lower performance of the solar cells. In order to eradicate this shortcoming, we need to selenize the film to adjust the Sb:Se ratio.

5.2 References.

[1] A. Zhao, Silicon Solar Cells Physics of Silicon Solar Cells Future of Solar Cells, (2015) 7–8.

[2] V. Kumar, E. Artegiani, A. Kumar, G. Mariotto, F. Piccinelli, A. Romeo, E ff ects of post-deposition annealing and copper inclusion in superstrate Sb 2 Se 3 based solar cells by thermal evaporation, Sol. Energy. 193 (2019) 452–457. https://doi.org/10.1016/j.solener.2019.09.069.

[3] C. Yuan, X. Jin, G. Jiang, W. Liu, C. Zhu, Sb2Se3 solar cells prepared with selenized dc-sputtered metallic precursors, J. Mater. Sci. Mater. Electron. 27 (2016) 8906–8910. https://doi.org/10.1007/s10854-016-4917-3.

[4] P. Prabeesh, V.G. Sajeesh, I. Packia Selvam, M.S. Divya Bharati, G. Mohan Rao, S.N. Potty, CZTS solar cell with non-toxic buffer layer: A study on the sulphurization temperature and absorber layer thickness, Sol. Energy. 207 (2020) 419–427. https://doi.org/10.1016/j.solener.2020.06.103.

[5] R. Tang, Z.H. Zheng, Z.H. Su, X.J. Li, Y.D. Wei, X.H. Zhang, Y.Q. Fu, J.T. Luo, P. Fan, G.X. Liang, Highly efficient and stable planar heterojunction solar cell based on sputtered and post-selenized Sb2Se3 thin film, Nano Energy. 64 (2019) 103929. https://doi.org/10.1016/j.nanoen.2019.103929.

[6] X. Hu, J. Tao, Y. Wang, J. Xue, G. Weng, C. Zhang, S. Chen, Z. Zhu, J. Chu, 5.91%-efficient Sb2Se3 solar cells with a radio-frequency magnetron-sputtered CdS buffer layer, Appl. Mater. Today. 16 (2019) 367–374. https://doi.org/10.1016/j.apmt.2019.06.001.

[7] Y. Zhou, L. Wang, S. Chen, S. Qin, X. Liu, J. Chen, D.J. Xue, M. Luo, Y. Cao, Y. Cheng, E.H. Sargent, J. Tang, Thin-film Sb2Se3 photovoltaics with oriented one-dimensional ribbons and benign grain boundaries, Nat. Photonics. 9 (2015) 409–415. https://doi.org/10.1038/nphoton.2015.78.

[8] Z.G. Ivanova, E. Cernoskova, V.S. Vassilev, S. V. Boycheva, Thermomechanical and structural characterization of GeSe2-Sb2Se3-ZnSe glasses, Mater. Lett. 57 (2003) 1025–1028. https://doi.org/10.1016/S0167-577X(02)00710-3.

[9] A. Shongalova, M.R. Correia, B. Vermang, J.M.V. Cunha, P.M.P. Salomé, P.A. Fernandes, On the identification of Sb2Se3 using Raman scattering, MRS Commun. 8 (2018) 865–870. https://doi.org/10.1557/mrc.2018.94.

Chapter 6

Study of Front Contact

This chapter is related to the study of the front contact ITO/ZnO and FTO/SnO_2 and thier effect on Sb_2Se_3 solar cell.The surface morphology, optical and electrical properties and the performance of the antimony selenide film will be studied and discussed.

6.1 ITO/ZnO and FTO/SnO_2 front contact.

The performance of solar photovoltaic cells depends on their design, material properties, and fabrication technology [1]. The front contact plays an important role by having an impact on the electrical and optical properties of the solar cells. These materials are unique as they offer high optical transmissivity in the visible region and low electrical resistivity [2]. ITO, ZnO, SnO_2 and FTO are used as high resistant layer due to their desired optical and electrical properties. The transparent conductive layer is complicated system because of their electron affinity and band gap. It is because of this complexity they have a heterojunction structure and in this structure the band offset and interface properties are of main significance [3,4]. Values of the electron-hole mobility, charge carrier and band gap are listed in Table 6.I. [5–7].

Table 6.I. Parameters.

	Band gap (eV)	Electron mobility ($cm^2/V/s$)	Hole mobility ($cm^2/V/s$)	Carrier density
ITO	3.72	30	5	4.3×10^{23}
ZnO	3.27	100	25	1×10^{19}
FTO	3.65	15	-	1.46×10^{20}
SnO_2	4.11	3.6	1	2.4×10^{18}

FTO, ITO, SnO_2 exhibits good transparency owing to the wide band-gap, as well as they show a low electrical resistivity due to the high carrier concentration which is caused by the oxygen vacancies. FTO is mechanically, chemically and

electrochemically stable and so they can be directly coated on glass, whereas a passivation layer is required in case of ITO [8,9].

6.1.1 Experimental details.

Here we are going to discuss the two front contacts used by us. The first front contact is made by the deposition of two layers: 80 nm thick intrinsic ZnO and 1 μm thick ITO by RF sputtering, respectively with a power of 60 W and 160 W with a substrate temperature of 150 °C with continuous oxygen flux (O_2-0.5 sccm) at 150 °C. Consecutively the second used transparent conducting layer (TCO) is fluorine doped tin oxide (FTO) followed by a high resistivity transparent (HRT) un-doped tin oxide (SnO_2 → TO) layer deposited by Pilkington on soda lime glass (NSG TEC 12D). The samples were transferred into the vacuum evaporation unit where Sb_2Se_3 was deposited on glass/TEC and glass/ITO/ZnO stack at a base pressure of 3.6×10^{-4} Pa and with a substrate temperature of 300 °C. The material source (Sb_2Se_3 lumps) is heated in a graphite crucible at a temperature range of 700–800 °C in order to be evaporated at a deposition rate of approximately 0.20 nm/sec. To complete the cell 30 nm of gold was deposited by thermal evaporation.

6.1.2 Characterization.

Ultraviolet visible (UV-VIS) spectroscopy was used to record the absorption spectra. Absorption of radiation causes electronic transitions from the ground state to the excited state in atoms or molecules. Band gap is the minimum energy required for electronic transition from the valence band to the conduction band. So, measuring the band-gap energies for the materials used in photovoltaic cell is important. Beer-Lambert law states that the absorbance of a solution is directly proportional to the concentration of the absorbing species in the solution and the path length. $A = \varepsilon\, c\, L = \log_{10}(I_o/I)$, A = absorbance, ε = molar absorptivity or extinction coefficient, c = concentration of the absorbing species L = path-length I_o = intensity of light before passing through the sample I = intensity of light after passing through the sample %T = $(I/I_o) \times 100$. The reflectance (R) of the sample can be evaluated by the relation R + T + A = 1.

The absorption spectrum represents the minimum energy required for electronic transition from the valence band to the conduction band is the absorption edge of the solution. The wavelength at the absorption edge can be used to calculate the energy band-gap. The optical properties of ITO/ZnO, and FTO/SnO_2 films are measured. Fig 6.1 and 6.2 shows the optical transmission of the as deposited ITO/ZnO and FTO/SnO_2 films. At the wavelength from 500 nm to 800 nm, the average transmittance is nearly 82% for ITO/ZnO and 81.0% for FTO/SnO_2 films, respectively. High transparency in the visible region greater than 80 % was observed, in accordance with the requirements for TCO applications. Also it can be associated with good structural homogeneity [6]. The presence of interference fringe in Fig 6.1. is due to multiple reflections that occurs at film/air and film/substrate interface. These reflections in films come into view when the surface is smooth. High resistance transparent ZnO or SnO_2 films on ITO or FTO films can be used to passivate CdS surface which could eliminate the leakage current caused by the pinhole effects of CdS and thus improves the short circuit current remarkably [10].

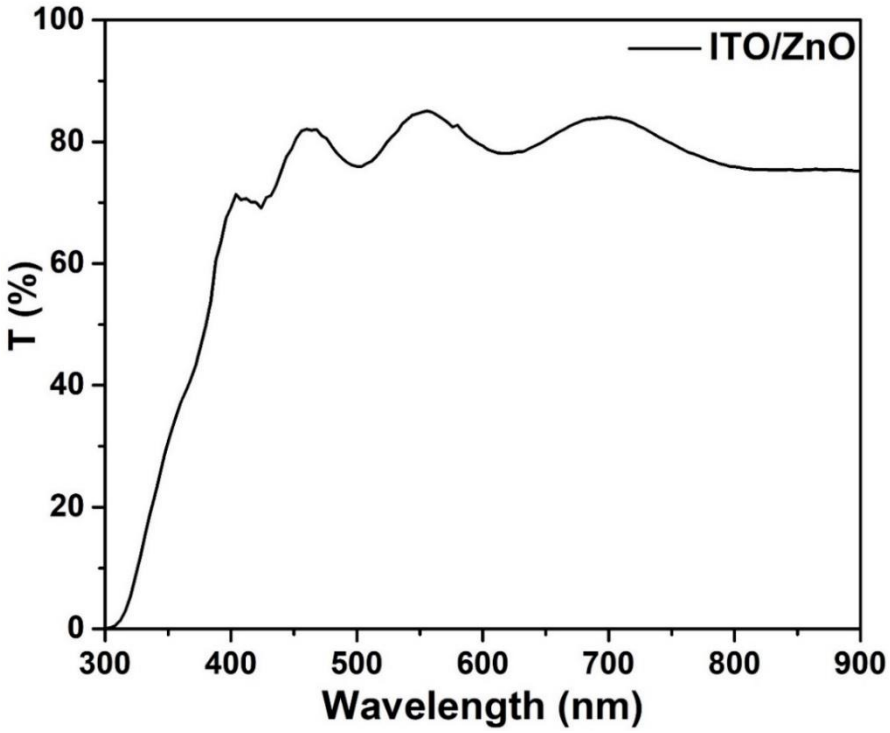

Figure 6.1. Transmittance plot of ITO/ZnO.

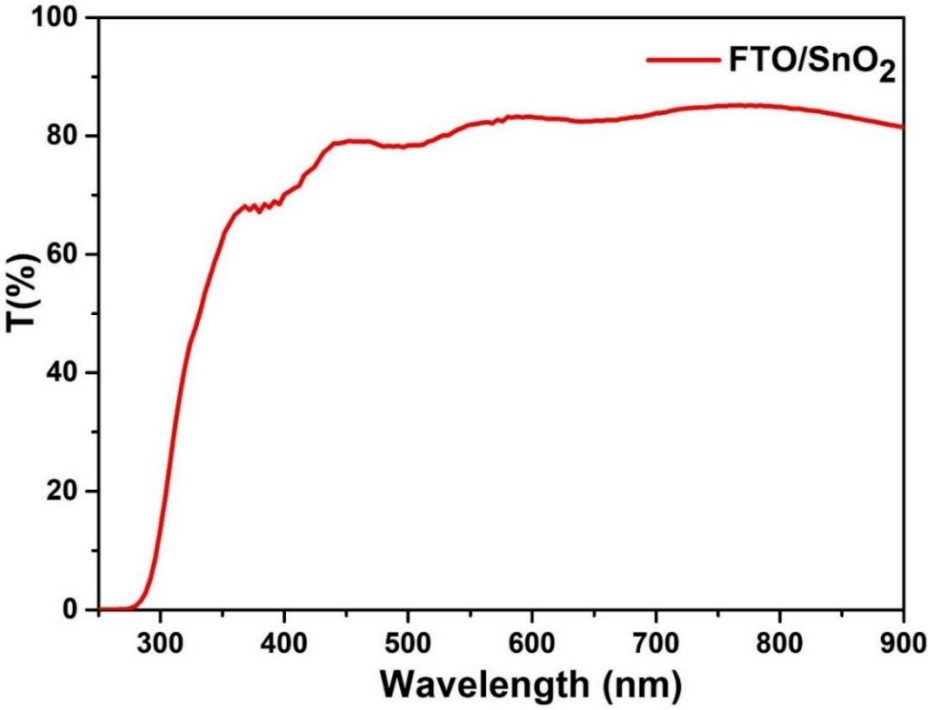

Figure 6.2. Transmittance plot of FTO/SnO_2

Fig 6.3 shows XRD patterns of Sb_2Se_3 deposited directly on ZnO and SnO_2 by thermal evaporation. All the diffraction peaks are indexed to the orthorhombic Sb_2Se_3 with the space group of Pnma 62 (JCPDS Card No. 15-0861). We found no peak attributed to the detrimental Se phase due to low temperature vacuum evaporation deposition.The main diffraction peaks of (211), (221), (061) is quite evident with both the substrate, there are some additional (hk0) peaks (020), (120), (130), according to Kanghua Li et.al. (120) is a dominant peaks when ZnO is used as buffer layer [11] . Deposition without CdS buffer layers leads to the growth of unwanted hk0 peaks which perturbs the performance of the device and its perfromance which has been discussed by Huafei et. Al [12] .

Atomic force microscopy (AFM) is the one of the mostly used versatile and powerful technique for the analysis of samples in the nano-scale level. This technique provides various types of surface measurements like grain size, RMS roughness, average roughness, peak-to-peak height, skewness, and kurtosis. Two-dimensional AFM images of the deposited ZnO, SnO_2 on ITO and FTO along with the final Sb_2Se_3, is presented in Fig. 6.4(a, b). The deposited ZnO with sputtering shows very small

grains as compared to that of the SnO_2 provided to us by the company. Surface shows distinct grain distribution with compact granular topography. The grain size varied from 16 to 60 nm with average roughness of the deposited ZnO and SnO_2 thin film was around 4.6 nm and 19 nm (see in Table 6.II).The higher value of roughness was due to nucleation and grain growth.Fig 6.4(c, d) represents the deposited Sb_2Se_3 it is quite visible that the growth of antimony selenide is columunar in nature, compact and without pinholes.

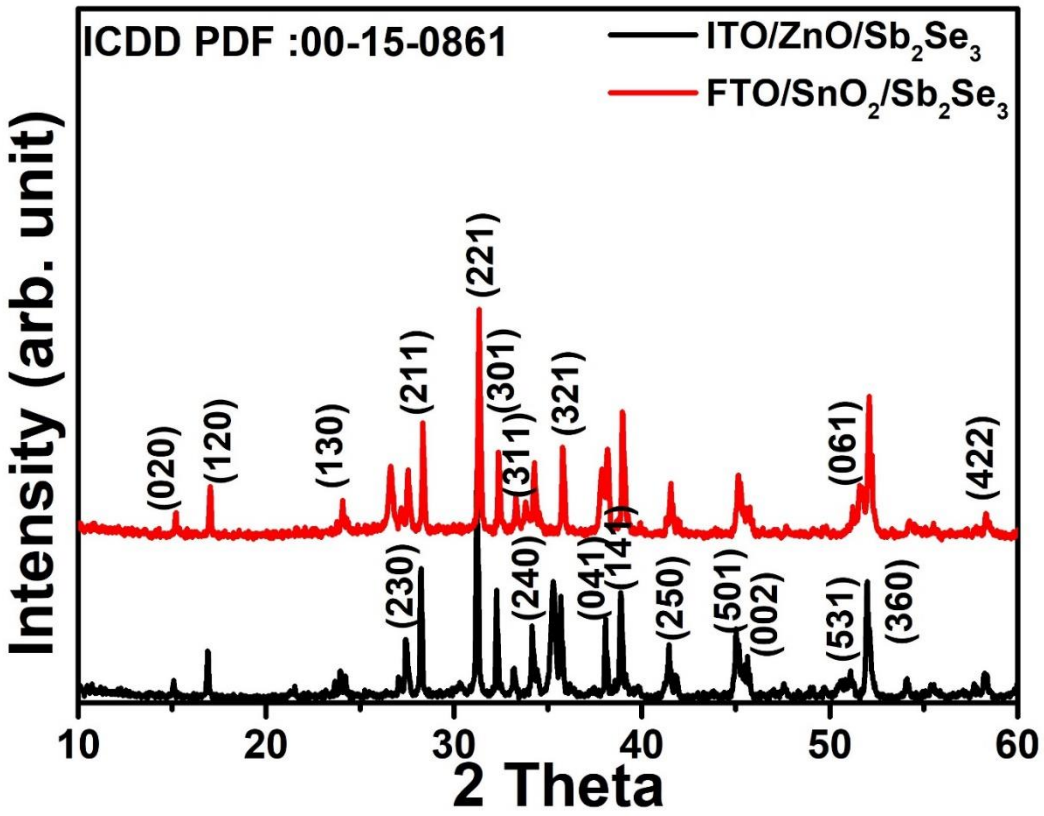

Figure 6.3. Xrd of Sb_2Se_3 on ZnO and SnO_2.

The parameters reported in the Table 6. II. such as skewness (Ssk) and kurtosis (Ska) give the measurement of the asymmetry and the sharpness. The value of skewness (Ssk) can either be zero, positive, or negative. The skewness factor becomes zero if the height distribution is symmetrical. For an asymmetrical height distribution, the surface has more peaks than valleys which leads to a positive value of skewness. If the surface of the film is more planar, then the value of skewness turns out to be negative. Another parameter kurtosis (Ska) measures the distribution with a reference value of 3. If the kurtosis value is equal to 3 it signifies mesokurtic which is Gaussian

amplitude distribution, and platykurtic if less than 3 which indicates that the surface is flat. The kurtosis factor for the films is nearly 1 which shows that the surface has a gaussian amplitude.

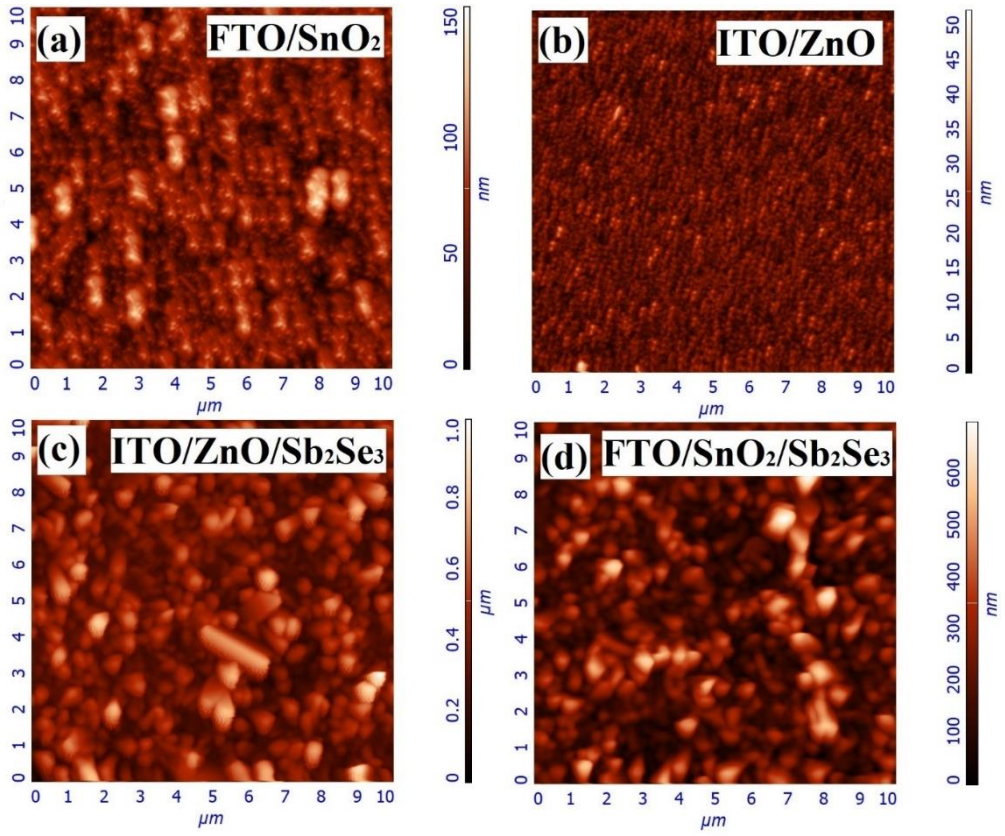

Figure 6.4. AFM images of ZnO, SnO_2, Sb_2Se_3 on both in clockwise direction.

Table 6. II. Calculated parameters-root mean square roughness (RMS), average roughness (R_{av}), skewness (Ssk), kurtosis (Ska), and grain size.

Parameters	ITO/ZnO	FTO/SnO_2	ITO/ZnO/Sb_2Se_3	FTO/SnO_2/Sb_2Se_3
RMS roughness (nm)	4.60137	18.9198	132.032	103.957
R_{av} (nm)	3.58196	14.7565	104.733	81.0995
Skewness (Ssk)	0.598789	0.606553	0.93756	1.00045
Kurtosis (Ska)	1.16281	0.746922	0.754625	1.09907
Grain size (nm)	15.92	59.6801	383.76	218

6.1.3 Electrical Study.

Once illuminated, photogenerated electrons in Sb_2Se_3 would inject into ZnO and SnO_2, swept by the built-in field and finally collected by ITO and FTO respectively. The photogenerated holes drift within the depletion region, diffuse through the quasi-neutral region of Sb_2Se_3 film and finally are collected by Au electrodes. The current–voltage characteristics of our best Sb_2Se_3 solar cells under 100 $mWcm^{-2}$ simulated AM1.5G irradiation are shown in Figure 5. The best device for the TEC based solar cell exhibited a short-circuit current density (J_{sc}) of 16.4 $mAcm^{-2}$, an open circuit voltage (V_{oc}) of 156 mV, and a fill factor (FF) of 26.8%, corresponding to a solar to electricity conversation efficiency (η) of 0.7%, and the highest efficiency for ITO based Sb_2Se_3 solar cells is 1.4%. The performance of the devices was relatively low. Studies done by K. Shen et al. also suggest that SnO_2/CdS combination can amplify the efficiency by two folds[13].

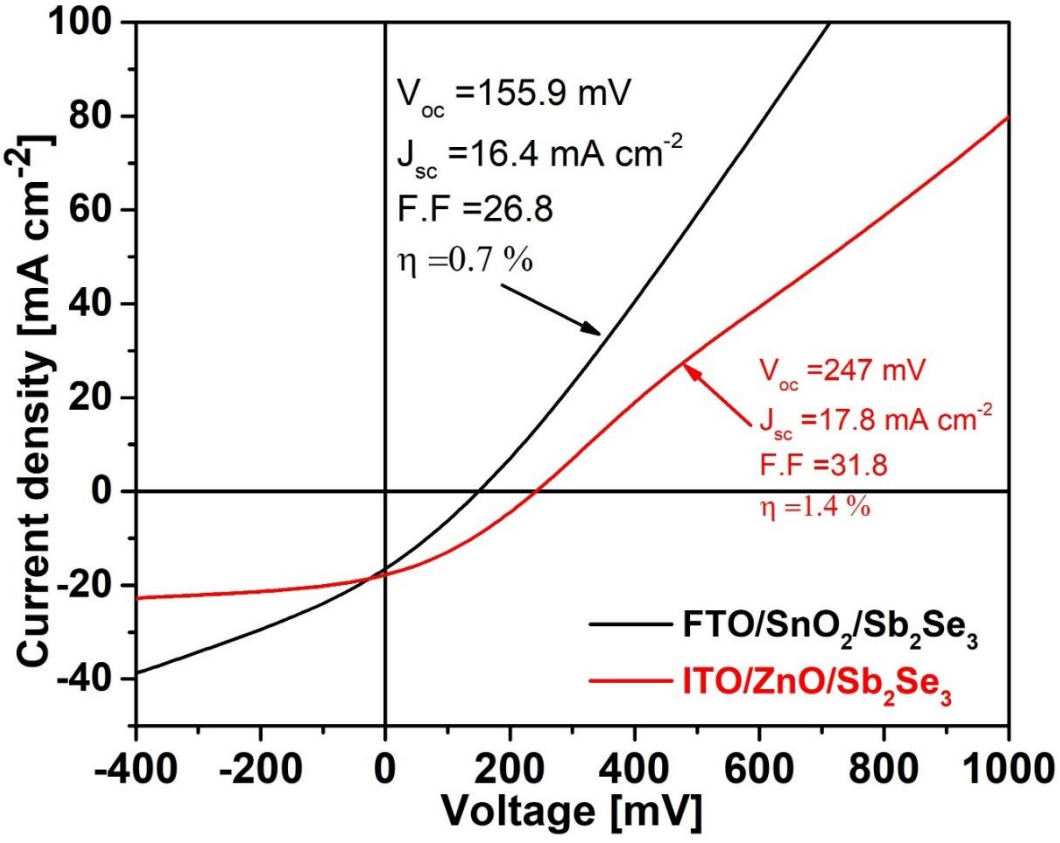

Figure 5. J–V characteristics of a well-behaved Sb_2Se_3 device.

6.1.4 Conclusion.

Our finding suggest that we were able to synthesize Sb_2Se_3 solar directly on ITO/ZnO and FTO/SnO_2 substrate. The main diffraction peaks of (211), (221), (061) is quite evident with both the substrate, there are some additional (hk0) peaks. AFM images of the deposited ZnO, SnO_2 on ITO and FTO post Sb_2Se_3 deposition have average grain size of 4 to 60 nm respectively. The performance of the device such as the current density (J_{sc}), open circuit voltage (V_{oc}) and the FF of the FTO/SnO_2 is very less compared to the ITO/ZnO. The champion cell reports an efficiency of 1.4%. Report by Huafei et al. suggest that addition of CdS suppress some of the dominant hk0 unwanted peaks. As far the transparency is considered both are equally transparent and good to be used for solar cell application however an additional buffer is required for better performance.

6.2 Reference.

[1] M.I. Kabir, S.A. Shahahmadi, V. Lim, S. Zaidi, K. Sopian, N. Amin, Amorphous silicon single-junction thin-film solar cell exceeding 10 % efficiency by design optimization, Int. J. Photoenergy. 2012 (2012). https://doi.org/10.1155/2012/460919.

[2] M.I. Hossain, A. Hongsingthong, W. Qarony, P. Sichanugrist, M. Konagai, A. Salleo, D. Knipp, Y.H. Tsang, Optics of Perovskite Solar Cell Front Contacts, ACS Appl. Mater. Interfaces. 11 (2019) 14693–14701. https://doi.org/10.1021/acsami.8b16586.

[3] J.C.K. X. Wu R. G. Dhere, C. DeHart, D. S. Albin, A. Duda, T. A. Gessert, S. Ashar, D. H. Levi and P. Sheldon, 16.5%-efficient CdS/CdTe polycrystalline thin-film solar cells, Proc. 17th Eur. PVSEC. (2001) 995–1000. http://www.sciencedirect.com/science/article/pii/S0038092X04001434.

[4] T. Minami, Present status of transparent conducting oxide thin-film development for Indium-Tin-Oxide (ITO) substitutes, Thin Solid Films. 516 (2008) 5822–5828. https://doi.org/10.1016/j.tsf.2007.10.063.

[5] T. Liu, X. Zhang, J. Zhang, W. Wang, L. Feng, L. Wu, W. Li, G. Zeng, B. Li,

Interface study of ITO/ZnO and ITO/SnO2complex transparent conductive layers and their effect on CdTe solar cells, Int. J. Photoenergy. 2013 (2013). https://doi.org/10.1155/2013/765938.

[6] Z.Y. Banyamin, P.J. Kelly, G. West, J. Boardman, Electrical and optical properties of fluorine doped tin oxide thin films prepared by magnetron sputtering, Coatings. 4 (2014) 732–746. https://doi.org/10.3390/coatings4040732.

[7] C.A. Amorim, C.J. Dalmaschio, E.R. Leite, A.J. Chiquito, Fluorine doped SnO2 (FTO) nanobelts: Some data on electronic parameters, J. Phys. D. Appl. Phys. 47 (2014). https://doi.org/10.1088/0022-3727/47/4/045301.

[8] Techinstro, Difference Between Ito and Fto Coated Glass, (n.d.) 8–10. https://www.techinstro.com/difference-ito-fto-coated-glass/.

[9] T. Tesfamichael, G. Will, M. Colella, J. Bell, Optical and electrical properties of nitrogen ion implanted fluorine doped tin oxide films, Nucl. Instruments Methods Phys. Res. Sect. B Beam Interact. with Mater. Atoms. 201 (2003) 581–588. https://doi.org/10.1016/S0168-583X(02)02226-7.

[10] M.A. Matin, M. Mannir Aliyu, A.H. Quadery, N. Amin, Prospects of novel front and back contacts for high efficiency cadmium telluride thin film solar cells from numerical analysis, Sol. Energy Mater. Sol. Cells. 94 (2010) 1496–1500. https://doi.org/10.1016/j.solmat.2010.02.042.

[11] K. Li, R. Kondrotas, C. Chen, S. Lu, X. Wen, D. Li, J. Luo, Y. Zhao, J. Tang, Improved efficiency by insertion of Zn1−xMgxO through sol-gel method in ZnO/Sb2Se3 solar cell, Sol. Energy. 167 (2018) 10–17. https://doi.org/10.1016/j.solener.2018.03.081.

[12] H. Guo, Z. Chen, X. Wang, Q. Cang, C. Ma, X. Jia, N. Yuan, J. Ding, Significant increase in efficiency and limited toxicity of a solar cell based on Sb2Se3 with SnO2 as a buffer layer, (2019) 14350–14356. https://doi.org/10.1039/c9tc04169a.

[13] K. Shen, C. Ou, T. Huang, H. Zhu, J. Li, Z. Li, Y. Mai, Mechanisms and modification of nonlinear shunt leakage in Sb2Se3 thin film solar cells, Sol. Energy Mater. Sol. Cells. 186 (2018) 58–65. https://doi.org/10.1016/j.solmat.2018.06.022.

Chapter 7
Vacuum annealing study of the absorber

In the chapter we presented our work on antimony selenide (Sb_2Se_3) thin films with varying thickness (1000, 700 and 500 nm) prepared by low temperature thermal evaporation method. Solar cells were fabricated in the superstrate configuration of Glass/ITO/ZnO/CdS/Sb_2Se_3/Au and Glass/TEC/CdS/Sb_2Se_3/Au. The absorber layer was annealed in vacuum at 300 and 350 °C and studied.

7.1 Vacuum annealing studies of Sb_2Se_3 on Glass/ITO/ZnO/CdS.

In this work, superstrate structure of Glass/ITO/ZnO/CdS/Sb_2Se_3/Cu/Au were fabricated in order to analyze the performance of the Sb_2Se_3 thin films photovoltaic devices by varying the thickness of the absorber layer. The CdS and the Sb_2Se_3 layers were deposited by thermal evaporation process without selenization of the absorber. The influence of absorber thickness on the device performance of finished cells was investigated comprehensively by the application of atomic force microscopy (AFM) and X-ray diffraction (XRD).

7.1.1 Experimental details.

Antimony selenide (Sb_2Se_3) absorber based thin film solar cells with varying thickness were synthesized in superstrate configuration by a low-temperature fabrication process based on vacuum evaporation (VE). In order to understand its properties, we have preferred to study the absorber when deposited on stack with its typical device configuration. More in detail, by radio frequency (RF)-magnetron sputtering we deposited a stack of 400 nm thick indium tin oxide (ITO) film on a soda-lime glass with 90 % In_2O_3 and 10 % SnO_2 target in Ar + 2 % O_2 atmosphere and with a substrate temperature of 400 °C. Subsequently, by RF magnetron sputtering we deposited a 100 nm thick i-ZnO film, in an atmosphere of Ar + 2 % O_2,

again with a substrate temperature of 400 °C. The stack was then annealed in vacuum at 10^{-4} Pa at 450 °C.

On the ITO/ZnO stack, CdS was deposited by thermal evaporation at a pressure of 10^{-4} Pa, and substrate temperature of 150 °C, with a thickness of 150 nm. To improve its crystalline structure, the layer was subsequently annealed in vacuum at 450 °C

The samples were then moved into a different vacuum evaporation chamber, with a fine control of crucible temperature is installed, where Sb_2Se_3 was deposited on the Glass/ITO/ZnO/CdS stack. Absorbers with thickness of 1 μm, 700 nm and 450 nm were deposited at a base pressure of $3.6x10^{-4}$ Pa and with a substrate temperature of 300 °C. The material source (Sb_2Se_3 lumps) was heated at a temperature ranging from 700 to 800 °C in order to be evaporated at a deposition rate of approximately 0.20 nm/sec.

Post deposition treatment was applied by annealing the samples in vacuum at a pressure of 1.8 x 10^{-4} Pa to a temperature of 300 °C and 350 °C for about 60 minutes. For back contact, a 30 nm thick Au film was deposited by thermal evaporation without heating the substrate.

7.1.2 Measurement and characterization

7.1.2.1 Structural Characterization.

Three types of samples were prepared and studied: in the first case the absorber was deposited at a substrate temperature of 300 °C (A_{300}), in the second and third case the absorbers were deposited at the same temperature but were annealed in vacuum for 60 minutes at 300 °C (VA_{300}) and 350 °C (VA_{350}) respectively, in order to improve their crystallinity. Samples from these batches were selected for material characterization and device analysis.

In Fig 7.1 typical XRD patterns of the three different types of samples are shown, the patterns are in the 20 to 60 2 theta range because no reflection was registered outside

of this interval. The diffraction peaks agree well with the orthorhombic Sb_2Se_3 (JCPDS 15-0861).

However, we observe different reflections for each differently treated absorber, showing that the annealing step affects the crystalline properties. If for all the samples (221), (141), (041) and (061) peaks are observed, for VA_{350} the (220) and (040) reflections become intense. The difference is quite important since the (hk1) orientation corresponds to grains vertically oriented on the substrate, while the (hk0) oriented grains are horizontally stacked. Since the carriers move along the device, (hk1) oriented Sb_2Se_3 films exhibit better carrier collection [3].

Moreover, particularly for the A_{300} and VA_{300} cases, two different peaks at 26.5 and 35.3 appear that are not attributable to Sb_2Se_3. The first one is the (100) peak of hexagonal Se and the second one corresponds to the (101) orientation of Sb. This last has been already detected by Y. Zhou et al. [12] but without attribution. These peaks are weak for A_{300} and stronger for VA_{300} but disappear after annealing at 350 °C (VA_{350}) demonstrating that annealing in vacuum can give place to selenium loss with the formation of pure antimony but also that with a higher annealing temperature the secondary phases are reduced.

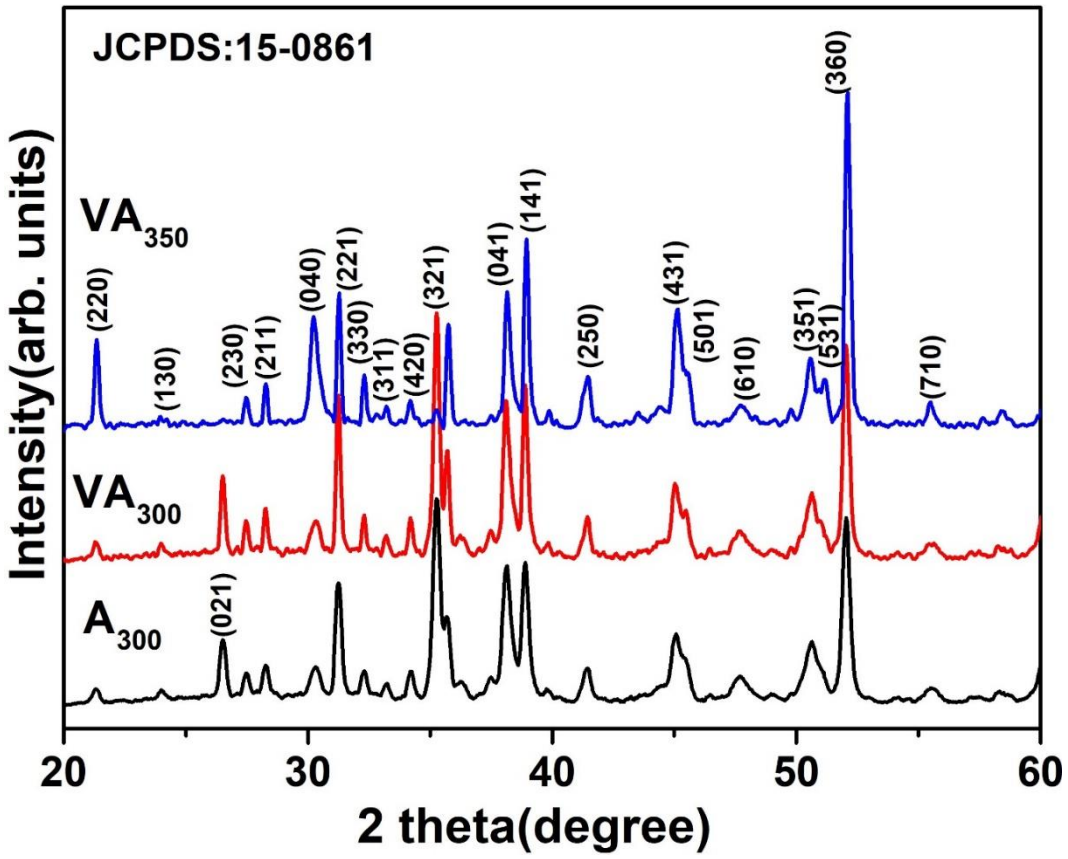

Figure 7.1. X-ray diffraction pattern of Sb_2Se_3 films on ITO/ZnO stack at different annealing temperature.

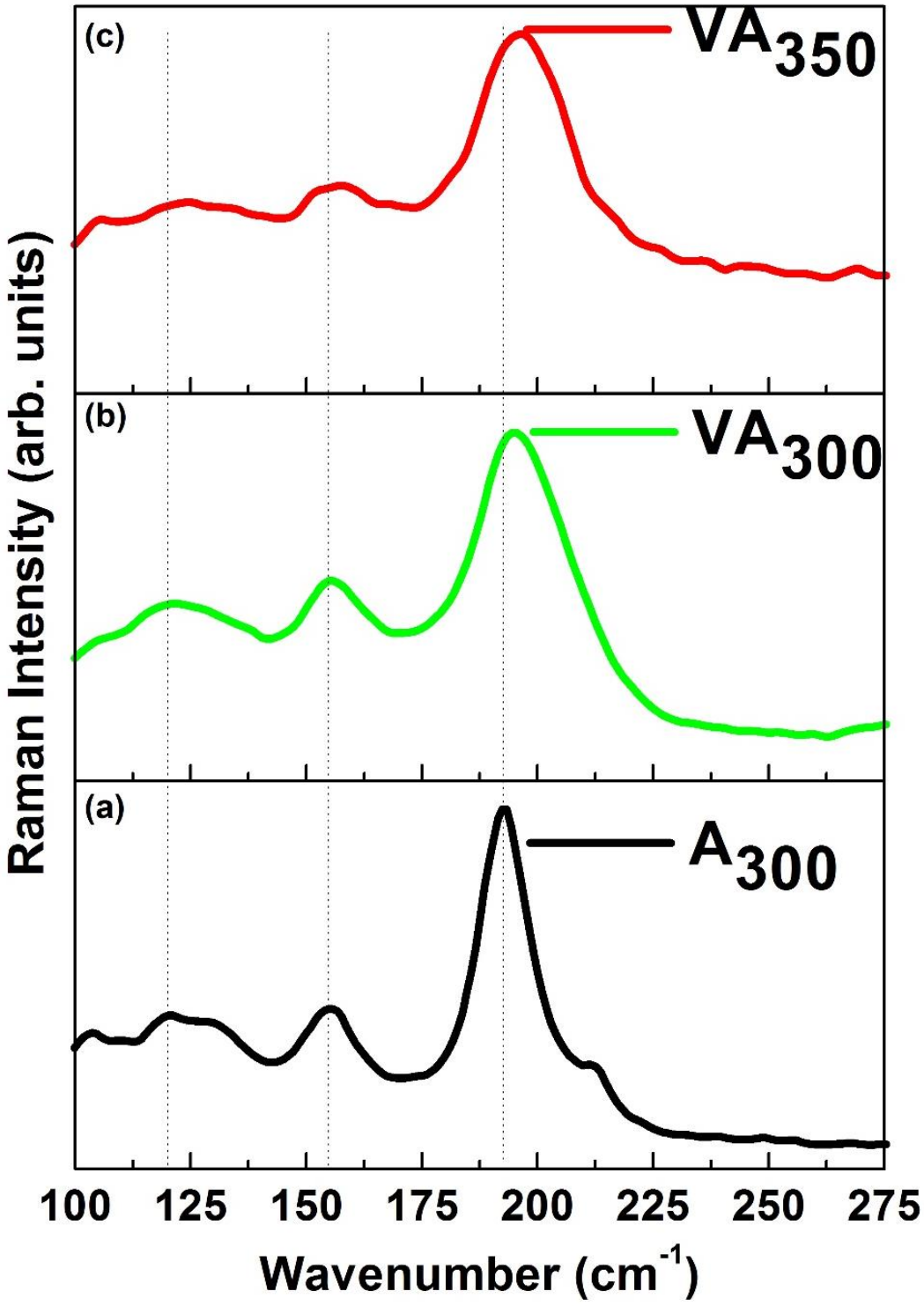

Figure 7.2. Micro-Raman Spectra on Sb_2Se_3 films (a) as deposited, (b) Vacuum annealed at 300 °C, (c) Vacuum annealed at 350 °C.

In fig. 7.2, Raman spectra of Sb_2Se_3 films are displayed. The collected peaks for all types of samples are in good agreement with what has been previously reported in literature [13][14]. The Raman spectrum of the A_{300} thin film exhibits a paramount

band peaked at about 192 cm^{-1} and some other more less pronounced bands at about 120, 129, 155, and 211 cm^{-1}, commonly assigned to the Sb-Se stretching vibration modes. In particular, the bands occurring at about 155, 192, and 211 cm^{-1} can be assigned to vibrational modes of Sb_2Se_3 in orthorhombic phase. The small vibrational bands at 103 and 129 cm^{-1} can be assigned to Se_6 ring of rhombohedral Sb_2Se_3 [15]. The band at 192 cm^{-1} is clearly defined in terms of intensity and of spectral profile, suggesting a good crystallinity degree of this film.

After post deposition annealing the Raman bands at 155 and 192 cm^{-1} exhibit larger broadening accompanied by a frequency shift to higher values, while the band near to 211 cm^{-1} gradually disappears. For VA_{300} the 103 and 129 cm^{-1} peaks disappear and only the main 120, 155 and 192 cm^{-1} peaks remain, attesting the disappearance of the rhombohedral Sb_2Se_3 while the broadening of these spectral components, related to orthorhombic Sb_2Se_3, suggests a quite random structural rearrangement. Finally, the overall Raman intensity of VA_{350} turns out appreciably quenched: the peaks at 120 and 155 cm^{-1} disappear, only the 192 cm^{-1} main peak is observable but also with decreased intensity. The crystalline quality of the material is, in this case, reduced.

AFM of the as deposited with varying thickness (1000, 700, 450 nm) has been discussed in the previous chapter. In this chapter the study of morphology of the as deposited and treated absorber layers, was performed using AFM. Comparing in fig. 7.3 (a) A_{300}, (b) VA_{300} and (c) VA_{350} we can see that after the annealing the absorbers show a different grain structure. For VA_{300} there is a structural rearrangement in agglomerates of bigger grains compared to A_{300}, while the VA_{350} shows agglomerates of smaller grains. Root mean square roughness (R_q) was calculated for the three cases: 48 nm for A_{300}, 77 nm for VA_{300} and 60 nm for VA_{350}.

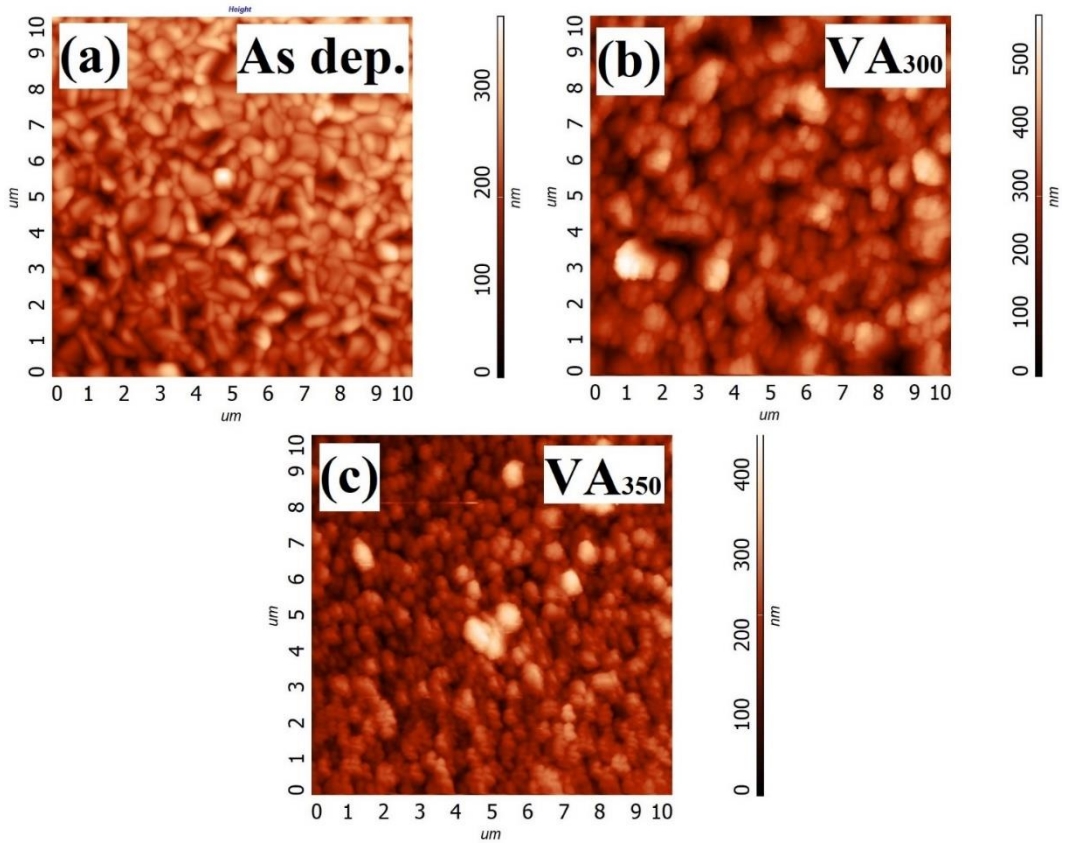

Figure 7.3. AFM images of Sb_2Se_3 films on (a) as deposited, (b) vacuum annealed at 300 ºC, (c) vacuum annealed at 350 ºC.

7.1.2.2 Performance of the cells.

Completed devices with gold contact delivered conversion efficiencies between 1 and 2 %, the values are reported in table 7.I. The solar cells have been subsequently annealed at 190 °C in air and their efficiencies were measured and compared with the values before treatment. In most of the fabricated devices the series resistance (R_s) decreased, and shunt resistance (R_{sh}) increased resulting in an improved fill factor, as shown in table 7. II. However, only in case of VA_{350} the back contact annealing improves the device quality reaching the best efficiency of 2 %.

Table 7. I. Performance values of reported samples in fig 7.4 a before back contact annealing.

Sample ID	**V_{oc} (mV)**	**J_{sc} (mA cm^{-2})**	**FF (%)**	**η (%)**	**R_s (Ω cm^{-2})**	**R_{sh} (Ω cm^{-2})**
A_{300}	268	12.8	31	1.1	100	240
VA_{300}	325	14.3	38	1.7	80	390
VA_{350}	332	14.4	39	1.8	90	530

Table 7. II. Performance values of reported samples in fig 7.4 b after back contact annealing.

Sample ID	**V_{oc} (mV)**	**J_{sc} (mA cm^{-2})**	**FF (%)**	**Ιη (%)**	**R_s (Ω cm^{-2})**	**R_{sh} (Ω cm^{-2})**
A_{300}	261	11.4	32	0.9	100	260
VA_{300}	325	14.4	38	1.7	80	400
VA_{350}	325	16.1	38	2	80	480

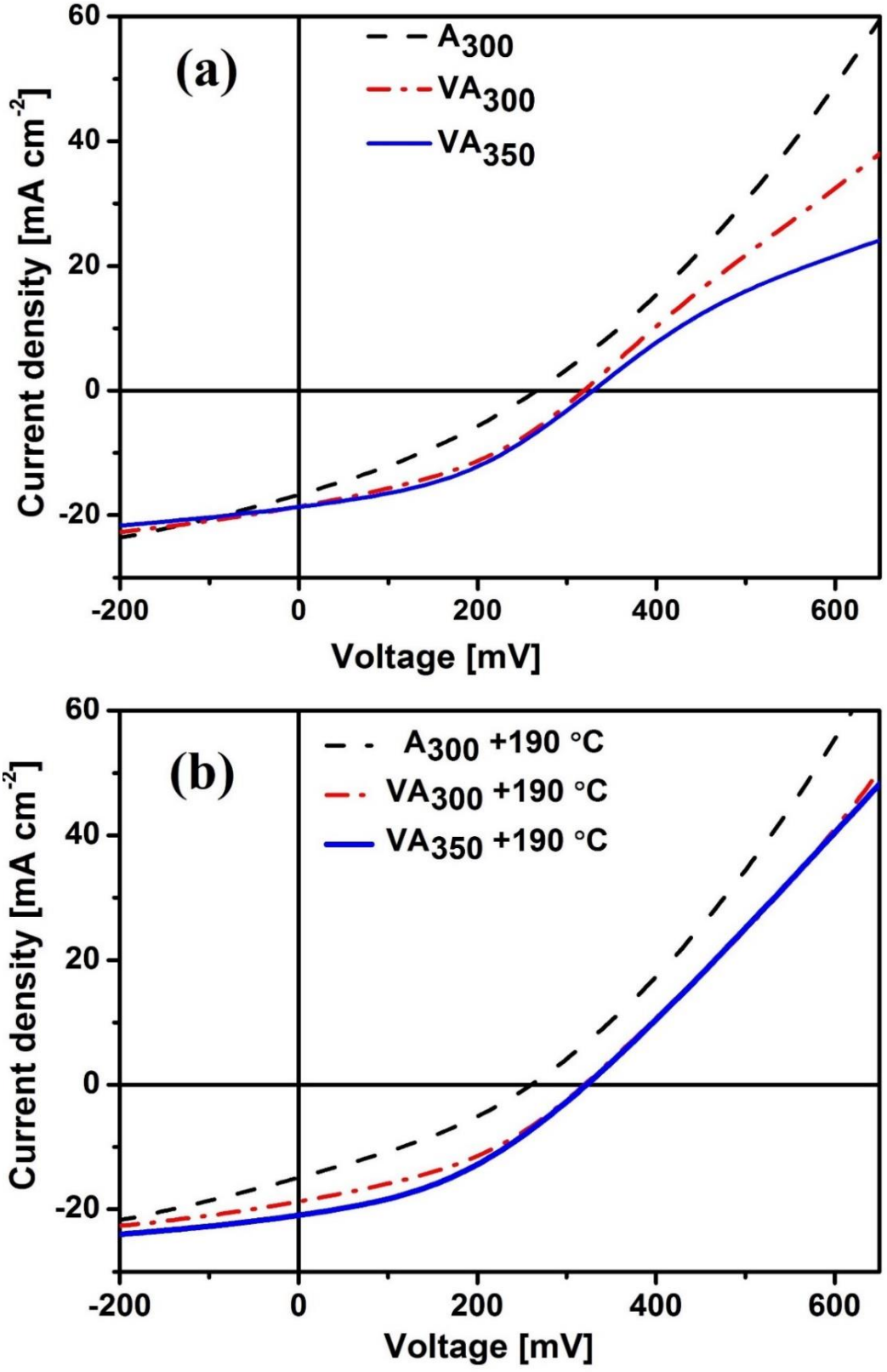

Figure 7.4 (a, b). J-V characteristics of the as deposited and vacuum annealed samples, as deposited and vacuum annealed samples with back contact annealing.

Looking at the J-V curves, shown in fig 7.4(a, b), the devices with absorbers annealed at 300 °C and 350 °C show a higher open circuit voltage. For the VA_{300} this can be easily justified by the improved crystallinity increases the device performance. For the VA_{350} case the situation is more complicated since the absorber has reduced crystal quality but on the other hand secondary phases have been reduced. Moreover, the annealing after back contact deposition shows that the strong rollover is drastically reduced; demonstrating that this additional process step affects specifically the back contact.

The structural and morphological characterization done on the absorber layer suggested that annealing at 300 °C compared to the one at 350 °C led to a better carrier collection, but this was not confirmed by the devices' performance. In fact, contrary to expectations, VA_{350} samples reached slightly higher values of V_{oc} and J_{sc}. An explanation of this can be that an increased conductivity and reduced recombination is not observed in terms of improved efficiency because the carrier collection is limited by the back contact, as also suggested by the roll-over presence in the J-V characteristics shown in fig. 7.4.

7.2 Vacuum annealing studies of Sb_2Se_3 on Glass/TEC/CdS.

In this part of the chapter, we will discuss about Sb_2Se_3 solar cells prepared in superstrate configuration (Glass/FTO/TO/CdS/Sb_2Se_3/Au). The front contact (TCO-transparent conductive oxide) consists of a fluorine doped tin oxide (FTO) layer followed by a high resistivity transparent (HRT) un-doped tin oxide (SnO_2 → TO) layer industrially deposited on soda lime glass (NSG TEC 12D). CdS is deposited on the FTO/TO stack by thermal evaporation at a pressure of 10^{-4} Pa, and with a substrate temperature of 150 °C, with a thickness of 150 nm. After deposition, the layer is annealed in the same deposition chamber in vacuum at 450 °C to improve its crystalline structure and its stability to the subsequent depositions.

The absorber thickness has been optimized and fixed to 450 nm, the layer is deposited at a substrate temperature of 300 °C and with a base pressure of $3x10^{-4}$ Pa. Post deposition the cells were annealed in vacuum at 350 °C as we can see from our

previous study that annealing at 350 °C leads to a better performance of the device. Finally, the back contact Au of 30 nm is deposited by thermal evaporation at a base pressure of $1x10^{-3}$ Pa, followed by post deposition annealing at 150 °C in air.

7.2.1 Measurement and characterization.

The XRD pattern of the Sb_2Se_3 films is shown in Fig. 7.5. The diffraction patterns consist of well resolved peaks which have been indexed to *Pbmn* space group in orthorhombic symmetry. All the diffraction peaks of the thin films were well matched with the JCPDS card no PDF 15-0861. The observed peaks corresponding to reflection planes (211), (221), (301), (321), (141) and (061), provide clear evidence for the formation of a stibnite structure for the Sb_2Se_3 thin films under study. The detailed study of the as deposited and annealed films registers the dominance of the preferred (hk1) peaks with the presence of two CdS compound peaks at 2Θ = 26.5 ° and 52 ° [16][17]. The texture coefficient (TC) of plane represents the texture of a particular plane, whose deviation from the standard sample implies the preferred growth. It is calculated by the Harris formula (see eq.1):

$$T(hkl) = \frac{I(hkl)}{Io(hkl)}\left[\frac{1}{n}\sum_{i=1}^{N}\frac{I(hkl)}{Io(hkl)}\right]^{-1} \qquad (1)$$

Where $I_{(hkl)}$ is the measured diffraction peak intensity of (hkl) plane, and $I_{o(hkl)}$ is the standard XRD peak intensity, n is the number of reflections considered for calculation. A texture coefficient value larger than 1 indicates enhanced texture orientation along that particular plane compared to the standard orientation [18]. The different texture coefficients highlight the difference in crystal orientation and quantitatively evaluate and compare the crystallite

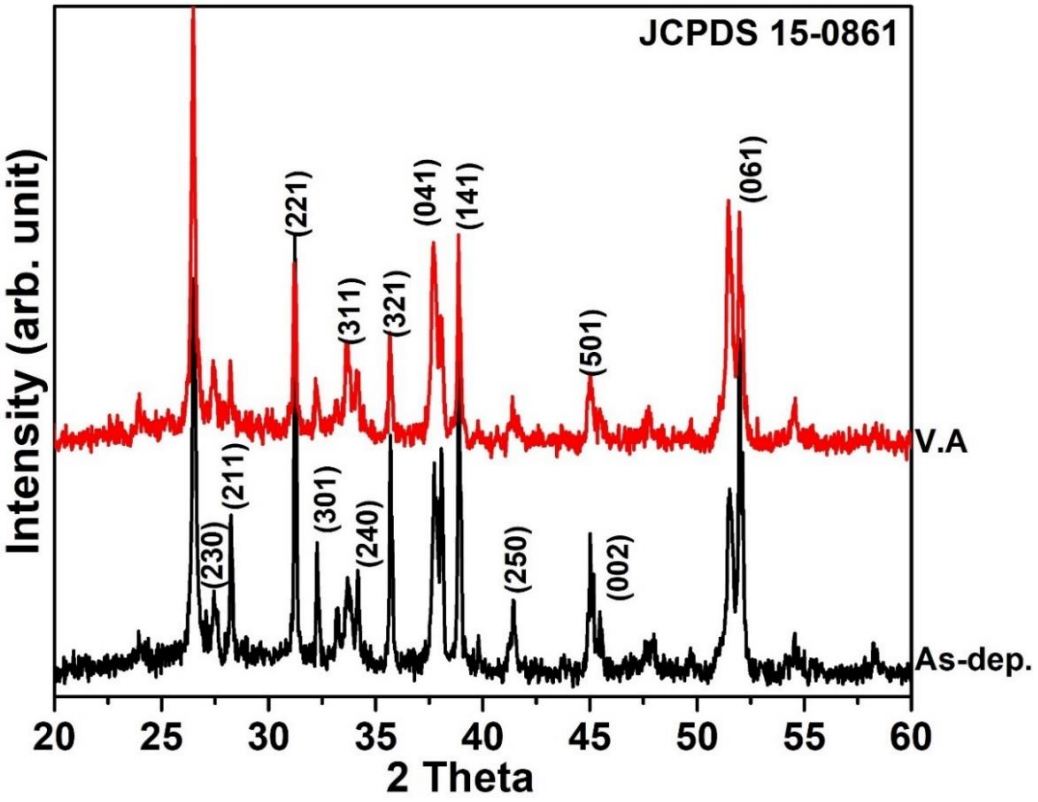

Figure 7.5. X-ray diffraction pattern of Sb_2Se_3 films on TEC/CdS stack.

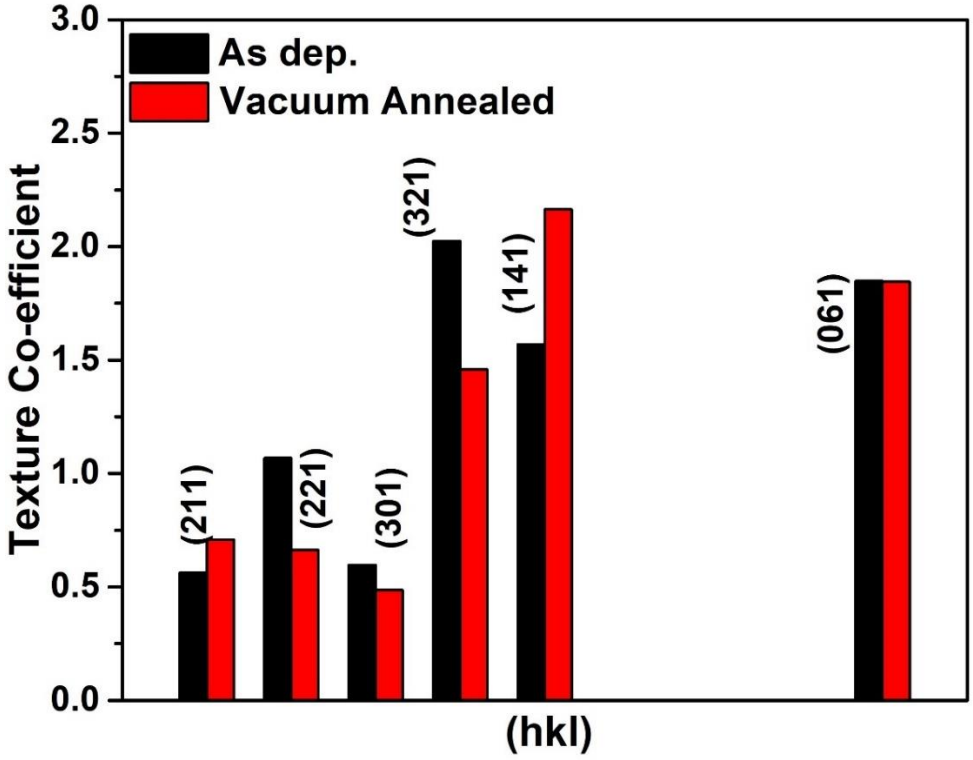

Figure 7.6. Texture coefficient of as deposited and annealed film.

behavior. The TC of the Sb_2Se_3 layer is presented in Fig. 7.6 it shows the spontaneous growth of the (221) high orientation peak, upon further calculation we realize that (321) is also a very predominant peak which is reduced in favor of (141) orientation through a post-deposition annealing. This shows that, despite the apparently similar spectra and the stronger (221) peak intensity, there is a different preferred orientation if the layer is subjected to post-deposition annealing.

Fig. 7.7(a, b) shows the top view AFM images of the as deposited and annealed films, while Table 7.III reports the *root mean square* (*RMS*), which indicates the roughness of the film, and the mean grain size analysis of the samples. AFM image of the as deposited case exhibits dense, homogenous and relatively large grains (0.5-1 µm). After annealing in vacuum, the grains are smaller (less than 0.5 µm), with different more round-shape, and with a clear loss in compactness.

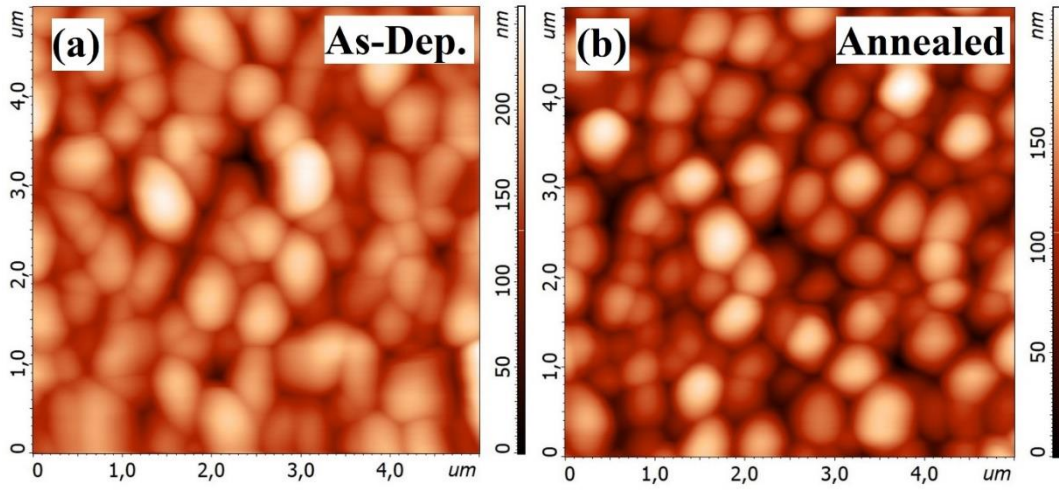

Figure 7.7(a, b). AFM image of as deposited and vacuum annealed Sb_2Se_3 films.

Table 7. III: AFM analysis (referred to Fig. 7.7) showing root mean square (RMS) roughness (Sq) and mean grain size of the samples.

Sample I. D	RMS, Sq. (nm)	Mean grain size (nm)
As-Dep	31	511
Ann.	32	479

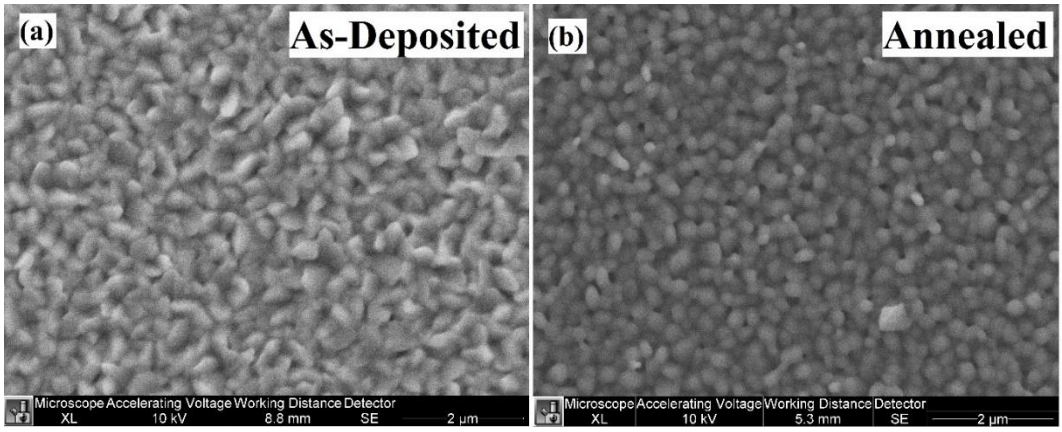

Fig. 7.8 shows the SEM pictures of the as deposited and annealed films, the samples are in good agreement with the morphology observed with AFM.

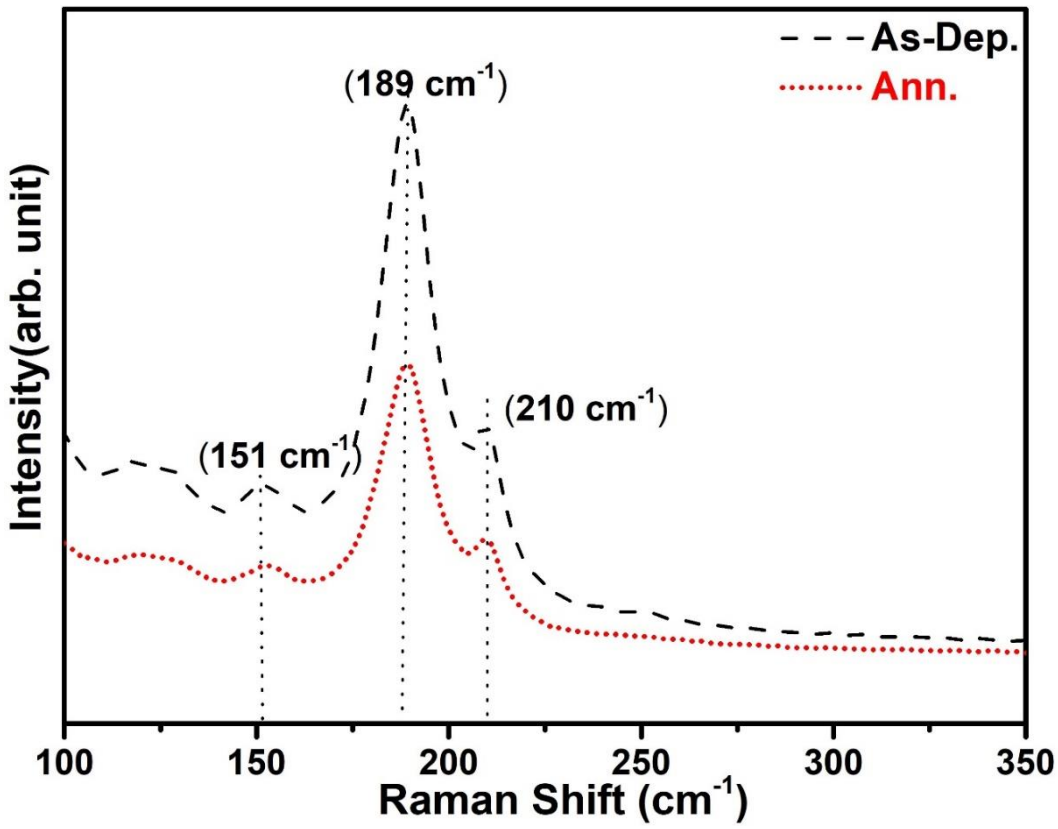

Figure 7.9 Raman Spectra for Sb_2Se_3 thin films as deposited and annealed.

Raman analysis of as deposited and vacuum annealed is shown in fig. 7.9, demonstrates the overall absence of large number of secondary phases. All the

samples deliver similar spectrum, with the main Sb_2Se_3 peaks at the same position without evident shifts.

7.2.2 Electrical Characterization.

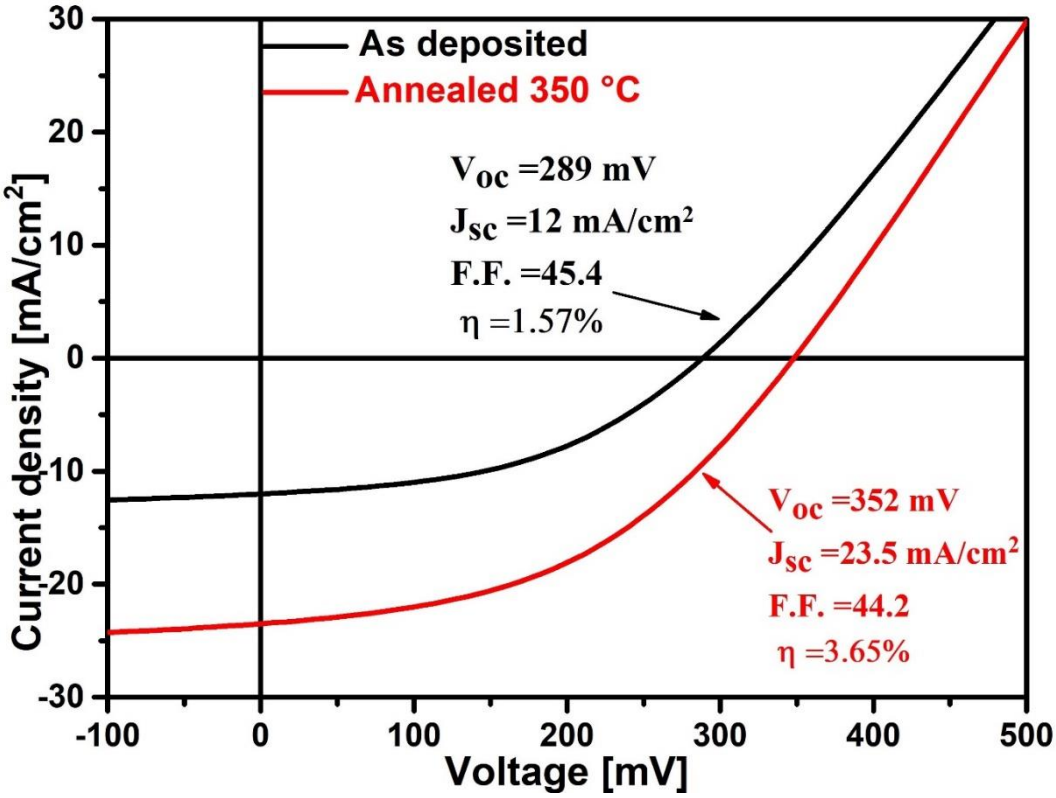

Figure 7.10. J-V curves of the as deposited and annealed devices.

J-V characteristics of the devices are presented in Fig. 7.10 efficiencies are very different when as-deposited and annealed Sb_2Se_3 layers are compared, resulting to be the lowest and the highest efficiencies of the set. As a matter of fact, best device with as deposited absorber layer shows an open circuit voltage (V_{oc}) of 289 mV, a fill factor (F.F.) of 45.4 %, and a very low short circuit current density (J_{sc}) of 12 mA/cm^2, corresponding to a power conversion efficiency of 1.57 %. While devices with absorber layer annealed in vacuum perform a V_{oc} of 352 mV, a J_{sc} of 23.5 mA/cm^2 and F.F.= 44 % resulting in an efficiency of 3.65 %. All the parameters show a clear improvement, except for the fill factor which remains equal, however 45-44 %

fill factor value is one of the highest obtained. This behavior can be explained if we examine the EQE presented in Fig. 7.11. The device corresponding to the as-deposited absorber case shows a very low response on all range of wavelengths which highlights a general low quality of the absorber material with a large loss in carrier collection. If the same absorber is annealed at 350 °C, the finished device shows a very good response, particularly near the junction (at the low wavelength region), while it loses response in the long wavelength region, where the photons are collected away from the junction near the back contact.

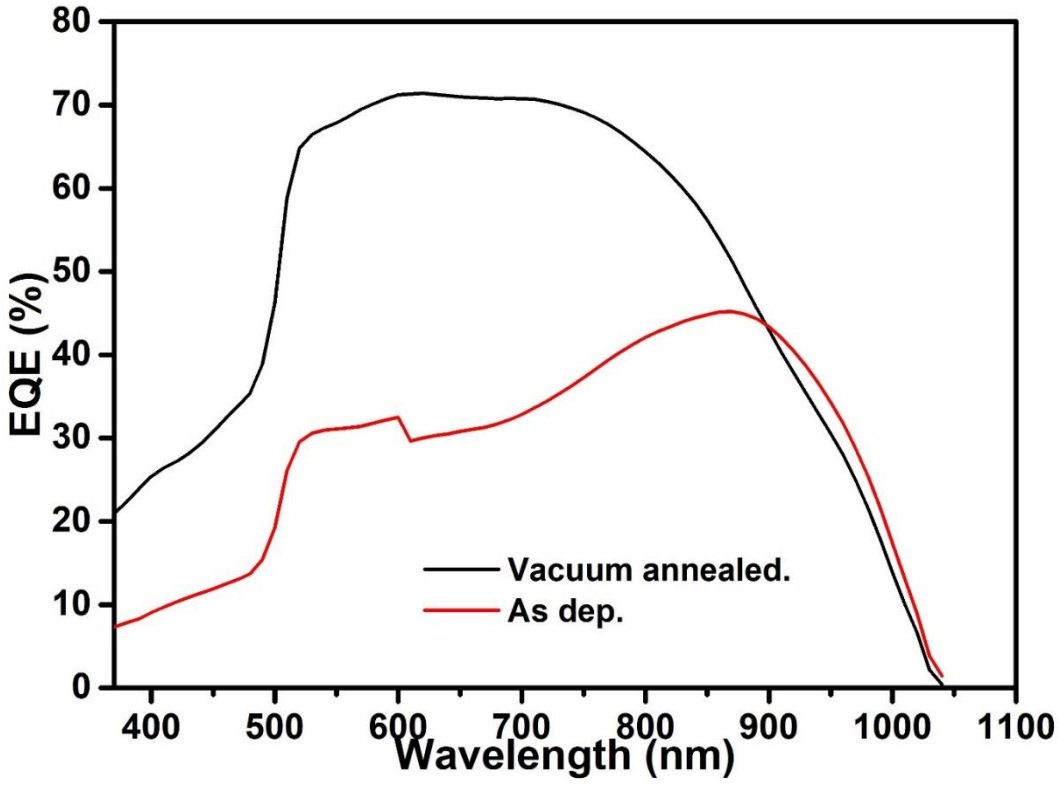

Figure 7.11. Corresponding EQE spectra of the as deposited and annealed samples.

7.3 Cu as an additional back contact study.

Due to the small free carrier path, generally high efficiency Sb_2Se_3 solar cells are fabricated with absorber thickness in the range of 400-600 nm [7,11], thinner than the presented 1 μm thick Sb_2Se_3 layer. Moreover, a prominent roll-over is observed in these JV curves as shown in fig. 7.4, suggesting that despite the high work function of gold, back contact still needed to be engineered further.

With these considerations, we have added copper on top of the Sb_2Se_3 layer to enhance carrier collection. Attempts of inserting Cu at the back contact has been already reported but the results were disappointing, probably for the large thickness of the copper layer [19]. However we have previously reported that a very small amount of copper is sufficient for enhancing the electrical properties in CdTe [20], in analogous way the back contact of Sb_2Se_3 solar cells could be improved by a similar inclusion of copper.

Different sets of samples with vacuum annealed absorbers at 300 °C and at 350 °C were made by adding a thin Cu layer in order to have the following stack: glass/ITO/ZnO/CdS/Sb_2Se_3/Cu/Au. The studies were pursued by inserting either a 3 Å or a 5 Å copper thick layer deposited by vacuum evaporation. Subsequently the devices have been annealed at 190 °C for 20 minutes in order to study the effect of Cu diffusion into the Sb_2Se_3 bulk. A significant change in all performance parameters was registered for different Cu thickness (3 Å and 5 Å): shown in Fig. 7.12 and 7.13, also the details are available in table 7. IV and 7. V the values of VA_{300} and VA_{350} are presented.

7.3.1 Electrical Characterization.

For VA_{300} 3 Å Cu, the J_{sc} improves of about 40 % compared with the samples without Cu. Moreover, after back contact (b.c.) annealing, the V_{oc} improved from 300 to 340 mV and the FF reported a rise of 10 % (absolute value), on the other hand J_{sc} did not change. R_s dramatically decreased and R_{sh} improved, proving that copper diffusion with b.c. annealing enhances the device performance remarkably.

The major improvement was typically obtained with the larger amount of copper (5 Å) and lower annealing temperature of the absorber. On the contrary, absorbers annealed at 350 °C did not improve at the same level. Overall parameters are shown in table 7. (IV-V). The carrier recombination reduces in the region near the b.c. with the introduction of Cu, the better structural properties of VA_{300} lead effectively to higher conversion efficiencies. Our best cell performed V_{oc} = 339 mV, J_{sc} = 20.7 mA

cm^{-2}, FF = 50 %, R_s = 35 Ω and R_{sh} = 743 Ω, corresponding to a power conversion efficiency of 3.5 %.

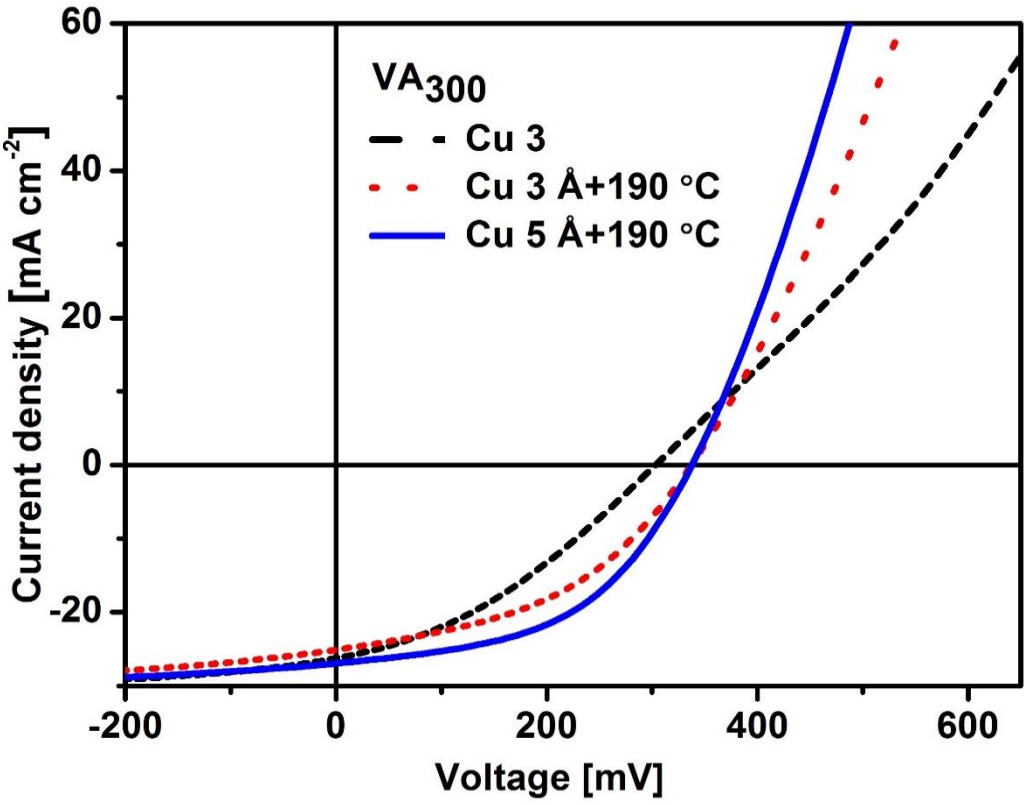

Figure 7.12. J-V characteristics of the vacuum annealed samples at 300 °C, 3 Å and 5 Å of Cu with back contact annealing.

Table 7. IV. Performance values of reported samples with 3 Å Cu layer.

Sample ID	**Cu (Å)**	**B.c. annealing**	**V_{oc} (mV)**	**J_{sc} (mA cm^{-2})**	**FF (%)**	**η (%)**	**R_s (Ωcm^{-2})**	**R_{sh} (Ω cm^{-2})**
VA_{300}	3	No	303	20.6	34	2.2	71	353
VA_{300}	3	Yes	339	20	44	2.8	48	493
VA_{350}	3	Yes	332	19	40	2.5	57	469

Table7. V. Performance values of reported samples in fig. 5 with 5 Å Cu layer.

Sample ID	Cu (Å)	B.c. annealing	V_{oc} (mV)	J_{sc} (mA cm^{-2})	FF (%)	η (%)	R_s (Ωcm^{-2})	R_{sh} (Ω cm^{-2})
VA_{300}	5	Yes	339	20.7	49	3.5	35	743
VA_{350}	5	Yes	325	19.7	41	2.6	52	500

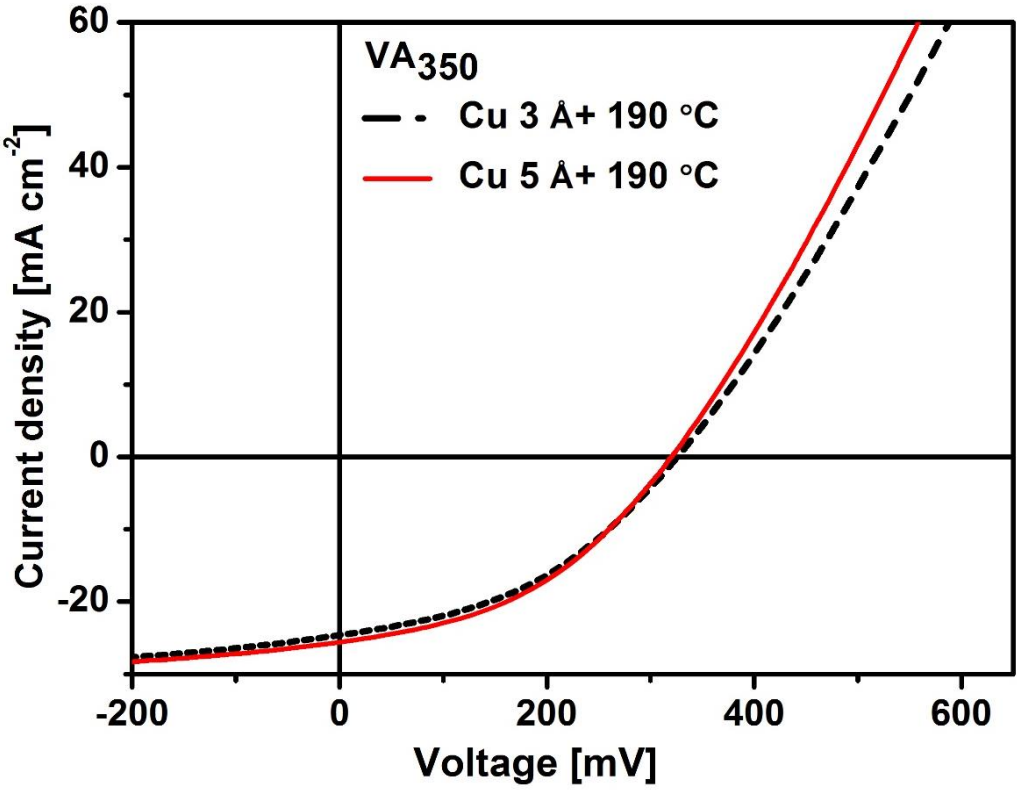

Figure 7.13. J-V characteristics of the vacuum annealed samples at 350 °C, 3 Å and 5 Å of Cu with back contact annealing.

Similarly, we also incorporated Cu with the best reported result conditions on TEC/CdS/Sb_2Se_3/Cu/Au superstructure and the study of the electrical study reported champion cell performance of 2.6% shown in fig. 7.14, the reported values are lesser than that discussed earlier in this chapter with Cu in the back contact.

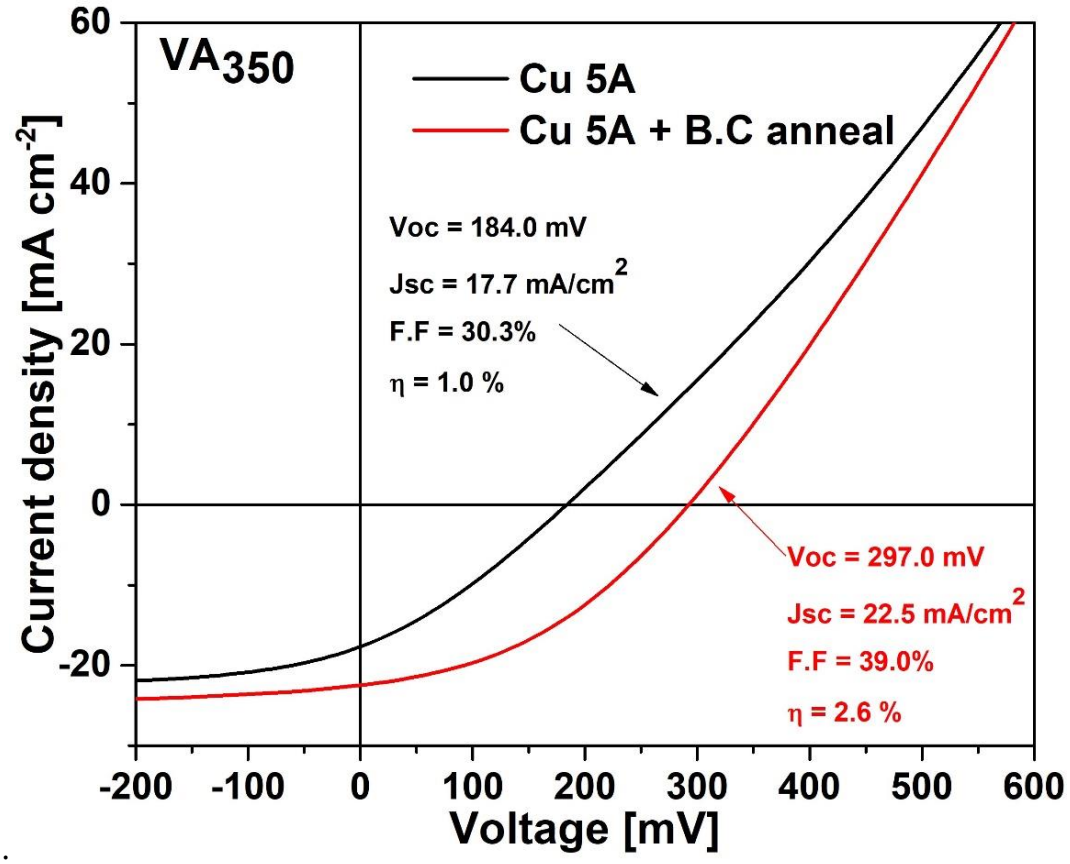

Figure 7.14. J-V characteristics of the vacuum annealed samples at 350 °C and 5 Å of Cu with back contact annealing.

7.4 Overall conclusion.

In this chapter we discussed the vacuum annealing study were, we demonstrated ITO/ZnO/CdS/Sb_2Se_3 superstrate based solar cells via low temperature thermal evaporation process. The studies demonstrate that annealing the samples in vacuum at 300 and 350 °C produce a compact and stoichiometric structure with PCE of 2%. Successively, the back contact was annealed at 190 °C which further improved the efficiency cells were annealing at 190 °C, obtaining improved efficiencies for all the different types of samples. Structural and morphological analysis has revealed that a rearrangement of the structure is obtained by annealing the absorber layer in vacuum. By annealing the absorber at 300 °C the Sb_2Se_3 structure shows a prevalent (hk1) orientation, more performing for carrier collection, while after annealing at 350 °C a larger number of (hk0) reflections is registered. Similarly we also, studied the vacuum

annealing of Glass/TEC/CdS/Sb_2Se_3 where the champion cell reported a PCE of 3.65% which is amongst the highest reported till date via thermal evaporation. The as deposited and annealed films show well resolved preferred (hk1) peaks. SEM and AFM shows homogeneous, pin hole free film. Raman analysis shows no formation of secondary phases. This process, with the optimized buffer layer, can be a base step for high efficiency low temperature growth Sb_2Se_3 devices, with potential for flexible solar cells.

To conclude overall we have successfully fabricated CdS/Sb_2Se_3 superstrate based solar cells via low temperature thermal evaporation process without selenization. Successively, the cells were treated with copper followed by subsequent annealing of the back contact which improved the efficiency of the cell. Copper inclusion improves radically the back contact of the device, enhancing the effect of the Sb_2Se_3 post-deposition annealing at 300 °C and 350 °C. An efficiency of 3.5 % was reached for the absorber annealed in vacuum at 300°C with a 5 Å thick Cu layer on top of it, which is to our knowledge, the best efficiency for Sb_2Se_3 for thermal evaporation without selenization.

7.5 Reference

[1] M.A. Green, Y. Hishikawa, E.D. Dunlop, D.H. Levi, J. Hohl-Ebinger, M. Yoshita, A.W.Y. Ho-Baillie, Solar cell efficiency tables (Version 53), Prog. Photovoltaics Res. Appl. 27 (2019) 3–12. https://doi.org/10.1002/pip.3102.

[2] M. Leng, M. Luo, C. Chen, S. Qin, J. Chen, J. Zhong, J. Tang, Selenization of Sb2Se3 absorber layer: An efficient step to improve device performance of CdS/Sb2Se3 solar cells, Appl. Phys. Lett. 105 (2014). https://doi.org/10.1063/1.4894170.

[3] D.B. Li, X. Yin, C.R. Grice, L. Guan, Z. Song, C. Wang, C. Chen, K. Li, A.J. Cimaroli, R.A. Awni, D. Zhao, H. Song, W. Tang, Y. Yan, J. Tang, Stable and efficient CdS/Sb2Se3 solar cells prepared by scalable close space sublimation, Nano Energy. 49 (2018) 346–353. https://doi.org/10.1016/j.nanoen.2018.04.044.

[4] C. Chen, R. Kondrotas, J. Tang, C. Wang, W. Chen, X. Wen, G. Niu, L. Gao, Y. Zhao, K. Li, S. Lu, J. Zhang, Vapor transport deposition of antimony

selenide thin film solar cells with 7.6% efficiency, Nat. Commun. 9 (2018). https://doi.org/10.1038/s41467-018-04634-6.

[5] R. Vadapoo, S. Krishnan, H. Yilmaz, C. Marin, Self-standing nanoribbons of antimony selenide and antimony sulfide with well-defined size and band gap, Nanotechnology. 22 (2011). https://doi.org/10.1088/0957-4484/22/17/175705.

[6] J.J. Carey, J.P. Allen, D.O. Scanlon, G.W. Watson, The electronic structure of the antimony chalcogenide series: Prospects for optoelectronic applications, J. Solid State Chem. 213 (2014) 116–125. https://doi.org/10.1016/j.jssc.2014.02.014.

[7] X. Liu, J. Chen, M. Luo, M. Leng, Z. Xia, Y. Zhou, S. Qin, D.J. Xue, L. Lv, H. Huang, D. Niu, J. Tang, Thermal evaporation and characterization of Sb2Se3thin film for substrate Sb2Se3/CdS solar cells, ACS Appl. Mater. Interfaces. 6 (2014) 10687–10695. https://doi.org/10.1021/am502427s.

[8] S. Messina, M.T.S. Nair, P.K. Nair, Antimony Selenide Absorber Thin Films in All-Chemically Deposited Solar Cells, J. Electrochem. Soc. 156 (2009) H327. https://doi.org/10.1149/1.3089358.

[9] Y. Zhou, M. Leng, Z. Xia, J. Zhong, H. Song, X. Liu, B. Yang, J. Zhang, J. Chen, K. Zhou, J. Han, Y. Cheng, J. Tang, Solution-processed antimony selenide heterojunction solar cells, Adv. Energy Mater. 4 (2014) 4–11. https://doi.org/10.1002/aenm.201301846.

[10] O.S. Hutter, L.J. Phillips, K. Durose, J.D. Major, 6.6% Efficient Antimony Selenide Solar Cells Using Grain Structure Control and an Organic Contact Layer, Sol. Energy Mater. Sol. Cells. 188 (2018) 177–181. https://doi.org/10.1016/j.solmat.2018.09.004.

[11] M. Luo, M. Leng, X. Liu, J. Chen, C. Chen, S. Qin, J. Tang, Thermal evaporation and characterization of superstrate CdS/Sb 2Se3 solar cells, Appl. Phys. Lett. 104 (2014). https://doi.org/10.1063/1.4874878.

[12] Y. Zhou, L. Wang, S. Chen, S. Qin, X. Liu, J. Chen, D.J. Xue, M. Luo, Y. Cao, Y. Cheng, E.H. Sargent, J. Tang, Thin-film Sb<inf>2</inf>Se<inf>3</inf> photovoltaics with oriented one-dimensional ribbons and benign grain boundaries, Nat. Photonics. (2015). https://doi.org/10.1038/nphoton.2015.78.

[13] Z.G. Ivanova, E. Cernoskova, V.S. Vassilev, S. V. Boycheva, Thermomechanical and structural characterization of GeSe2-Sb2Se3-ZnSe glasses, Mater. Lett. 57 (2003) 1025–1028. https://doi.org/10.1016/S0167-

577X(02)00710-3.

[14] A. Shongalova, M.R. Correia, B. Vermang, J.M.V. Cunha, P.M.P. Salomé, P.A. Fernandes, On the identification of Sb2Se3 using Raman scattering, MRS Commun. 8 (2018) 865–870. https://doi.org/10.1557/mrc.2018.94.

[15] K. Nagata, K. Ishibashi, Y. Miyamoto, Y. Miyamoto, Related content Raman and Infrared Spectra of Rhombohedral Selenium, (1981).

[16] A. Maiti, S. Chatterjee, A.J. Pal, Sulfur-Vacancy Passivation in Solution-Processed Sb2S3 Thin Films: Influence on Photovoltaic Interfaces, ACS Appl. Energy Mater. 3 (2020) 810–821. https://doi.org/10.1021/acsaem.9b01951.

[17] Y. Zhou, Y. Li, J. Luo, D. Li, X. Liu, C. Chen, H. Song, J. Ma, D.J. Xue, B. Yang, J. Tang, Buried homojunction in CdS/Sb2Se3 thin film photovoltaics generated by interfacial diffusion, Appl. Phys. Lett. 111 (2017). https://doi.org/10.1063/1.4991539.

[18] L. Guo, C. Grice, B. Zhang, S. Xing, L. Li, X. Qian, F. Yan, Improved stability and efficiency of CdSe/Sb2Se3 thin-film solar cells, Sol. Energy. 188 (2019) 586–592. https://doi.org/10.1016/j.solener.2019.06.042.

[19] J. Zhang, R. Kondrotas, S. Lu, C. Wang, C. Chen, J. Tang, Alternative back contacts for Sb 2 Se 3 solar cells, Sol. Energy. 182 (2019) 96–101. https://doi.org/10.1016/j.solener.2019.02.050.

[20] E. Artegiani, D. Menossi, H. Shiel, V. Dhanak, J.D. Major, A. Gasparotto, K. Sun, A. Romeo, Analysis of a novel $CuCl_2$ back contact process for improved stability in CdTe solar cells, Prog. Photovoltaics Res. Appl. (2019) pip.3148. https://doi.org/10.1002/pip.3148.

Chapter 8
Selenization study of the absorber

This chapter focuses on the detailed study and analysis of selenization process. Selenization was performed in two methods: 1) In situ co-selenization and post deposition selenization 2) Ex-situ selenization and chemical etching study of the back surface.

8.1 In-Situ co-selenization and post-selenization Studies.

Sb_2Se_3 is a promising alternative light-absorber material for thin-film solar cells, however by depositing it by thermal evaporation, it appears to decompose slightly leading to Se deficiency. In this work we propose two alternative routes for the supply of selenium in the deposition of Sb_2Se_3 thin films. First method is the co-evaporation of Se and Sb_2Se_3 while the second is the post deposition selenization. Superstrate Glass/FTO/TO/CdS/Sb_2Se_3/Au configured thin film cells are grown using thermal evaporation. X-ray diffraction (XRD) patterns confirm the presence of CdS peaks along with the preferred (hk1) oriented grains, which are suppressed upon selenization. Studies performed by X. Liu et al. indicate that Sb_2Se_3 films partly decompose during thermal evaporation, leading to Se deficiency. This generates, in the Sb_2Se_3 bulk, selenium vacancies (V_{Se}) giving place to deep recombination centres that affect the performance of the device [1]. In this paper we explore two methods to mitigate the Se loss: (a) by simultaneously evaporating Sb_2Se_3 and Se during the absorber growth (co-selenization); (b) by a post-deposition selenization which results in a two-step process where in the first place Sb_2Se_3 is deposited on the buffer layer and then, in the second step, Se is fluxed at 350 °C in order to recrystallize and adjust the stoichiometry. The influence of selenization on the Sb_2Se_3 thin films was investigated by atomic force microscopy (AFM), X-ray diffraction (XRD), Raman spectroscopy, External Quantum Efficiency (EQE) and current-voltage (J-V) characteristics.

8.1.1 Experimental details.

Sb_2Se_3 solar cells are prepared in superstrate configuration (Glass/FTO/TO/CdS/Sb_2Se_3/Au). The front contact (TCO-transparent conductive oxide) consists of a fluorine doped tin oxide (FTO) layer followed by a high resistivity transparent (HRT) un-doped tin oxide (SnO_2 → TO) layer industrially deposited on soda lime glass (NSG TEC 12D). CdS is deposited on the FTO/TO stack by thermal evaporation at a pressure of 10^{-4} Pa, and with a substrate temperature of 150 °C, with a thickness of 150 nm. After deposition, the layer is annealed in the same deposition chamber in vacuum at 450 °C to improve its crystalline structure and its stability to the subsequent depositions.

The absorber thickness has been optimized and fixed to 450 nm, the layer is deposited at a substrate temperature of 300 °C and with a base pressure of $3x10^{-4}$ Pa.
During the co-selenization process Se powder is evaporated simultaneously with Sb_2Se_3 from distinct graphite crucibles at different varying rates. Selenium rates (R_{Se}) have been fixed relatively to the evaporation rate of Sb_2Se_3 (R_{Sb2Se3}), we have considered R=2, R=1 and R=0.5 with R= R_{Se}/R_{Sb2Se3}. The post deposition heat treatment of as deposited and co-selenized samples is done at 350 °C.

Table 8. I (a). As-deposited, annealed and co-selenized samples.

Sample I.D.	Co-Selenization	Post deposition heat treatment (°C)
As-Dep	-	-
coSel-1	R=1	-
coSel-0.5-Ann	R=0.5	350
coSel-1-Ann	R=1	350
coSel-2-Ann	R=2	350

Post-deposition selenization is instead performed directly at a substrate temperature of 350 °C; the rate of the additional Se evaporation step is also calculated on the previous Sb_2Se_3 deposition rate: R= R_{Se}/R_{Sb2Se3}. Samples' details along with their ID

are discussed in table 8.I(a, b). The Sb_2Se_3 lumps and Se pellets are heated in graphite crucibles at a temperature range of 600-700 °C and 280-350 °C respectively.
The back contact consists of a 30 nm thick Au film deposited by thermal evaporation at a base pressure of $1x10^{-3}$ Pa, followed by post deposition annealing at 150 °C in air.

Table 8. I (b). Post deposition selenized samples.

Sample I.D	Post-Selenization heat treatment (350 °C)
postSel-0.5	R=0.5
postSel-1	R=1
postSel-2	R=2

8.1.2 Structural characterization.

The XRD pattern for the differently grown Sb_2Se_3 films are shown from Fig. 8.1, 8.3 and 8.5. The diffraction patterns consist of well resolved peaks which have been indexed to *Pbmn* space group in orthorhombic symmetry. All the diffraction peaks of the thin films were well matched with the JCPDS card no PDF 15-0861. The observed peaks corresponding to reflection planes (211), (221), (301), (321), (141) and (061), provide clear evidence for the formation of a stibnite structure for the Sb_2Se_3 thin films under study. The detailed study of the as deposited and selenized films registers the dominance of the preferred (hk1) peaks with the presence of two CdS compound peaks at 2Θ = 26.5 ° and 52 ° [2][3]. This is corroborated also by analysis of Sb_2Se_3 deposited on SnO_2 which does not show the above-mentioned peaks.

It is evident that co-selenized samples reduce the presence of the CdS compound notably enhancing the presence of (061) and (141). For the post-selenized samples, CdS detection is almost suppressed, moreover an additional dominant (041) peak is observed. Note that no additional Se diffraction peaks are detected, despite that Se supply is in excess during the in-situ selenization process. As a matter of fact, the substrate temperature during Se evaporation is above the melting point of Se and thus excludes possible condensation of Se vapor into the sample.

The texture coefficient (TC) is calculated by the Harris formula (see eq.1):Texture coefficient value greater than 1 indicates enhanced texture orientation along that particular plane compared to the standard orientation [4].

$$T(hkl) = \frac{I(hkl)}{Io(hkl)}\left[\frac{1}{n}\sum_{i=1}^{N}\frac{I(hkl)}{Io(hkl)}\right]^{-1} \quad (1)$$

Where $I_{(hkl)}$ the measured diffraction peak intensity of (hkl) plane, and $I_{o(hkl)}$ is the standard XRD peak intensity, n is the number of reflections considered for calculation.

As shown in the fig. 8. (2, 4 and 6), the Sb_2Se_3 layer grows spontaneously with a (221) high orientation, however when the texture coefficient is calculated we realize that (321) is also a very predominant peak which is reduced in favor of (141) orientation through a post-deposition annealing or co-selenization. This last orientation is present together with the (041) peak when instead a post-selenization is applied. In this case the (221) orientation has a stronger incidence compared to the other cases, while the (061) is largely reduced.

This shows that, despite the apparently similar spectra and the stronger (221) peak intensity, there is a different preferred orientation if the layer is subjected to co-selenization and post-deposition selenization. Also, this suggests that by adding selenium we perform a different restructuring of the crystals, which moreover depends on the way of incorporating selenium.

The crystallite size and lattice strain of the present samples are calculated by analyzing the peak broadening of the XRD pattern using Scherrer's formula (see eq.2).

$$d(hkl) = \frac{k\lambda}{ß\,Cos\Theta} \quad (2)$$

Where λ is the wavelength of the X-ray radiation (1.5405 Å), Θ is the Bragg's angle, ß is the FWHM (Full Width at Half Maximum) in radians, and k a constant related to crystallite shape and is taken as 0.94 [5][6].

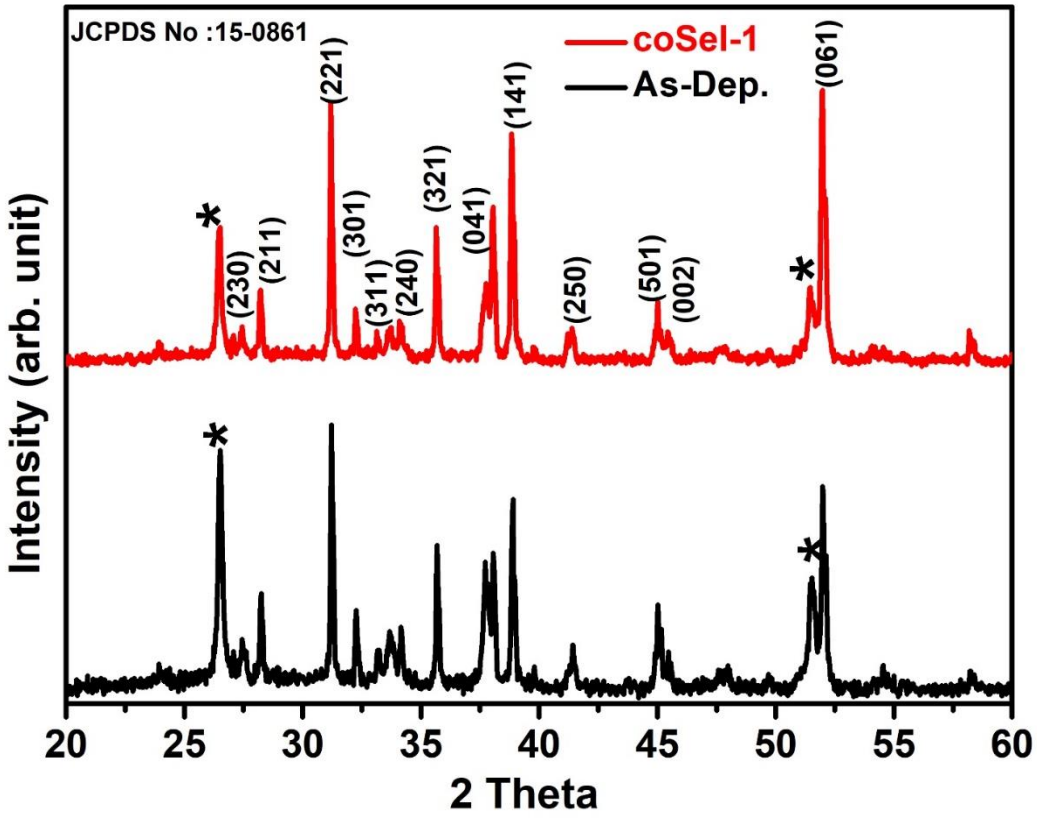

Figure 8.1. XRD pattern of the as deposited and co-selenized samples

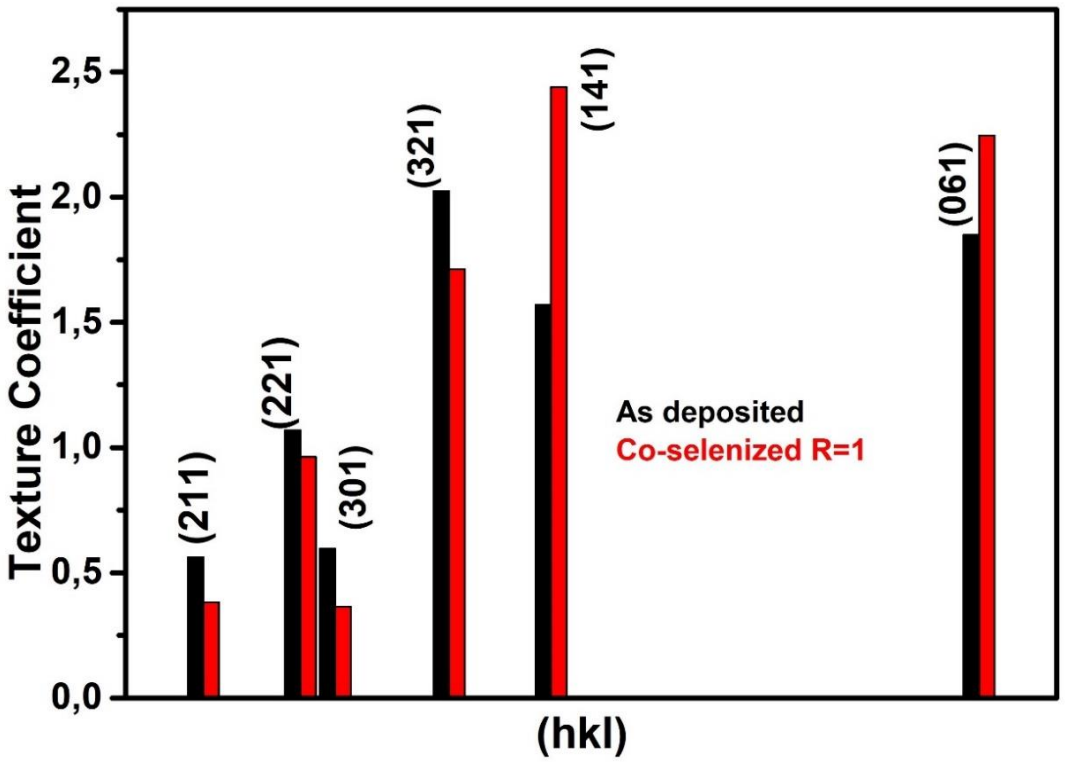

Figure 8.2. TC of the as deposited and co-selenized samples

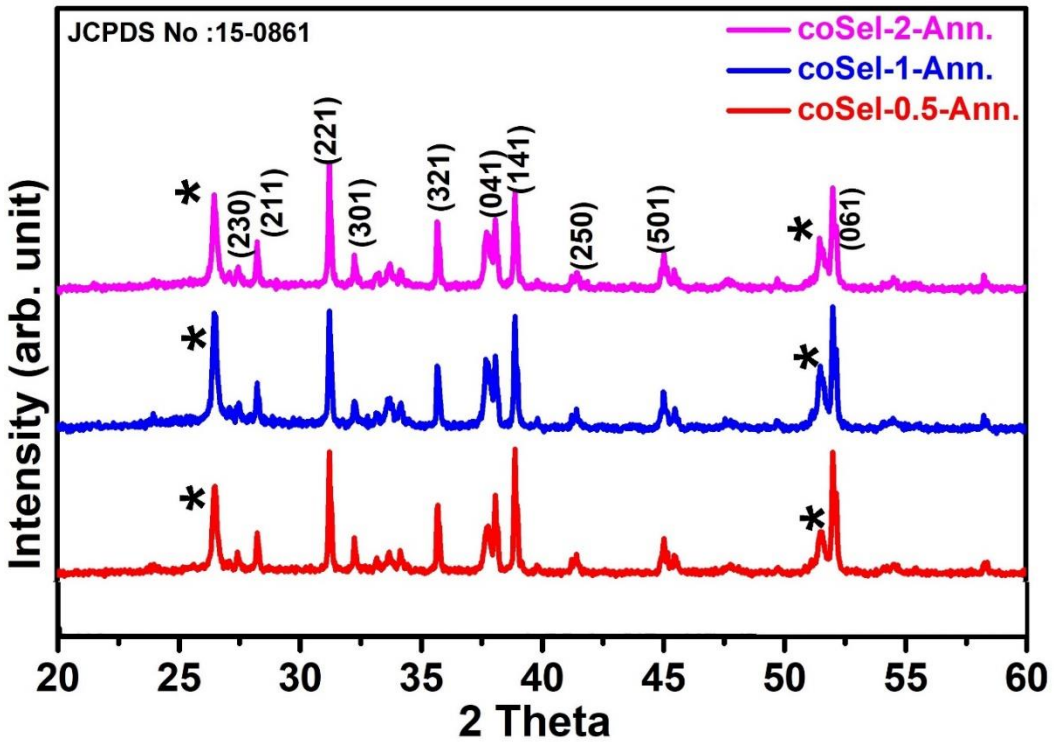

Figure 8.3. XRD spectra of the vacuum annealed sample and co-selenized samples.

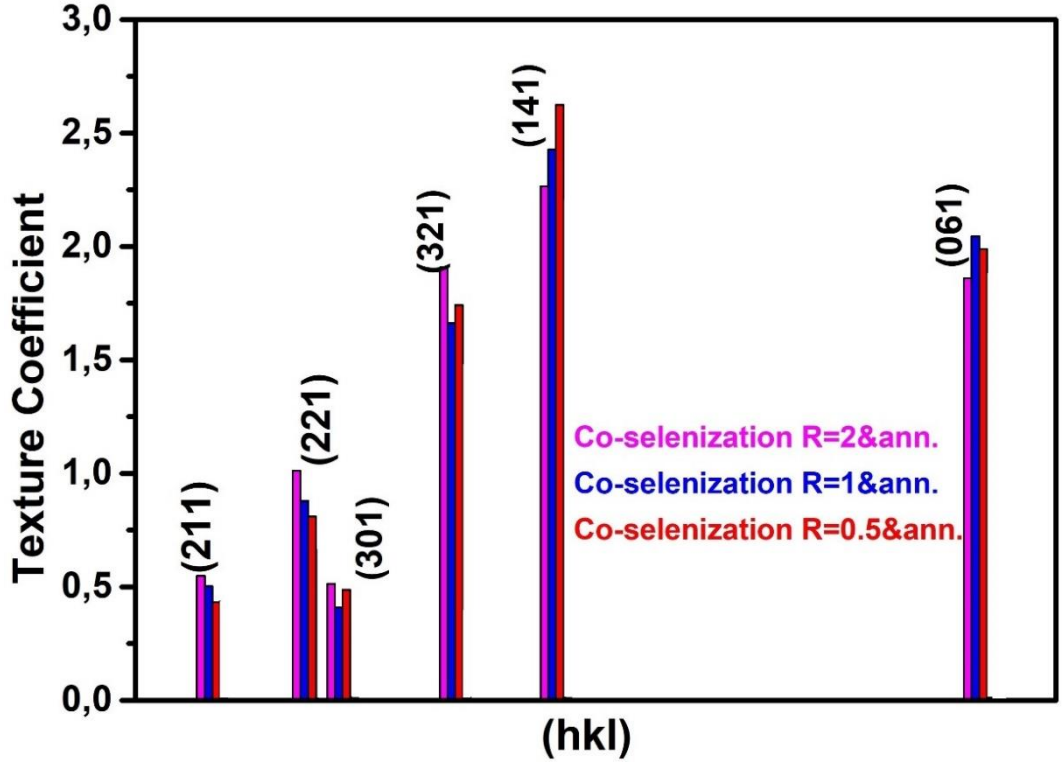

Figure 8.4. TC of the vacuum annealed sample and co-selenized samples.

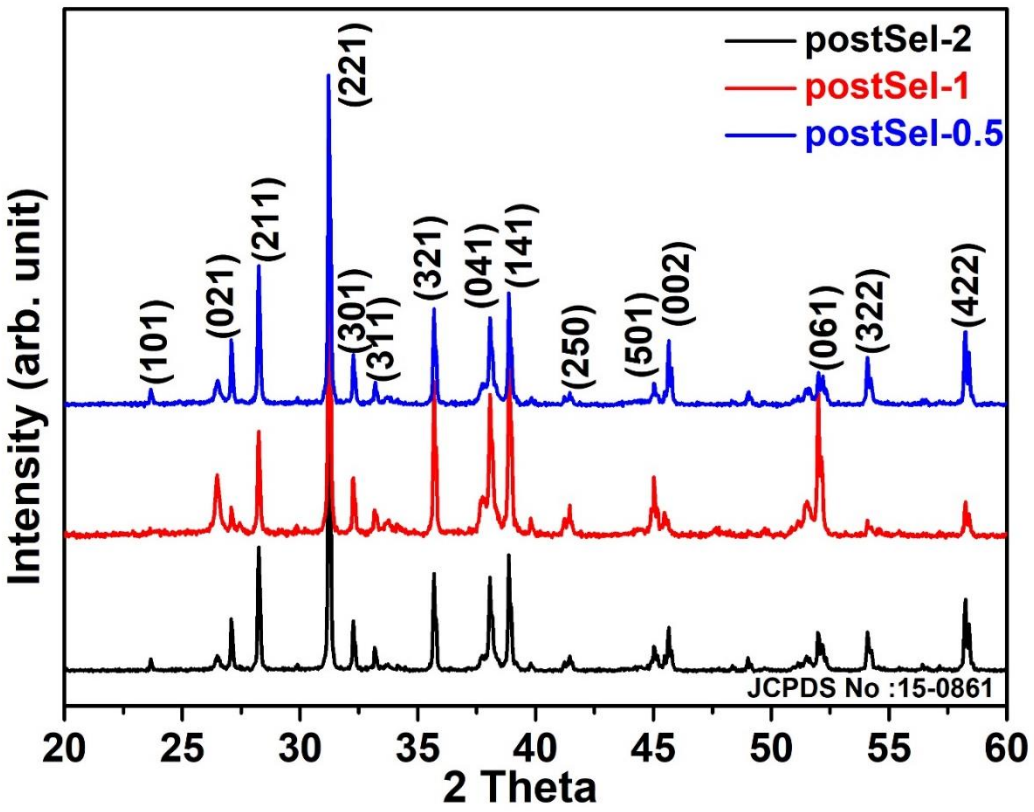

Figure 8.5. XRD pattern of post-selenized samples.

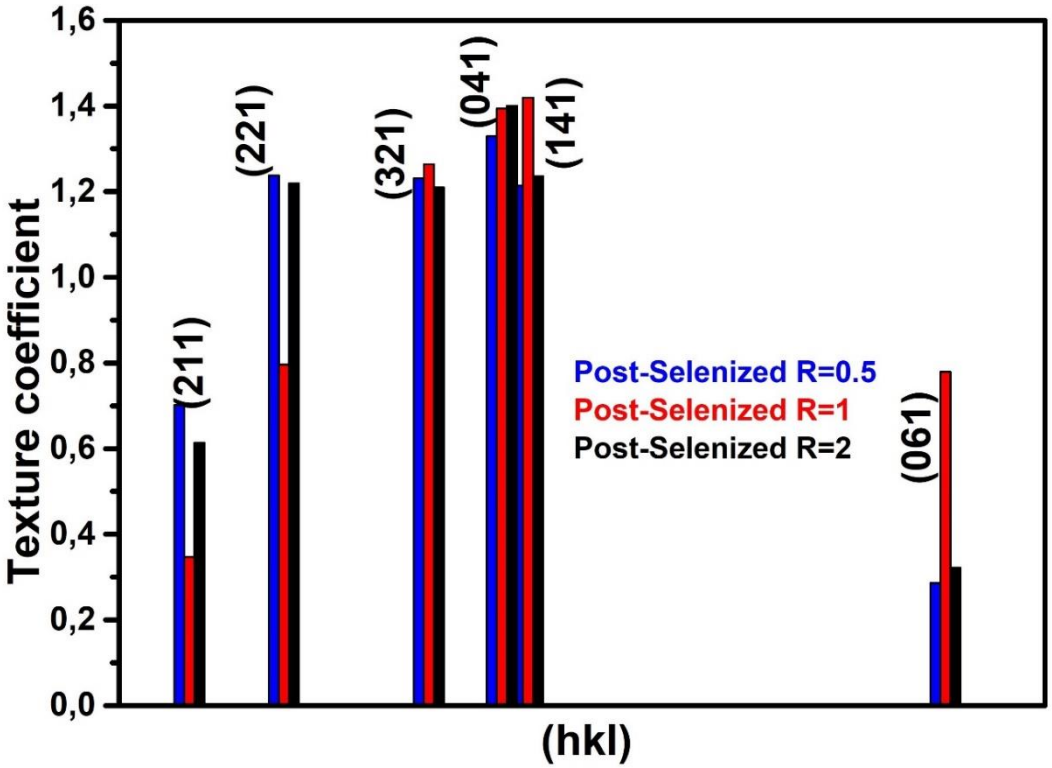

Figure 8.6. TC of post-selenized samples.

The micro strain (S) of the films is estimated by using the formula S = ßcosϴ/4. The average crystallite size and micro strain for all the as-deposited, co-selenized and post-selenized samples are discussed in Table 8.II (a, b), which clearly shows the increase of micro strain with selenization rate for post-selenization process. The average crystallite size of the as deposited thin films is around 71 nm and it also nearly the same for the co-selenized and post-selenized samples.

By analyzing the pattern with Rietveld-refinements [7] by exploiting the MAUD software [8] we can observe that the lattice parameters of as-deposited, co-selenized and post-selenized layers are different. In particular the lattice parameters of as-deposited absorber are in line with what has been measured and/or calculated from other laboratories [9][10][5]. Lattice parameters b and c are very similar irrespective of the different treatments, instead the lattice parameter a change. In the as-deposited case this value is 11.6 Å, quite like what is observed in the literature; however, it shrinks to 11.59 Å (negative displacement) when the absorber is co-selenized and annealed at 350 °C. When the absorber is annealed at 350 °C in selenium atmosphere the a-value is repristinated to larger sizes, even closer to the standard value for Sb_2Se_3 [11].

We observe that the micro strain for this last case is quite larger compared to the as-deposited case: probably the positive displacement of the lattice parameter generates an evident micro strain. This is confirmed for each post-selenized case, demonstrating that the inclusion of selenium by post-selenization at 350 °C delivers a very different condition. As a matter of fact, the presence of selenium at high temperature recrystallizes the layer, possibly reducing the selenium vacancies and for this reason restoring the original a-lattice path. The result is a layer that stoichiometrically is not selenium-poor but at the same time with large grains (as observed in the crystallite size and in the following AFM images). The effectiveness of this treatment in mitigating the selenium deficiency is also suggested by the absence of the CdS peaks in the XRD spectra: probably Se diffuses even in the window layer damaging it.

Table 8. III (a). Lattice parameters and average crystalline size of the as deposited and co-selenized Sb_2Se_3 thin films.

Sample I. D	Lattice parameters (Å)	FWHM (221) and (141) (ß)	Average crystallite (nm)	Micro strain (S)
As-Dep.	a=11.602 b=11.764 c=3.971	0.1215 0.1270	71	4×10^{-3}
coSel-1	-	0.1245 0.1175	71	6×10^{-3}
coSel-0.5-Ann.	-	0.1285 0.1100	72	5.8×10^{-3}
coSel-1-Ann.	a=11.593 b=11.754 c=3.970	0.1490 0.1340	65	5.4×10^{-3}

Table 8. III (b). Lattice parameters and average crystalline size of the post-selenized Sb_2Se_3 thin films.

Sample I. D	Lattice parameters (Å)	FWHM (221) and (141) (ß)	Average crystallite (nm)	Micro strain (S)
postSel-1	a=11.616 b=11.755 c=3.970	0.1220 0.1350	68	1.3×10^{-2}
postSel-0.5	-	0.1052 0.0955	87	9.2×10^{-3}
postSel-2	-	0.1270 0.1090	74	1×10^{-2}

Fig. 8.7, 8.8 and 8.9 shows the top view AFM images of the films, while Table 8. IV (a, b) reports the root mean square (RMS) roughness, which indicates the roughness of the film, and the mean grain size analysis of the samples. AFM image of the as-deposited case exhibits dense, homogenous and relatively large grains (0.5-1 µm), while the co-selenized samples also shows similar grains with few pinholes. After co-selenization and annealing the grains are smaller (less than 0.5 µm), with different more round-shape, and with a clear loss in compactness. No difference in morphology is observed for the different Se evaporation rates.

On the other hand, when the layers are selenized after deposition, the surface presents a different morphology compared to the co-selenized ones. The grains are larger, reaching similar sizes of the as-deposited case, but with a much larger compactness: the boundaries are well over posed and the grains well aligned. The post-selenized samples with rate $R_{Se} = 2\ R_{Sb2Se3}$ are observed to have pinholes. The post-selenized sample with $R_{Se} = 0.5\ R_{Sb2Se3}$ also have few pinholes along with few very small grains which may be the reason for recombination losses and poor performance of the solar cell. Sample with $R_{se} = 1\ R_{Sb2Se3}$ has a dense compact structure with well resolved grains and grain boundaries which is the reason for the comparatively better performance of the cells from its counterparts.

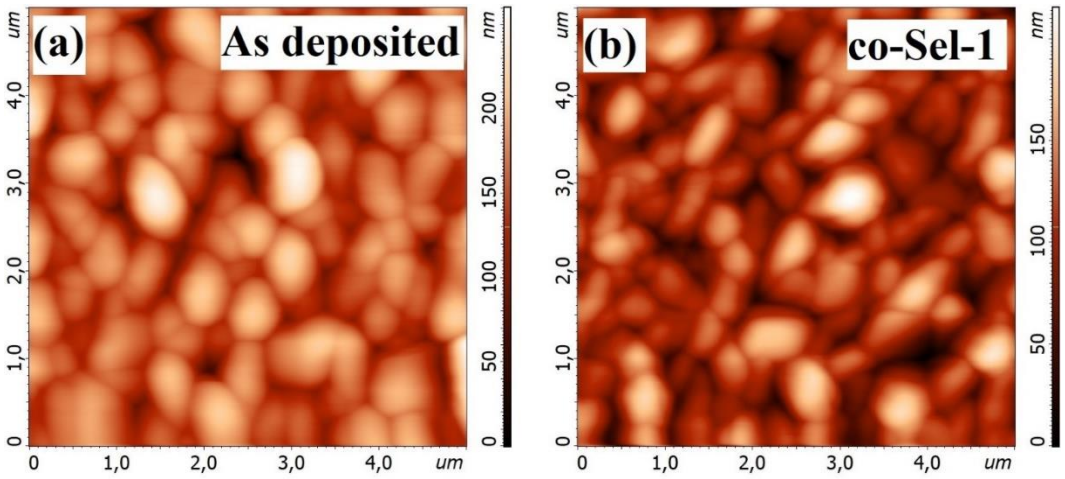

Figure 8.7. AFM image of the as-deposited and co-selenized samples.

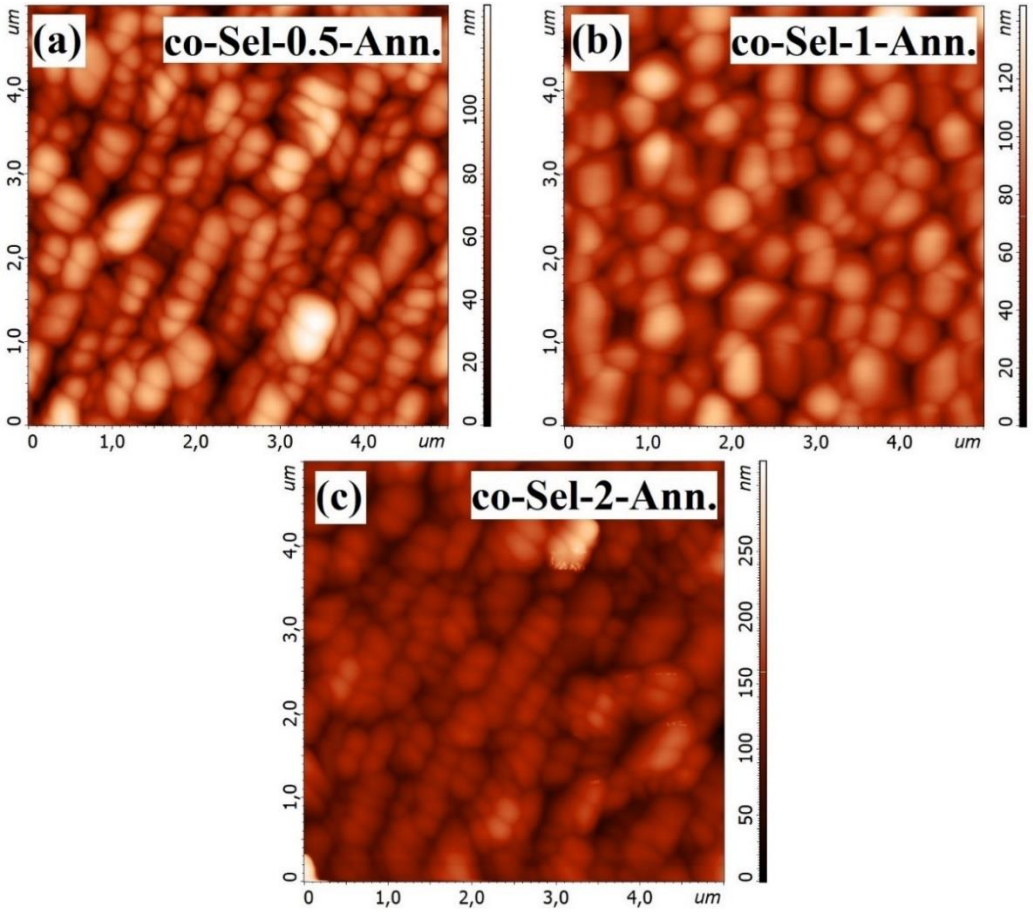

Figure 8.8 AFM image of the vacuum annealed, co-selenized samples.

Table 8. IV. AFM analysis (referred to Fig.8. (7,8 and 9)) showing root mean square (RMS) roughness (Sq) and mean grain size of the samples.

Sample I. D	RMS, Sq (nm)	Mean grain size (nm)
As-Dep	31	511
coSel-1-Ann	20	368
postSel-1	43	554

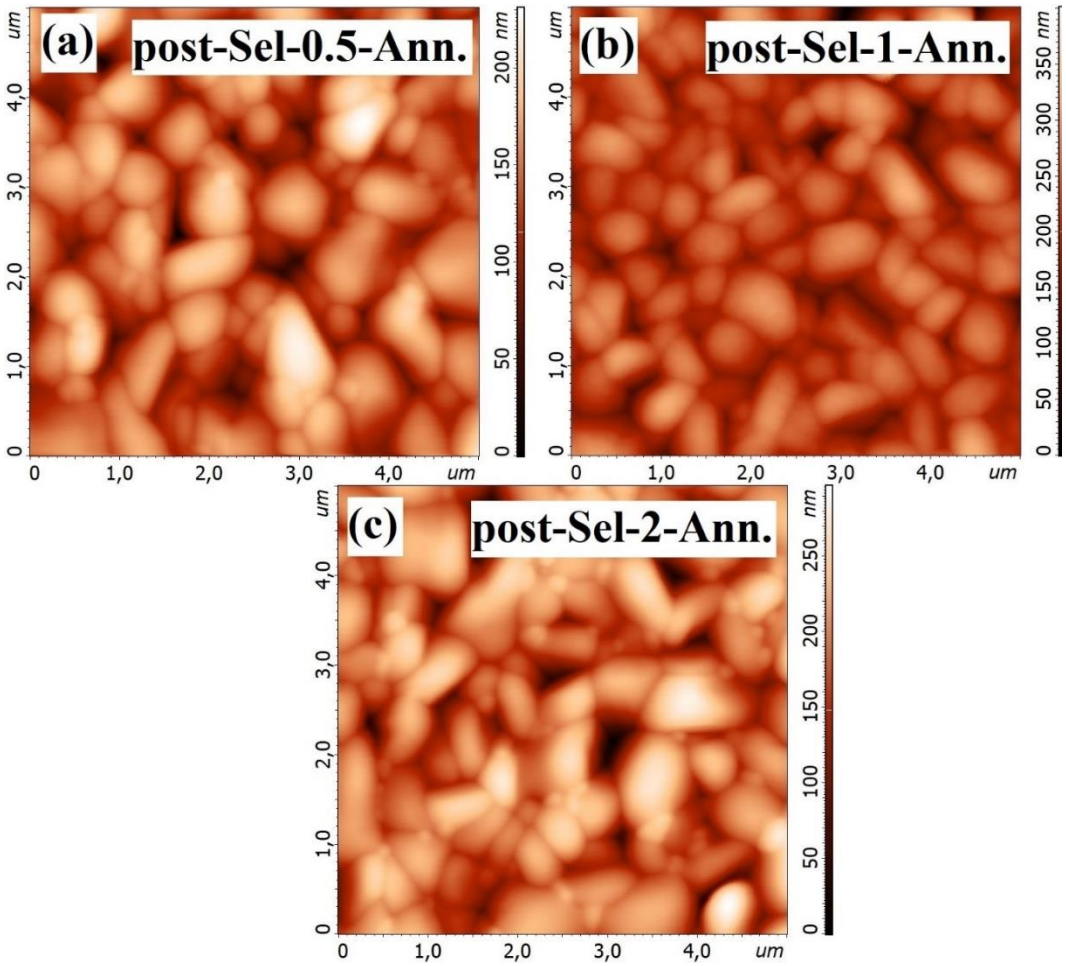

Figure 8.9. AFM image of the post-selenized samples.

We observed that with co-selenization and/or post deposition annealing, a change of the initial conditions, which results in reduction of grain size, that is coherent with the observed reduction of a-lattice parameters and crystallites.

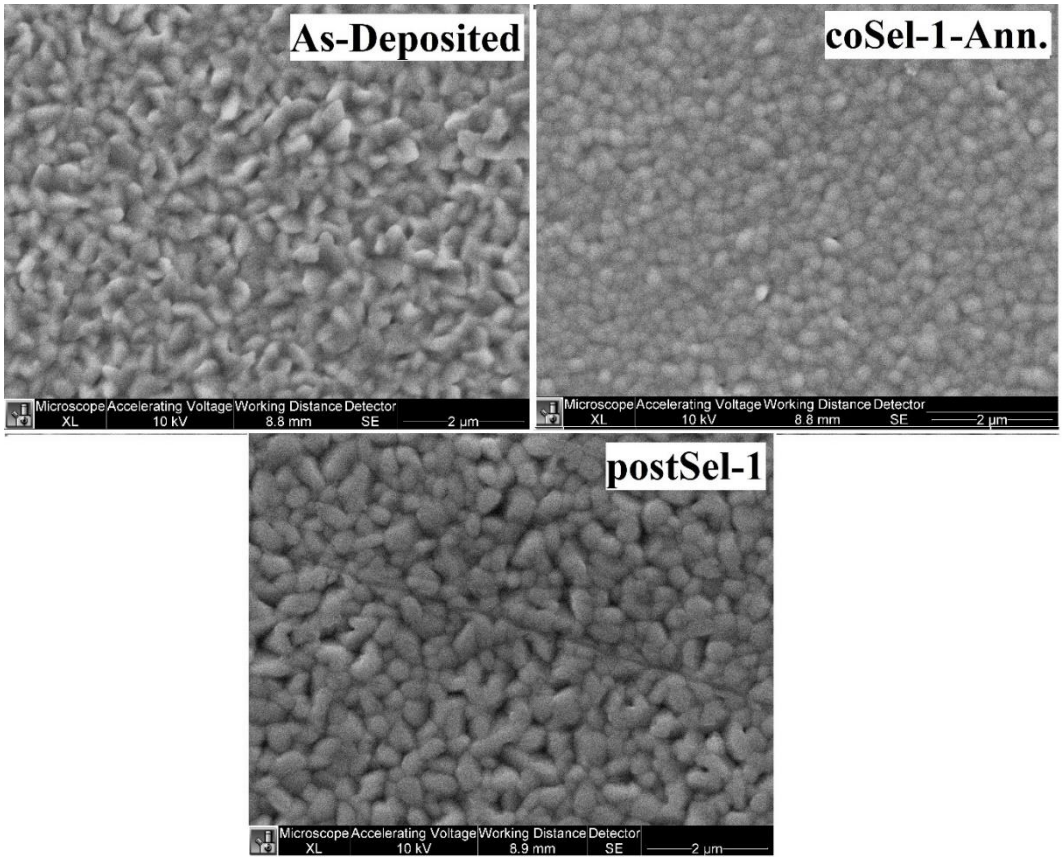

Figure 8.10 . SEM image of the as deposited, co and post-selenized samples.

In fig. 8.10 the SEM pictures of the of the as deposited, co and post-selenized samples confirm the morphology observed with AFM, however these wider views give a clearer idea of the homogeneity of the structure: the enhanced grain size is even more evident for the post-selenized layer while for the co-selenized absorbers reported reduction in grain size.

Raman analysis of as-deposited, co-selenized and post-selenized samples, shown in fig. 8.11, demonstrates the overall absence of large number of secondary phases. All the samples deliver a very similar spectrum, with the main Sb_2Se_3 peaks at the same position without evident shifts to highlight. Indicating that during co-selenization as well as post-deposition selenization no elemental selenium phase is formed, and the stoichiometry is preserved.

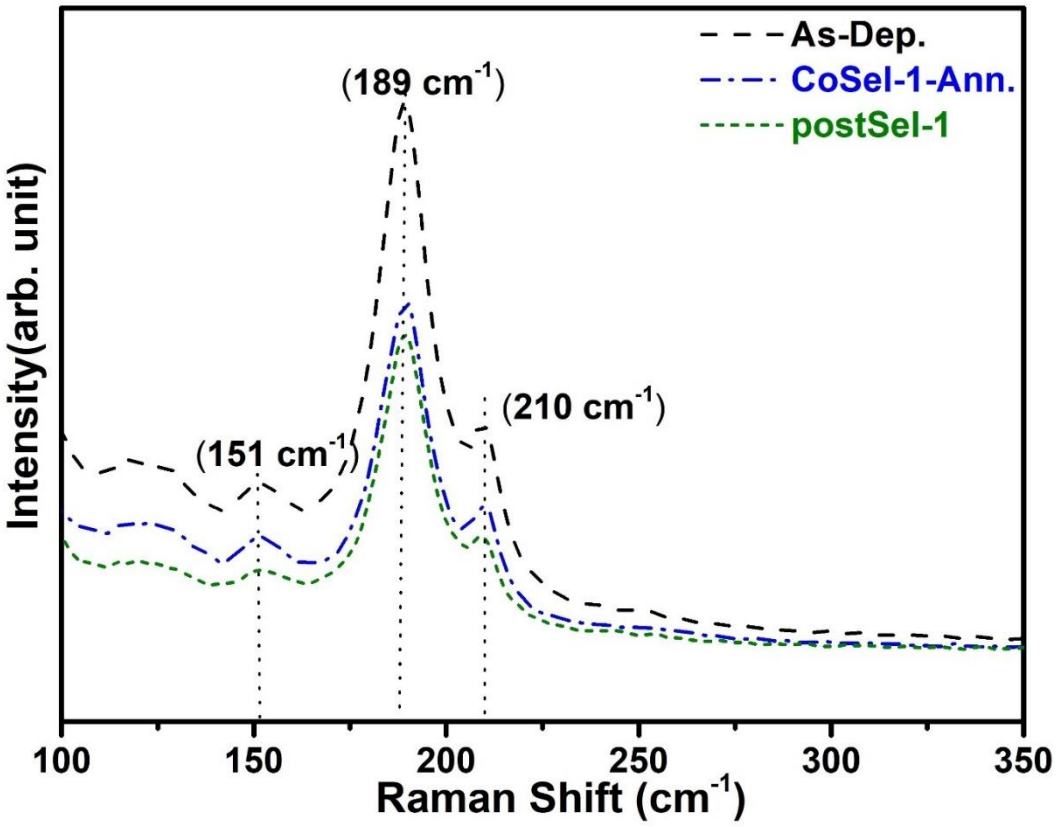

Figure 8.11. Raman spectra of the as deposited, co and post-selenized samples.

8.1.3 Electrical Study.

In this section we did the electrical study of the samples in order to analyze the effect of Se inclusion on the cell performance, efficiencies together with electrical parameters of the superstrate TEC/CdS/Sb_2Se_3/Au devices are summarized in Table. 8.V (a, b). Moreover, the J-V characteristics of the devices are presented in Fig. 8.12 Efficiencies are very different when as-deposited and co-selenized is compared.

As a matter of fact, the best device with as-deposited absorber layer shows an open circuit voltage (V_{oc}) of 289 mV, a fill factor (F.F.) of 45.4 %, and a very low short circuit current density (J_{sc}) of 12 mA/cm^2, corresponding to a power conversion efficiency of 1.57 %.

For devices made with absorber deposited by co-selenization at different rates (R=2, R=1, R=0.5) a maximum V_{oc} of 317 mV, J_{sc} of 25.8 mA/cm^2, with a F.F. of 43.4 %

(conversion efficiency of 3.55 %) are obtained in the R=1 case. The champion cell of post-selenized sample, again the R=1 case, registers PCE of 3.45%, V_{oc} of 345 mV, J_{sc} of 25 mA/cm^2 with a F.F. of 40.7 %. In any case we can observe for this kind of devices a further increase in current density.

This behavior can be explained if we examine the EQE presented in Fig. 8.13. The device corresponding to the as-deposited absorber case shows a very low response on all range of wavelengths which highlights a general low quality of the absorber material with a large loss in carrier collection. On the other hand, the co-selenized absorber layers deliver devices which have a larger EQE response in the long wavelength region, above 750 nm. However, these devices have a slight reduction in EQE in the 500 nm region, which suggests the deterioration of the junction. This explains why we measure a higher current density in these cases, but the overall efficiency remains the same.

If we now consider the EQE of the devices made with post-deposition selenization, we register a further improvement of the EQE in the long wavelength region, and again the result is a slight increase in short current density. However, for these devices the loss in the short wavelength's region is even larger. This suggests that incorporation of additional selenium on the back improves the performance of the semiconductor by possibly increasing lifetime and reducing recombination effects and enhancing the overall quality of the back contact.

The presence of CdS is clearly observed in the XRD for as deposited absorbers, less observed in the co-selenized absorbers and least observed in the post-deposition absorbers. The lower the CdS peaks, the lower the response in the short wavelength region, but at the same time the higher the response at long wavelengths. The reduced detectability of CdS peaks, culminating in their almost total suppression in the post-selenized samples, suggests that there is a decomposition of the window layer at the junction due to the increased presence and diffusion of Se in the layer. Besides, in previous studies on $CdSe_xTe_{1-x}$ based solar cells [12], we have already proved the degradation of the CdS after the selenization of the layer above it. Moreover, the collapse of the EQE response occurs between 750 nm and 700 nm, which is the wavelength region corresponding to the bang gap of CdSe (around 1.72 eV),

indicating the possible formation of this not photoactive compound at the junction. Thus, while the stoichiometry of the absorber is enhanced by the co-selenization and even more by

the post-selenization process, the quality of the junction deteriorates; the presence of the CdS appears to be a limiting factor in improving the devices. A possible solution could be the replacement of the CdS with a more suitable buffer layer, such as TiO_2.

In any case, we would like to highlight that the efficiencies reported between 3.5 % 3.6% despite not being the highest in absolute terms, are to our knowledge the highest obtained with low temperature vacuum evaporation and with CdS buffer layer.

Table 8. V(a). Statistics of device performance for Sb_2Se_3 solar cells with as deposited and co-selenization at different rates.

Sample I.D	V_{oc} (mV)	J_{sc} (mA/cm^2)	FF (%)	η (%)
As-Dep	289	12	45.4	1.57
coSel-1	345	22.2	39.7	3.05
coSel-0.5-Ann	324	25.3	42.6	3.5
coSel-1-Ann	317	25.8	43.4	3.55
coSel-2-Ann	324	22.9	39	2.89

Table 8. V(b). Statistics of device performance for post-selenized samples.

Sample I.D	V_{oc} (mV)	J_{sc} (mA/cm^2)	FF (%)	η (%)
postSel-0.5	303	19.3	39.6	2.32
postSel-1	345	25	40	3.45
postSel-2	331	23.0	40.7	3.1

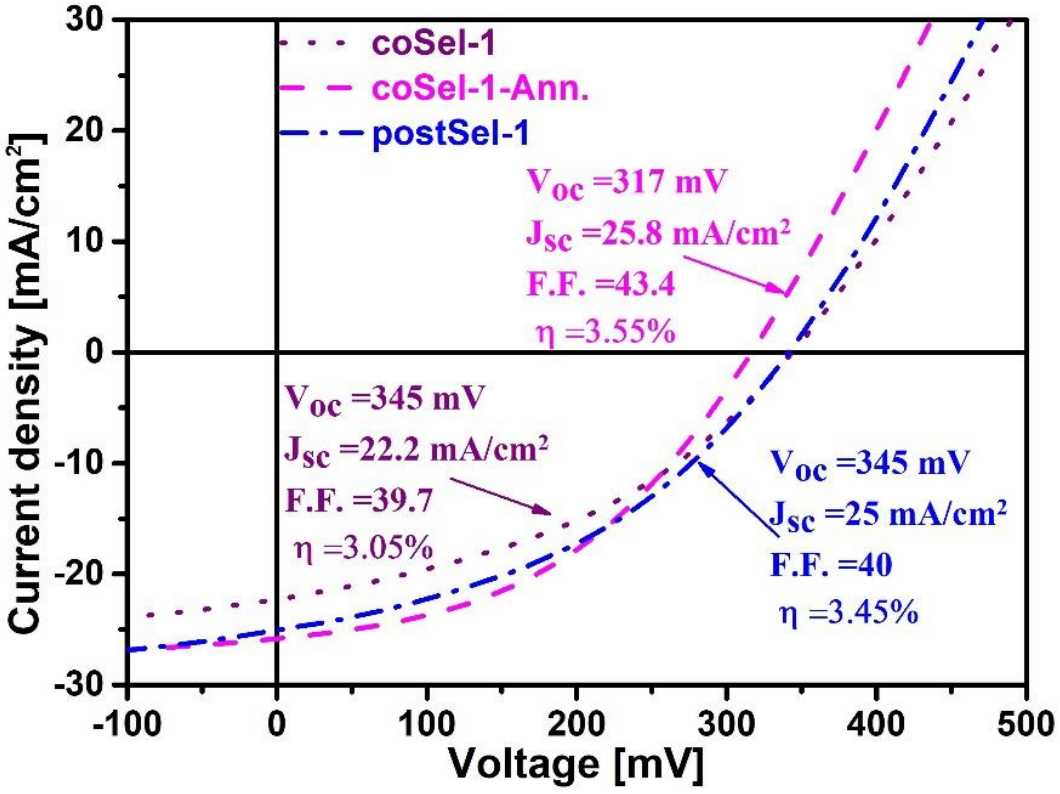

Figure 8.12. J-V curves of the co-selenized and post-selenized samples.

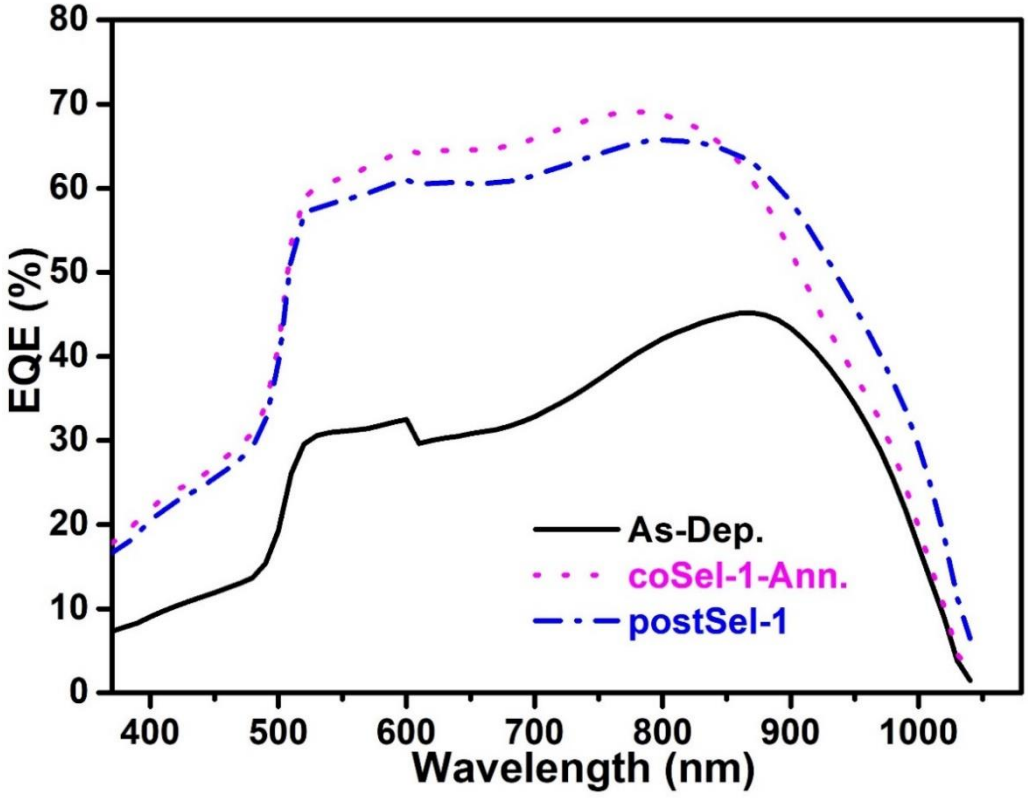

Figure 8.13. EQE spectra of the as deposited, co and post-selenized devices.

8.1.4 Conclusion.

To summarize, we systematically investigated in situ selenization of the superstrate Sb_2Se_3 films. From the measurements and analysis, we conclude that selenization plays a key role in improving the absorber quality, possibly compensating Se loss which occurs during thermal evaporation and vacuum annealing. The crystal growth is strongly affected by the co-selenization and/or post deposition treatments, Sb_2Se_3 layers show a good orientation on the first place, by organizing along the c line perpendicularly to the substrate. With co-selenization the crystal structure changes, the CdS is reduced, and the orientation of the grains is more randomly distributed, furthermore the grain size is generally decreased, and the a-lattice parameter is shrinked. However, the crystal quality improves when Se is added by post-deposition treatment, resulting in larger and more compact morphology. In this case the a-lattice path is enlarged getting closer to standard Sb_2Se_3 values, while micro strain is observed. Finally, the presence of CdS peaks is almost totally suppressed.

The selenium treatments lead to an enhanced current density observed by J-V characterization and confirmed by external quantum efficiency, where a remarkable gain at long wavelengths is observed; this effect is stronger for post-deposition selenium incorporation. However, the reduced response in the short wavelength range does not allow for champion efficiency.

8.2 Ex-situ or post deposition selenization.

In the presented work, Antimony selenide (Sb_2Se_3) based thin films have been grown in superstrate configuration by low temperature thermal evaporation process. For re-incorporation of Se to adjust the stoichiometry and increase crystallization of the absorber has been done in this paper. Solar cells were fabricated in the superstrate configuration of Glass/ITO/ZnO/CdS/Sb_2Se_3/Cu/Au. Post deposition selenization of the as deposited samples at 300 and 400 °C in argon environment were carried out.

8.2.1 Preparation of device.

Antimony selenide (Sb_2Se_3) absorber based thin film solar cells were deposited in superstrate configuration by a low-temperature fabrication process based on vacuum evaporation (VE). In order to understand its properties, we have preferred to study the absorber when deposited on stack with its typical device configuration. More in detail, by radio frequency (RF)-magnetron sputtering we deposited a stack of 400 nm thick indium tin oxide (ITO) film on a soda-lime glass with 90 % In_2O_3 and 10 % SnO_2 target in Ar + 2 % O_2 atmosphere and with a substrate temperature of 400 °C. Subsequently, by RF magnetron sputtering we deposited a 100 nm thick i-ZnO film, in an atmosphere of Ar + 2 % O_2, again with a substrate temperature of 400 °C. The stack was then annealed in vacuum at 10^{-4} Pa at 450 °C.

On the ITO/ZnO stack, CdS was deposited by thermal evaporation at a pressure of 10^{-4} Pa, and substrate temperature of 150 °C, with a thickness of 150 nm. To improve its crystalline structure, the layer was subsequently annealed in vacuum at 450 °C. The samples were then moved into a different vacuum evaporation chamber, with a fine control of crucible temperature, where Sb_2Se_3 was deposited on the Glass/ITO/ZnO/CdS stack. The material source (Sb_2Se_3 lumps) was heated at a temperature ranging from 700 to 800 °C in order to be evaporated at a deposition rate of approximately 0.3 nm/sec. Absorbers with thickness of 700 nm were deposited at a base pressure of $3.6x10^{-4}$ Pa and with a substrate temperature of 320 °C. Post deposition selenium treatment were carried out by heating each Sb_2Se_3 sample with Se pallets at temperature 300 °C and 400 °C at 200 mbar, in argon environment, for 30 minutes.

8.2.2 Characterization.

X-ray diffraction analysis of the Sb_2Se_3 films on Glass/ITO/ZnO/CdS stacks are shown in Figure 8.14, in particular: as deposited and selenized samples (at two different temperatures: 300 °C and 400 °C). The diffraction peaks correspond to the orthorhombic Sb_2Se_3 (JCPDS 15-0861) [3,4]. Selenization treatment at 300 °C exhibits strong (221), (211) peaks as compared to the selenization done at 400 °C. However, both films show a slightly increased orientation suggesting that a positive

recrystallisation of the grains is occurred. The films exhibit both [hk1] and [hk0] orientation peaks, of which the preferrable [hk1] reflections are dominant. These planes consist of one –dimensional $(Sb_4Se_6)_n$ ribbon standing on the substrate with a certain angle making is easier for the carrier transportation compared to [hk0] planes which are parallel to the substrate [5].

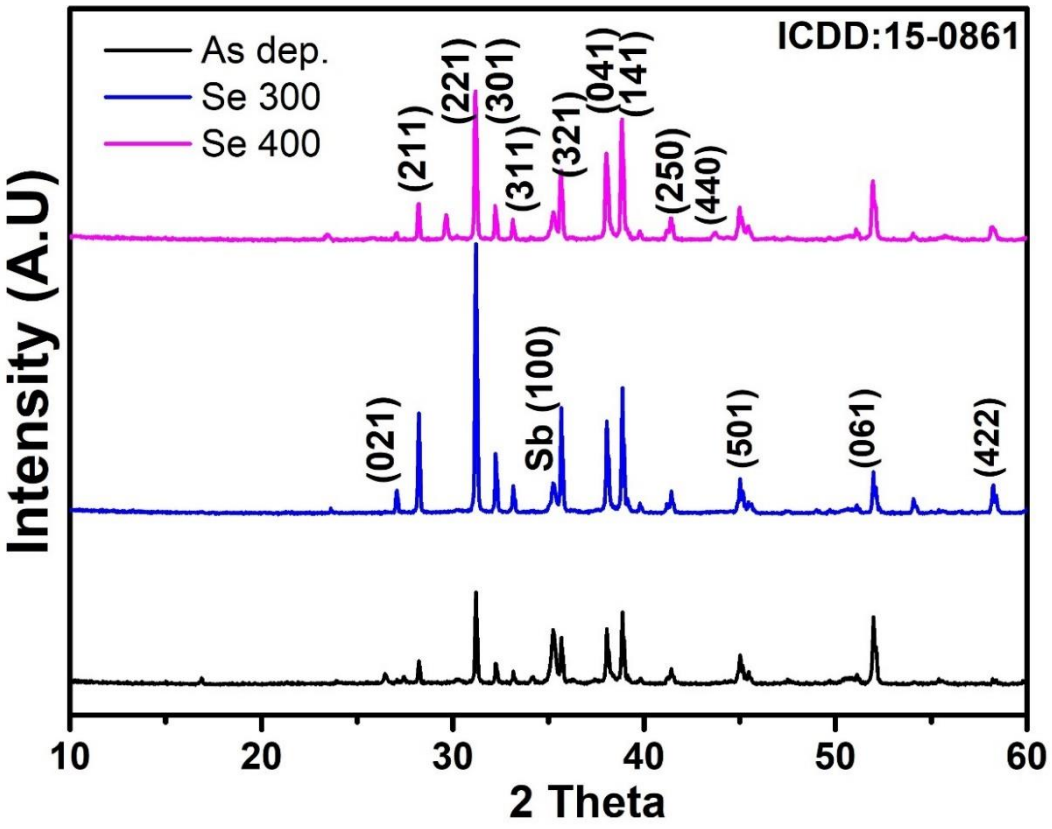

Figure 8.14. X-ray diffraction patterns of Sb_2Se_3 films: as deposited, selenized at 300°C and selenized at 400°C.

Moreover, a peak at of pure antimony is strongly reduced after post-deposition treatment, demonstrating that the selenization of the layer is a good path for improving the absorber stoichiometry.

This is quite coherent with the XRD analysis, the observed recrystallization is confirmed and the selenization treatment shows the ability in improving the crystal quality of the Sb_2Se_3 layers.

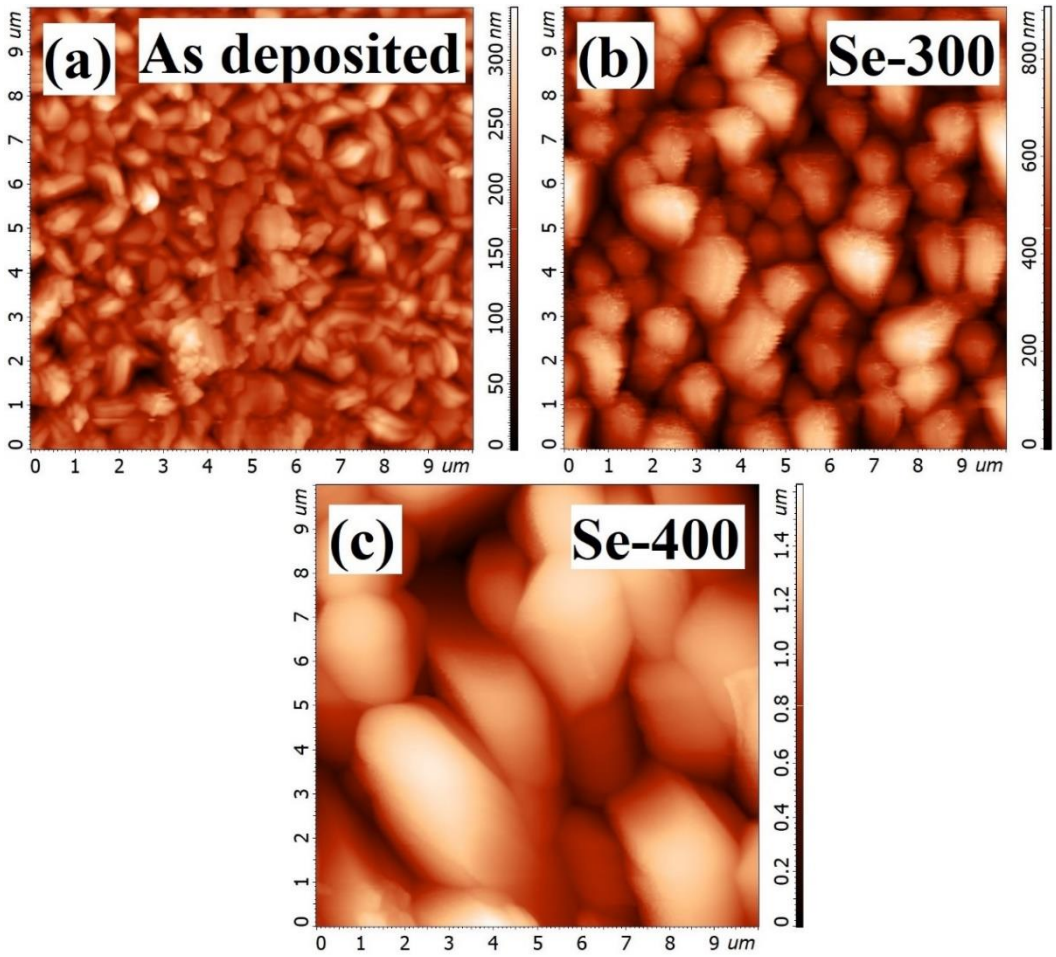

Figure 8.15. Schematic view of (a) as deposited, (b) selenized at 300 °C, (c) and selenized at 400 °C.

In order to analyze the morphology of the as deposited and treated absorber layers and understand the effects of post deposition treatment on their structure, AFM analysis was performed. In figure 8.15, the AFM pictures of as-deposited Sb_2Se_3 layers (a), selenized at 300 °C (b) and 400 °C (c). The films are compact, free of cracks and pinholes, nevertheless after selenization the absorbers show a very different morphology. The layers selenized at 300 °C show an enlargement of the grain size and at the same time a reduced compactness of the films. On the other hand, Sb_2Se_3 selenized at 400°C reveal a further enhancement of the grain size but also a structural rearrangement in agglomerates and generation of much bigger grains in the order of up to 5 micrometers. This is quite coherent with the XRD analysis, the observed recrystallization is confirmed and the selenization treatment shows the ability in improving the crystal quality of the Sb_2Se_3 layers.

More details about the structure of Sb_2Se_3 thin film were obtained from Raman scattering spectra. The three different films perform a very similar spectrum, with same peaks all attributable to the stoichiometric Sb_2Se_3 as shown in fig 8.15. The peaks around 152 cm^{-1}, 192 cm^{-1} and 211 cm^{-1} are assigned to Sb_2Se_3 orthorhombic phase. The main peak, at 192 cm^{-1}, is largely reduced for the 400 °C selenized case, this suggests a gradual degradation of the material quality in terms of composition, that cannot be judged by the AFM analysis where we observe that higher the temperature the larger the grain size.

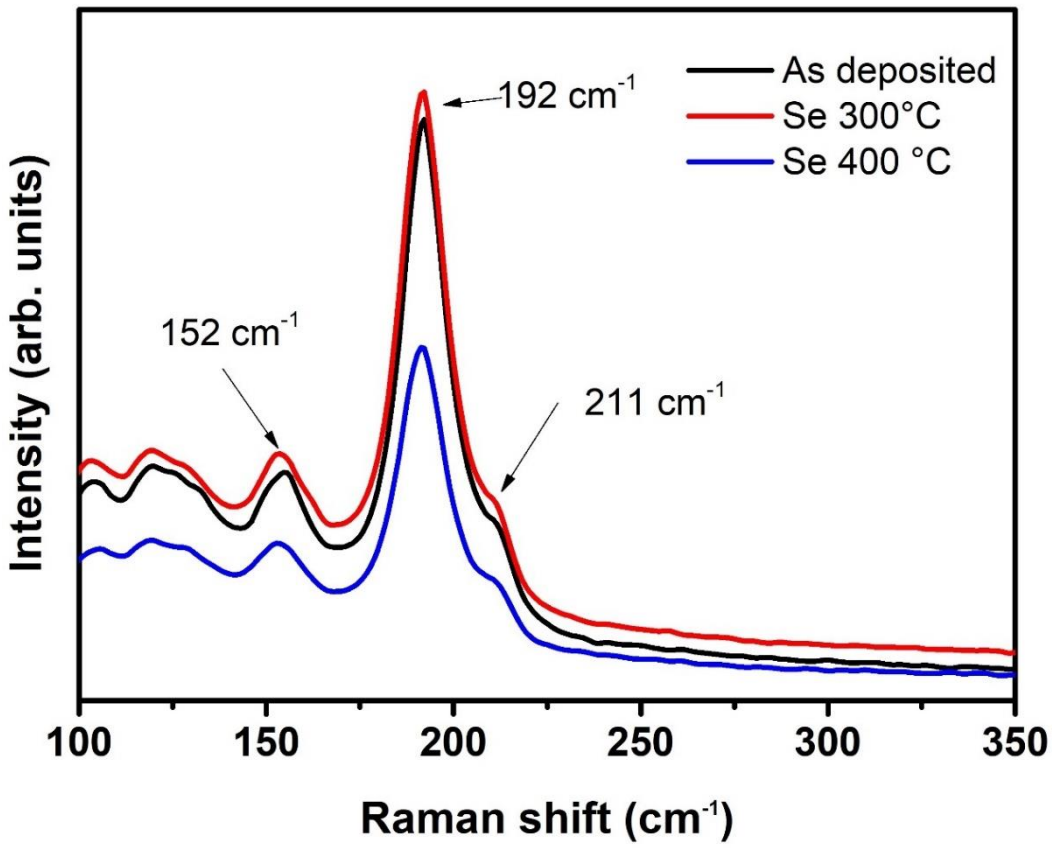

Figure 8.15: Raman Spectra of Sb_2Se_3 absorbers deposited on the CdS/ZnO/ITO stack: as deposited, selenized at 300 °C and selenized at 400 °C.

8.2.3 Electrical study.

Many devices have been prepared with and without selenized absorber layers. The J-Vs of best devices with as-deposited and selenized Sb_2Se_3 are shown in fig. 8.16. and

8.17. respectively. As-deposited Sb_2Se_3 based devices delivered conversion efficiencies of 2.7% as shown in fig. 8.16. The solar cells have been annealed at 190 °C in air after back contact deposition. In fig 8.17, a sharp decrease in the performance is observed after selenization, which is in contrast of what has been reported above in terms of material quality. The efficiency reduction is mainly due to the large decrease in current and fill factor with an increase of series resistance. Moreover, for the 400 °C treated absorber case a double diode effect is observed. Post deposition Selenization of the deposited sample under Argon environment shows PCE of 1 %.

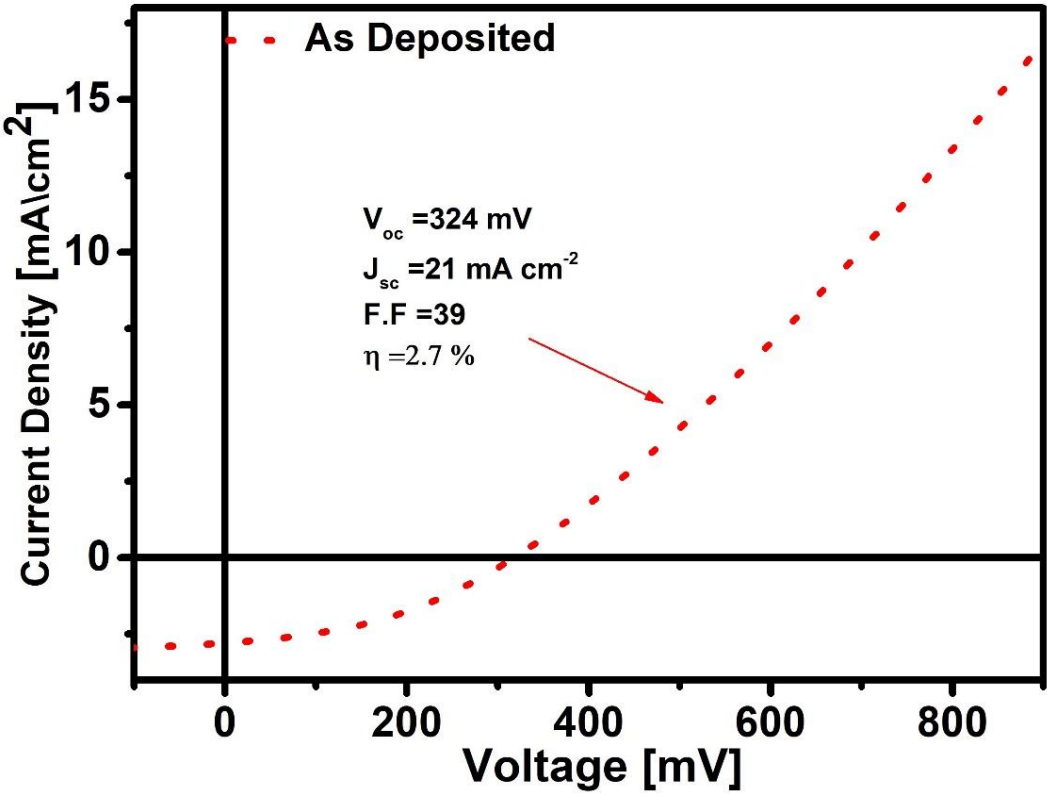

Figure 8.16. J-V characteristics of Sb_2Se_3 based solar cells as-deposited.

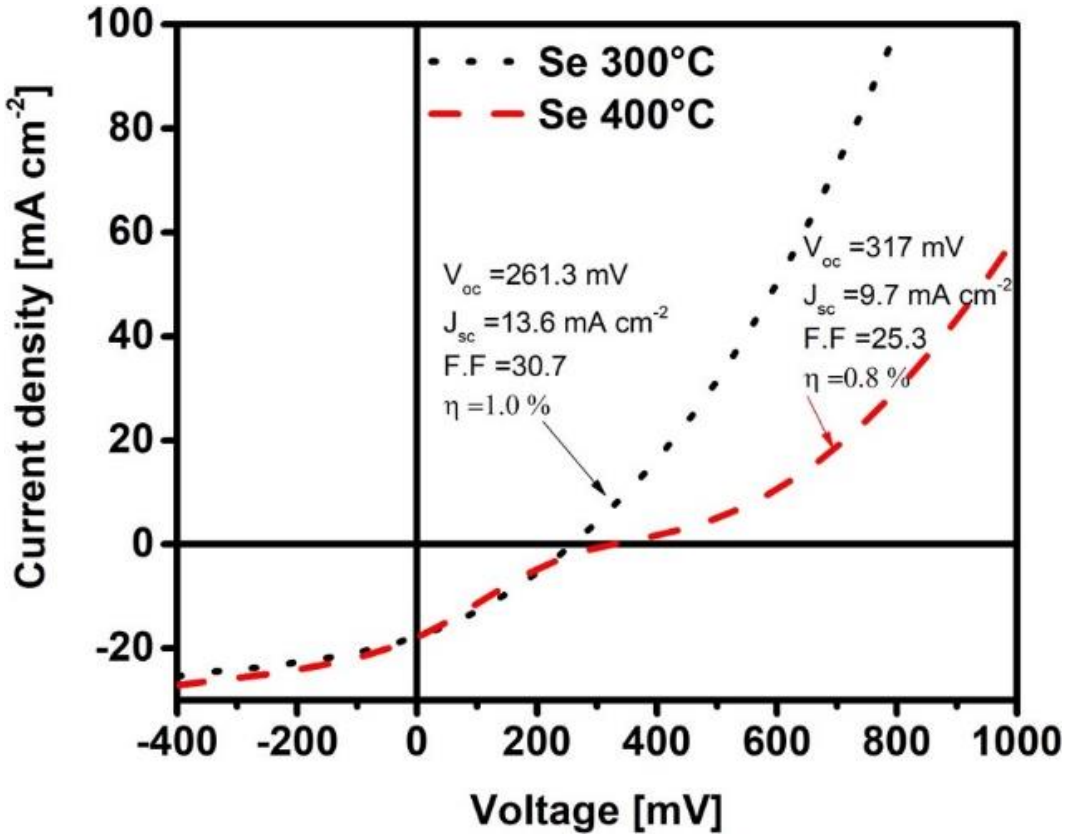

Figure 8.17. J-V characteristics of salinized Sb_2Se_3 based solar cells at 300 and 400 °C.

8.2.4 Conclusion.

Antimony Selenide thin films were deposited by thermal evaporation and selenized at different temperatures. Selenized samples show an increased grain size as selenization temperature increases, with a change in morphology when 400 °C is reached. The X-ray diffraction analysis suggests the formation of crystalline films with the preferred [hk1] orientations, with a slight increase when selenization is applied. Raman spectra suggest a small degradation of the sample with 400 °C but confirms for all the layers the correct Sb_2Se_3 stoichiometry. On the contrary the efficiencies of devices with selenized samples are reduced. In summary the selenization procedure is a promising step for increasing device quality but more investigation must be done in order to improve junction quality. Post deposition Selenization of the deposited sample under Argon environment shows that the champion solar cell showed a conversion efficiency of 1.0 % with a V_{oc} of 261.3 mV, Jsc of 13.6 mA cm^{-2} and FF of 30.7% which is less than the as deposited sample.

8.3 Chemical etching of Sb_2Se_3 solar cells.

Sb_2Se_3 solar cells have record power conversion efficiency at near 10% [13]. The device performance depends on the orientation of the nanoribbon it is for this reason most of the stress is given on the deposition condition, and also to optimise it [14][13][15][16]. The behaviour of the front contact and back contact are still poorly understood. Free elemental selenium and Sb_2O_3 have been identified at the surface of Sb_2Se_3 films, however the impact of this on device performance have not yet been properly investigated [17][18]. Surface modification can lead to an enhanced performance of the device. Br-MeOH, methyl ammonium iodide, hydrogen iodide are the commonly used etching agents for surface modification [19,20]. In this work we will use Br-MeOH etching for surface treatment of the as deposited and post-selenized samples as the probability of unreacted selenium is highest in the post-selenized case.

8.3.1 Br-MeOH treatment and study.

The sample preparation method has already been discussed in chapter 8.2, after the deposition of Sb_2Se_3 the samples are treated with Br-MeOH. We take 40 ml of methanol and add 4 drops of bromine, then Sb_2Se_3 is dipped for 2 secs and then immediately washed and dried with argon gas, post etching gold back is deposited via thermal evaporation and cell performance is studied. The X-ray diffraction study of the treated sample has been done but it does not suggest any change major change in the crystallographic orientation and is represented in fig 8.18. All the dominant (hk1) are found to be present, post Br-MeOH treatment there is a slight increment in the intensity of the (hk1) peaks suggesting a slight modification in crystallinity leading to a better performance of the solar cells.

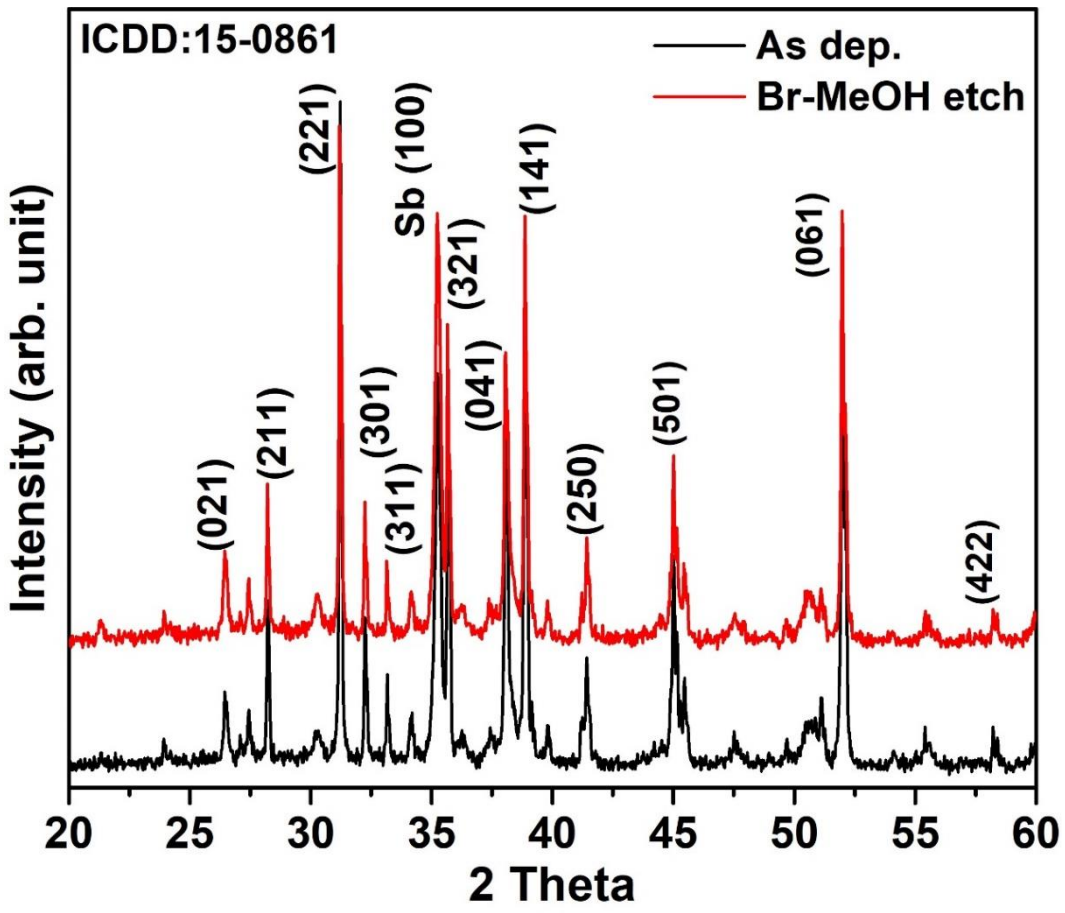

Figure 8.18: X-ray diffraction patterns of Sb_2Se_3 films: as-deposited, as-deposited after Br-MeOH etching.

8.3.2 Electrical Study.

The J-V of the best devices with as-deposited and bromine ethanol etched Sb_2Se_3 respectively are shown in fig 8.19 and 8.20. J-V of as-deposited Sb_2Se_3 based devices with and without bromine methanol etching delivered conversion efficiencies between 2 and 3%.

The J-V behavior is like the non-etched ones but there is a significative increase in open circuit voltage which suggests that one detrimental effect is in the surface of the absorber where selenium in excess could have been deposited. The V_{oc} is larger than the initial as deposited samples, confirming that the quality of the absorber layer has improved, but on the other hand current and fill factor values remain low. Which suggests a gradual degradation of the junction with the increase of the annealing temperature that gives place to a non requested counterbalance in the efficiency improvement.

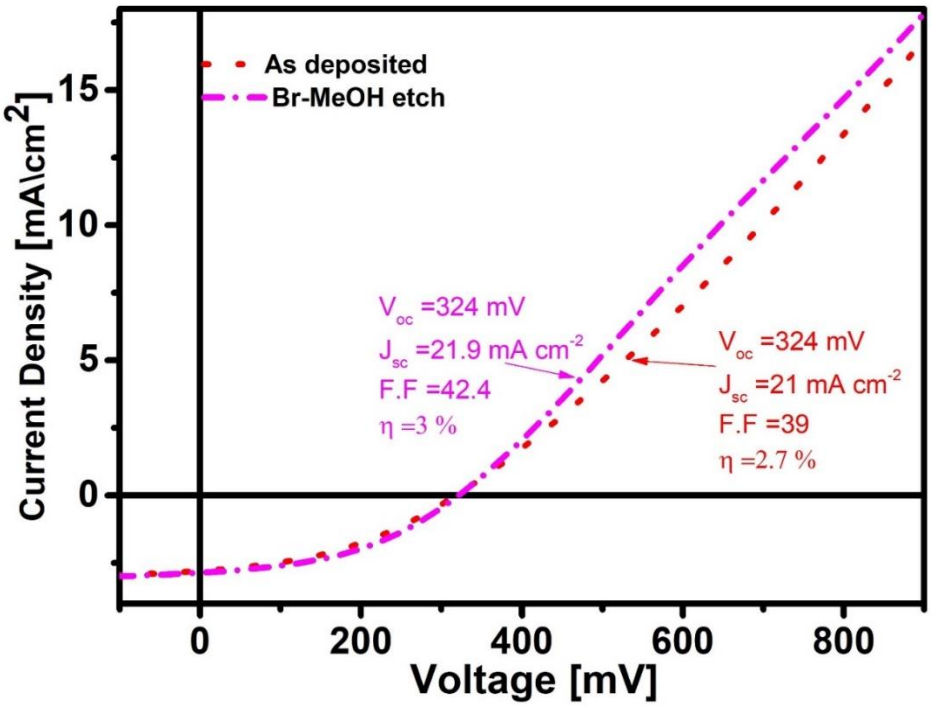

Figure 8.19. J-V characteristics of as-deposited and Br-MeOH etched Sb_2Se_3 solar cells.

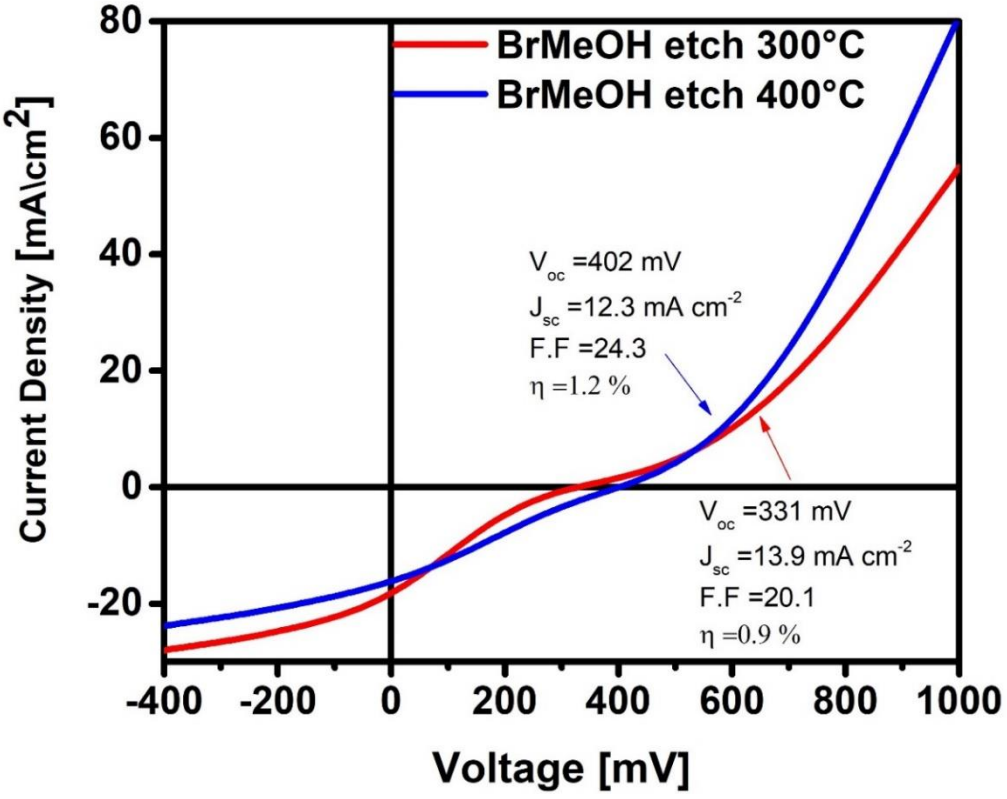

Figure 8.20. J-V characteristics of finished solar cells with Br-MeOH etched Sb_2Se_3 absorbers for both 300 and 400 °C.

8.3.3 Conclusion.

This work shows the material and the electrical characterization of the as deposited and Br-MeOH etched samples, the study reveals the preferred [hk1] orientation of the Sb_2Se_3 deposited via thermal evaporation for both with a better device performance for bromine ethanol etched one. Post deposition selenization of the deposited sample under argon environment shows the champion solar cell delivered a conversion efficiency of 1.2 % with a V_{oc} of 402 mV and FF of 24.3%, the analysis reveals that Br-MeOH etching led to an increase in V_{oc} by 25 % and the F.F increases by nearly 20 %. Overall, the study clarifies the role of etching and provides us with the insight in optimizing Sb_2Se_3 back contact.

8.4 Reference.

[1] X. Liu, J. Chen, M. Luo, M. Leng, Z. Xia, Y. Zhou, S. Qin, D.J. Xue, L. Lv, H. Huang, D. Niu, J. Tang, Thermal evaporation and characterization of Sb2Se3thin film for substrate Sb2Se3/CdS solar cells, ACS Appl. Mater. Interfaces. 6 (2014) 10687–10695. https://doi.org/10.1021/am502427s.

[2] A. Maiti, S. Chatterjee, A.J. Pal, Sulfur-Vacancy Passivation in Solution-Processed Sb2S3 Thin Films: Influence on Photovoltaic Interfaces, ACS Appl. Energy Mater. 3 (2020) 810–821. https://doi.org/10.1021/acsaem.9b01951.

[3] Y. Zhou, Y. Li, J. Luo, D. Li, X. Liu, C. Chen, H. Song, J. Ma, D.J. Xue, B. Yang, J. Tang, Buried homojunction in CdS/Sb2Se3 thin film photovoltaics generated by interfacial diffusion, Appl. Phys. Lett. 111 (2017). https://doi.org/10.1063/1.4991539.

[4] L. Guo, C. Grice, B. Zhang, S. Xing, L. Li, X. Qian, F. Yan, Improved stability and efficiency of CdSe/Sb2Se3 thin-film solar cells, Sol. Energy. 188 (2019) 586–592. https://doi.org/10.1016/j.solener.2019.06.042.

[5] S. Polivtseva, J.O. Adegite, J. Kois, D. Mamedov, S.Z. Karazhanov, J. Maricheva, O. Volobujeva, A novel thermochemical metal halide treatment for high-performance Sb2Se3 photocathodes, Nanomaterials. 11 (2021) 1–14. https://doi.org/10.3390/nano11010052.

[6] N.J. Mathew, R. Oommen, U.R. P, J.M. N, STRUCTURAL AND MORPHOLOGICAL STUDIES OF Sb 2 S 3 THIN FILMS, J. Ovonic Res. 6

(2010) 259–266.

[7] P. Paufler, R. A. Young (ed.). The Rietveld Method. International Union of Crystallography. Oxford University Press 1993. 298 p. Price £ 45.00. ISBN 0–19–855577–6, Cryst. Res. Technol. 30 (1995). https://doi.org/10.1002/crat.2170300412.

[8] L. Lutterotti, S. Gialanella, X-ray diffraction characterization of heavily deformed metallic specimens, Acta Mater. 46 (1998). https://doi.org/10.1016/S1359-6454(97)00222-X.

[9] A. Mavlonov, T. Razykov, F. Raziq, J. Gan, J. Chantana, Y. Kawano, T. Nishimura, H. Wei, A. Zakutayev, T. Minemoto, X. Zu, S. Li, L. Qiao, A review of Sb2Se3 photovoltaic absorber materials and thin-film solar cells, Sol. Energy. 201 (2020) 227–246. https://doi.org/10.1016/j.solener.2020.03.009.

[10] V.L. Deringer, R.P. Stoffel, M. Wuttig, R. Dronskowski, Vibrational properties and bonding nature of Sb2Se3 and their implications for chalcogenide materials, Chem. Sci. 6 (2015) 5255–5262. https://doi.org/10.1039/c5sc00825e.

[11] Y. Zhou, M. Leng, Z. Xia, J. Zhong, H. Song, X. Liu, B. Yang, J. Zhang, J. Chen, K. Zhou, J. Han, Y. Cheng, J. Tang, Solution-processed antimony selenide heterojunction solar cells, Adv. Energy Mater. 4 (2014) 4–11. https://doi.org/10.1002/aenm.201301846.

[12] E. Artegiani, A. Gasparotto, P. Punathil, V. Kumar, M. Barbato, M. Meneghini, G. Meneghesso, F. Piccinelli, A. Romeo, A new method for CdSexTe1-x band grading for high efficiency thin-absorber CdTe solar cells, Sol. Energy Mater. Sol. Cells. 226 (2021) 111081. https://doi.org/10.1016/j.solmat.2021.111081.

[13] Z. Li, X. Liang, G. Li, H. Liu, H. Zhang, J. Guo, J. Chen, K. Shen, X. San, W. Yu, R.E.I. Schropp, Y. Mai, 9.2%-Efficient Core-Shell Structured Antimony Selenide Nanorod Array Solar Cells, Nat. Commun. 10 (2019) 1–9. https://doi.org/10.1038/s41467-018-07903-6.

[14] Y. Zhou, L. Wang, S. Chen, S. Qin, X. Liu, J. Chen, D.J. Xue, M. Luo, Y. Cao, Y. Cheng, E.H. Sargent, J. Tang, Thin-film Sb2Se3 photovoltaics with oriented one-dimensional ribbons and benign grain boundaries, Nat. Photonics. 9 (2015) 409–415. https://doi.org/10.1038/nphoton.2015.78.

[15] X. Liu, J. Chen, M. Luo, M. Leng, Z. Xia, Y. Zhou, S. Qin, D. Xue, L. Lv, H. Huang, D. Niu, J. Tang, Thermal Evaporation and Characterization of Sb 2 Se 3 Thin Film for Substrate Sb 2 Se 3 / CdS Solar Cells, (2014).

[16] D.B. Li, X. Yin, C.R. Grice, L. Guan, Z. Song, C. Wang, C. Chen, K. Li, A.J. Cimaroli, R.A. Awni, D. Zhao, H. Song, W. Tang, Y. Yan, J. Tang, Stable and efficient CdS/Sb2Se3 solar cells prepared by scalable close space sublimation, Nano Energy. 49 (2018) 346–353. https://doi.org/10.1016/j.nanoen.2018.04.044.

[17] L. Wang, D.B. Li, K. Li, C. Chen, H.X. Deng, L. Gao, Y. Zhao, F. Jiang, L. Li, F. Huang, Y. He, H. Song, G. Niu, J. Tang, Stable 6%-efficient Sb2Se3 solar cells with a ZnO buffer layer, Nat. Energy. 2 (2017) 1–9. https://doi.org/10.1038/nenergy.2017.46.

[18] C. Chen, Y. Zhao, S. Lu, K. Li, Y. Li, B. Yang, W. Chen, L. Wang, D. Li, H. Deng, F. Yi, J. Tang, Accelerated Optimization of TiO2/Sb2Se3 Thin Film Solar Cells by High-Throughput Combinatorial Approach, Adv. Energy Mater. 7 (2017) 1–8. https://doi.org/10.1002/aenm.201700866.

[19] R.A. Awni, D.B. Li, C.R. Grice, Z. Song, M.A. Razooqi, A.B. Phillips, S.S. Bista, P.J. Roland, F.K. Alfadhili, R.J. Ellingson, M.J. Heben, J. V. Li, Y. Yan, The Effects of Hydrogen Iodide Back Surface Treatment on CdTe Solar Cells, Sol. RRL. 3 (2019) 1–9. https://doi.org/10.1002/solr.201800304.

[20] S.C. Watthage, A.B. Phillips, G.K. Liyanage, Z. Song, J.M. Gibbs, F.K. Alfadhili, R.B. Alkhayat, R.H. Ahangharnejhad, Z.S. Almutawah, K.P. Bhandari, R.J. Ellingson, M.J. Heben, Selective Cd removal from CdTe for high-efficiency te back-contact formation, IEEE J. Photovoltaics. 8 (2018) 1125–1131. https://doi.org/10.1109/JPHOTOV.2018.2830302.

Chapter 9
Conclusion & future prospect

In our laboratory, superstrate configuration of Sb_2Se_3 solar cells were fabricated by low temperature thermal evaporation process and achieving an efficiency greater than 3.5%. Continuous study and optimization of our processes will lead to a higher efficiency for the Sb_2Se_3 based devices. In this thesis, we focused on the study of the solar cell buffer layer, Sb_2Se_3 absorber layer, front contact, back contact, selenization and etching. The thesis completely covers the proposed objectives. Structural properties and phase purities of the films were investigated by XRD and Raman spectroscopy. Elemental compositions of the films were calculated by EDXS equipped with SEM. The important photovoltaic properties such as band gap and absorption coefficient were calculated from the UV-visible absorption spectra. The major results obtained from this work are discussed below:

1) To study the influence of buffer layer, 3 types of buffer layers were used. Various thickness of CdS film (50, 90, 150 nm) were grown via thermal evaporation followed by Sb_2Se_3 growth. XRD registered the preferred (hk1) planes, where the champion cell reported an efficiency of 1.7% with 150 nm CdS thickness. CdS deposited via chemical bath deposition shows dense and pin-hole free Sb_2Se_3 film growth and showed an efficiency of 1.5%. The reported band gap of CdS grown by thermal evaporation and CBD are 2.4 and 2.37 eV respectively. Finally, TiO_2 buffer layer was studied with varying thickness using spin coating technique. Film grown on TiO_2 shows pronounced (hk0) plane with band gap of 3.97 eV and the reported efficiency of the champion cell was less than 0.5% with 5 drops of TiO_2. In conclusion we can say that the performance of the CdS by thermal evaporation and CBD are near about the same, but TiO_2 buffer layer requires more in-depth study.

2) The optimized thickness of the absorber layer deposited by thermal evaporation was 450 nm. The work revealed the preferred (hk1) plane for the 1D Sb_2Se_3. The SEM and the AFM images reveal that the films are homogeneous, crack free with fewer pin holes. Finally, the study also

concludes that the as deposited films are Sb rich which might be the reason for lower performance of the solar cells. To sum up we present non-toxic, stable method of solar-cell fabrication with a certified device efficiency of 2.0 % irrespective of the front contact.

3) Sb_2Se_3 was directly synthesized on ITO/ZnO and FTO/SnO_2 substrate. There is presence of the preferential (hk1) diffraction peaks (211), (221), (061) with both the substrate. Deposited Sb_2Se_3 on ZnO and SnO_2 have average grain size of 4 to 60 nm respectively. The champion cells reported 1.4% on ITO/ZnO front contact.

4) Study of vacuum annealed Sb_2Se_3 at 300 and 350 °C were carried out on Glass/ITO/ZnO/CdS/Sb_2Se_3 and Glass/TEC/CdS/Sb_2Se_3. Superstrate solar cells annealed at 300 °C showed prevalent (hk1) orientation, while samples annealed at 350 °C showed a larger number of (hk0) peaks. The champion cells reported PCE of 2% and 3.65% respectively.

5) Cu was introduced as additional back contact using thermal evaporation which improved the performance of the cell. 5 Å of copper improved the back contact of the device, enhancing the efficiency from 2 % to 3.5 % with the Glass/ITO/ZnO/CdS/Sb_2Se_3 configuration.

6) In situ selenization of the superstrate Sb_2Se_3 films were carried out in the thermal evaporation chamber. The measurements and analysis, conclude that selenization plays a key role in improving the absorber quality. The crystal growth is dependent on the co-selenization and/or post deposition treatments. Co-selenized and post-selenized samples reported PCE of 3.55% and 3.45 % respectively. However, the crystal quality improves when Se is added by post-deposition treatment, resulting in larger and more compact morphology.

7) Post deposition selenization were also performed in argon environment. The best solar cell showed a conversion efficiency of 1.0 % which was less than the as deposited sample. Selenization procedure is a promising step for

increasing device quality, but more study and investigation needs to be done. Br-MeOH etching was performed with the post-selenized samples and a PCE of 1.2% is reported, which was just a slight increase in the efficiency.

In the future, following factors should be considered to improve the PCE of Sb_2Se_3 solar cells:

(1) Enhancement of the photocurrent in the short-wavelength region of the spectrum; by using ZnO, TiO_2, or SnO_2 to improve the EQE in the short-wavelength range. Optimization of the different buffer layer must be done in accordance with the thermal evaporation process.

(2) Carrier management and optimization is one of the most important aspects to be kept in mind. Improvement of the V_{OC} and FF is a complex task and requires device engineering approach to control and passivate the recombination losses of charge carriers, to identify the defects and to measure their formation energies, energy levels, and density.

(3) Lattice matching and band alignment is key to device engineering and optimization of these parameters would help to enhance the PCE and intern the performance.

(4) Improvement of the absorber/back contact interface, aiming to ensure ohmic behavior by surpassing the rollover effect.